Radio Emission from Broad Absorption Line Quasars: Origins and Implications

JAMES WILLIAM PETLEY

Radio Emission from Broad Absorption Line Quasars: Origins and Implications

James Petley

A Thesis presented for the degree of
Doctor of Philosophy

Centre for Extragalactic Astronomy
Department of Physics
Durham University
United Kingdom
July 2024

Abstract

A fraction of quasars display signatures of outflowing winds with velocities of up to $0.1c$ in their UV/optical spectra. These Broad Absorption Line Quasars (BALQSOs) have been studied for over 40 years but a consensus understanding of their appearance is yet to emerge. In particular, BALQSOs have been known to exhibit different behaviour at radio wavelengths to the general population, a key feature that both plausible orientation or evolutionary models must be able to explain.

After providing the necessary background and motivation (Chapters 1 and 2), I build on the study of Morabito et al. (2019) by utilising the second data release of the LOFAR Two Metre Sky Survey to study the largest sample of radio-detected BALQSOs ever assembled. We firmly place BALQSOs in the radio-quiet regime and demonstrate that they have a significant enhancement in radio emission as compared to non-BALQSOs at low frequencies. We use composite optical spectra of different populations to demonstrate that radio-detection is connected to features visible in the wind component of the spectra. Although we cannot determine the origin of radio emission in the vast majority of sources, this provides a clear connection between the radio and the wind itself (Chapter 3).

Following on, I engage with the latest research on radio-quiet quasars by folding in other recently discovered connections between quasar optical spectra and radio emission. Quasars with redder optical colours have been found to show a similar radio enhancement as BALQSOs which is explored deeply in the theses of Lizelke Klindt and Victoria Fawcett both also at Durham University (Klindt, 2022; Fawcett, 2022). Also, quasars with stronger C IV blueshifts as compared to their C IV equivalent widths, also characterised as having a higher *"C*IV *distance"*, show an enhancement in radio-detection fraction. We noted that BALQSOs preferentially occupy the red quasar population and have higher average C IV distances and aimed to elucidate connections and differences between these features. We show that each of these optical features has its own connection to radio-detection fraction although colour seems to be the most dominant. We also apply the current standard for estimating radio emission from wind shocks and find that they can plausibly explain a substantial fraction of radio emission in radio-quiet quasars with only moderate efficiencies, suggesting advancement of these models is needed in order for them to become useful discriminatory tools (Chapter 5).

During the course of Chapter 3, I discovered differences in the relationship be-

tween radio-detected HiBALs and LoBALs, the two key subsets of BALQSOs. LoBALs showed more dramatic changes in their optical spectra when radio-detected as compared to HiBALs. We therefore designed a study to compare similar HiBALs and LoBALs at high resolution. We utilise the eMERLIN radio interferometer to obtain sub-arcsecond images of ten sources and study their radio properties on kpc scales (Chapter 6). We find only one of the sources is resolved, indicating very compact emission for these BALQSOs. LoBALs appear to retain a greater fraction of their flux at high resolution although this is tempered by having to extrapolate fluxes from low frequencies for many of the sources. For sources with similar wind properties, the red sources appear to be brighter and retain a greater fraction of their flux.

I conclude by outlining the key results of the work within the thesis and providing an overall interpretation. I look to the future where I can build on this work and anticipate key developments in the field.

Declaration

The work in this thesis is based on research carried out at the Centre for Extragalactic Astronomy, Department of Physics, Durham University between October 2020 and July 2024. The work was supervised by Dr. Leah K. Morabito of the same institute. No part of this thesis has been submitted elsewhere for any other degree or qualification and it is all my own work unless referenced to the contrary in the text.

The research presented in Chapters 3 and 4 have been published. Chapter 5 has been written in the style of a publication and will be submitted shortly. Details on the publications follow.

Publications

- *Chapter 3:* **"Connecting radio emission to AGN wind properties with Broad Absorption Line Quasars"**
  J. Petley, L. Morabito, D. Alexander, A. Rankine, V. Fawcett, D. Rosario, J. Matthews, T. Shimwell, A. Drabent **MNRAS, 515, 4 (2022)**

- *Chapter 4:* **"How does the radio enhancement of broad absorption line quasars relate to colour and accretion rate?"**
  J. Petley, L. Morabito, A. Rankine, G. Richards, N. Thomas, D. Alexander, V. Fawcett, G. Calistro Rivera, I. Prandoni, P. Best, S. Kolwa **MNRAS, 529, 3 (2024)**

In addition to work included in this thesis, the author has been involved in other

work and collaborations during the period of the PhD which have resulted in the following publications:

- **"A panchromatic view of infrared quasars: excess star formation and radio emission in the most heavily obscured systems"**
  C. Andonie, D. Alexander, D. Rosario, B. Laloux, A. Georgakakis, L. Morabito, C. Vilforth, M. Avirett-Mackenzie, G. Calistro Rivera, A. Del Moro, S. Fotopoulou, C. Harrison, A. Lapi, J. Petley, G. Petter, F. Shankar **MNRAS, 517, 2 (2022)**

- **"The LOFAR Two-Metre Sky Survey. VI. Optical identifications for the second data release"**
  M Hardcastle, M. Horton, W. Williams and 49 other colleagues **A&A, 678 A151 (2023)**

- **"Ubiquitous radio emission in quasars: predominant AGN origin and connection to jets, dust and winds"**
  G. Calistro Rivera, D. Alexander, C. Harrison, V. Fawcett, P. Best, W. Williams, M. Hardcastle, D. Rosario, D. Smith, M. Arnaudova, E. Escott, G. Gürkan, R. Kondapally, G. Miley, L. Morabito, J. Petley, I. Prandoni, H. Röttgering, B. Yue **Submitted to MNRAS - preprint** `https://arxiv.org/abs/2312.10177` **(2023)**

- **"Exploring the radio loudness of SDSS quasars with spectral stacking"**
  M. Arnaudova, D. Smith, M. Hardcastle, S. Das, A. Drake, K. Duncan, G. Gürkan, M. Magliocchetti, L. Morabito, J. Petley, S. Shenoy, C. Tasse **MNRAS, 528, 3 (2024)**

- **"A novel Bayesian approach for decomposing the radio emission of quasars: I. Modelling the radio excess in red quasars"**
  B. Yue, P. Best, K. Duncan, G. Calistro Rivera, L. Morabito, J. Petley, I. Prandoni, H. Röttgering, D. Smith **MNRAS, 529, 4 (2024)**

- **"Into the Depths: Unveiling ELAIS-N1 with LOFAR's deepest sub-arcsecond wide-field images"**

  J. de Jong, R. van Weeren, F. Sweijen, J. Oonk, T. Shimwell, A. Offringa, L. Morabito, H. Röttgering, R. Kondapally, E. Escott, P. Best, M. Bondi, H. Ye, J. Petley **Submitted to A&A (2024)**

- **"Unveiling AGN Outflows: [OIII] Outflow Detection Rates and Correlation with Low-Frequency Radio Emission"**

  E. Escott, L. Morabito, J. Scholtz, R. Hickox, C. Harrison, D. Alexander, M. Arnaudova, D. Smith, K. Duncan, J. Petley, R. Kondapally, G. Calistro Rivera, S. Kolwa **Submitted to MNRAS (2024)**

Acknowledgements

Throughout my PhD, I have been grateful for, and often needed, the support of many people in the astronomy community as well as my friends and family. These words cannot convey all my thanks but I hope to encapsulate and record some small fraction of my appreciation. I am indebted to:

- My incredible supervisor Leah Morabito, for your expertise, leadership and understanding. We were still locked down when I began this work but I have always felt you were aware of the encouragement and support I needed. It is my hope that we continue to work together for many years to come.
- David Alexander for your continuous enthusiasm for AGN science and Durham astronomy. Even though we did not have formal meetings, I am sure your advice and searching questions are visible in this thesis.
- STFC. This work was supported by the Science and Technology Funding Council [ST/T506047/1 and ST/V506643/1]
- My LOFAR teammate Emmy Escott, for making some of the most memorable and enjoyable moments of this PhD. You were the perfect addition to the group!
- My examiners Christian Knigge and Dimitri Gadotti for an enjoyable viva and helpful suggestions to improve the quality and clarity of this work.
- Shufei Rowe for all your help while travelling and funny chats at coffee.
- The LOFAR and AGN group in Durham over the past 4 years. Vicky Fawcett, for being a friendly and inspiring role model, Carolina Andonie, for your comradery and incredible generosity in a time of need, Nicole Thomas, Matthijs van der Wild, Jonny Pierce, Brivael Laloux, Aice Eldveldt, David Rosario, Sthabile Kolwa, Ciera Sargent
- My key collaborators. Amy Rankine, for your openness and support for my own ideas, Gordon Richards, for the thoughtful feedback and reference support, and James Matthews for your key comments and encouragement early on in my studies.

- PhD Group: My office mates for your conversation and patience over the years, Scott, Joaquin, Mac, Martina, Filip and Carolina. To all other students here at Durham. In particular: Hannah, Tom, Duncan, Sarah, Marcus, Victor, Yuankang, Makun, Dom, Sutti, Zoe, Craig, Aurelie, Dakshesh, Beni and others

- The LOFAR-VLBI group for fantastic busy weeks and technical support. I have learnt so so much from all of you. In particular, Frits Sweijen, Roland Timmerman, Jurjen de Jong, Christian Groeneveld, Neal Jackson, Tim Shimwell, Martin Hardcastle, Vijay Mahatma

- Everyone in Hatfield College who has supported me in my studies. I'd like to especially thank the Middle Common Room for many formals and academic events. Also, to Ann Maclarnon for leading the college throughout my time in Durham, allowing me to give back to the community and taking an interest in how I'm doing.

- My housemates for the past 4 years. Pete, Cal, Yusuf and Livia.

- To Kinky Jeff and the Swingers and Durham Ultimate Frisbee for keeping me sane through a global pandemic and the struggles of a PhD. I would particularly like to thank Alice Towle for dealing with my increasing absence this year! We all need the music.

- To Alex for all your love, support and hilarity. You have probably had much more of an influence on the outcome of this thesis than you realise. It has been a tough 4 years at times but I've always felt that we could trust and rely on each other whenever needed. I'm so excited about our adventures together in the Netherlands.

Contents

List of Figures

List of Tables

Dedication

Mum, Dad and Helen for timely advice, warm support and endless love.

No I don't know the path
Or what kind of pith I've amassed.
Long lines of questions,
Lessons, lessons, lessons

666 - Bon Iver

1 Introduction

The galaxies that we observe in our local universe often have histories reaching back over 10 billion years. Despite this vast time to evolve, many astronomers now believe that relatively short phases of activity, powered by the most compact objects in the universe, likely determine the evolutionary path that these galaxies take. The most massive black holes appear to grow alongside their galaxies implying an energy transfer between the black hole and its host. This is best represented by the correlation between black hole mass and bulge velocity dispersion, a proxy for the central stellar mass, which cannot be explained my the negligible gravitational effect of the black hole (Kormendy et al., 2013). However, when studying the galaxies containing these massive black holes, we have struggled to catch these changes "in-the-act". Even when we can observe powerful interactions, it has proven to be extremely difficult to tie black holes to an overall reduction in star formation.

Supermassive black hole systems can display various signatures of outflowing gas. Across a wide range of wavelengths, astronomers have been asking similar questions of these outflows. Do these outflows impart significant amounts of energy into the galaxy? Does this energy increase or decrease star formation rates on short and long timescales? Are certain outflow forms the most important when it comes to the feedback process? Are other processes more important than outflows when it comes to modulating star formation (eg. heating, gas consumption)?

Since the 1960s astronomers have been studying quasars, the most luminous objects in the universe. These sources should be the easiest in which to observe the interplay of black holes and their galaxy since the most powerful sources should have the strongest effects. However, it is often hard to piece together observations in the complex, multi-phase environments surrounding quasars. Radio emission provides an unobscured view of these dramatic events and as our telescopes improve I have been able to search more widely than ever before for objects that may be at their cosmological crossroads.

In this thesis, I use radio observations of different quasar populations to test hypotheses of their prominence as a phase in galaxy evolution and identify the physical mechanisms driving their radio emission. Through this, we can understand the nature of some of the most promising populations for quasar evolution and feedback with the aim of placing these populations more accurately in the overall galaxy evolution context.

I provide, in this introductory chapter, the relevant context in which to understand my thesis. In Chapter § 2 I provide a short introduction to radio astronomy techniques used in the thesis as well as personal contributions to the LOFAR-VLBI pipeline which were made during my studies. Chapters § 3, Appendix 4 and Appendix 5 contain work on the radio properties of different quasar populations in the style of journal publications. The nature of these publications is that the introduction to each is not entirely sufficient to cover all relevant information needed to understand the work completely. They instead focus on the key aspects of each study so that a non-specialist reader can take away the key results.

Here, I take the chance to spend more time discussing the field and thereby

provide greater motivation to the content of the thesis. I have attempted to be as thorough as I deem necessary in order to achieve these aims.

In § 1.1 I provide an overview of our understanding of Active Galactic Nuclei (AGN) followed by a discussion of high luminosity AGN (quasars) (§ 1.2). I proceed by introducing Broad Absorption Line Quasars (BALQSOs) in § 1.3, which are the sources I focus most on throughout the thesis. Then, in § 1.4, I include further discussion of the radio properties of quasars leading right up to the state of the field at the time of writing this thesis.

1.1 Active Galactic Nuclei

Edward Fath (1909) was potentially the first to observe unusual emission in the nucleus of a nearby galaxy. Fath noted that while the spectrum of the nebula in Andromeda was similar to that of the Sun, *"N.G.C. 1068, on the other hand, has few absorption lines and five bright lines"*. This was the first hint that something peculiar was occurring in the core of some "nebulae" (see Figure 1.1).

After Edwin Hubble showed that these "nebulae" were in fact other galaxies (Hubble, 1926), work on the central region of these objects continued. Carl Seyfert (1943) studied six objects in great detail and found that the emission lines were broadened, with some showing Doppler broadened profiles of up to $8500\,\mathrm{km\,s^{-1}}$. Another key observation of this work was that the broadening widths were correlated with the fraction of light of the galaxy coming from the central nucleus. Galaxies with these properties are still often named after Seyfert today.

The consensus view, attributing the features to black holes, was still three decades away and required the input of astronomers studying the opposite end of the electromagnetic spectrum. In general, we now refer to the observational effects of black holes in the centre of galaxies as Active Galactic Nuclei (AGN).

In the following sections, I briefly discuss the different key components of all AGN. These are:

1. **Supermassive Black Hole** - The central dense object which provides the potential energy for all other processes.

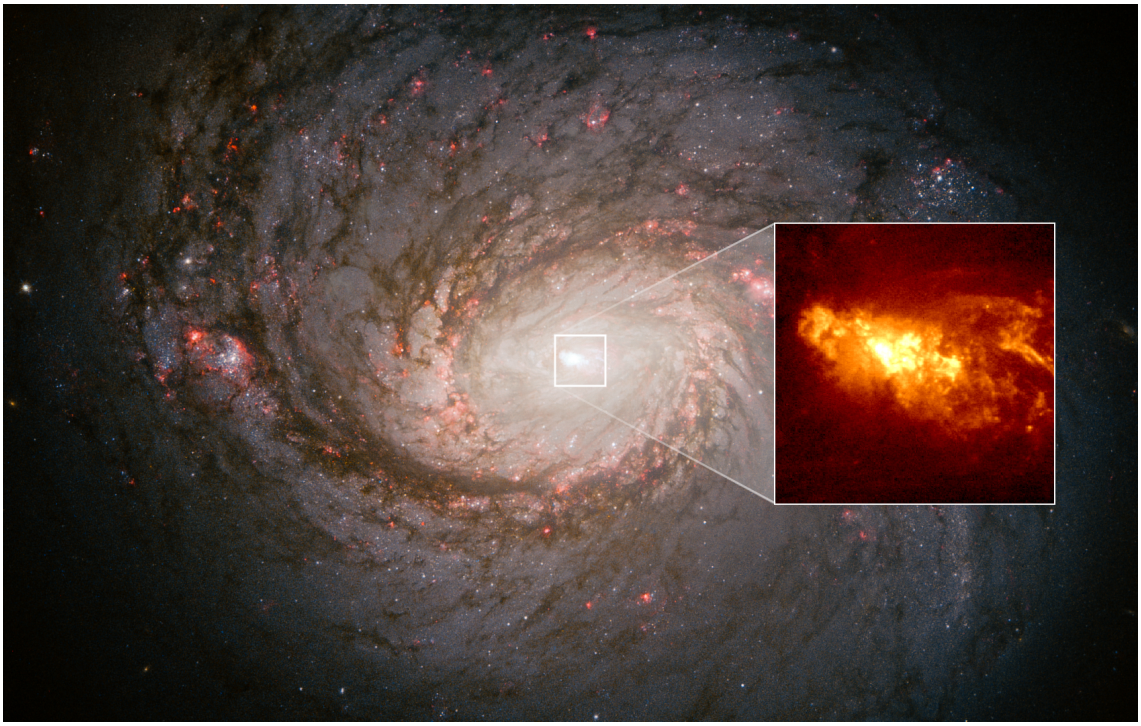

Figure 1.1: HST image of the spiral galaxy NGC 1068, hosting the first AGN to be observed in Fath (1909). The zoomed patch highlights the radiation being delivered to hydrogen clouds in the centre of the galaxy by the bright AGN buried below. We would now refer to this source as a Type 2 Seyfert galaxy, where the broad line region is obscured by some sort of dust component.
Credits: NASA, ESA, Alex Filippenko (UC Berkeley), William Sparks (STScI), Luis C. Ho (KIAA-PKU), Matthew A Malkan (UCLA), Alessandro Capetti (STScI)

2. **Accretion Disc** - Material falling onto the black hole which emits largely in ultraviolet and optical frequencies.

3. **X-ray Corona** - The X-ray emitting plasma surrounding the supermassive black hole.

4. **Emission Line Region and Torus** - Clouds irradiated by the accretion disc. Contains an obscuring region known as the dusty torus.

1.1.1 Super Massive Black Hole

The supermassive black hole (SMBH) at the centre of the AGN is probably the simplest aspect of the whole system. Famously, "black holes have no hair"[1] and can be described entirely by their mass (hereafter M_{BH}), charge and angular momentum (Israel, 1968). However, despite this fundamental simplicity to the heart of AGN, many questions and complexities arise as soon as the passage of time is considered. How do these black holes grow and what effect does that have on their surroundings?

The growth of black holes is typically measured via their Eddington ratio. This is determined by observing the luminosity of an AGN and comparing it to the theoretical Eddington luminosity, above which the force from radiation pressure is larger than the gravitational force of the black hole. If the radiation pressure is greater than the gravitational force then material will be pushed away from the black hole and cannot be accreted in a stable manner. Under assumptions of spherical symmetry and that, in the highly ionised region around the black hole, the radiation cross-section is that of the electrons (Thomson cross-section, σ_T), but most of the mass is in protons, m_p, we can obtain the following equation for this limiting luminosity, L_{Edd}:

$$L_{Edd} = \frac{4\pi G M_{BH} c m_p}{\sigma_T} \tag{1.1}$$

The Eddington ratio, λ, is simply the ratio of the observed luminosity of the AGN over the theoretical Eddington luminosity, $\lambda = L_{AGN}/L_{Edd}$.

[1] Normally attributed to John Wheeler who himself attributes to Jacob Bekenstein

The Eddington luminosity can be calculated in other systems such as stars where the mass to be converted to energy in the system already exists within the star. However, in the case of the black hole, the mass needed for the luminosity is falling onto the black hole, increasing its mass all the time. Some fraction of the mass accreted will enter the black hole and increase its overall mass and some fraction will be radiated away and contribute to the overall luminosity of the black hole. We can therefore consider the mass accretion rate needed to power a black hole at its Eddington luminosity (i.e. $\lambda = 1$). With the fraction of mass energy converted to luminosity as ϵ, and the mass accretion rate as $\dot{M}$ we can define this limiting accretion rate:

$$\begin{aligned} \epsilon \dot{M}_{Edd} c^2 &= \frac{4\pi G M_{BH} c m_p}{\sigma_T} \\ \dot{M}_{Edd} &= \frac{4\pi G M_{BH} m_p}{c \epsilon \sigma_T} \end{aligned} \tag{1.2}$$

To understand the scale of the energy that could potentially be produced by a large black hole it is helpful to look at these two parameters in solar units and years. In this case, we obtain:

$$\begin{aligned} L_{Edd} &= 3.28 \times 10^5 \frac{M_{BH}}{M_\odot} L_\odot \\ \dot{M}_{Edd} &\approx \frac{10^{-9}}{\epsilon} \frac{M_{BH}}{M_\odot} M_\odot yr^{-1} \end{aligned} \tag{1.3}$$

The value of ϵ depends on how the material is accreted and will be discussed in the next section, but with a typical value of 0.1, a black hole will double in mass every 100 million years if it can accrete at the Eddington limit. We will discuss this accretion disc further but this fact alone provides strong constraints on the early history of black holes that go on to be AGN.

1.1.2 Accretion Disc

Matter which comes into the gravitational sphere of influence of the black hole and has net angular momentum will tend to form a disc. This is because interactions between the particles must conserve angular momentum perpendicular to the overall net angular momentum L of the material. These interactions heat the material which will then radiate energy away, thereby reducing the magnitude of these perpendicular components until the material has formed a disc. The structure of this disc will be defined by the equilibrium between the radiation forces within the disc and the gravitational and rotational forces upon it.

In the case of accretion onto a black hole, we typically assume that the disc is geometrically thin and optically thick. However, without the transfer of angular momentum from the inner region of the accretion disc to the outer there would be no way for matter to actually move inwards and feed the black hole. Viscous forces are needed in order to produce this transfer of angular momentum away from the black hole. Although the exact origin of these forces was unknown a way forward in modelling the accretion flow was found in the classic work of Shakura & Sunyaev (1973). They showed, under the assumption that the transfer is facilitated by turbulence alone, the overall structure of the thin disc case can be solved using a dimensionless parameter α. The understanding now is that the viscous forces originate from magneto-rotational instabilities within the disc (Balbus & Hawley, 1991). With this model, they could determine the temperature of the disc for 3 different regimes with different sound speeds depending on whether radiation or gas pressure is dominant and the main source of opacity.

Under the assumption that in small radial intervals, the disc is in thermal equilibrium, we can integrate along the radius of the disc with a blackbody spectrum in each interval dependent only on the temperature. The overall spectrum of the accretion disc is then a composite black body spectrum which peaks in the ultra-violet regime for moderately accreting super-massive black holes. The conversion efficiency of the thin disc model depends on the black hole spin since the spin changes the radii at which stable orbits cease.

Accretion discs are not a unique feature of AGN and some of the most well-

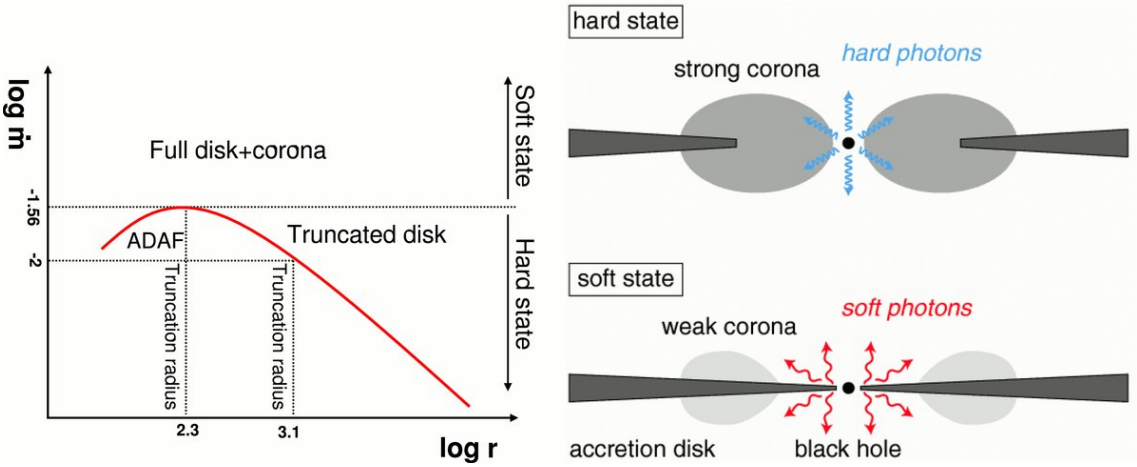

Figure 1.2: Schematic of the soft and hard states of black hole accretion. **Left:** Above a minimum mass accretion rate the system can sustain the standard optically thick disk of Shakura & Sunyaev (1973) all the way down to the last stable orbit around the black hole. Below this, we will have some sort of ADAF flow close to the black hole which connects to a truncated disk at some radius. **Right:** Pictoral representation of the two states.
Credit: Liu & Taam (2009)

studied accretion flows are in X-ray binaries (XRBs). These systems generally display changes between two states referred to as "soft" and "hard" (see Figure 1.2). The "soft" state is characterised well by the optically thick, geometrically thin disc models similar to those proposed by Shakura & Sunyaev (1973). The "hard" state is observed with a different X-ray spectral slope and only appears at low values of λ implying some sort of transition to a different accretion flow. However, it is important to note that both states show signs of the other. That is to say that in the "soft" state one still observes an excess high energy photons compared to the optically thick model alone and in the "hard" state one can still observe the signature of the same disk but with a relatively lower contribution to the overall luminosity.

Since the accretion rate in the hard state is lower, the density of the flow is also lower. This means that radiative cooling is far less efficient. To explain the hard state, models of optically thin accretion have been developed which allow for much hotter accretion flows via a geometrically thick and optically thin flow. A classic solution to this scenario is the Advection Dominated Accretion Flow (ADAF) of Narayan & Yi (1995). The name refers to the fact that advection is assumed to be the dominant cooling mechanism of the flow as opposed to radiative cooling in the

optically thick model. This hotter flow is much less radiatively efficient compared to the optically thick disk model.

For a more detailed discussion of all of these different flows, the reader is referred to the review of Done et al. (2007).

The presence of a similar transition in the accretion flow of AGN is not as firmly established as it has been in the XRB systems. However, the physics of both systems should be largely similar and largely defined by the accretion rate, λ. We therefore expect a transition around $\lambda \approx 10^{-3} - 10^{-2}$ based on the studies of XRBs (e.g. Esin et al., 1997). This transition refers to the soft $\rightarrow$ hard change in state. However, when in the hard state, XRBs can undergo an outburst where they have much higher accretion rates while maintaining hard x-ray flux (e.g. Corbel et al., 2000).

In recent years, observations of apparent state changes in AGN have increased dramatically, enabled by the increased availability of multi-epoch photometric and spectroscopic studies of AGN. The term changing-look AGN was coined in Matt et al. (2003) to describe AGN with X-ray or optical features varying significantly on timescales of years. The changing-look term is largely a catch-all term for several different processes that can affect the spectral features of AGN. For the most part, X-ray variations have been typically explained by changes in column density along the line of sight (Mereghetti et al., 2021) while the UV/optical changes are more likely due to changes in the accretion disk emission. These objects are typically referred to as changing-state AGN (Sniegowska et al., 2020) and there is some evidence that the transitions could be due to critical Eddington ratio transitions that change the structure of the accretion disk (e.g. Ruan et al., 2019; Ai et al., 2020). Key work from Körding et al. (2006a,b) compared X-ray binary systems directly to AGN and found that they have similar jet-accretion relations. However, the most direct challenge to this extrapolation from X-ray binaries is that the corresponding transition timescale should be $\approx 10^7$ times longer so it would be surprising to observe any of these systems. For a recent review of changing-look AGN, investigating changing-obscuration and changing-state separately the reader is referred to Ricci & Trakhtenbrot (2023).

1.1.3 X-ray Corona

X-ray binaries were discussed in the previous sections as they allow for nearby studies of accretion disk physics in greater detail than in distant AGN. However, the majority of X-ray emission from distant AGN does not come from the disk itself since the innermost disk temperature is not large enough to produce these photons. Instead, as indicated in Figure 1.2 and Figure 1.3, we theorise that some sort of corona (hot electron plasma surrounding the black hole/accretion disk) is Compton upscattering photons into the X-ray bands.

The temperature of this corona is around $100\,\mathrm{k\,eV}$ ($>10^9\,\mathrm{K}$) and produces a characteristic power law spectral slope (Elvis et al., 1994). We also observe additional high-energy features from the re-processing of these X-ray photons by other regions surrounding the corona such as the accretion disc, torus and BLR (see below). This is typically known as the "reflection" component of X-ray spectra. Finally, at lower energies, we observe an additional component above the characteristic power law. This is referred to as the "soft excess" and its origin is not yet decided (see Sobolewska & Done (2007) for a study of three potential explanations).

1.1.4 Emission Line Regions

At greater radii from the SMBH, we find regions of line-emitting gas. AGN have largely been characterised based on the different features presented by this emission line region. In *type 2* AGN we see only "narrow" emission with Doppler broadened velocities of $< 500\,\mathrm{km\,s^{-1}}$. This emission can be extended and observed in nearby galaxies and can reach distances $>20\,\mathrm{k\,pc}$ (Mulchaey et al., 1996; Congiu et al., 2017). Overall, the excited gas which produces these narrow features is known as the Narrow Line Region (NLR).

In *type 1* AGN we observe a composite of the NLR with an additional component from the Broad Line Region (BLR). The BLR is located much closer to the SMBH and displays Doppler broadening due to velocities of $5000-10\,000\,\mathrm{km\,s^{-1}}$ for gas with a higher density than the NLR. If one assumes that the gas is gravitationally bound then one can estimate the mass of the SMBH based on the velocities observed

and an estimate of the size of the BLR. This has been noted as a possibility since the work of Woltjer (1959) before it was commonly accepted that black holes were at the centre of galactic nuclei.

How are type 1 and type 2 sources then related? We also observe strong infrared emission from AGN suggestive of an optically thick structure of dust and gas. This has been named the *dusty torus* although the debate of its geometry is not at all settled. However, it is thought that this may be the origin of the type 1 and type 2 dichotomy (Antonucci, 1993; Heisler et al., 1997). Unification theories have arisen that attempt to explain the properties of two or more classes of AGN via changes in the viewing angle of the same underlying object. For type 1 and type 2 AGN in the "strong" unification scenario, these AGN are fundamentally the same but in type 2 we are observing through the dusty torus which obscures the BLR. This model is generally accepted although some intrinsic differences in the dust structure of type 2 AGN have been found (Ramos Almeida et al., 2011).

1.1.5 Summary

The overall schematic spectral energy distribution (SED) of each of these components is shown in Figure 1.3. AGN are luminous across the whole range of the electromagnetic spectrum. This allows for many varied methods of selecting AGN from a parent population using different regimes and diagnostics. A key problem that this wide range of emission wavelength presents is that it is often difficult to separate AGN emission from that of the host galaxy. Figure 1.3 represents this for the case of a starburst galaxy in which the SED is very similar aside from a slight difference in the far-infrared due to a cooler dust temperature. With only photometry, the same issue can present itself in optical data where both the accretion disk and stars emit strongly.

1.2 Quasars

In most areas of astronomy, understanding of phenomena usually begins with the brightest sources. Advancements in radio astronomy drove the early studies of AGN

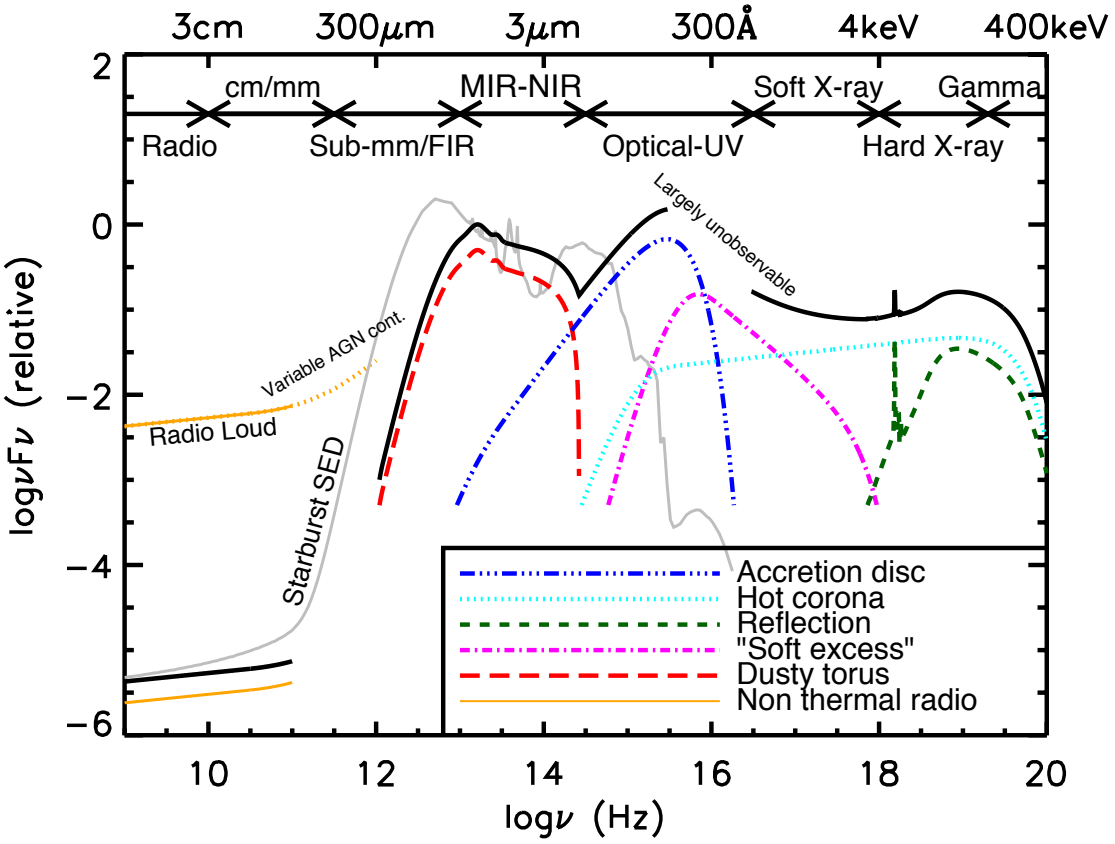

Figure 1.3: Schematic spectral energy distribution of an unobscured AGN. Different components are highlighted in different colours and the overall spectrum in black is compared to a typical starburst galaxy in grey. One key feature is the dramatic difference in flux between radio-loud and radio-quiet sources, spanning many orders of magnitude.
Credits: From the thesis of Harrison (2014)

and, while the field was still in its infancy, astronomers were discovering sources largely in order of their sky brightness at low resolution. From the discovery of radio emission from outside the solar system in the 1930s (Jansky, 1933), we were already observing the black hole at the centre of our galaxy. Jansky had not set out looking for these distant radio waves and was really trying to understand disturbances to telephone signals.

Grote Reber, the first radio astronomer in the proper sense, built his own 9.5m diameter parabolic radio telescope and mapped the sky at 160MHz (curiously both of these early studies were at low frequencies from which the field then moved away for a significant time). Reber found emission maxima in Sagittarius (the Milky Way centre), Cygnus, Cassiopeiae and Canis Major (Reber, 1944). At the time Reber assumed all the sources were associated with the Milky Way and largely came from stars, leading to a discussion on these sources representing the different spiral arms of our own galaxy.

Soon though, with improved interferometers more and more discrete radio sources were identified and many were quickly associated with galaxies (e.g. Greenstein, 1961). However, some sources appeared apparently to be associated with stars (Matthews & Sandage, 1963). The optical counterparts were compact, bright and blue when viewed with optical telescopes; stars were the natural interpretation. 3C 48 appeared to be the first clearly identified radio star in 1960 but after Schmidt (1963) identified a similar source (3C 273) as having a redshift of 0.158 the nature of 3C 48 was re-evaluated. With the potential of a high-redshift source in mind, emission lines were identified with a redshift of 0.368 (Greenstein & Matthews, 1963). Papers on both of these sources were published in the same edition of *Nature* (Schmidt, 1963; Greenstein & Matthews, 1963; Oke, 1963) and the descriptor quasi-stellar radio sources was used the following year (Greenstein & Schmidt, 1964).

The term "quasar" has since developed as the popular nomenclature both inside and outside of the astronomy community. Often though, objects will be referred to as Quasi Stellar Objects (QSOs). According to Schmidt (1970) QSOs are quasars selected purely on the basis of optical (now also UV) spectra.

In relation to AGN, quasars are simply the most luminous category. Typically

this means that the accretion disk and torus of the AGN are much brighter than any other components of the host galaxy. Although there is no clear definition, a bolometric luminosity $> 10^{45}\,\mathrm{erg\,s^{-1}}$ is sometimes used. This measurement is normally made by measuring a luminosity in one or more bands and then scaling a known quasar SED to fit the points. The integral of this SED is then used as the bolometric luminosity (e.g. Shen et al., 2020). For comparison, $10^{45}\,\mathrm{erg\,s^{-1}}$ is around 10 times greater than the combined luminosity of all the stars in the Milky Way. When we observe broad emission lines in quasar spectra, we assume that these are more luminous versions of the type 1 AGN. When we do not observe the broad lines (and sometimes narrow lines (Greenwell et al., 2024)) we associate quasars with the type 2 AGN and sometimes refer to them as "obscured quasars" if the obscuring column density is high enough. There is some evidence to suggest that the majority of quasars are not detectable at optical wavelengths (Donley et al., 2007; Hickox et al., 2007).

1.2.1 Red Quasars

The optical colour of quasars is typically blue due to being dominated by the accretion disk emission which peaks in the rest frame ultra-violet. Quasars are now often identified using optical/UV spectra such as those of the Sloan Digital Sky Survey (SDSS). Therefore, across at least the full SDSS range, we observe the spectra to have increasing flux towards bluer colours. However, if one examines the colour distribution of quasars in SDSS we find a tail towards redder colours (see Figure 4.1). These sources can be split out from the general population via various methods but as a whole, they are termed "red quasars".

Attempts have been made to unify red and blue quasars in a similar fashion to that of type 1 and type 2 quasars (Rose et al., 2013). In this scheme, red quasars are just the subset of quasars in which we look through some amount of dusty torus which increases the reddening but is not enough to extinguish the broad line emission. However, some studies suggest differences in the properties of red quasars which would not be expected in this unification scenario.

Some examples include weaker X-ray emission (Wilkes et al., 2001; Ma et al.,

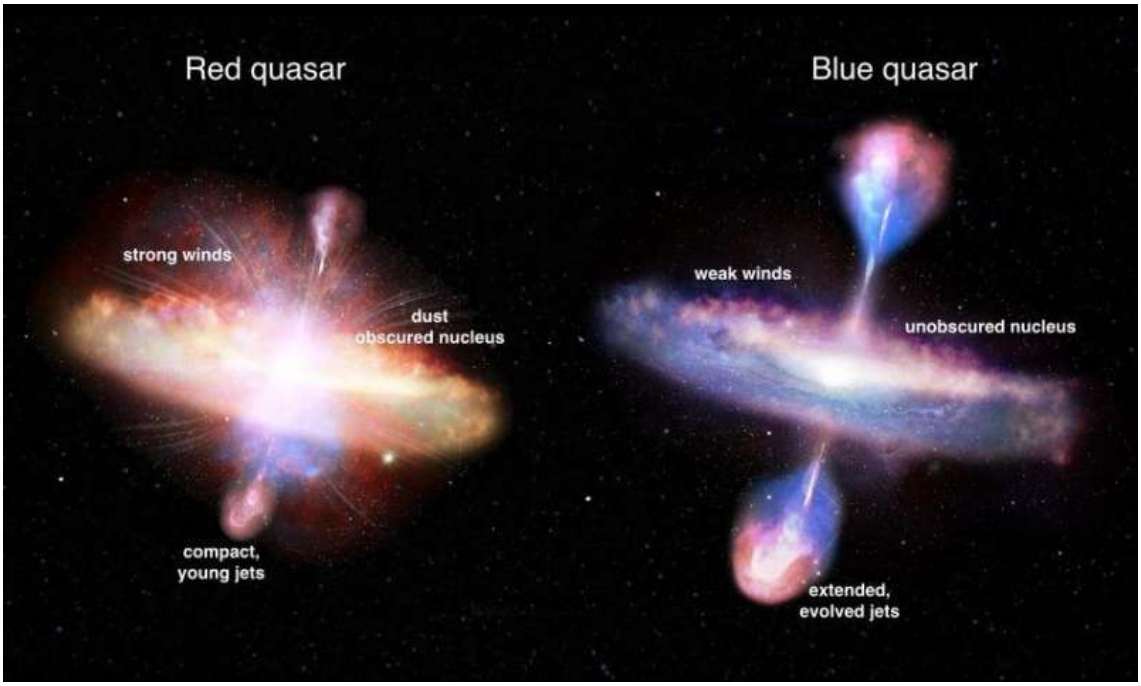

Figure 1.4: Schematic explanation for red and blue quasars indicting the distinguishing features associated with red quasars. Based on these features, some suggest that red quasars are one piece in the overall history of a quasar in which dust and gas are removed to leave behind a blue quasar.
Credits: S. Munro and L. Klindt

2024), outflow property differences (Calistro Rivera et al., 2021) and a relation to mergers (Glikman et al., 2015). Probably the largest difference has been found in recent studies of the radio properties of red quasars but we reserve this discussion for a later section (§ 1.4.2).

These differences have largely been accommodated by an evolutionary model in which red quasars are the earlier progenitors of the general blue quasar population. This tends to be placed into a larger overall picture in which starburst galaxies develop all the way through to early-type low star formation rate galaxies via a quasar phase (Hopkins et al., 2008; Alexander & Hickox, 2012). The implication is that the fraction of red quasars we observe can be thought of as the fraction of time a typical quasar spends as red before blowing off its cocoon of dust.

Curiously red quasars also contain an increased prevalence of broad absorption line quasars, a class which will be discussed in the following section (Richards et al., 2003; Urrutia et al., 2009; Glikman et al., 2012). This connection could support either the orientation or evolutionary hypothesis for red quasars depending on our

understanding of broad absorption line quasars. The broad absorption line quasars also present a similar radio difference which is discussed extensively in § 1.4.3.

1.3 Broad Absorption Line Quasars

The presence of broad blueshifted absorption lines in the spectra of quasars seems to have first been identified in Lynds (1967). Features bluewards of Si IV and C IV were both found to have the same redshift offset suggestive of a rapidly expanding envelope of gas around the source. Studies continued and the first review of these quasars Weymann et al. (1981) referred to them as Broad Absorption Line Quasars or (BAL) QSOs. Even this early review noted some interesting properties of these sources, highly relevant to the conclusions of this thesis. Firstly, the BALQSO fraction was estimated to be between 1 and 10%. Second, there was a tentative suggestion that "BAL QSOs tend not to be radio sources".

BALQSOs and Galaxy Evolution

There are two ways in which one can interpret the BALQSO fraction in the general quasar population. One is a *"geometric unification"* approach in which BAL winds are present in all quasars, an intrinsic feature of accretion discs, but subtends some fraction of possible viewing angles of quasars. In this case, the observed fraction of quasars equals the fraction of viewing angles. The second is in an *"evolutionary scheme"* in which the covering fraction of BAL winds is much larger than the observed BALQSO fraction, but the time in which a quasar exhibits a *"BAL phase"* is shorter than the quasar lifetime.

These schemes have different implications for the importance of BALQSOs to AGN feedback and galaxy evolution. In the geometric picture, BALQSOs may be important for feedback but operate continuously and we would not expect to see any different host galaxy features in BALQSOs compared to general QSOs. Alternatively, in the evolutionary scheme, BALQSOs could be a phase in the evolution of a galaxy and, with a much larger opening angle, may have a unique role to play in the history of a galaxy. BALQSOs in the orientation scheme must have lifetimes

greater than those in the evolutionary model and so the signatures of each on the long-term evolution of a galaxy may be quite different.

If BALQSOs are associated with a particular phase in galaxy evolution, it is thought that this would be an earlier phase than other quasars largely due to their association with reddening (see § 1.2.1). BALQSOs are more likely to show dust extinction and absorption than other quasars (Sprayberry et al., 1992; Reichard et al., 2003). This means that the BALQSOs fraction typically observed in flux-limited optical surveys will be lower than the intrinsic quasar fraction as absorption shifts enough of the flux to longer wavelengths for BALQSOs to be preferentially undetected (Hewett & Foltz, 2003). They are also more likely to be classified as red quasars via their optical colours (Richards et al., 2003; Urrutia et al., 2009). Other evidence for this hypothesis includes suggestions that BALQSOs may have higher star formation rates than non-BALQSOs (Wethers et al., 2020; Chen et al., 2021) although these results are not conclusive and usually focus on LoBALs in particular.

Looking to other wavelengths, X-ray studies of BALQSOs have always found that BALQSOs show a weakness in their X-ray emission compared to non-BALQSOs (Gallagher et al., 1999; Stalin et al., 2010). However, the reason for this difference has been debated. Some state that X-ray weakness is entirely due to strong absorption and that after correction the underlying X-ray emission is similar (Green et al., 2001; Grupe et al., 2003). In contrast, others have found that the difference is intrinsic to the quasar SED (Sabra & Hamann, 2001; Morabito et al., 2014). Either way, X-ray observations have not conclusively ruled in favour of any particular BALQSO wind structure.

Another interpretation could be that BALQSOs are in fact a feature of all quasars but additionally their opening angle evolves over time due to various factors. We observe that the fraction of highly obscured quasars increases with redshift (e.g. Gilli et al., 2022) and there is potential for similar behaviour for BALQSOs (Bischetti et al., 2023). This is especially true if the wind launching mechanism is itself connected to other evolving properties like the accretion rate or state of the dusty torus.

1.3.1 BALQSO Structure

Blueshifted absorption occurs when outflowing material scatters photons associated with the emission line out of our line of sight. Given their high velocities and modulation of the spectrum associated with the accretion disk, BALQSOs have most often been interpreted as originating in a bi-conical wind rising directly from the accretion disk.

All BALQSOs show absorption troughs associated with high ionisation emission lines, most prominently C IV followed by Si IV. Some BALQSOs additionally show absorption from low-ionisation lines such as Al III and Mg II. Quasars containing only the high ionisation features are called HiBALs and the subset that contains low-ionisation absorption are termed LoBALs. The fraction of BALQSOs in optically selected quasars is around 10-15% (e.g. Weymann et al., 1991; Reichard et al., 2003) with around 10% of those being LoBALs. However, estimates can vary quite significantly simply based on definitions and the use of metrics vs visual inspection (Trump et al., 2006; Dai et al., 2007; Allen et al., 2010).

The physical mechanism responsible for this phenomenon is not greatly understood and it is also unclear whether the BALQSOs are simply the lower ionisation end of Ultra Fast Outflows (UFOs) (Chartas et al., 2002; Pounds et al., 2003b) which are observed in X-rays and also thought to be associated with a disc wind. Although thermal processes and magneto-hydrodynamics may be important to outflow processes in quasars, probably the most plausible force which leads to high-velocity outflows is radiation pressure on spectral lines also known as "line driving". When gas is fully ionised the radiation pressure available is only from electrons. However, if the gas is only partially ionised then new opacity is available in the form of spectral lines and significant velocities can be achieved even at accretion well below the Eddington luminosity.

The key to both launching and also observing BALQSOs could then be how to prevent the strong X-ray source of the AGN from over-ionising the gas. The ionisation state of gas around an AGN is usually described via the ionisation parameter, U. This parameter characterises the ratio between photons that can ionise a particular element and the rate at which recombination can occur which depends on the

electron density, n_e. The dimensionless parameter is therefore defined as

$$U = \frac{\int_{\nu_1}^{\infty} \frac{L_\nu}{h\nu} d\nu}{4\pi r^2 c n_e} \tag{1.4}$$

where ν_1 is the minimum frequency for ionisation of the given element. Normally, values of U presented are in reference to hydrogen ionisation and typically have a range of $10^{-3} \rightarrow 1$ in AGN.

One way to prevent this over-ionisation, therefore, is by changing the strength of the X-ray source (reducing the numerator of 1.4) or by increasing the distance between the gas and the X-ray source or by increasing the density n_e (increasing the denominator of 1.4). Without changing the accretion structure, the first two effects can be achieved by increasing the black hole mass. Larger black hole masses mean larger stable orbits, lower gas velocities and therefore a lower temperature of the innermost radius of the accretion disk. Since the temperature of the innermost radius defines the highest energy photons, this leads to fewer ionising photons in the spectrum for AGN with large black hole masses. This implies that the incidence of BAL features should scale with black hole mass. Interestingly, LoBALs, which require a lower ionisation parameter than HiBALs, have been found to have black hole masses and accretion rates consistent with that of the general population (Schulze et al., 2017). However, this has only been studied with highly luminous quasars with $M_{BH} > 10^8 M_\odot$ suggesting that the effect of black hole mass may not be the key factor in preventing over-ionisation.

Shielding of the gas from the ionising radiation could instead be the key factor. Murray et al. (1995) invoked a separate gas component to provide the shielding in between the X-ray source and the disk wind. This model was able to form a disk wind with a 5° opening angle and C IV emission features similar to those in BALQSOs. The origin of this separate gas component though was not clear and further simulations such as Proga et al. (2000) have shown that the wind can shield itself from the emission, referred to as self-shielding.

Other simulations have started with a wind already in place and simulated the observational features of the wind. This avoids the need to simulate the accretion flow and wind dynamics in detail which would be vastly more computationally ex-

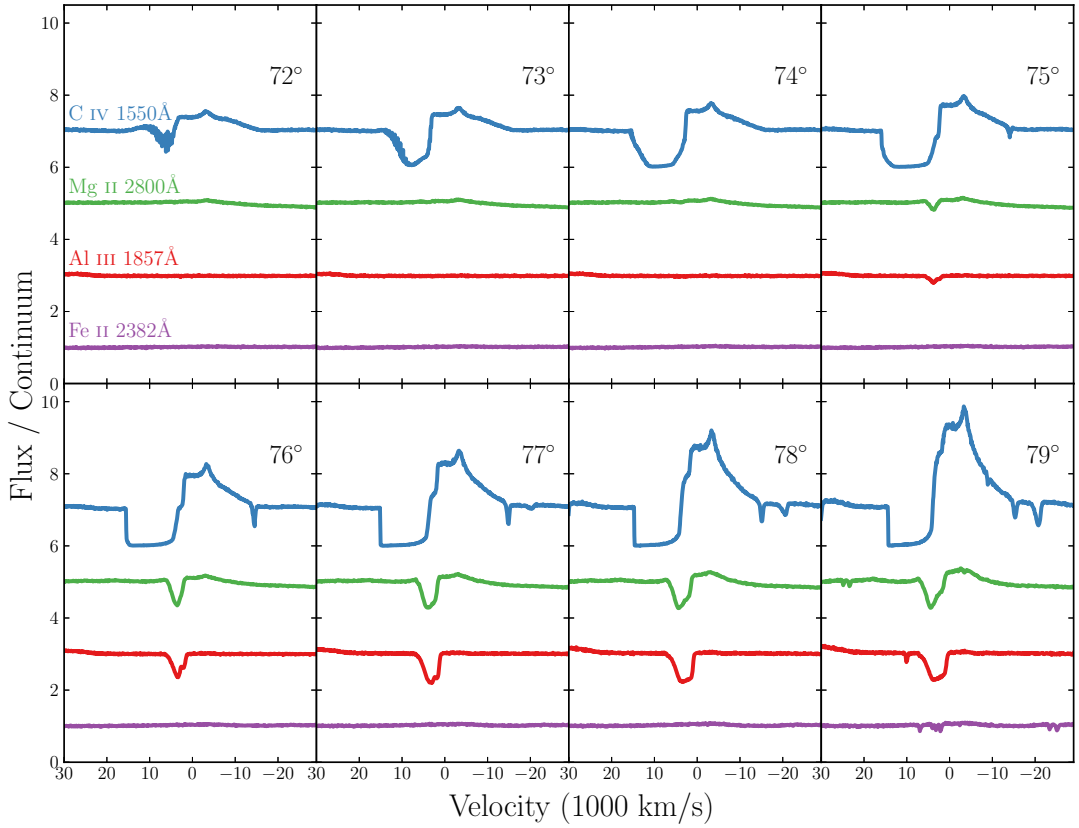

Figure 1.5: BAL type features reproduced in simulations of clumpy bi-conical AGN wind presented in Matthews et al. (2016). The angles describe different lines of sight through the wind with 90° representing a view straight through the thin accretion disk
Credits: Matthews et al. (2016)

pensive and uncertain. Higginbottom et al. (2013) set up a smooth, single-phase disc wind launched between 300 and 600 times the gravitational radii of the black hole ($0.01-0.02\,\mathrm{pc}$ for their quasar-like black hole). They can then irradiate the wind with a Shakura & Sunyaev (1973) type disc and a central X-ray emitting source and model the radiative transfer processes through the wind. The wind was given an opening angle between 70° and 82° and was successful in reproducing C IV BAL features for sight lines through the wind. However, LoBAL features could not be reproduced and the C IV profiles were highly sensitive to the X-ray luminosity (over-ionisation problem). The simulations were also based on a mass outflow rate equal to the mass accretion rate of the black hole. Matthews et al. (2016) incorporated clumping of the wind into the same model (and improved handling of recombination lines) which affects the ionisation state within the wind. This model was able to reproduce both HiBAL and LoBAL features with the LoBAL features emerging at higher inclinations (see Figure 1.5).

Some efforts have been made to go in the opposite direction by attempting to infer physical parameters such as the mass outflow rate and geometry of the BAL wind from observed spectra. When multiple absorption lines are observed, and not saturated, it is often possible to extract information such as the covering fraction and optical depth (e.g. Hamann et al., 2000; Arav et al., 2001; de Kool et al., 2000, 2002).

In recent years, BAL modelling has been significantly improved by *SimBAL* (Leighly et al., 2018). They create a large bank of synthetic spectra using the photoionisation code *Cloudy* (Ferland et al., 2013). They can then sample the space using Markov-Chain Monte Carlo methods to calculate various physical parameters with uncertainties for their model. Leighly et al. (2018) modelled an SDSS quasar and found a launching radius of $1-2\,\mathrm{pc}$, a mass outflow rate of $17-28\,\mathrm{M}_\odot$ and a Eddington ratio of the quasar $\lambda = 0.06$. The major benefit of this spectral synthesis method of modelling is that the spectra is taken as a whole. This means that *lines which are not observed are also constraining the model.* However, a major drawback is that these models have only been applied to FeLoBALs, a rarer subclass of BALQSOs, which show additional absorption features compared to LoBALs primarily in

Fe II. The extra features help constrain the models and the creators of *SimBAL* feel it is not yet ready to be applied to the general population.

SimBAL has now been applied to over 50 FeLOBALs (Choi et al., 2022a,b). They found a wide range of outflow locations but could largely split the population into two groups, one with a radius from the central source of $1-10\,\mathrm{pc}$ and another with distances $\gtrsim 100\,\mathrm{pc}$. Interestingly, none of the inferred radii was small enough to be consistent with a disk wind, with the lower radii group more consistent with winds originating in the torus. For the winds at much larger radii (kpc scale), they suggest a cloud shock model, such as the one in Faucher-Giguère et al. (2012), which is consistent with their results. Furthermore, they find that the force available from radiative line driving does not correlate with outflow velocity, suggesting another launching mechanism is at work, at least for the highest-velocity winds. They find a correlation between the outflow velocity and reddening, which suggests either that radiation pressure on dust is important in launching high-velocity outflows (e.g. Soliman & Hopkins, 2023; Thompson et al., 2015) or that the wind itself is contributing significant reddening and that the highest velocity outflows simply have more mass and energy leading to the observed correlation.

1.3.2 Identifying BALQSOs

Identifying the BALQSO subset of the overall quasar population has largely been made possible by visual inspection of spectra to identify the absorption features. However, some more systematic approaches have been taken. Weymann et al. (1991) suggested a diagnostic, the balnicity index (BI), which we typically use to define BALQSOs in this work. In essence, the BI is modified equivalent width with some conditions that reduce the impacts of noise and narrow absorption.

The procedure works by defining a continuum over the region in which we are measuring the absorption. Typically, this can be done by fitting other regions of the spectra without strong emission and absorption features and then extrapolating to the region of interest. The balnicity index is then defined as

$$BI = -\int_{25000}^{3000} [1 - f(V)/0.9] C dV \tag{1.5}$$

where $f(V)$ is the continuum normalized flux as a function of velocity displacement from the emission line velocity. The value of C is introduced to force some minimum width of absorption to be obtained before integration. C is 0 until the bracketed quantity has been positive continuously for 2000km s^{-1}. Overall, the balnicity index can be measured for all quasars and has a minimum value of 0 and maximum value of 20000km s^{-1}. Defining BALQSOs as quasars with a balnicity index > 0 produces a sample with very clear features but will necessarily miss systems with lower levels of absorption and more complex absorption features which do not satisfy the requirement for C becoming 1 across the absorption region. We thus obtain clean, but not complete, samples using the balnicity index.

A more generous diagnostic was suggested in Hall et al. (2002) and expanded upon in Trump et al. (2006) and is referred to as the absorption index (AI).

$$AI = \int_0^{29000} [1 - f(V)]C'dV \tag{1.6}$$

In this index C' is defined to be 1 when $f(V) < 0.9$ for at least 1000km s^{-1}. Clearly, from the definitions, we can see that more sources will have a positive AI than a positive BI. A key question in BALQSO research is that of the intrinsic BALQSO fraction. Clearly, samples selected by visual inspection, BI or AI will have very different fractions. Knigge et al. (2008) studied this impact in detail and found a clear bi-modality in the logspace of the AI distribution for quasars with the BI > 0 sources selecting largely the higher AI distribution.

Both of these metrics still stop integrating at some point bluewards of the C IV line in order to avoid contamination of the metric from the Si IV emission and absorption. However, some quasars have been found with broad absorption line outflows with velocities larger than $0.1c$ (Jannuzi et al., 1996; Rogerson et al., 2015). These have since been described as Extremely high-velocity outflows (EHVOs) and would also be missed using AI or BI definitions. In Rodríguez Hidalgo et al. (2020) a modified BI is used to search for C IV outflows greater than $0.2c$. They found 40 such objects that would probably still be classed as BALQSOs but have maybe orders of magnitude more kinetic power than more "typical" BALQSOs.

1.4 Radio emission from AGN

From discussing the discovery of quasars in § 1.2, largely powered by radio observations, we have taken a digression largely into the higher frequency optical, UV and X-ray properties of these sources. Now we return to the radio properties of quasars to discuss in what ways radio studies continue to advance our understanding of accretion onto SMBHs and the impact that may have on galaxies.

Radio emission, particularly at low frequencies, has two key properties that distinguish it from other regimes and give us extra information on quasars:

1. **Synchrotron Radiation** - Radio emission is typically produced by synchrotron radiation which probes regions with significant magnetic fields and free electrons. This allows us to study some of the highest energy interactions occurring within AGN and with their host galaxy

2. **Unobscured** - Gas and dust do not absorb such long wavelengths allowing radio emission to travel to us without attenuation from intervening processes that affect much of the AGN spectral energy distribution (SED)

Synchrotron Radiation

Synchrotron radiation is a linearly polarised emission produced by the acceleration of relativistic electrons in a magnetic field. The overall flux density from a synchrotron source can be characterised by a power law relation. For the flux density, S_ν, at a frequency ν the power law is defined as

$$S_\nu \propto \upsilon^{-\alpha} \tag{1.7}$$

where α is the "spectral index" of the radio source. We now explain the emergence of this power law relation.

An electron in a magnetic field of a particular strength, B, will gyrate at a certain frequency, ν_G, depending on that strength:

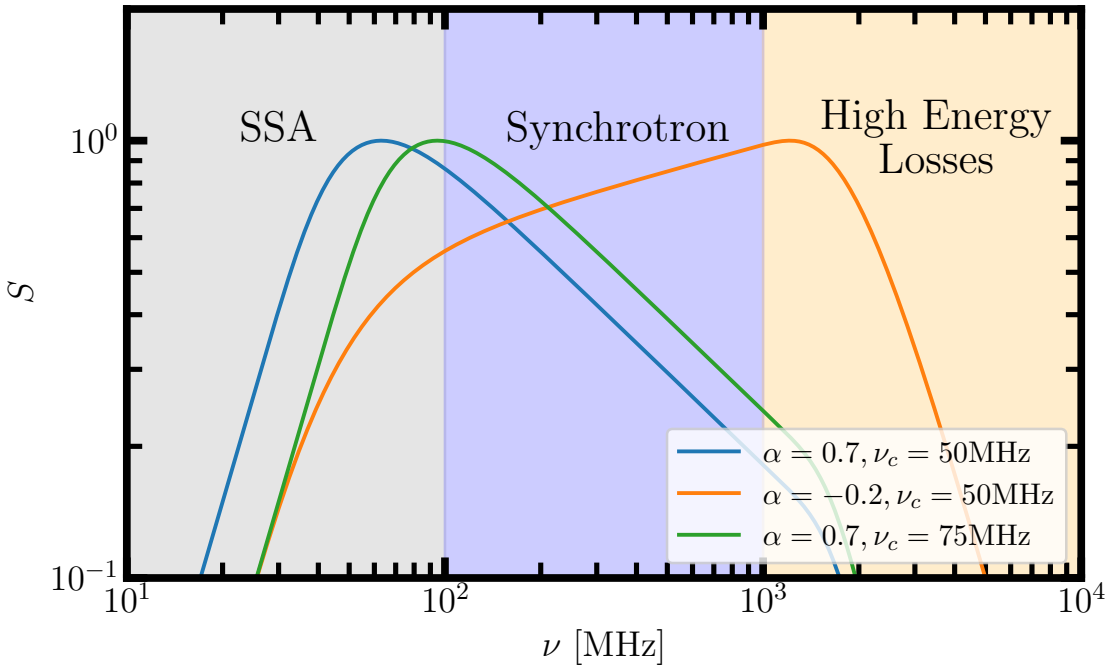

Figure 1.6: Schematic radio spectrum resulting from synchrotron emission and absorption. 3 spectra are plotted with varying spectral index, α, and critical frequency, ν_c, at which synchrotron self-absorption takes over. The border between different regimes will depend on the density of the medium and the age of the source. Equations used to plot arbitrary spectra adapted from Pacholczyk (1970).

$$\nu_G = \gamma^2 \frac{eB}{2\pi m_e} \tag{1.8}$$

$$\nu_G \text{ [MHz]} = 2.8\gamma^2 B \text{ [Gauss]} \tag{1.9}$$

Here, γ is related to the speed of the electron v via:

$$\beta = v/c \tag{1.10}$$

$$\gamma = (1 - \beta^2)^{-1/2} \tag{1.11}$$

The power radiated as this electron is accelerated by the magnetic field can be calculated through Larmor's equation. The power will depend on the pitch angle of the electron with respect to the magnetic field but by averaging over all pitch angles we can obtain the average power observed for a single electron:

$$\langle P \rangle = \frac{\sigma_T c}{6\pi} \beta^2 \gamma^2 B^2 \tag{1.12}$$

where σ_T is the Thomson cross-section of an electron. Although the electron will radiate with this power in all directions, an observer will largely see a pulsing pattern as relativistic beaming leads to sharp peaks in the radiation power each time the electron is travelling in the direction towards the observer. To calculate the final observed power spectrum one needs to take the Fourier transform of this series of pulses.

The resulting power spectrum is related to the modified Bessel function, the complete derivation being too detailed for this discussion. However, the key result is that, for a single electron, the power spectrum can be shown to have a logarithmic gradient $\approx 1/3$ up to some critical frequency with the magnitude of the power depending on the kinetic energy of the electron and the strength of the magnetic field.

Now we turn to calculating the overall features of synchrotron spectra for an ensemble of electrons in an astrophysical source. Since we combine the spectra of

many electrons, each with this characteristic spectrum, the overall spectral index (the negative of the power spectrum gradient) must always be $> -1/3$ if no other processes are occurring.

Typically the kinetic energy distribution of the electrons is approximately a power law, $n(E)dE \propto E^{-\delta}dE$. We can calculate the emission coefficient, j_ν, which is the amount of energy emitted per unit time, per unit frequency, into a solid angle by

$$j_\nu d\nu = \langle P \rangle \; n(E)dE \tag{1.13}$$

$$j_\nu d\nu \propto \left(\frac{\sigma_T c}{6\pi}\gamma^2\beta^2 B^2\right)(E^{-\delta})dE \tag{1.14}$$

We make the assumption that the power from each electron is radiated entirely at a single frequency close to that of the peak value for the spectrum from a single electron, $\nu \approx \gamma^2 \nu_G$. Using the equation for the relativistic energy of an electron we obtain

$$E \approx \left(\frac{\nu}{\nu_G}\right)^{1/2} m_e c^2 \tag{1.15}$$

If we differentiate with respect to the frequency, ν, we obtain

$$\frac{dE}{d\nu} \approx \left(\frac{1}{2}\right)\left(\frac{1}{\nu\ \nu_G}\right)^{1/2} m_e c^2 \tag{1.16}$$

We can now substitute this into our equation for the emission coefficient to find that

$$j_\nu \propto \left(\frac{\sigma_T c}{6\pi}\gamma^2\beta^2 B^2\right)\left(\left(\frac{\nu}{\nu_G}\right)^{1/2} m_e c^2\right)^{-\delta}\left(\frac{1}{2}\right)\left(\frac{1}{\nu\ \nu_G}\right)^{1/2} m_e c^2 \tag{1.17}$$

This is a bit complicated! But to understand the canonical synchrotron power law slope we can ignore all the constants and focus on the relationship frequency and magnetic field (which is proportional to the rotational frequency, ν_G) and emission.

$$j_\nu \propto (\gamma^2 B^2)(\nu/\nu_G)^{-\delta/2}(\nu\nu_G)^{-1/2} \tag{1.18}$$

$$j_\nu \propto (\nu B)\left(\frac{\nu}{B}\right)^{-\delta/2}(\nu B)^{-1/2} \tag{1.19}$$

$$j_\nu \propto B^{(\delta+1)/2}\nu^{(1-\delta)/2} \tag{1.20}$$

So clearly, if the energy distributions of electrons follow a power law, δ is related to the spectral index by $\delta = 2\alpha + 1$. Typical synchrotron spectra have a spectral index $\alpha \approx 0.7$ which suggests an electron energy distribution defined by $\delta \approx 2.4$.

Synchrotron Self-Absorption

What then stops synchrotron emission from reaching infinitely large fluxes at low frequency? The answer is *synchrotron self-absorption* which modifies the spectrum at low frequencies. Essentially, at low frequencies, any synchrotron source will become optically thick since the brightness temperature (the temperature that would produce equivalent flux to the synchrotron emission) will approach the effective electron temperature and electrons in the field can start absorbing other photons being produced. This imparts a characteristic slope of 5/2 (i.e $\alpha = -5/2$) at low frequencies. The more compact an emitting source is, the higher the brightness temperature meaning the frequency at which the source is optically thick will also be higher.

The relativistic electrons lose energy over time at a rate proportional to their energy squared. This means that for a typical source, the spectral index will tend to steepen at higher frequencies. The overall effect of all of these features of synchrotron emission is shown in Figure 1.6 which highlights different regimes of absorption, emission and high energy losses.

I have explicitly chosen not to indicate the contribution of free-free emission and thermal emission as these typically contribute more at higher frequencies which are not studied extensively within this thesis. In the frequency ranges I focus on, synchrotron emission processes are expected to dominate. For example, in the review of Condon et al. (1992) it is shown that at 1.4 GHz the free-free component contributes $< 10\%$ of the radio emission in a starburst galaxy and only dominates in the 30 GHz

to 200 GHz region.

1.4.1 Radio Emission Mechanisms

The strength of radio emission in AGN has largely been characterised in relation to the optical emission originating in the accretion disc. Kellermann et al. (1989) measured the ratio of radio luminosity (5 GHz) to rest-frame B band luminosity (4400 Å) of 114 quasars and found a bi-modality in the distribution of this parameter, R, divided at $R \approx 10$. Sources with $R > 10$ are typically referred to as radio-loud while the rest of the population are radio-quiet. [2]

Around 10% of sources can be identified as radio-loud and are typically the sources associated with large extended jet structures, often dwarfing the host galaxy in which they originate (e.g. Figure 1.8).

The radio-quiet population is not as well understood and a dominant emission mechanism for these sources has not emerged. Instead, it is thought that several different emission mechanisms could play a role and could be present in objects at a similar level at the same time (see review of Panessa et al. (2019)). Below is a discussion of the four prominently theorised contributors to the emission in radio-quiet sources.

Radio Jets

Accretion onto an SMBH can lead to the ejection of material in a powerful collimated jet, typically travelling at relativistic speeds (Begelman et al., 1984). The exact mechanism for generating this power is not decided, but the leading theory is probably that of Blandford & Znajek (1977) in which spin energy is extracted via a strongly magnetised accretion disk. At the base of these jets, blobs of synchrotron radiation which are strongly self-absorbed, due to the density, have overlapping spectra that typically result in flat or slightly inverted ($\alpha \lesssim 0$) spectra (e.g. Lobanov,

[2] I believe there is sometimes some confusion in the use of radio-quiet with some astronomers including sources that are not radio-detected within the category of radio-quiet and others using additional terms such as "radio-silent". In this thesis, I aim to only use radio-quiet when a source is actually radio-detected.

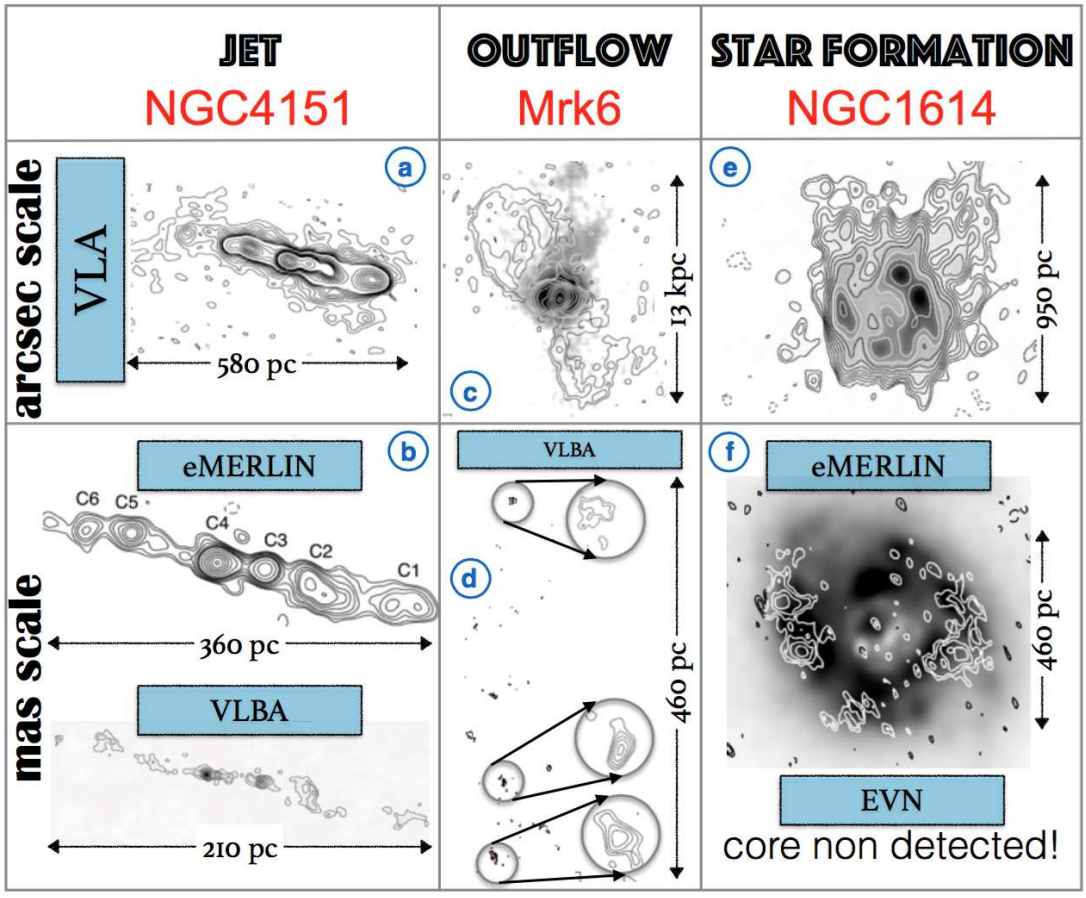

Figure 1.7: Resolved radio structures observed with various radio instruments for three sources with different physical origins for the emission. Structures can often be resolved below the kpc scale, a scale below that observed in this thesis.
Credits: Panessa et al. (2019)

1998).

Powerful extended radio sources have typically been classified into two types based on the prescription of Fanaroff & Riley (1974). FRI sources are typically brighter towards the inner region of the jet, while FRII sources have higher flux density coming from hot spots at the end of radio lobes. There have been attempts to link these two classes to different accretion states of the AGN (Jackson & Rawlings, 1997). The FRIs would be examples of radiatively inefficient accretion (low λ, hard state, ADAFs etc.) and the FRIIs would be radiatively efficient (high λ, standard Shakura & Sunyaev (1973) accretion). However, considering that a jet travelling at 0.5 c will take 1 Myr to travel 150 kpc, this is most likely a large overestimate of speeds at the head of the jet. Simulations such as those in Hardcastle (2018) find that it takes 10s of Myrs to create sources of that size. Over these times, the accretion flow onto the SMBH could be greatly different from when the jet was launched making it very difficult to directly tie the large-scale morphology to different accretion states. Additionally, Mingo et al. (2022) demonstrate that the radio morphology is in fact linked to stellar mass and not the accretion properties of the AGN showing that the environment in which the jets move is a more important factor. Combined, these results rule out the accretion dichotomy connection for FRIs and FRIIs.

Rather than looking at the radio morphology, an alternative classification can be made by looking at the optical spectra of radio galaxies. This has led to the High-Excitation Radio Galaxy (HERG) and Low-Excitation Radio Galaxy (LERG) classifications based on the strength of different emission lines. Best & Heckman (2012) studied these two groups and found that the LERGs typically have $\lambda < 0.01$ while the HERGs have $0.01 < \lambda < 0.1$ supporting the idea of an accretion structure change between the two populations. However, in recent years, the difference in these populations has become increasingly blurred with the accretion and galaxy properties of these two groups showing significant overlap in observations (Mingo et al., 2022; Whittam et al., 2018, 2022) and simulations (Thomas et al., 2021).

Although the most powerful large-scale radio jets are relatively rare, there are increasingly more signs that the presence of jets in AGN is actually very common.

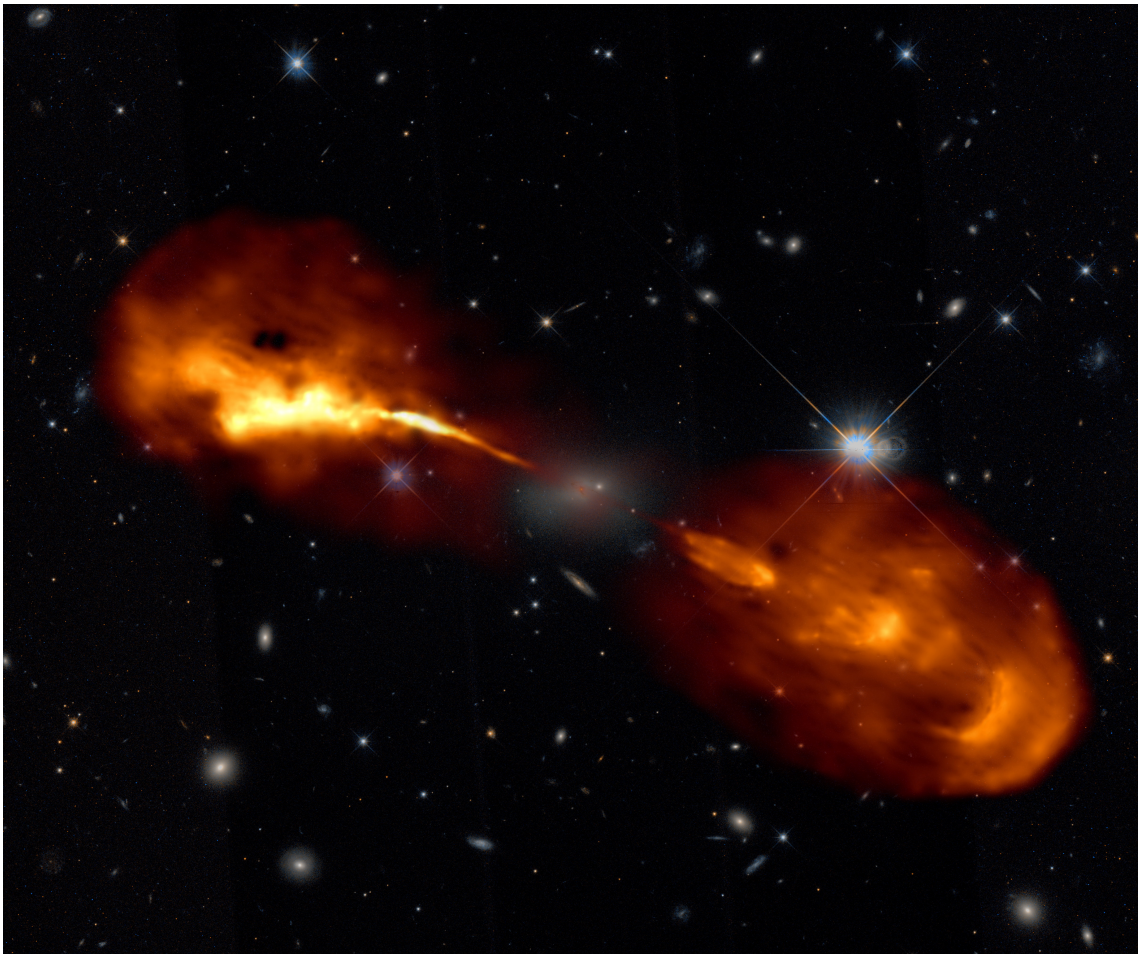

Figure 1.8: Example of powerful radio jets in Hercules 8 (3C 348), a nearby bright radio source. This jet is powered by a black hole in the galaxy centre with a mass of $M_{BH} = 4 \times 10^9 M_\odot$. It is thought that energy is extracted via the spin of the black hole to power the jet.
Credits: R. Timmerman/ASTRON

For example, Baldi et al. (2018) studied 103 optically selected nearby galaxies with the enhanced Multi Element Remotely Linked Interferometer Network (eMERLIN). For the AGN in their sample, they achieved 26 detections from 38 sources. The size of these sources are below 100pc with most below 50pc. Around half the sample showed jet-like structures with the rest having a compact core. Jarvis et al. (2021) studied known radio-detected AGN with large ionised gas ([O III]) luminosities with the VLA. They found that 67 per cent of the sample had spatially extended radio emission suggestive of them being lower luminosity sub-galaxy scale equivalents to large radio-loud jet sources.

Shifting to a large-scale approach, Macfarlane et al. (2021), and more recently Yue et al. (2024), have modelled the entire LOFAR Two Metre Sky Survey (LoTSS) radio population using just two components, star formation and radio jets. The star formation component is based on the FIR-radio correlation (discussed more in the star formation section below), while the jet component is modelled by a luminosity-dependent power law which fits well for the radio-loud population and is extrapolated down to lower luminosities. They can reproduce the observed radio flux density probability distributions and radio-loud fractions from LoTSS extremely well with the radio jet luminosity dominating above fluxes of $\sim$1 mJy in LoTSS.

Star Formation

As mentioned in § 1.2, one of the brightest radio sources in the sky, Cassiopeia A, is a supernova remnant within our own galaxy. As star formation increases in a galaxy, the number of supernova remnants increases and so we expect a considerable amount of radio emission to be produced in star-forming galaxies. This radio emission also exhibits a typical synchrotron spectrum slope as the shock regions surrounding the supernova are similar to those in AGN winds (Condon et al., 1992).

The effectiveness of radio as a measure of star formation rate has been demonstrated by the far-infrared - radio correlation for star-forming galaxies (Sopp et al., 1991; Sargent et al., 2010; Calistro Rivera et al., 2017; Gürkan et al., 2018; Smith et al., 2021). The far-infrared is used as an indicator of dust and cold gas, key components in the formation of new stars in galaxies.

In some cases, star formation can also be traced via free-free from H II regions but has very different characteristic spectra and is usually overwhelmed by synchrotron radiation at frequencies lower than 30 GHz (Condon et al., 1992).

Wind Shocks

Winds exist in AGN on many different scales, from X-ray-observed UFOs all the way up to molecular outflows on super-galactic scales seen in sub-mm emission. If the wind velocities exceed the local sound speed, they can create shock waves through the interstellar medium. Within the shocked ambient medium behind the shock front, a large number of free electrons can be generated with the potential for synchrotron radiation.

Nims et al. (2015) constructed a simple wind shock model building on the work of Faucher-Giguère et al. (2012). They model a very luminous AGN ($10^{46}\,\mathrm{erg\,s^{-1}}$) launching a wind containing a kinetic energy that is 5% of the AGN luminosity. They show that in the model described in Figure 4.8, the shocked wind (SW) region reaches temperatures of order $\sim 10^{10}\,\mathrm{K}$ and the shocked ambient medium (SAM) reaches temperatures of order $\sim 10^{7}\,\mathrm{K}$. They also show that over a typical quasar lifetime of $\sim 10^{7}\,\mathrm{yr}$ the shock can reach sizes $\geq 1\,\mathrm{kpc}$. These temperatures are high enough to generate relativistic electrons through the shocks. Assuming some distribution in the energies of the electrons and assuming wind energy to relativistic electron efficiency based on observations of supernovae they obtain the following equation (Eq 31 in Nims et al. (2015)):

$$\nu L_{\nu} \approx 10^{-5} \xi_{-2} L_{AGN} \left(\frac{L_{kin}}{0.05 L_{AGN}} \right) \tag{1.21}$$

Here the parameter ξ_{-2} is the conversion efficiency of wind kinetic energy to relativistic electrons as a percentage and is roughly 1 for supernova shocks (Thompson et al., 2006) (i.e 1% of the energy is imparted to the electrons). The overall conclusion is that wind shock radio emission could contribute at least at a similar level to that of star formation radio emission. Admittedly this model is rather simple but it demonstrates the potential for wind shocks to explain a significant amount of emission in radio-quiet quasars, especially when we are observing sources which we

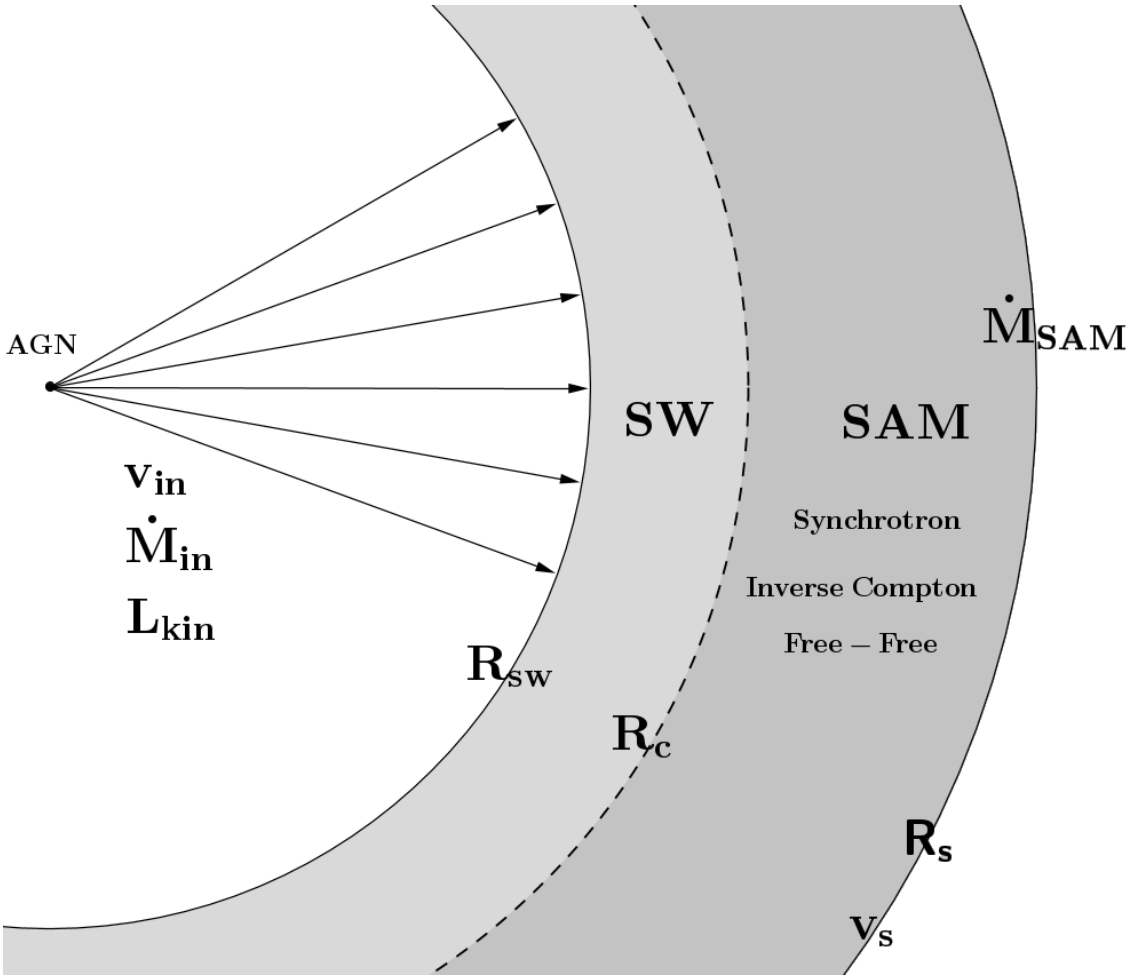

Figure 1.9: Wind shock radio emission model from Nims et al. (2015). An AGN-powered wind will create a forward shock and reverse shock with a region in between described as the shocked ambient medium (SAM in the figure). If wind shocks do contribute significantly to radio-quiet radio emission, then the radio luminosity will provide some of the best measures of kinetic power in quasars. This would have important implications for models of AGN feedback. A test of this model is performed in Appendix 4 (see Figure 4.8)
Credit: Nims et al. (2015)

know for certain contain winds with significant velocity (e.g. BALQSOs).

Coronal Emission

Several studies have found a correlation between the X-ray and radio luminosity in radio-quiet AGN (Wang et al., 2006; Panessa et al., 2007; Laor & Behar, 2008). This has led to the suggestion that the corona (see § 1.1.3) may be the source of the radio emission itself. There is not a firmly established mechanism for this but it is clear that within the corona we expect a large number of free electrons which could produce emission in the presence of magnetic fields.

The corona is an extremely small region surrounding the SMBH. It would therefore experience an extremely strong synchrotron self-absorption effect at much higher frequencies than those indicated in Figure 1.6. In fact, to observe radio emission from the corona one must observe at millimetre wavelengths (Behar et al., 2015). We therefore largely ignore the coronal emission origin when discussing the radio-detected samples studied throughout the rest of the thesis.

1.4.2 Radio emission in red quasars

Researchers, primarily at Durham, recently found a connection between red quasars and radio emission. The appearance of red quasars has now been demonstrated to be an effect of dust obscuration (Fawcett et al., 2022). Since radio emission is not obscured by dust, in the unification picture for red and blue quasars we should observe no difference in the radio properties of the two populations.

The key to this simple test is in the selection of the red and blue populations. Since the red quasar definition is mostly arbitrary, it is simplest to take a single-parent sample of quasars and then split them into colour groups in the same way. Klindt et al. (2019) took SDSS quasars between $0.2 < z < 2.4$ as a parent sample. The distribution of the photometric colour of quasars varies with redshift. Therefore, in small redshift bins, they took the $g - i$ distribution and selected the reddest and bluest 10% of quasars to be their two samples. After cross-matching with the Faint Images of the Radio Sky at Twenty-Centimetres (FIRST) (Becker et al., 1995), they discovered that the red quasars have a $\approx 2 - 3$ times larger radio detection fraction

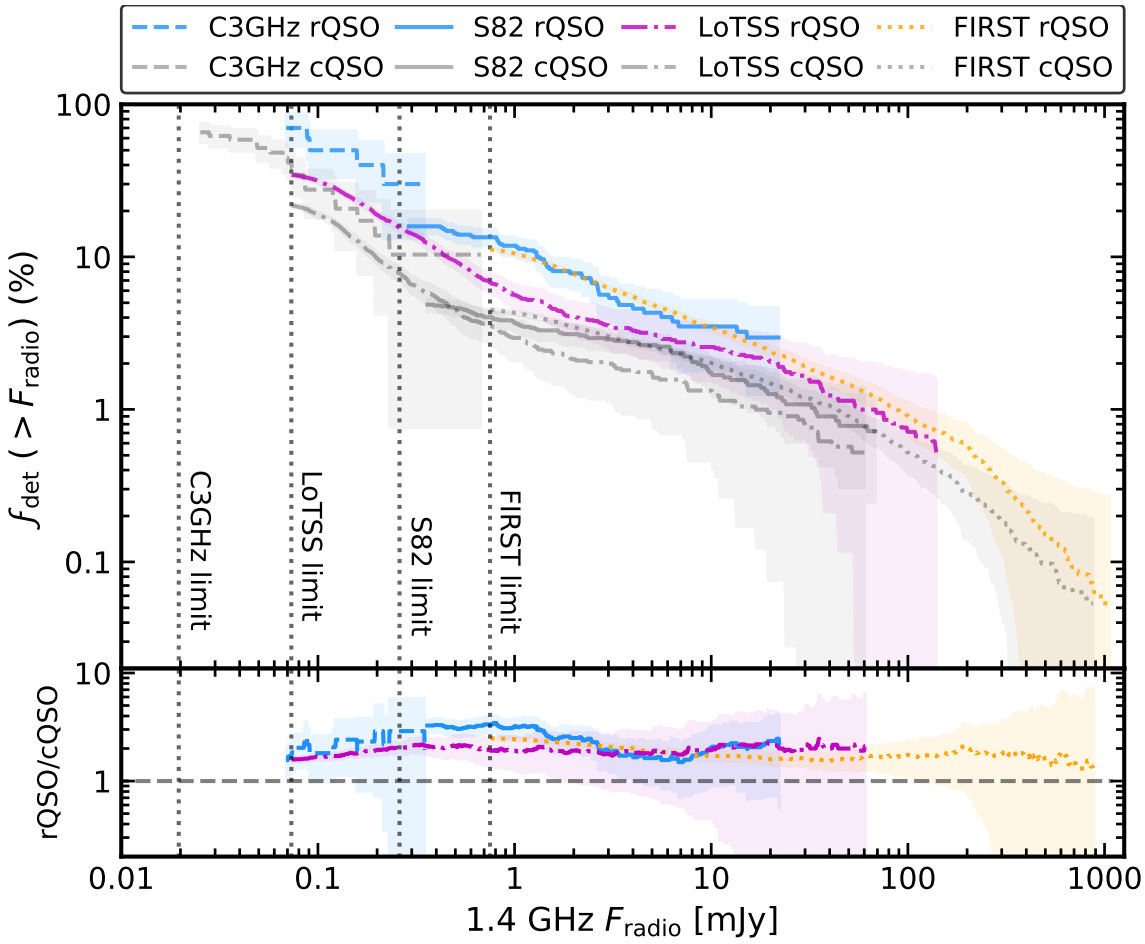

Figure 1.10: Radio enhancement of red quasars as demonstrated in Fawcett et al. (2021). This enhancement persists across all flux scales and at several different frequencies.
Credit: Fawcett et al. (2021)

than the blue quasars. This result continues to hold after matching samples in their six-micron luminosity, a measure of the torus luminosity which itself scales with the bolometric luminosity of the AGN, and redshift distributions.

This result has led to further studies attempting to constrain the scale and source of this enhancement. Fawcett et al. (2020) used deeper surveys from the VLA to show that the enhancement is largely in the radio-intermediate/radio-quiet regime before Rosario et al. (2020) demonstrated that the differences extend to low frequencies using LoTSS DR1 (Shimwell et al., 2019).

In a study similar to that of Appendix 5, Rosario et al. (2021) utilised high-resolution eMERLIN observations to show that the red quasars are more likely to be extended at this scale. This means that although at low resolution red quasars appear more compact, when we look at compact sources in more detail they then show an enhancement relative to similar blue quasars on host-galaxy scales. Most recently, through a targeted DESI quasar program to select more reddened sources missed in SDSS, Fawcett et al. (2023) demonstrated that this radio, dust connection extends to even more reddened sources.

The overall picture, revealed by these studies, is that red quasars have radio enhancement that can be attributed to the AGN but operate on small scales and lower fluxes than those associated with powerful jets. This is largely at odds with the unification scheme for red quasars where the phenomena is a product of viewing angles through a dusty torus. Instead, the dust itself has some connection to the radio emission. I believe there are largely two ways to interpret these results. Firstly, the dust is located on torus scales and plays a role in accretion, either affecting the accretion flow or providing significant shielding that allows for stronger line driving and outflows in red quasars (e.g. Soliman & Hopkins, 2023). Secondly, the dust is not contained to such a small radius and is instead simply tracing increased ISM density on nuclear scales (possibly related to the work on obscured quasars of Andonie et al. 2023). The enhanced radio emission is then a signature of jets or winds interacting with a more dense environment causing increased small-scale radio emission.

1.4.3 Radio emission in BALQSOs

We described in § 1.4.2 how the fact that radio emission is largely unobscured allows for it to be a powerful test for quasar unification theories. BALQSO radio properties have been studied for 4 decades now but do not seem to have been able to rule either way on the geometric or evolutionary scenarios for BALQOs. Here we outline key studies that provide the most immediate context for the whole thesis.

As noted at the beginning of § 1.3, BALQSOs were noted to be deficient in radio emission upon initial investigation (Weymann et al., 1981). Stocke et al. (1992) performed a VLA study of 68 BALQSOs and found no strong radio sources while a complimentary spectroscopic study of radio-loud selected quasars contained no BALQSOs. This led to the hypothesis that quasars can produce relativistic collimated jets or uncollimated sub-relativistic winds such as BALQSOs but not both at the same time. This theory is still somewhat supported today as inverse correlations between wind strength and radio properties have been found by other methods (Mehdipour & Costantini, 2019; Richards et al., 2021). However, as is often the case, exceptions have since been found and radio-loud BALQSOs were found in Brotherton et al. (1998) and Becker et al. (2000).

Large Surveys

With the arrival of the Faint Images of the Radio Sky at Twenty-centimetres (FIRST; Becker et al., 1995), large radio surveys at a much greater depth were possible. Radio detections in FIRST plus a bright r band magnitude were used to define potential quasar candidates for spectroscopic follow-up in the FIRST Bright Quasar Survey (Gregg et al., 1996; White et al., 1999). 29 BALQSOs were found in this sample out of 636 confirmed quasars and their properties were discussed in Becker et al. (2000). A key result was that the fraction of HiBALs in quasars with $z > 1.4$ (the observable HiBAL range) was 18%; 1.5-2 times the fraction found in optically selected quasar surveys depending on whether the BALQSOs were defined by BI or visual inspection. Interestingly, they also found that one-third of the BI > 0 sources were LoBALs while in optically selected BALQSOs that fraction is just 10%. Studying the relations between BI and radio luminosity and also a discussion of the morphology

of the sources, the authors favour a "unification by time picture" for an explanation of their results in which BALQSOs are young or recently refuelled quasars.

However, a reanalysis of the BALQSOs in this sample in Hewett & Foltz (2003) highlighted that a more consistent approach when selecting the optically selected counterparts to a radio-selected sample yields a much smaller difference in the BALQSO fraction. They estimate that an optical survey with similar limits as the FIRST bright quasar survey would have a BALQSO fraction of $\approx 20\%$ effectively removing this apparent radio enhancement. However, the lack of radio-loud BALQSOs was again highlighted as BALQSOs were half as likely to be detected at fluxes above 1 mJy in FIRST.

Urrutia et al. (2009) discovered a surprising result within the FIRST-2MASS survey (Glikman et al., 2007). This survey cross-matched FIRST with the 2MASS Infrared Survey (Skrutskie et al., 2006) to find potential red quasar candidates. Urrutia et al. (2009) additionally added SDSS photometry and visually inspected the remaining sources to remove spurious cross-matches between the three source catalogues. Within the redshift range in which BALQSOs could be identified ($0.9 < z < 2.6$ for LoBALs; $z > 1.7$ for HiBALs), they found that an astonishing 7 (or 12 using AI) out of 19 sources were BALQSOs. Furthermore, all objects with Mg II were LoBALs and LoBALs accounted for 32% of the overall population. This constitutes a $\times 74$ larger fraction than in the latest optically selected sample at the time, presented in Trump et al. (2006).

The LOw-Frequency ARray (LOFAR; van Haarlem et al., 2013) represents a step change in radio astronomy potential, particularly at low frequencies. With a dense core and remote stations in the Netherlands, it can reach high sensitivity at a comparable resolution to FIRST. Also as a digitally controlled telescope, it can slew essentially instantaneously making it much faster to perform wide-scale surveys at speed. The premier survey of LOFAR is the LOFAR Two Metre Sky Survey, which had its first public data release in 2019 (LoTSS DR1; Shimwell et al., 2019). This release only contained 2% of the eventual target coverage of the full survey but already provided 325,694 radio sources.

Morabito et al. (2019) crossmatched this release with the latest SDSS quasar

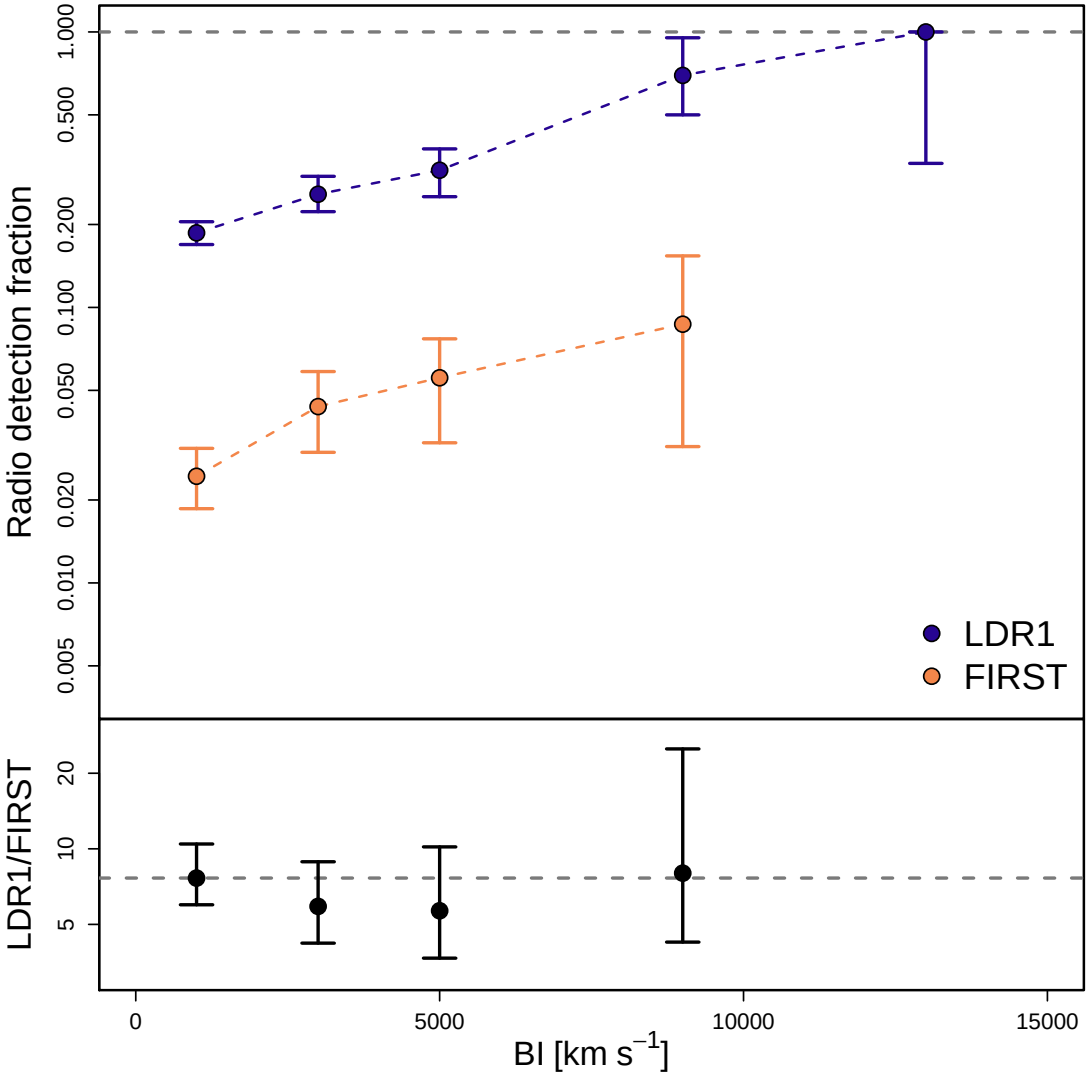

Figure 1.11: The correlation between BALQSO radio detection fraction in LoTSS DR1 and balnicity index. The same correlation within FIRST is also shown. The correlation between detection fraction and balnicity index was a strong motivation for the work in this thesis.
Credits: Figure 13 from Morabito et al. (2019)

catalogue Pâris et al. (2018) to study the radio properties of BALQSOs as compared to non-BALQSOs. As discussed in § 2.2.1, the combination of sensitivity and frequency of LoTSS greatly increases the source density of the survey and means that the population observed is largely radio-quiet and has not been previously observed. This unveiled an enhancement in the radio-detection fraction of BALQSOs. HiBALs are twice as likely to be detected and LoBALs are just over three times more likely to be detected than non-BALQSOs.

Other important results were that the LoTSS to FIRST spectral indices were flatter for BALQSOs as compared to non-BALQSOs, although it should be noted that due to the sensitivity differences all spectral indices were biased to being more flat. Additionally, a correlation was found between BI and radio-detection fraction (see Figure 1.11) indicating an even closer connection between the wind and radio properties than previously believed. Crucially, the BI did not correlate with the radio-loudness or radio luminosity of the BALQSOs detected, implying a physical separation between the wind and radio emission.

Radio-detection fraction is used regularly throughout this thesis and relating these results to luminosity can sometimes appear counter-intuitive. To assist the reader in interpretation we show how BALQSOs can have higher detection fractions despite similar or lower average luminosities in Figure 1.12. We assume two different broken power law distributions for BALQSOs and non-BALQSOs and derive detection fraction and luminosity properties from there. The distributions are not based on actual measurements of BALQSOs but should give the reader a feeling for how these different results may be produced.

High resolution studies

Rather than trying to study a large number of BALQSOs, others have taken the approach of studying a smaller number in much greater detail in order to understand their radio properties. These types of studies often focus on more radio-luminous, and therefore often most radio-loud, sources which can bias them towards larger jet-like structures which we know are typically responsible for this type of emission. In addition, higher frequency provides higher resolution with easier calibration and

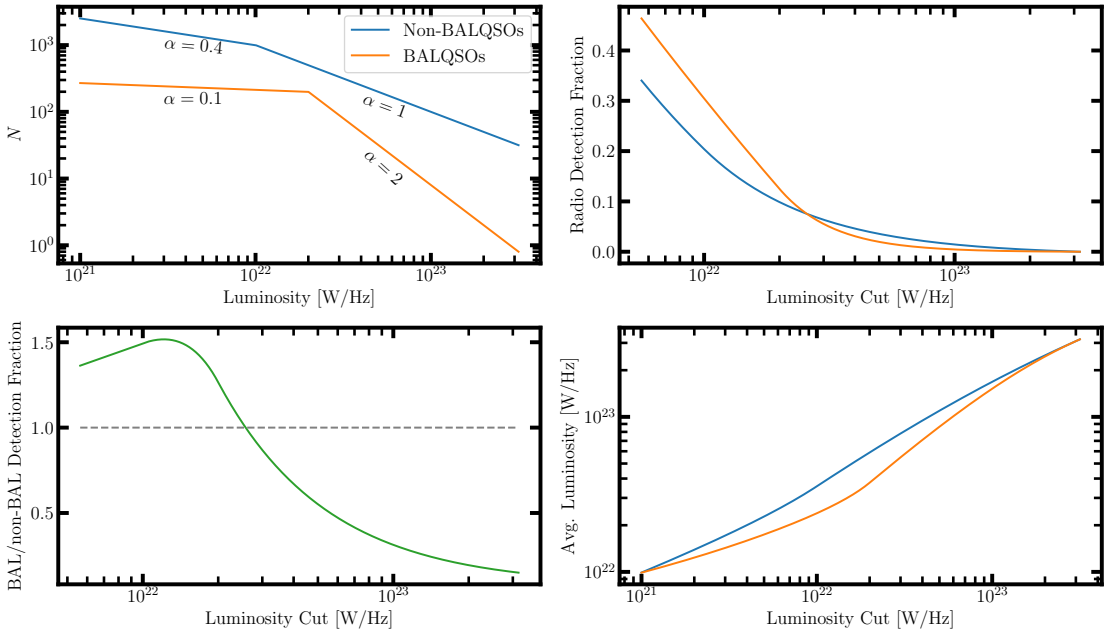

Figure 1.12: Schematic to show how BALQSOs can achieve higher detection fractions at particular luminosities without having an overall increase in radio luminosity. *Upper left:* Source numbers for a given luminosity. *Upper right:* Radio detection fraction given a particular cut in luminosity. *Lower left:* BALQSO detection fraction divided by non-BALQSO detection fraction for a particular luminosity cut. *Lower right:* Mean radio-luminosity of each group given a particular luminosity cut.
In this example, we assume that all quasars have radio emission at some level and choose two different power-law components for BALQSOs and non-BALQSOs. This corresponds to the observation that BALQSOs are more radio-quiet but may have additional wind or frustrated jet components at lower luminosities compared to non-BALQSOs. Although the spectral indices and breakpoints are arbitrarily chosen here, the code used is self-consistent so all plots are derived from two broken-power law distributions

most leading observatories have operated at $\gg 1\,\mathrm{GHz}$. This adds a bias towards smaller sizes since larger lobes contain lower energy electrons for longer.

High-resolution samples, as is the case in my own work of Appendix 5, are often created with the practicality of observation in mind and tend not to have easily comparative samples of non-BALQSOs. Nevertheless, the results are intriguing and inform the large-scale studies of radio-quiet BALQSOs within the thesis.

If BALQSOs can be unified geometrically with non-BALQSOs and the radio emission is dominated by jets, we would expect that at high-resolution morphologies should be *largely consistent within BALQSOs* as this scenario would imply similar jet-wind inclination differences for all BALQSOs. This is because jets are expected to be launched perpendicular to the accretion disk therefore, since most BALQSO models propose equatorial winds, we may expect a slight enhancement in resolved sizes for BALQOs as compared to non-BALQSOs.

Jiang & Wang (2003) studied three BALQSOs with the European VLBI Network (EVN). All of these sources were compact and one was observed with a flat spectrum, implying an observation very close to the jet axis. This in itself is hard to explain via an equatorial wind. Kunert-Bajraszewska & Marecki (2007) obtained high-resolution observations at 4 different frequencies of a BALQSO using the Very Long Baseline Array (VLBA) and eMERLIN and found a compact steep spectrum source with a two-sided morphology. Although this is indicative of a young jetted source, it is much more consistent with an equatorial wind.

Liu et al. (2008) studied four LoBALs and four HiBALs, identified with the VLA, using the EVN and eMERLIN. Only one of these eight sources contained a two-sided structure. The rest were either unresolved or contained only one visible component on a scale less than 300 pc. They still infer synchrotron emission as the origin of radio-emission and also suggest that these BALQSOs may be very young radio sources. After building a sample at low resolution to study spectral index properties (Montenegro-Montes et al., 2008), Montenegro-Montes et al. (2009) studies a sub-sample of five with the VLBA. They find resolved structure in two of the five objects. Again they propose that these results are consistent with radio-detected BALQSOs being part of a very young jet population.

1.5 Thesis Structure

This thesis furthers the study of BALQSOs and radio emission. The initial motivation was the result of Morabito et al. (2019) which found a higher incidence of radio emission in BALQSOs with LOFAR and a tentative connection to the wind properties. BALQSOs have always been associated with being largely radio-quiet and this new work highlights the power of the next generation of radio telescopes and surveys by uncovering a dramatic enhancement at lower fluxes.

The main questions that this thesis addresses are:

1. **What is the physical origin of the radio enhancement observed in BALQSOs?**

2. **What can radio emission tell us about the structure of BALQSOs? Does it rule out or favour particular orientation models?**

3. **How are BALQSOs related to red quasars which show a similar enhancement? Could they explain each other's radio properties?**

Ultimately the answers to these questions have implications for the study of BALQSOs as a whole and therefore their importance in the context of AGN feedback. If one can establish radio origins then one can aim to quantify and measure the mechanism producing it. For example, this could involve stating jet powers or the size, speed and density of wind shock regions. Both of these scenarios are of great relevance to the next generation of cosmological simulations which have increasingly complex AGN feedback models that require calibration. Understanding the structure of BALQSOs will also have implications for feedback as a wider covering fraction implied by an evolutionary model means that the wind is more likely to coincide with the galactic disk and have either a positive or negative effect on star formation in the galaxy.

In the latest large-scale cosmological simulations, AGN feedback is still implemented in a rather simplistic manner. Typically they are based on either a "quasar" mode or "radio" mode based on whether the impact of the quasar is simply heating or if velocities are injected into the surrounding particles (e.g. Davé et al., 2019).

Normally a transition is implemented via accretion rate but, in general, the overall effect of these modes is calibrated to match observed black hole-galaxy correlations. The study of BALQSOs in detail could open up new avenues of modelling AGN feedback and could allow us to test our simulations by estimating radio emission from sources within the simulations.

Finally, if the nature of BALQSOs is in some way connected or tied to the properties and conclusions made around red quasars this will tie together two of the largest and most widely researched sub-populations of quasars. Then, any result regarding one population should have a corollary for the other when understood through such a connection.

The thesis is structured as follows:

- **Chapter 2 - Methods and Data**

  I present an overview of the methods used throughout this paper with a focus on radio interferometry. I discuss the two telescopes used predominantly in the thesis. I also describe contributions I made to the LOFAR-VLBI pipeline, a significant commitment while completing the rest of the thesis.

- **Chapter 3 - Connecting radio emission to AGN wind properties with Broad Absorption Line Quasars**

  I present a study of BALQSOs with the largest radio-detected sample of quasars produced to date. I show that the spectra of BALQSOs is different for radio-detected sources compared to non-radio-detected sources and this difference is particularly pronounced for LoBALs.

- **Chapter 4 - How does the radio enhancement of broad absorption line quasars relate to colour and accretion rate?**

  Using spectral fits from Rankine et al. (2021) I present a study that attempts to place radio emission from BALQSOs in the context of other quasar populations with enhanced radio emission. I find that colour appears to be a stronger driver of radio emission than the presence of a BAL wind. However, BALs still retain a small radio enhancement across accretion rate and colours.

- **Chapter 5 - A high-resolution study of BALQSOs**

  After identifying a comparative sample of HiBALs and LoBALs from § 3, I observe 10 BALQSOs at 1.4 GHz at high-resolution. I find detections for 8 targets but only resolve one. I study the flux ratios at different frequencies and resolutions and find that LoBAL radio emission must either be more compact or have a flatter spectral index.

- **Chapter 6 - Conclusions and Future Work**

  I contextualise the main findings of the thesis. I outline and also suggest future work to improve our understanding of BALQSOs and their radio emission.

It is true: we love life, not because we are used to living but because we are used to loving.
There is always a certain madness in love.
But also there is always a certain method in madness.

Thus Spoke Zarathustra - Friedrich Nietzsche

2

Methods and Data

In this chapter, I outline and explain some of the key methods used throughout the thesis. Particularly relevant is a discussion of radio interferometry, which has its own quirks as compared to other wavelengths. This will lead to a discussion of the key telescopes and surveys utilised throughout the other chapters.

2.1 Radio Interferometry

In § 1.2, I briefly discussed the discovery of quasars and the influence of radio astronomy on that discovery. Early development of the field in the 30s and 40s was led by single-dish antenna telescopes. However, for a single dish of diameter D, the angular resolution, θ on the sky is defined by the Rayleigh criterion,

$$\theta = 1.22\frac{\lambda}{D} \tag{2.1}$$

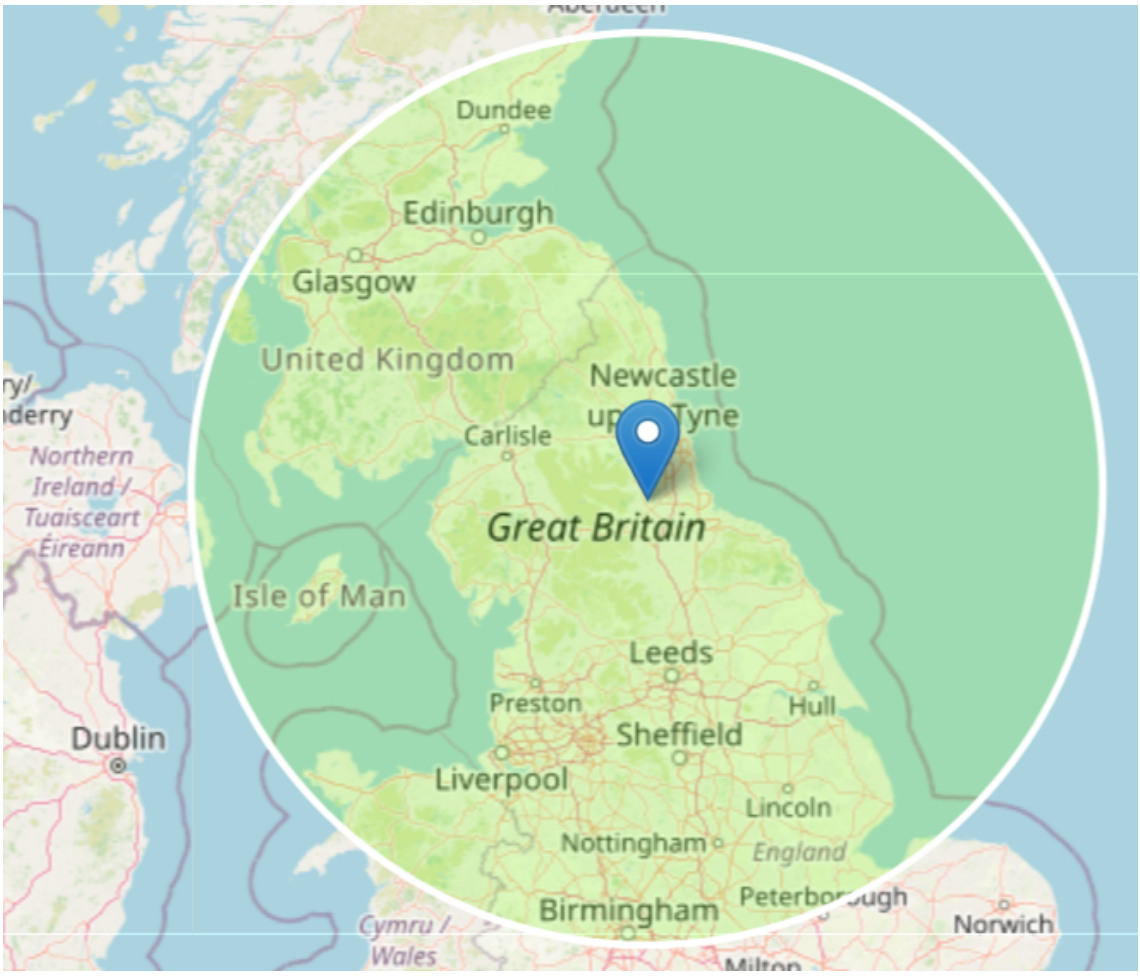

Figure 2.1: Proposed low-frequency telescope, Birmingham-Edinburgh Super Telescope (BEST), with a dish diameter of 500 km. To obtain a focal ratio of 0.4, the main receiver must be located 78 km above the Durham Astronomy building, a significant engineering and public expenditure challenge. This telescope could observe 144 MHz at 1″, and would avoid the need for interferometric techniques.

where λ is the wavelength of observation. If I want to buy an optical telescope to go in my garden and do sub-arcsecond observations, I only need a 12.5 cm diameter telescope. I can easily buy this myself for a few hundred pounds. However, to reach the same resolution at 144MHz, the observational frequency of the LOFAR high-band antennas, I would need a dish with a diameter of 500 km. In Figure 2.1 I present this hypothetical telescope and highlight the infeasibility of such an instrument. The largest steerable radio telescope in the world at Green Bank, USA is 100 m in diameter and the largest dish is the Five-hundred-meter Aperture Spherical Telescope (FAST) in China. This has proved to be the practical engineering limit for some time. Astronomers have naturally realised the implications of these facts early on and the development of the first radio interferometers for astronomy began in the 1940s.

By observing the sun rising over the sea, McCready et al. (1947) were able to measure the interference patterns between light arriving directly at their cliff-top antenna and light being reflected from the sea to that antenna. If the emission was coming from the Sun as a whole, there should be no interference patterns as waves coming from all parts of the sun would not preferentially superimpose at any particular point. However, if increased emission was coming from a much smaller part of the Sun, then one can observe minima and maxima in the pattern as the Sun rises and the waves superimpose at the clifftop receiver. They found that they were only able to observe interference patterns when there was more intense sunspot activity, a key support in their argument for radio emission association with sunspots. This work also pointed towards two other key ideas for radio interferometry. One was noting that the pattern variations were not perfectly sinusoidal, most likely due to variable refraction in Earth's atmosphere, the other was realising that the power derivation involved a Fourier transform but that with a single observation, the exact components of this transform could not be ascertained. However, *"It is possible in principle to determine the actual form of the distribution in a complex case by Fourier synthesis using information derived from a large number of components."*. These observations were carried out by Ruby Payne-Scott, a pioneer in radio astronomy who left the field just 4 years later to raise a family. At the time, no maternity

leave was available.

2.1.1 Principles of Radio Interferometry

In general, radio interferometry is about measuring the coherence between electromagnetic waves at two separate points. In the simplest case, a two-component monochromatic interferometer observing a point source, we measure two voltages, V_1 and V_2, which oscillate with an angular frequency ω, with a time delay of τ_g between the first and second antenna. We can multiply these voltages together to find

$$V_1 V_2 = \left(\frac{V^2}{2}\right) \left[\cos\left(2\omega t - \omega\tau_g\right) + \cos\left(\omega\tau_g\right)\right] \tag{2.2}$$

If we time average this equation we can filter out the faster varying cosine component [1] to leave only the effect of the time delay, R_c the cosine correlation,

$$\langle V_1 V_2 \rangle = R_c = \left(\frac{V^2}{2}\right) \cos\left(\omega\tau_g\right) \tag{2.3}$$

This would be enough to characterise a point source but, in practice, we actually observe a varying sky brightness, I, from a source, $\hat{s}$. We can approximate this as a collection of point sources as before but we now must also consider the anti-symmetric (sinusoidal) part of the on-sky distribution to be able to capture the two-dimensional distribution. We define a new sine correlation, R_s, and a measurement known as complex visibility, V (not a voltage and different to V of Equation 2.3!), which can be defined as

$$V = R_c - iR_s = Ae^{-i\phi} \tag{2.4}$$

$$\tag{2.5}$$

Here, we combine the sine and cosine correlations into a complex correlation

[1] $2\omega t$ wraps rapidly over time while $\omega\tau_g$ is constant over the time period of the measurement

with an amplitude, A, and a phase, ϕ. This is what we extract from the correlator. We can then consider how this complex visibility relates to the sky brightness, I, in a direction, $\hat{s}$:

$$V = \int I(\hat{s}) \exp(-i2\pi\vec{b} \cdot \hat{s}/\lambda) d\Omega \tag{2.6}$$

$$= \int I(\hat{s}) \exp(-i2\pi c\tau_g \nu) d\Omega \tag{2.7}$$

We give this relation firstly in terms of the vector, $\vec{b}$, between the two antennae and secondly in terms of the time delay, τ_g, between the two sources.

At this point, one may consider whether we should expect any coherence from some sort of extended source modelled in this way, where each individual point source is not coherent with another. The key is the van Cittert-Zernicke theorem which states that at large distances a specially incoherent source will appear to have some degree of coherence related by an inverse Fourier transform to the sky brightness. If we replace the $\vec{b}$ vector in the previous set of equations with a three-dimensional description with u (north), v (east) and w (up) and then the $\hat{s}$ with a three-dimensional description of l, m and n we can define the relation between the sky brightness and complex visibilities. u, v and w are measured in units of the observing wavelength λ.

If $w = 0$, meaning that the antennas are in the same plane, the equations can be simplified into a two-dimensional Fourier transform:

$$\frac{I(l,m)}{(1-l^2-m^2)^{1/2}} = \int\int V(u,v) \exp[+i2\pi(ul+vm)]\ du\ dv \tag{2.8}$$

This approximation is generally good as long as we are measuring a small region of the sky.

Therefore, if we can perfectly sample all points in the $u-v$ plane, we can take the inverse Fourier transform presented to obtain precisely the sky brightness distribution $I(l,m)$. Since u and v define baseline separations in terms of wavelength, it is clear that in an array of N antennas, we actually sample $N(N-1)/2$ different baselines but $N(N-1)$ visibilities since we can also look at the inverse (complex

conjugate) correlation. A snapshot of these points is not enough to be able to take the inverse Fourier transform.

Fortunately, while the positions of our antennas typically remain at a fixed location on Earth, the projected baseline varies as the Earth rotates (i.e. while looking at the same source position on the sky, the wavelength separation between two points varies). This means that over time a single baseline will trace out an ellipse in the $u - v$ plane over a 12 hour period allowing us to further fill out the $u - v$ plane without increasing the number of antennas in the array. This process is known as Earth-Rotation Synthesis, with Martin Ryle leading this advancement at Cambridge (Ryle, 1962).

2.1.2 Imaging

Actually turning these discrete visibilities into an image has its own caveats. Even with a full 12-hour observation, with a finite number of baselines, we are not able to fully sample all spatial frequencies in the $u-v$ plane. Instead, radio astronomers have developed methods of *deconvolution* in order to extract the "true" sky brightness.

Deconvolution appears in the topic of imaging in radio astronomy due to the consideration of the effect of sampling a set of points in the $u-v$ plane. Let $W(u, v)$ be our set of points in the $u-v$ plane. We can think of our sampling as some sort of weighting function of the true distribution $V(u, v)$. In areas in which we have gaps, we are weighting the true sky visibility down to zero. However, where we do sample we can choose our weighting. The simplest case is to simply use our measured value where we have it (called natural weighting) but other approaches exist to give a different balance between the known and unknown regions of the $u - v$ plane. Now in frequency space, we can think of our observation as a multiplication of the true distribution and our weighted sampling. This is how convolution and deconvolution appear since via the convolution theorem a multiplication in the frequency domain becomes a convolution in the spatial domain:

$$\mathcal{F}^{-1}\{\mathcal{F}\{u\} \cdot \mathcal{F}\{v\}\} = u \otimes v \tag{2.9}$$

where in our case, if we take the inverse Fourier transform of our weighted visibilities we find

$$I^D(l,m) = \mathcal{F}^{-1}\{W(u,v) \cdot V(u,v)\} = b(l,m) \otimes I(l,m) \tag{2.10}$$

where I^D is the so-called "dirty" image and is the convolution of the true image $I(l,m)$ with the effects of our sampling $b(l,m)$ known as the dirty beam. Thus to obtain a model of the true image we attempt to deconvolve the effects of the dirty beam, or the "weighting function" $W(u,v)$.

If the true sky distribution is a set of point sources then the dirty image will contain copies of the dirty beam each centred on the position of the point source. The brightness of the imprinted beam pattern will vary depending on the brightness of the source. Although this assumption about the sky is clearly not true, it is good enough to allow for the most widely used deconvolution algorithm in the radio astronomy community, CLEAN (Högbom, 1974).

The algorithm is rather simple but produces effective results for most radio images. The aim is to start with the dirty image and subtract true source flux until, ideally, we are left with Gaussian noise while building up a clean model of what we believe the true source to look like as a collection of point sources. The process is as follows:

1. Find the brightest pixel in the dirty image

2. Subtract some fraction, g, of the dirty beam $b(l,m)$ from the dirty image $I^D(l,m)$ at the location of the pixel. g is usually referred to as the gain. This is valid under the assumption that the sky is made of point sources

3. Add the flux of this pixel to the clean model

4. Repeat steps 1-3 as many times as the user requires. Usually, an automated stopping criterion is used based on when the next pixel to be selected is below some multiple of the rms of the image. This means we are no longer certain we are cleaning true flux

5. After stopping we convolved the model flux components with a model of the beam, typically a 2-D Guassian. We then add this back on top of the dirty image which at this point should be mostly noise

Several variants of this algorithm are present which can balance accuracy vs computational complexity in various ways. It should be noted that, although the pixel selected for cleaning is chosen in the imaging space, when we subtract some fraction of the dirty beam we are also subtracting in the visibility space of the dirty image. This means that cleaning one pixel actually improves the quality of the image as a whole since every pixel sees the effect of every visibility and vice versa.

A key feature included in most implementations of this algorithm is that of masks. If one has prior knowledge of the location and extent of flux in an image, one can restrict the algorithm to only clean pixels within the masked region. This should increase the accuracy of the model as areas of noise outside of the mask that have potentially high flux will be ignored and not included in the clean model. Deconvolution is in almost all cases an under-determined problem in its mathematical presentation. This means that the interpolation and extrapolation of areas in the $u - v$ plane can have many "equally valid" solutions in the mathematical sense. However, we can greatly improve the results by providing constraints from physical arguments ("a priori" information).

2.1.3 Calibration

All of the above has been presented in the absence of significant noise and effects that must be corrected and calibrated in order to obtain a science-quality image. Here I briefly outline some of the most important effects when it comes to an array such as LOFAR along with a brief introduction to the mathematical formalism used.

In the previous section, we were discussing visibilities in u, v which is defined as the spacing between antennas in units of wavelength. Now, we would like to consider the noise and effects inserted by the antennas themselves as well as other effects. We can ignore the u, v coordinates momentarily and consider the antennas 1 and 2. To capture full polarisation information, complex visibilities in practice are made up of

2×2 matrices containing the visibility measured across the same polarisation and cross of each between the two antennas. We can begin by ascribing all the changes that have occurred to a single visibility to one matrix, the Jones matrix J_{12}:

$$V_{12}^{\text{observed}} = J_{12} V_{12}^{\text{sky}} \tag{2.11}$$

Our task is then to find the best possible measure of J_{12} in order to obtain a visibility close to the true sky signal. We do this by decomposing J_{12} into as many effects as we want to correct or calibrate for, each corresponding to its own 2×2 matrix. This is equivalent to assuming that each effect is linear and occurs in a specific order from the initial signal through to our final measurement. Since these are matrices, they in general do not commute, although several effects can be described by diagonal or rational matrices which have their own commutation properties that may allow for simplification.

The exact number of components that J_{12} is split into is largely dependent on the telescope and/or software being used for an observation. For example, the widely used Common Astronomy Software Applications for radio astronomy (`CASA`) splits J_{12} into eight separate components (Bean et al., 2022). In order of the signal interaction, they are: the ionospheric effects, the tropospheric effects, parallactic angle rotation, the optical properties of the antenna, the polarisation leakage, the time and polarisation-dependent gain response (probably the most important in most telescopes), the amplitude and phase bandpass response of the electrical components in the receiver and finally phase correction based on any offsets in antenna-position.

Typically, these calibrations are usually performed by using calibrator sources. Some of the brightest sources in the sky have been observed many times with great detail and as such have known structure, flux and spectral properties. We can solve for several of the previous effects by fitting data to known models of these calibrators and throwing out ("flagging") data which cannot be fit within the model beyond some tolerance. I will not go into extreme detail here but provide an example. If we know that a source shows little variability in its flux then any observed changes in the amplitude of the antenna over the time of observation must be due to effects within the instrument. We can try to parameterise and fit a model for these changes

over time and then shift the amplitude of each visibility based on the model so that they now remain roughly constant.

Each of the effects described has its own effect which can be understood through a Jones matrix representation. We can therefore find these Jones matrices independently in many cases before applying them to the signal in the correct order.

Self-Calibration

Even after applying all the various calibrations described in the previous section, we may still find artefacts in images that are distinctly non-Gaussian or related to the beam shape of our telescope. For example, in Figure 2.2 I show a real-world example of direction-dependent errors in LOFAR-VLBI observations from Sweijen et al. (2022). These occur because of different conditions in the sky across the field of an image. Errors in the amplitude result in symmetric artefacts across the image while phase errors are asymmetric. How should we proceed when attempting to remove these features?

If a target has sufficient signal-to-noise then we can attempt to correct for these errors through a process known as *self-calibration*. We use the source to calibrate itself. The residual errors we are observing at this point originate on a per-antenna basis. As noted in § 2.1.1, the number of baselines which produce visibilities is a much larger number and so we have a problem which can be constrained.

The process of "self-calibration" is one of cycles in which we image our current data, clean it to produce a model of the true source, calibrate the original visibilities to best fit that model and then repeat. The process can be used for phase and amplitude corrections. Phase errors have a more direct impact on our knowledge of the source structure. Therefore phases are typically corrected for first and may involve several cycles solving for variation over different time intervals. Amplitude corrections also require greater signal-to-noise.

This technique is regularly used in radio astronomy and can provide significant image quality and noise improvements for the brightest sources. Often, we can then use the model solutions to improve our images in other directions once we are sufficiently satisfied with the self-calibration process. For example, in the LOFAR-

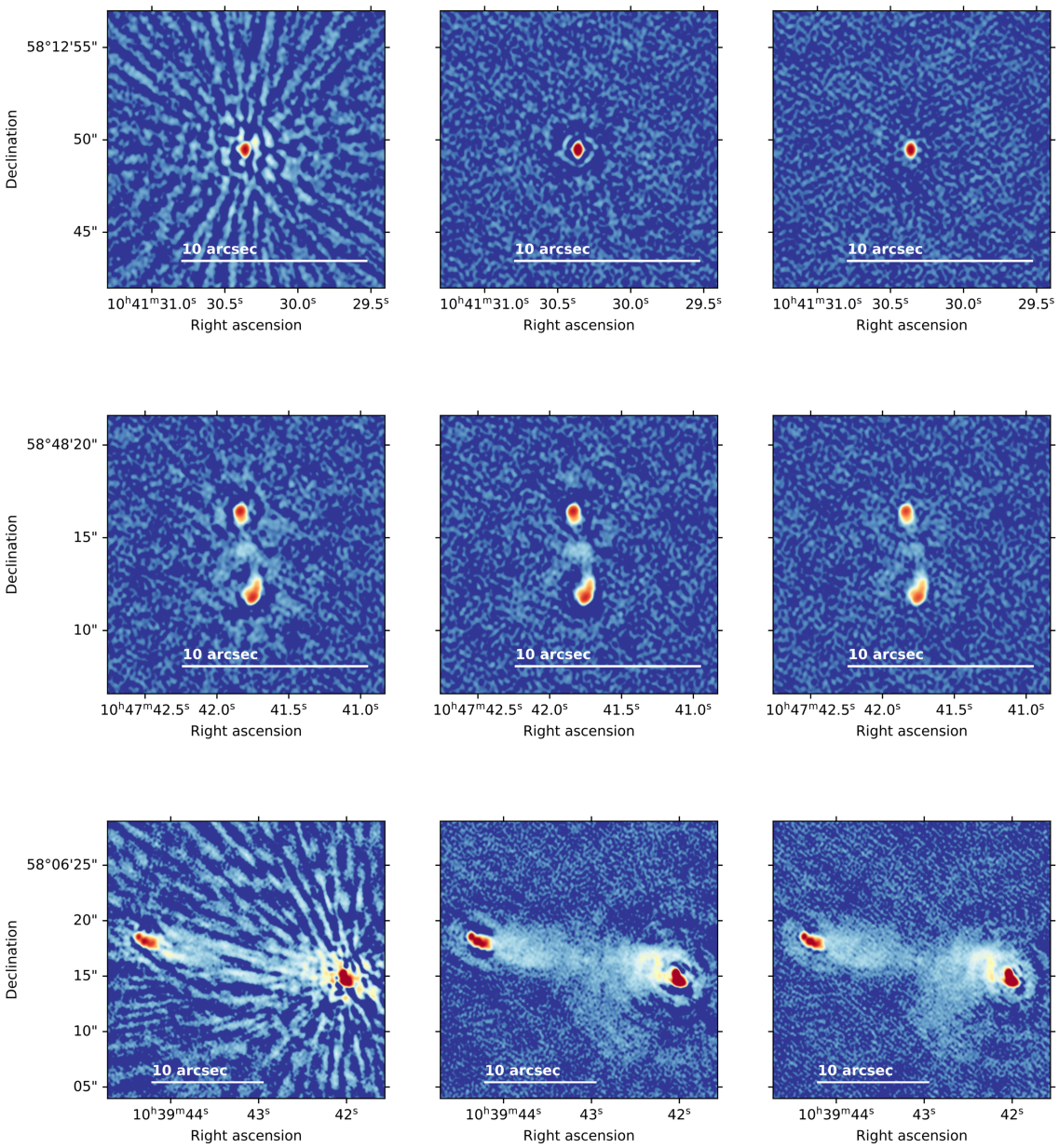

Figure 2.2: Example of self-calibration process for three sources observed with the full International LOFAR Telescope. The images on the left-hand side have already been corrected, as best as possible, for all effects independent of their specific position on the sky. From left to centre, the sources are corrected for different electron content above each station which introduces phase errors. From centre to right, the sources have their amplitudes calibrated.
Credits: Figure taken from Sweijen et al. (2022) with permission from the author

VLBI pipeline (see § 2.3.1), we use 10 rounds of self-calibration on a bright delay-calibrator in every field before applying those solutions to all target directions.

2.2 Radio Telescopes

Here I give a short overview of the two radio instruments directly used in this thesis and some of the calibration specifics important to each of them.

2.2.1 LOFAR

The Low-Frequency ARray (LOFAR; van Haarlem et al., 2013) is a phased array telescope consisting of over 70,000 small omnidirectional antennae spread across Europe. The array is split into two bands, the Low Band Atenna (LBA) for 10-80 MHz observations and the High Band Antenna (HBA) for 120-240 MHz. The antennae are grouped into "stations" with 24 central "core" stations in a small area in the Netherlands, 14 "remote" stations at a greater distance within the Netherlands and currently 14 "international" stations across other European countries. The telescope is unique in its sensitivity and resolution at low frequencies.

Until recently, the vast majority of publications utilising LOFAR only used the core and remote stations which are able to achieve a resolution of $\sim 6''$ for the HBA. This is still a step change for telescopes operating at such low frequencies and has allowed for new and varied science.

LOFAR has some additional calibration complexities as compared to an instrument such as the VLA due to both its system design and frequency range. For a detailed look into the systematic effects present I refer to the paper of De Gasperin et al. (2019), which sets out the key corrections applied in the `prefactor` software package.

Each remote and international station has a separate atomic clock to that of the core stations. Although these clocks are exceptionally accurate, they can drift from each other by up to a nanosecond every minute. At 150MHz, a single period is 6.67 nanoseconds so the timing errors create a frequency-dependent time delay which will quickly corrupt all data if not corrected for.

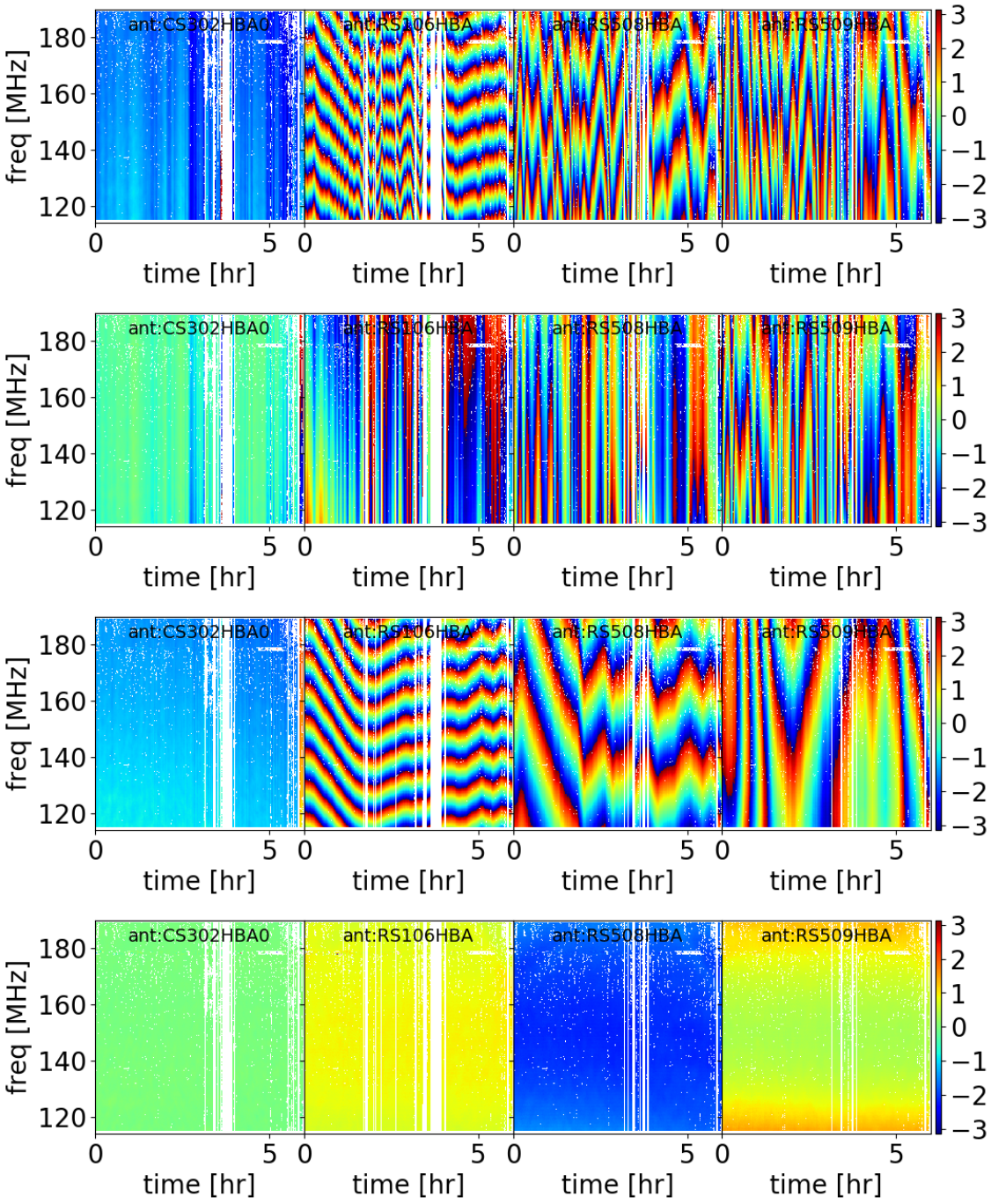

Figure 2.3: Example of solving for clock delays, ionospheric delays and Faraday rotation for three remote and one core HBA station. These figures are coloured by the visibility phase $(-\pi, +\pi)$ correction needed to achieve a particular calibrator model across time for the full HBA frequency range and display the phases for the correlation of X linearly polarised components. The upper panel shows the full corrections needed. The second panel has had clock drift removed, therefore we are only viewing the phase delays induced by the changing refractive index of the ionosphere. The third panel has had the ionosphere removed but clock drift is left in. You can see at times the phases reset when the clocks receive a GPS reset. The lower panel shows the final state of the solutions with frequency-dependent systematics removed. The phases are largely stable indicating a successful removal of the effects.
Credits: Taken from De Gasperin et al. (2019)

The ionosphere is the main source of complications for LOFAR as compared to other radio telescopes. The electron plasma in this layer of the atmosphere operates as a birefringent medium which both imparts a frequency-dependent time delay due to changing refractive index depending on the electron density and additionally induces a relative rotation between linear polarisations. These two effects are typically solved for separately as they have a different proportionality to frequency.

After solving for the bandpass (the frequency-dependent response of each antenna over time) in a similar manner to other telescopes, the standard LOFAR strategy is to solve for the clock and ionospheric effect simultaneously. An example of this is shown in Figure 2.3 where the refractive index of the ionosphere and clock drift are shown in the two middle panels. These "rainbow" plots are very typical of this type of calibration as one can clearly observe any frequency-dependent phase errors.

LOFAR-VLBI

With the inclusion of the international stations, the International LOFAR Telescope (ILT) can achieve an angular resolution of $\sim 0.2''$ using the HBA. This resolution surpasses that of ground-based optical telescopes and places low-frequency radio in the world of space telescopes, an incredible step forward for the field. This capability will ensure world-leading performance and relevance for LOFAR well into the era of the Square Kilometre Array Observatory (SKAO) which can only achieve a resolution of around $\sim 10''$ at the same frequency. However, the addition of the international stations presents a much greater calibration challenge which is why it has taken much longer to create images and a pipeline (Morabito et al., 2022b) incorporating the full array. Additional information on how this capability is achieved is described in § 2.3.1 where I also outline my own contributions to help make this processing possible and accessible.

2.2.2 eMERLIN

The enhanced Multi-Element Remotely Linked Interferometer Network (eMERLIN; Garrington et al., 2004) is the UK's premier radio astronomy instrument. The

array is made up of six $\sim$ 25 m diameter radio telescopes spread across the UK. Optionally, the array can also make use of the iconic Lovell telescope, the third-largest steerable radio telescope in the world, to roughly double the instantaneous sensitivity at the cost of halving the field of view. The longest baselines allow for gigahertz observations at resolutions well below an arcsecond.

Typical calibration with eMERLIN is typically much easier than with LOFAR, due to its frequency and small number of large dish antennae. The eMERLIN calibration pipeline[2] can achieve reliable results for bright sources all the way through to final imaging. The stage that actually occupies the most time (40% - 50%) in the processing of this data is the flagging of data corrupted Radio Frequency Interference (RFI). Radio signals power our model life and so telescopes are affected by radio, television, mobile phone and satellite transmissions which will leak power into observations. Fortunately, this kind of interference often displays characteristic behaviour which allows us to identify and remove it from our data. For example, interference often spikes in narrow frequency channels which are used for communication, it can be persistent or periodic and, since it comes from a position which is stationary compared to the slewing of a telescope during an observation, it will be incoherent. We can also leverage repeat observations to build knowledge up our understanding of RFI for a given telescope. This enables the development of general "RFI strategies" which can be optimised for each instrument and frequency band[3].

2.3 Contributions to LOFAR

The majority of this thesis reflects the work undertaken to further the understanding of BALQSOs and their radio emission. In this section, I aim to describe and record some of the efforts and contributions I have made to improve LOFAR radio imaging both in quality and accessibility.

[2] `https://github.com/e-merlin/eMERLIN_CASA_pipeline`

[3] Some examples of LOFAR strategies can be found at `https://git.astron.nl/RD/LINC/-/tree/master/rfistrategies`

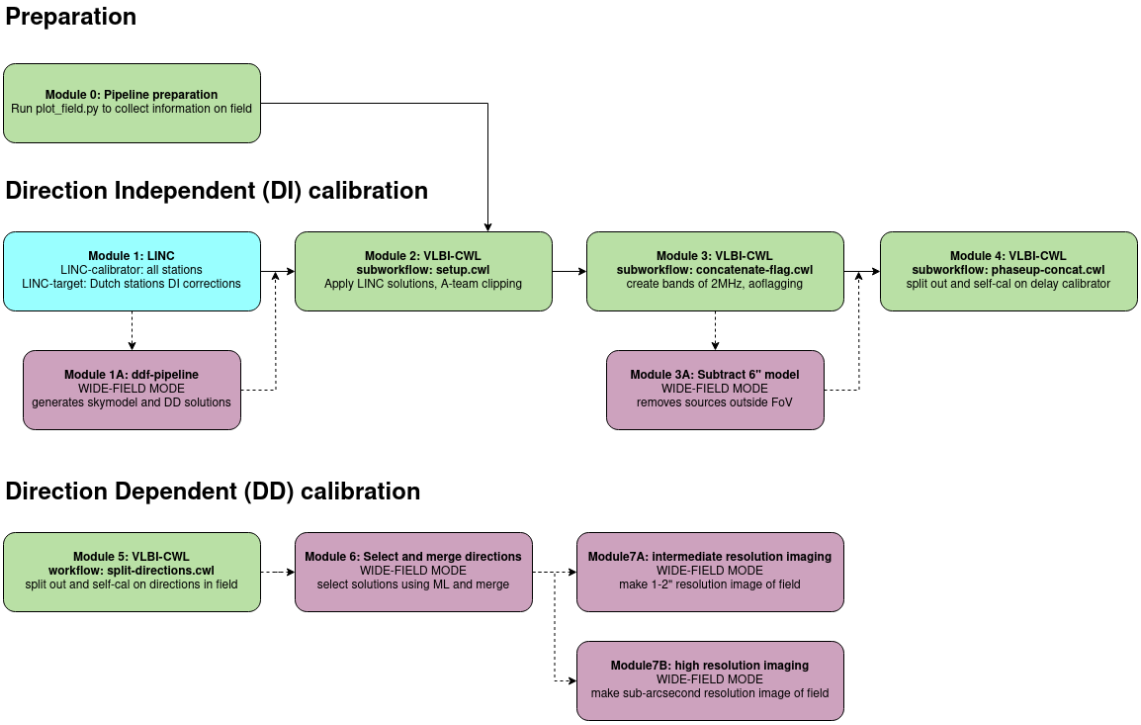

Figure 2.4: LOFAR-VLBI pipeline description

2.3.1 LOFAR-VLBI Pipeline

A typical 8-hour LoTSS observation with international stations included contains 230 sub-bands each of ~ 15 GB in size. Within the Measurement Set format typically used in radio astronomy, this is spread across > 20000 files. To process this data many different tools have been developed to perform calibration procedures (some of which are outlined in § 2.1.3) on all or part of the data. Controlling the flow of data, memory usage and computational power is a challenge to modern-day radio astronomy which is somewhat independent of the actual development of tools which solve a particular problem in the calibration procedure.

The main calibration correction that is needed is known as a delay calibration. This calibration arises from the fact that the ionosphere imparts a dispersive delay on the phases measured between baselines. The total electron content (TEC) above a station affects the arrival time of the radio waves at the antenna. For two antennas with different TECs above them, a phase error will be induced as the ionosphere imparts an additional delay between the two antenna measurements. There are two reasons why this is a particular issue for LOFAR.

Firstly, for LOFAR to achieve sub-arcsecond resolution, stations have been built all across Europe with the longest baselines stretching from Latvia to Ireland. Higher-frequency interferometers do not need to be as large and can avoid this correction under the assumption that the ionospheric conditions above each of their antennas are roughly identical and that the ionospheric effect is much smaller at these frequencies. For LOFAR this assumption does not hold and the TEC values across Europe can be very different and change during the period of an observation.

Secondly, the ionospheric delay is frequency-dependent and becomes more impactful at low frequencies. Specifically the delay, d, is related to the phase, ϕ, by $d = d\phi/d\nu \propto \nu^{-2}$. Therefore the delay calibration removes an overall frequency dependence from the phases. Removing the frequency dependence is crucial in enabling significant averaging in frequency space without simply condensing to noise. This is beneficial since we require a high signal-to-noise ratio to perform self-calibration, which can be facilitated by averaging.

To calibrate for these effects, as is often the case in astronomy, we use a reference source which is well-studied and has its structure modelled in detail. In this case, we target sources which are bright and compact as they will produce the most signal on the longest baselines which should experience the worst effects of these delays. We need to have such sources in every field in order to do this successfully. Jackson et al. (2016, 2022) created the Long Baseline Calibrator Survey (LBCS) in order to investigate whether these suitable calibrators actually exist at a high enough sky density. They found around 1 suitable delay calibrator per square degree which is fortunately less than the field of view of international LOFAR.

To calibrate a field, one can query the catalogue of LBCS sources to find a potential calibrator. We apply corrections to the data to simulate observing the calibrator at the centre of the field of view (phase-shifting) and average to reduce the data volume. We then perform self-calibration in this direction to solve for the dispersive delays. The source does not need to remain entirely compact to achieve good results as long as the solutions converge to a reasonable, smooth state. We then split into other directions of interest in a field, apply these delay solutions and either image directly or perform further self-calibration on these fainter or more

extended sources to capture direction-dependent effects in the field.

2.3.2 Pipeline Framework

The methods and initial release of the LOFAR-VLBI pipeline were outlined in Morabito et al. (2022b). The pipeline was written to attach to the end of the `prefactor`[4] pipeline which was used to process LOFAR HBA data for LoTSS and other work (De Gasperin et al., 2019). For this reason, the initial version of the LOFAR-VLBI pipeline was written within the `genericpipeline.py` framework [5]. The exact details need not be explained but this framework uses text files called parsets to control the operation of command line programs which are used to operate on the radio data. The pipeline also controls the distribution of computing power to different tasks and the generation of log files to record progress and issues.

The processing scale of International LOFAR represents a paradigm shift in the field of radio astronomy. Some parts of the pipeline must operate on the entire frequency range of the data at once. Even with considerable compression, this can be $> 2\,\mathrm{TB}$ of data which must be processed together. In comparison, the VLA produces a maximum data rate of $216\,\mathrm{GB/hr}$ with most observations producing much lower data volumes with longer averaging scales. In fact, VLA datasets can regularly be well under $1\,\mathrm{GB}$.

We also cannot average significantly in the frequency or time domain with LOFAR. For frequency, the principles of radio astronomy described above apply to monochromatic light. If we average over some frequency windows, $\delta\nu$, we introduce the effects of chromatic aberration. The effect of this is a reduction in sensitivity and resolution as we move radially away from the centre of an observation (bandwidth smearing). In time, averaging essentially condenses a larger area of the $u-v$ plane that the source was moving through to one point. Thereby reducing the overall amplitude of the complex visibility (time smearing) (Bridle & Schwab, 1999). We can therefore not average significantly prior to calibrating data as we will irreversibly reduce the sensitivity and quality of the data.

[4] `https://github.com/lofar-astron/prefactor`
[5] `https://github.com/lmorabit/lofar-vlbi`

Shortly after the beginning of this thesis the `prefactor` pipeline was renamed and transferred to a new workflow. The LOFAR Initial Calibration (LINC)[6] pipeline is now written in the Common Workflow Language (CWL) (Crusoe et al., 2021)[7]. Strictly speaking, CWL cannot run any programs itself and is simply an open standard for scientific workflows which came out of the bio-informatics community. Instead, software is built around the standard which allows for the interpretation, distribution and execution of workflows specified according to the standard. A reference implementation of this type of software is presented in the form of `cwltool`[8].

`cwltool` does not contain all of the features of other advanced tools, such as `Toil`[9] or `Arvados`[10], which come with out of the box support for cloud computing infrastructure like Amazon's AWS or Microsoft's Azure platforms. However, it does highlight some of the key benefits of the CWL system as compared to `genericpipeline.py`:

1. **Self-Validation**

   CWL *step* files specify all potential input directories, files and options for a command line program along with the output results that need to be collected. CWL *workflow* files specify overall input and assign them to *step* files that sum up to create the overall workflow. The input is type-checked. When a workflow is run by `cwltool` it first performs a validation step to check that the inputs provided and the workflow specified are logically consistent. If not it will immediately crash out of the pipeline. This creates clear, well-defined workflows and prevents simple errors like shutting down a several-hour run halfway through because you forgot to specify one input.

2. **Containerisation**

   A key issue in data processing as a collaboration is version control, reproducibility and transferability. This is a problem within software engineering in general and several tools have been developed to create essentially virtual

[6] `https://git.astron.nl/RD/LINC`
[7] `https://www.commonwl.org/`
[8] `https://github.com/common-workflow-language/cwltool`
[9] `https://github.com/BD2KGenomics/toil`
[10] `https://arvados.org/`

machines with the exact operating system and software needed to complete a particular task. These objects have become known as *containers*. The most popular container creation and distribution tool is `Docker` [11], which receives over 20 billion download requests to their container hosting hub every month. Within LOFAR, we are primarily using `apptainer` (formerly `singularity`) [12] which sees more use in the academic and high-performance computing community.

CWL has support for containers within steps and workflows. One can specify the container needed to run a particular workflow. It will check for a cached version of the container and if this doesn't exist it will download the container and use it to run the step or workflow in the exact environment needed. This adds another layer to stability and reproducibility since as a pipeline developer I can not only internally validate the workflow but also externally control the environment in which it runs.

3. **Parallelisation**

   The CWL standard has support for the parallelisation of steps or sub-workflows. The previous `genericpipeline.py` framework could also support parallelisation but not as intelligently. It could only parallelise across one task at a time, so even if the inputs for a later task were already prepared it would have to wait until the full pipeline got to that point. Since all inputs are specified at the start, CWL is able to start multiple steps at once as long as the inputs are ready and the computational resources are available. This can be much more efficient when operating on the 230 sub-bands of a LOFAR dataset.

4. **Garbage Collection**

   At the end of every CWL step only the specified outputs are collected and transferred to the next step which requires them as input. If a command-line program produces additional input it will at this point be deleted as long as that step has run successfully. Under default settings, this means that at

[11] `https://www.docker.com/`
[12] `https://apptainer.org/`

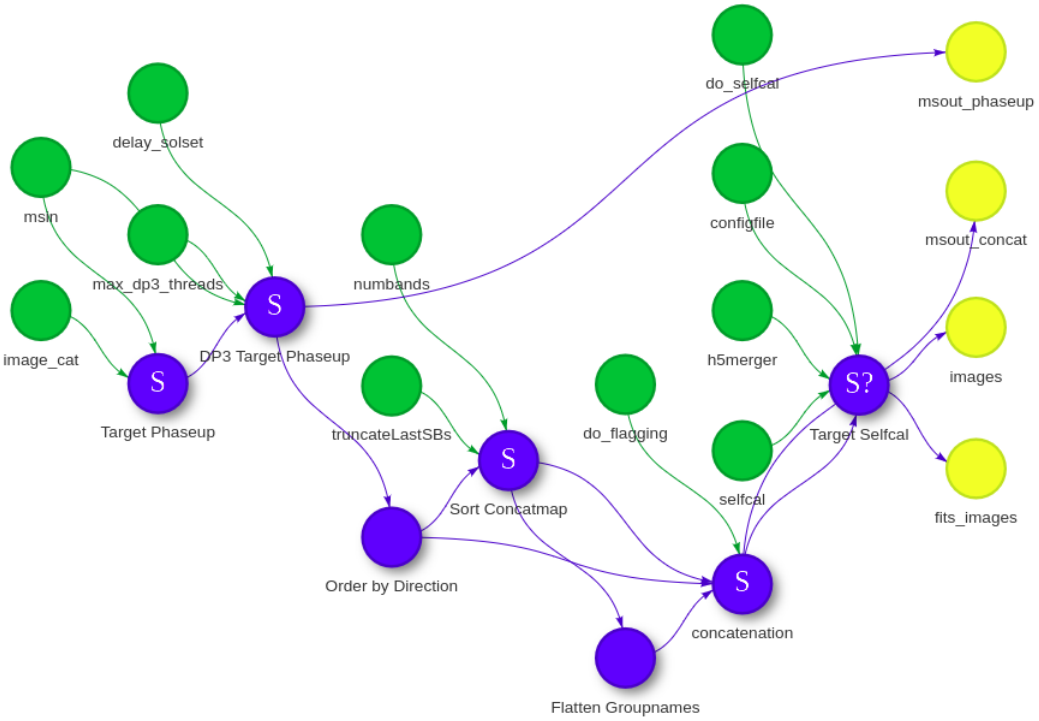

Figure 2.5: Schematic of the split-directions.cwl workflow that I primarily developed. In green are inputs, blue are steps and yellow are the final outputs of the workflow. Some of the steps in blue are, in reality, sub-workflows and contain several steps within them. Those with an S have in-built parallelisation and the question mark indicates that a step is potentially optional.

> the end of a workflow run only the wanted output should be present and any intermediate products will have been deleted along the way. For LOFAR this is important since copies of data can occupy TBs of disk space and it can be frustrating to control these products by hand. If the pipeline fails, however, it will always keep all the products of the step that failed, allowing for debugging without pieces missing.

To align with LINC, the LOFAR-VLBI working group took the decision to also move the pipeline to a CWL specification[13]. I took on the role of translating the direction-splitting task which is the second half of the overall LOFAR-VLBI pipeline. Most of this work consisted of translating the previous parset files into common workflow language standard files without changing too much. However, there were several additions to improve the efficiency and output quality of the pipeline and

[13] `https://git.astron.nl/RD/VLBI-cwl`

care taken to improve documentation.

The split-directions workflow aims to produce images in each of the target directions specified within a catalogue by the user (see § 2.3.3 for details on my contribution in this area). This requires the input visibility data, solutions from the delay calibrator and whether or not the user would like to perform additional self-calibration in these target directions.

To add parallelisation to the steps involved here required some careful adjustments since the parallelisation happens over several dimensions. We would like to scatter over the number of directions that the user has specified so that it can work in several directions at once if the computational resources are available. We would also like to scatter over the number of sub-bands (in this case typically 24 rather than 230; some concatenation occurs in the delay-calibration workflow). We also have a concatenation step where we need to gather all the measurement sets for a particular direction and stack them so that we end up with one calibrated measurement set in each target direction.

There are some `scatterMethods` available within the CWL specification but the development process and logic of this scattering were rather difficult. However, in the long term, we expect that users may want to image around 100 different directions per pointing so parallelising this process for them provides a great deal of value to them.

The overall structure of the workflow is shown in Figure 2.5. Each step needed to be translated with some extra steps put in to control the scattering process. The final optional self-calibration step was also not available within the `genericpipeline.py` framework and is the last piece in allowing a non-expert user the potential to create science-quality radio images of their targets without additional expertise.

The full version of the split-directions workflow at the time of writing can be seen in § 2.4.

2.3.3 Catalogues and Plotting

As described previously, one difficulty in utilising the LOFAR-VLBI pipeline is selecting a suitable delay calibrator. In the old version of the pipeline, there was a

step in which catalogues were downloaded containing the LoTSS and LBCS sources within a particular radius of the pointing centre. These LBCS sources were then simply sorted by radius from the pointing centre and if no changes were made the pipeline would simply use the first entry in the list of LBCS sources as the delay calibrator.

All of this was text-based and could create issues for users who were not well involved in the development of the pipeline. Additionally, some users found that their targets of interest were not even suitable for high-resolution imaging with international stations in the first place because of the limited field of view of the international stations and losses due to smearing. A lot of them found this out after running the pipeline for potentially weeks....

I decided to work on a tool that would allow users to visualise and understand the field that they are potentially working with and provide key information on the LBCS and LoTSS sources within it. This tool is now recommended to be run **before any other VLBI processing starts** and ideally, before you have even downloaded the data.

The heart of the script is the same catalogue downloading tools that build on what existed in the previous pipeline. It will produce the necessary delay calibrator and target field catalogues by default within 1.5 degrees of the pointing centre. It will also search on a wider radius for any extremely bright sources that could significantly affect observations within the field. It then moves to creating a diagnostic plot based on these catalogues.

An example output is shown in Figure 2.6 which is centred on the LoTSS pointing P250+33. We provide the user with information on all the potential delay calibrators at once along with the positions of potentially interesting sources in the field.

Key to preventing frustrating and time-consuming mistakes for those new to LOFAR-VLBI is the indication of the time and bandwidth-smearing effects on the overall sensitivity of the instrument at different radii from the pointing centre. We indicate regions where 20,40,60 and 80% of sensitivity may be expected to be lost along with the 1.5° field of view of the international stations. In the case where the user is only interested in one target in the field, they can specify the right

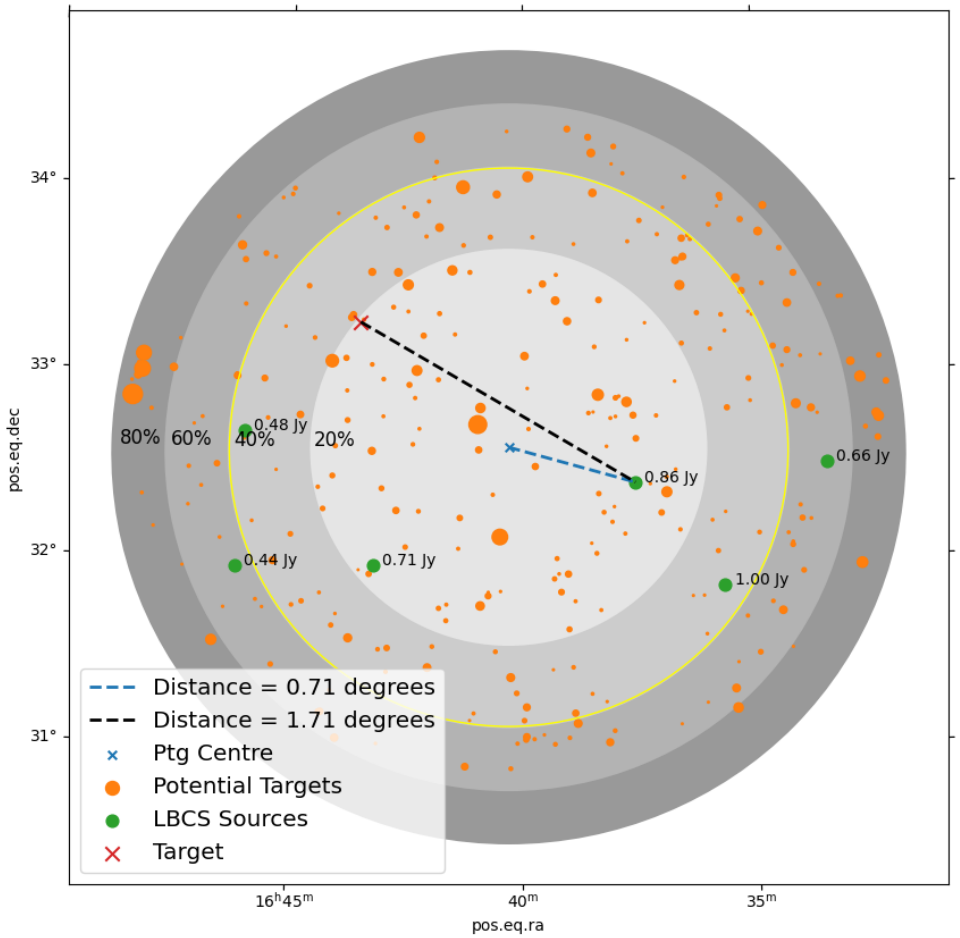

Figure 2.6: Example output for the plotting script I developed now recommended as the starting point of the LOFAR-VLBI pipeline. The green points are LBCS sources with their flux listed which could be an important factor in calibration. The orange points are all LoTSS sources above a user's chosen flux limit, the size corresponds to their brightness. We indicate the distance from the pointing centre to the currently chosen delay calibrator as well as the distance from that delay calibrator to a given target specified by the user. The shaded regions indicate the percentage flux lost due to smearing effects. The user can change averaging parameters and observe how these regions change. The yellow border indicates the 1.5-degree FOV of the LoTSS international stations.

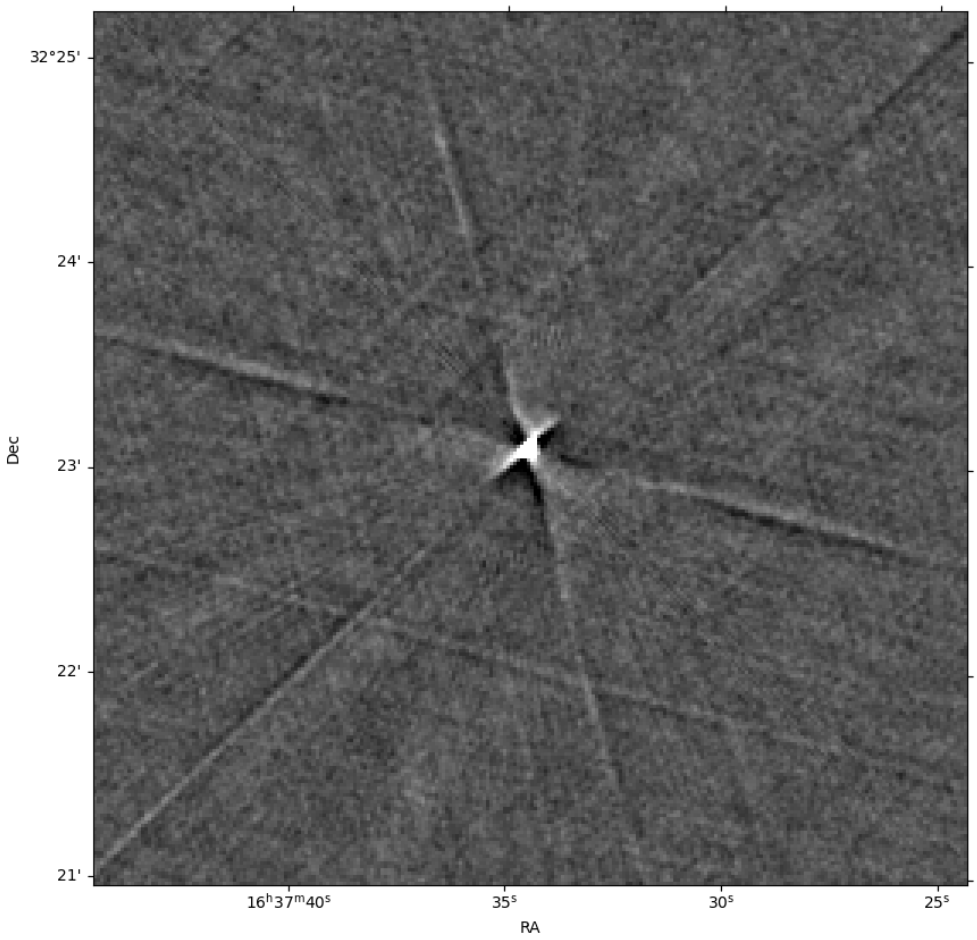

Figure 2.7: VLASS image of the L464658 LBCS source that was the primary delay calibrator for the example field in Figure 2.6. The user can use these plots to inspect whether the calibrators have any expected structure which can be useful later when verifying self-calibration.

ascension and declination of that target and have the relative position of their target to the current delay calibrator indicated. This can be useful as if there is a good delay calibrator slightly closer to the target it can be easier to transfer solutions by selecting that one instead.

An additional feature of the script is the incorporation of the quick look VLASS epoch 1 images which are publicly available. With the addition of the `--vlass` flag, the user can request the download and minimal processing of VLASS images for all of the delay calibrators within the field. The user can then inspect the VLASS images for any expected structure within the delay calibrators. This could aid in selecting a suitable calibrator and then verifying that self-calibration is proceeding as expected based on those images.

2.4 Code Listings

Below is the current state of the `split-directions.cwl` workflow which was initially translated by myself.

Listing 2.1: Split-directions.cwl workflow

```
class: Workflow
cwlVersion: v1.2
id: split-directions
label: Split Directions
doc: |
  This is a workflow for the LOFAR-VLBI pipeline that
  splits a LOFAR MeasurementSet into various target directions, applies delay calibrator solutions and then opt
  self-calibration on the target directions.

  This step should be run after the delay calibration workflow.

requirements:
  - class: SubworkflowFeatureRequirement
  - class: MultipleInputFeatureRequirement
  - class: ScatterFeatureRequirement

inputs:
    - id: msin
      type: Directory[]
      doc: The input MS. This should have coverage of the target directions.
    - id: delay_solset
      type: File
      doc: The solution tables generated by the VLBI delay calibration workflow in an HDF5 format.
    - id: image_cat
      type: File
      doc: The image catalogue (in CSV format) containing the target directions.
      default: lotss_catalogue.csv
    - id: max_dp3_threads
      type: int?
```

```
      default: 4
      doc: Number of cores to use per job for
        tasks with high I/O or memory.
    - id: numbands
      type: int?
      default: -1
      doc: The number of bands to group. -1 means all bands.
    - id: truncateLastSBs
      type: boolean?
      default: true
      doc: Whether to truncate the last subbands of the
        MSs to the same length.
    - id: do_selfcal
      type: boolean?
      default: false
      doc: Whether to do selfcal on the direction concat MSs.
    - id: configfile
      type: File
      doc: The configuration file to be used to run
        facetselfcal.py during the target_selfcal step.
    - id: h5merger
      type: Directory
      doc: The h5merger directory.
    - id: selfcal
      type: Directory
      doc: The selfcal directory.

    - id: linc
      type: Directory
      doc: |
        The installation directory for the
        LOFAR INitial Calibration pipeline.

steps:
    - id: target_phaseup
      label: Target Phaseup
      in:
        - id: msin
          source: msin
        - id: image_cat
          source: image_cat
        - id: delay_solutions
          source: delay_solset
      out:
        - id: parset
      run: ./subworkflows/split_parset.cwl
      scatter: msin

    - id: dp3_target_phaseup
      label: DP3 Target Phaseup
      in:
        - id: msin
          source: msin
        - id: parset
          source: target_phaseup/parset
          linkMerge: merge_flattened
        - id: delay_solset
          source: delay_solset
        - id: max_dp3_threads
          source: max_dp3_threads
      out:
        - id: msout
      run: ../steps/dp3_target_phaseup.cwl
      scatter: [msin, parset]
```

```
    scatterMethod: dotproduct

  - id: order_by_direction
    label: Order by Direction
    in:
      - id: msin
        source: dp3_target_phaseup/msout
    out:
      - id: msout
    run: ../steps/order_by_direction.cwl

  - id: collect_linc_libraries
    label: Collect neccesary LINC libraries
    in:
      - id: linc
        source: linc
      - id: library
        default:
          - scripts/sort_times_into_freqGroups.py
    out:
      - id: libraries
    scatter: library
    run: ../steps/collect_linc_libraries.cwl


  - id: sort_concatmap
    label: Sort Concatmap
    in:
      - id: msin
        source: order_by_direction/msout
      - id: numbands
        source: numbands
      - id: truncateLastSBs
        source: truncateLastSBs
      - id: linc_libraries
        source: collect_linc_libraries/libraries
    out:
      - id: filenames
      - id: groupnames
    run: ../steps/sort_concatmap.cwl
    scatter: msin

  - id: flatten_groupnames
    label: Flatten Groupnames
    in:
      - id: nestedarray
        source: sort_concatmap/groupnames
    out:
      - id: flattenedarray
    run: ../steps/flatten.cwl


  - id: concatenation
    label: concatenation
    in:
      - id: msin
        source: order_by_direction/msout
      - id: groups_specification
        source: sort_concatmap/filenames
      - id: group_id
        source: flatten_groupnames/flattenedarray
    out:
      - id: msout
    run: ./subworkflows/concatenation.cwl
```

```
      scatter: [msin, groups_specification, group_id]
      scatterMethod: dotproduct


    - id: target_selfcal
      label: Target Selfcal
      in:
        - id: msin
          source: concatenation/msout
        - id: configfile
          source: configfile
        - id: h5merger
          source: h5merger
        - id: selfcal
          source: selfcal
        - id: do_selfcal
          source: do_selfcal
      out:
        - id: images
        - id: h5parm
        - id: fits_images
      when: $(inputs.do_selfcal)
      run: ../steps/facet_selfcal.cwl
      scatter: msin

outputs:
    - id: msout_phaseup
      type:
        type: array
        items:
          type: array
          items: Directory
      outputSource: dp3_target_phaseup/msout
    - id: msout_concat
      type: Directory[]
      outputSource: concatenation/msout
    - id: images
      type:
        type: array
        items:
          type: array
          items: File
      outputSource:
        - target_selfcal/images
      pickValue: all_non_null
    - id: fits_images
      type:
        type: array
        items:
          type: array
          items: File
      outputSource:
        - target_selfcal/fits_images
      pickValue: all_non_null
    - id: h5parm
      type: File[]
      outputSource:
        - target_selfcal/h5parm
      pickValue: all_non_null
```

Why cover the same ground again?
It goes against my grain to repeat a tale
told once,
and told so clearly.

The Odyssey - Homer

3

Connecting radio emission to AGN wind properties with Broad Absorption Line Quasars

In this chapter, I present a paper published in the Monthly Notices of the Royal Astronomical Society (Petley et al., 2022) on the origin of radio emission in BALQSOs. The paper uses the LOFAR Two Metre Sky Survey (LoTSS) to assemble the largest sample of radio-detected BALQSOs. We then utilise the SDSS optical data to produce composite spectra of different populations finding differences between the radio-detected and non-radio-detected populations.

3.1 Introduction

The importance of black holes in overall cosmic history seems to grow with every paper and new discovery in the field. The key confirmed result that demonstrates black holes are not simply extreme isolated phenomena is the black hole mass-stellar velocity dispersion correlation (Ferrarese et al., 2000; Gebhardt et al., 2000; Kormendy et al., 2013). This immediately ties together the growth of black holes and their host galaxies raising many questions about what possible mechanisms could connect them. We now also understand through cosmological simulations that star formation rates need to be moderated by feedback mechanisms, usually involving black holes, for our simulations to align with the observed star formation history of the universe (Bower et al., 2006; Croton et al., 2006). Many galaxies have a compact central region emitting much more radiation than can explained by star formation in the same region. This non-stellar radiation is explained by accretion around supermassive black holes in these compact regions and the phenomena as a whole are referred to as Active Galactic Nuclei (AGN). The idea of AGN feedback has arisen as an explanation in which accretion processes at the smallest scales of a galaxy can have a large influence over its evolution for billions of years.

Quasars (also QSOs) are the most powerful class of observed AGN. The subclass of quasars known as Broad Absorption Line Quasars (BALQSOs) are some of the most important candidates for observing AGN $\rightarrow$ Host Galaxy feedback mechanisms as they show strong blue-shifted absorption troughs in the spectra due to fast-moving outflowing gas intersecting our line of sight. The rest of the QSO population does not show these distinctive absorption features. Since BALQSOs were first observed (Foltz et al., 1987), and their outflows defined and quantified (Weymann et al., 1991), much research has gone into probing how these sources differ from the general quasar population across all wavelengths. These investigations, especially at high and low (X-ray and radio) frequencies, are often limited by small number statistics as BALQSOs constitute only $\sim$10% of optically selected quasars (Trump et al., 2006; Gibson et al., 2009).

The presence of a particular fraction of quasars displaying these outflow signatures has been explained through two primary theories. One hypothesis is an orien-

tation approach where changing wind signatures are produced by different viewing angles of the quasar through the broad line region (Weymann et al., 1991; Ghosh & Punsly, 2007). The other is an evolutionary model where the observed fraction of BALQSOs is a measure of the lifetime of a BALQSO phase. This phase is usually postulated to be early in the life of the quasar due to connections with reddening and proposed mechanisms for removing material from the host galaxy (Lipari et al., 2009).

At typical redshifts for probing the height of cosmic star formation ($1.5 < z < 4$), see the review of Madau & Dickinson (2014), the lines used to identify BALQSOs become observable in the UV range covered by large-scale spectroscopic surveys such as the Sloan Digital Sky Survey (SDSS - York et al., 2000) having been redshifted out of the unobservable extreme ultraviolet region. All BALQSOs show high ionisation absorption features, particularly C IV (1550 Å), which provides the initial classification. BALQSOs with similar broad absorption features at Mg II or Al III are known as Low Ionisation BALQSOs (LoBALs). LoBALs are otherwise largely similar to HiBALs (Schulze et al., 2017) but have some key differences. Compared to HiBALs, LoBALs show higher gas column densities and velocities (Hamann et al., 2019), they have a greater fraction in dust-reddened samples (Urrutia et al., 2009) and they are fainter in the X-ray (Green et al., 2001). LoBALs account for around 10% of BALQSOs, the other 90% being HiBALs, and therefore have only seen limited studies in large sample sizes. The relationship between HiBALs and LoBALs is unclear but could be interpreted in the wider context of the BALQSO orientation and evolution hypothesis mentioned previously. In the orientation model, LoBALs could be a subset of the covering angle for BALQSOs where sufficient shielding from the radiation allows for the lower ionisation species to be observed in absorption. Others, however, place LoBALs in an evolutionary framework, usually in an earlier stage in the life cycle of the quasar than HiBALs due to features such as their increased reddening.

Many studies of the observable properties of BALQSOs, such as their UV continuum, as well as many derived parameters, such as their black hole masses, have found BALQSOs to be indistinguishable from the general quasar population (Black

Hole Mass: Schulze et al. 2017; UV: Dipompeo et al. 2012). This is often interpreted as strong support for the orientation interpretation as many features do not point towards a special evolutionary phase. However, there are some key differences of note which in many cases become further exaggerated in LoBALs.

A key feature of the UV spectra of BALQSOs is their significant reddening, particularly for LoBALs, which has generally been attributed to dust attenuation (Sprayberry et al., 1992; Reichard et al., 2003). This means that on average a BALQSO will need to be more luminous to be detected down to a given optical flux limit than an average QSO which also may cause underestimation of the intrinsic fraction of BALQSOs (Dai et al., 2007; Allen et al., 2010) when using optically selected surveys and has impact when using quasar SED templates in various aspects of analysis, a common practice in luminosity corrections and extrapolation of physical parameters such as star formation rate. BALQSOs are also intrinsically X-ray weak compared to non-BALQSOs (Clavel et al., 2005; Morabito et al., 2013), a property which is not orientation dependent and means X-rays are less important to the ionisation state of the outflowing BAL wind.

Radio wavelength studies of BALQSOs are of key importance since radio emission can be traced all the way from the dynamics of the black hole to the whole scale of the galaxy depending on the emission mechanism. Also, radio emission is not absorbed by intervening dust and can therefore provide an orientation-independent measurement of a radio-emitting process, apart from in rare cases of relativistic beaming. Classically, radio populations have been split into *radio-loud* and *radio-quiet* due to the apparent bi-modality of radio galaxies when looking at the ratio between their radio and optical luminosity (Kellermann et al., 1989). Early and subsequent studies have firmly placed the BALQSO population in the *radio-quiet* regime (Stocke et al., 1992; Becker et al., 2000; Morabito et al., 2019). While radio-loud emission is generally attributed to large-scale powerful jets which, if resolved, can allow for measurement of size and orientation (Barthel et al., 1989), radio-quiet sources have several possible emission mechanisms such as frustrated jets, wind shock emission and star formation. While radio-loud BALQSOs do exist and have been studied (Stocke et al., 1992; Brotherton et al., 1998), often historically

because they are brighter and easier to observe, they are a much lower fraction of overall radio-detected BALQSOs when compared to the general quasar population. This implies that BALQSOs are less likely to contain large-scale radio jets than the general quasar population.

Although BALQSOs are radio-quiet, much of the previous radio work on these sources has focused on the small fraction which are radio-loud. Surveys such as Faint Images of the Radio Sky at Twenty centimetres (FIRST; Becker et al., 1995) are more biased towards radio-loud sources and Very Long Baseline Interferometry (VLBI) observations of BALQSOs have focused on radio-loud sources with the aim to resolve and measure the orientation of the expected jet structure in these sources. A key result using FIRST, along with 2MASS (Skrutskie et al., 2006) and SDSS (Adelman-McCarthy, 2007), is that of (Urrutia et al., 2009) who found that when they created a sample of reddened, largely radio-loud, quasars there was a high fraction of BALQSOs in the sample, and all but one were LoBALs. This was seen as strong evidence for the evolutionary hypothesis as the reddening is considered a feature of an earlier stage in the life of a quasar as material is removed from the galaxy by feedback.

Previous VLBI observations of BALQSOs have revealed mixed results that have thus far failed to conclusively support one interpretation over the other. In Jiang & Wang (2003) 3 BALQSOs were observed with the European VLBI Network (EVN) and all sources had jet sizes less than 1kpc. They also observed a flat spectrum source with an orientation likely close to the line of sight, which would support the presence of BAL winds close to the jet axis. Doi et al. (2009) find a similar result when using the Optically Connected Array for VLBI Exploration (OCTAVE) instrument to observe 22 radio-loud BALQSOs. They find 4 compact inverted spectrum sources allowing for two possible explanations. Either the radio sources are very young, or they are observing Doppler-boosted emission along the line of the jet. In either case, those observations cannot be explained by the classic equatorial disk wind viewing angle of a standard quasar. In Bruni et al. (2013) 9 BALQSOs were studied with the EVN and Very Long Baseline Array (VLBA). They found a variety of structures with jet sizes from tens of parsecs to hundreds of kiloparsecs. They found this supported

the geometric interpretation where the sizes relate to different potential viewing angles of the wind with respect to the jet axis and that they could occur throughout quasar evolution allowing for jet sizes to grow to a range of sizes. Cegłowski et al. (2015) isolated BALQSOs with weaker wind strengths (lower balnicity index) and observed them with the EVN and VLBA. They find that these sources are on average potentially younger than other BALQSOs and are more radio-loud. However, the radio-loudness could be associated with different levels of absorption, also allowing for a geometric interpretation. All of these studies focused on radio-loud sources which are the exception to most BALQSOs. Although jets were observed in some of the sources it is not known whether this emission mechanism continues down to the radio-quiet sources or whether other mechanisms become the dominant component.

Other radio studies of BALQSOs aiming to use large samples have been limited to higher frequency surveys such as NVSS (Condon et al., 1998) and FIRST because these have been the most sensitive large area surveys available. This limits the sensitivity to the synchrotron emission which increases in luminosity at longer wavelengths. Therefore higher frequency surveys pick out more radio-loud sources which are not representative of the overall population. With the development of LOFAR (van Haarlem et al., 2013) we now have access to increased sensitivity at a resolution matched to that of FIRST, but at an order of magnitude lower sensitivity. As well as increased source counts, the lower frequency emission from quasars is dominated by optically thin synchrotron emission. Due to the shape of the synchrotron spectrum, the radio emission is brighter at lower frequencies when compared to the flat spectrum of radio emission from optically thick regimes which have a higher relative contribution at $\sim$ GHz frequencies.

In this paper we inspect and expand upon the work of Morabito et al. (2019) which utilised the LOFAR Two Metre Sky Survey (LoTSS) Data Release 1 (Shimwell et al., 2019). In that work, BALQSOs were found to have a detection fraction independent of luminosity, a result that is not seen at higher frequencies. Interestingly it was also tentatively found that detection fraction did correlate with absorption properties. This shows that the radio emission in BALQSOs is tied to the current state of the BAL wind and that structural models for BALQSOs need to be able to

also explain the radio properties of these sources.

We confirm some of the results from Morabito et al. (2019) using LoTSS DR2 (Shimwell et al., 2022b) which spans 5740 square degrees, or 13 times the area of LoTSS-DR1, with a median sensitivity of 83 μJy beam^{-1} at 144 MHz. This has allowed us to expand our statistical analysis of BALQSOs, particularly the rarer LoBALs which we can split out more easily, but also maintain high spectra clarity and avoiding some biases in Morabito et al. (2019) by introducing UV continuum signal to noise cuts while still creating a larger sample. We explore the potential explanations of the link between radio emission and wind strength by developing simple models for different geometries and evolution and testing them against our large sample. We also identify the potential focuses for future studies of BALQSOs.

Throughout this paper, we assume a cosmology defined by the parameters determined by the **Planck 2015** observations and published in Ade et al. (2016). This is a standard, flat ΛCDM cosmology with H_0= 67.8 km s^{-1} Mpc^{-1} and $\Omega_M = 0.308$. We use the spectral index convention of $S_\nu \propto \nu^{-\alpha}$.

3.2 Data and Methods

3.2.1 Radio Data

The core data dataset for this work is the LOFAR Two Metre Sky Survey (LoTSS) Data Release 2 (Shimwell et al., 2022b)[1]. This release of the 144 MHz survey covers 5740 square degrees across two separated fields with a median sensitivity of 83 μJy beam^{-1} at the central frequency. There are 4,396,228 sources above a detection limit of 5σ. At these frequencies, for most sources, we expect synchrotron emission to be the dominant contribution to the observed flux; the flux from this spectral slope increases as frequency decreases which reaches a fainter population when compared to surveys of similar sensitivity but at higher frequency.

There is a preliminary optical cross-matched catalogue in use based on the automatic matching of simple structure radio sources to optical images. However, this

[1] `https://lofar-surveys.org/surveys.html`

system struggles with more complex radio structures. At the time of writing, there is an ongoing citizen science project entitled the *"LOFAR Galaxy Zoo"*[2] taking place on the *Zooniverse* website. This project allows the public to help characterise more complicated extended emission systems that cannot be identified automatically and also allows users to identify potential optical counterparts. Sources currently being processed by the citizen science project have not yet been added to the cross-matched catalogue that was used for this paper. It is unlikely that the inclusion of sources in the LOFAR Galaxy Zoo would change the results of this paper significantly as they largely concern complex structure radio-loud sources which do not account for a large population of BALQSOs.

3.2.2 Balnicity Index and radio-loudness

Without knowledge of the exact geometry and energetics of BALQSO systems, the identification and characterisation of outflows in BALQSOs typically uses the Balnicity Index (BI) defined in Weymann et al. (1991) at the C IV. This can be thought of as some sort of proxy for the "wind strength" and has been used to compare BALQSO absorption properties. This index uses the depth and breadth of the absorption trough and is defined

$$\texttt{BI} = -\int_{25000}^{3000}[1-\frac{F(v)}{0.9}]C_B dv \tag{3.1}$$

v is the velocity in km s^{-1} with respect to the line centre. $F(v)$ is the flux after the removal of the QSO continuum, obtained by a fit to the original spectra, and C_B is a constant which is set to 1 if $F(v)$ is lower than 0.9 for 2000 km s^{-1} and 0 otherwise. This minimum velocity and absorption required for the integration to begin is set so that intervening systems in the absorption trough are removed and that the absorption is definitely broad. The continuum normalised flux is created by a fitting process which extracts the QSO continuum emission from spectra. Then, by dividing the whole spectra by that continuum, the genuine continuum emission will be normalised to one. Therefore a value of $F(v)$ of 0.9 means that the flux at

[2] `https://www.zooniverse.org/projects/chrismrp/radio-galaxy-zoo-lofar`

that frequency is at 90% that of the continuum fit at the same frequency. Although the standard practice is to define BALQSOs as all sources with BI > 0, there are some well-known considerations to be made when using this definition. Alternative outflow strength indices exist, such as the Absorption Index (AI; Hall et al., 2002; Trump et al., 2006), which do not require a minimum velocity in the integration limits. This means that the equation is identical to that above but the upper limit of the integral is 0 km s−1 rather than 3000 km s−1. Therefore using AI to classify BALQSOs will create larger, but potentially more contaminated, samples as visual inspection of sources with AI > 0 and BI $= 0$ includes sources that do not have clear absorption features. A study of sources with positive AI shows a bi-modality in the AI distribution where only the higher AI distribution contains genuine BALQSOs (Knigge et al., 2008). More advanced selection criteria can be used such as various machine learning techniques. However, these methods introduce their own uncertainties and contamination. Rather than potentially contaminate the sample we use the classic BI definition which ensures all of our BALQSOs show clear features at the C IV line line at the cost of missing some genuine BALQSOs.

Figure 3.1 displays the BI distribution of our final LoBAL and HiBAL sample; it is clear the LoBALs tend to have/occupy higher BI values compared to the HiBALs, which is consistent with previous observational studies (Reichard et al., 2003; Morabito et al., 2019) and simulations (Higginbottom et al., 2013; Matthews et al., 2016, 2020). In fact, the high BI end ($> 10{,}000$ km s^{-1}) of our sample is entirely dominated by LoBALs.

Radio-loudness is a concept that has been used to characterise whether a source shows an excess in radio emission when compared to optical (Kellermann et al., 1989). We define radio-loudness as the ratio (R) between the 144 MHz luminosity and the B-band ($\sim$ 450 nm) rest-frame luminosity. We use a similar approach to Morabito et al. (2019) which we briefly describe below. To obtain this optical luminosity we take the 3000 Å luminosity from SDSS DR12 and convert it to a flux based on the spectroscopic SDSS redshift of the source. We then correct this flux for extinction within the Milky Way (using Pei et al. 1992) and correct the rest frame emission for intrinsic extinction from the host galaxy using a Small Magellanic

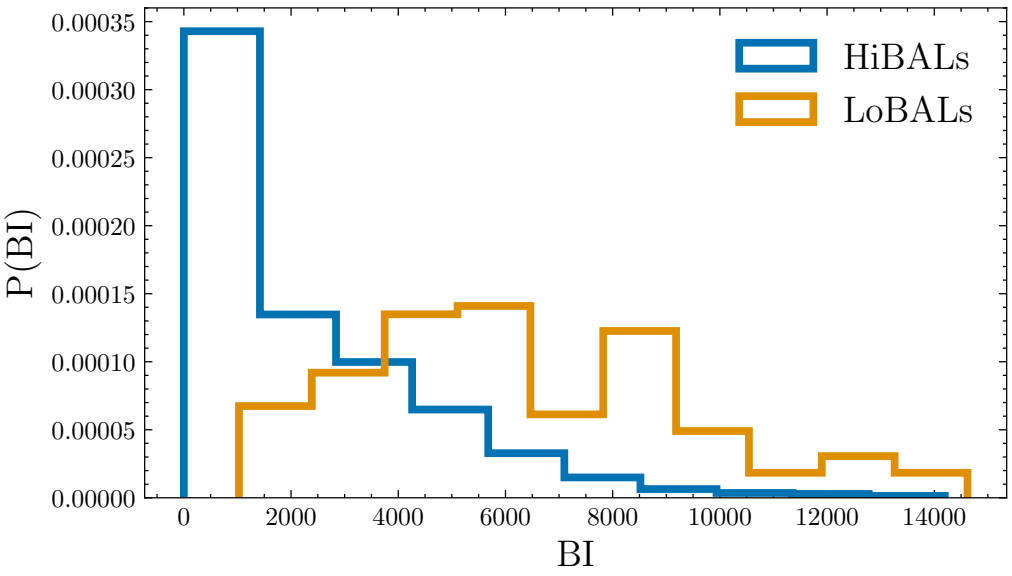

Figure 3.1: Balnicity index (BI) distributions for HiBALs (blue) and LoBALs (orange). Typically LoBALs have larger BI values than HiBALs, as measured from the C IV absorption.

Cloud (SMC) model which was found to be a good fit for BALQSOs by Reichard et al. (2003) which found a best fit value of $E(B-V) = 0.077$ for LoBALs. This intrinsic correction assumes $R_V = 2.93$ and uses the SMC curve to apply it to whatever rest frame wavelength we observed. We finally shift this corrected rest frame emission to the B-band using the mean spectral energy distribution (SED) for Type 1 Quasars from Richards et al. (2006). A correction is also applied when calculating the radio luminosity from the LoTSS total flux, assuming a synchrotron spectral index of $\alpha = 0.7$. This gives us a consistent measure for radio-loudness across the whole sample under the assumption that the SED and extinction curves for BALQSOs and non-BALQSOs are the same (see discussion of BALQSO wind-radio connection).

We investigate the radio-loudness to which our sample is complete as this is important in understanding what populations we can properly characterise. In Figure 3.2 we show that our combined spectroscopic and radio sample captures a large number of sources down to a radio loudness of $\log(R) \approx 0$.

Typically, the general quasar population can be split into a radio-loud and radio-quiet population. This can be seen in the distribution of these sources in Figure 3.2. The total distribution appears to be the result of two overlapping distributions with

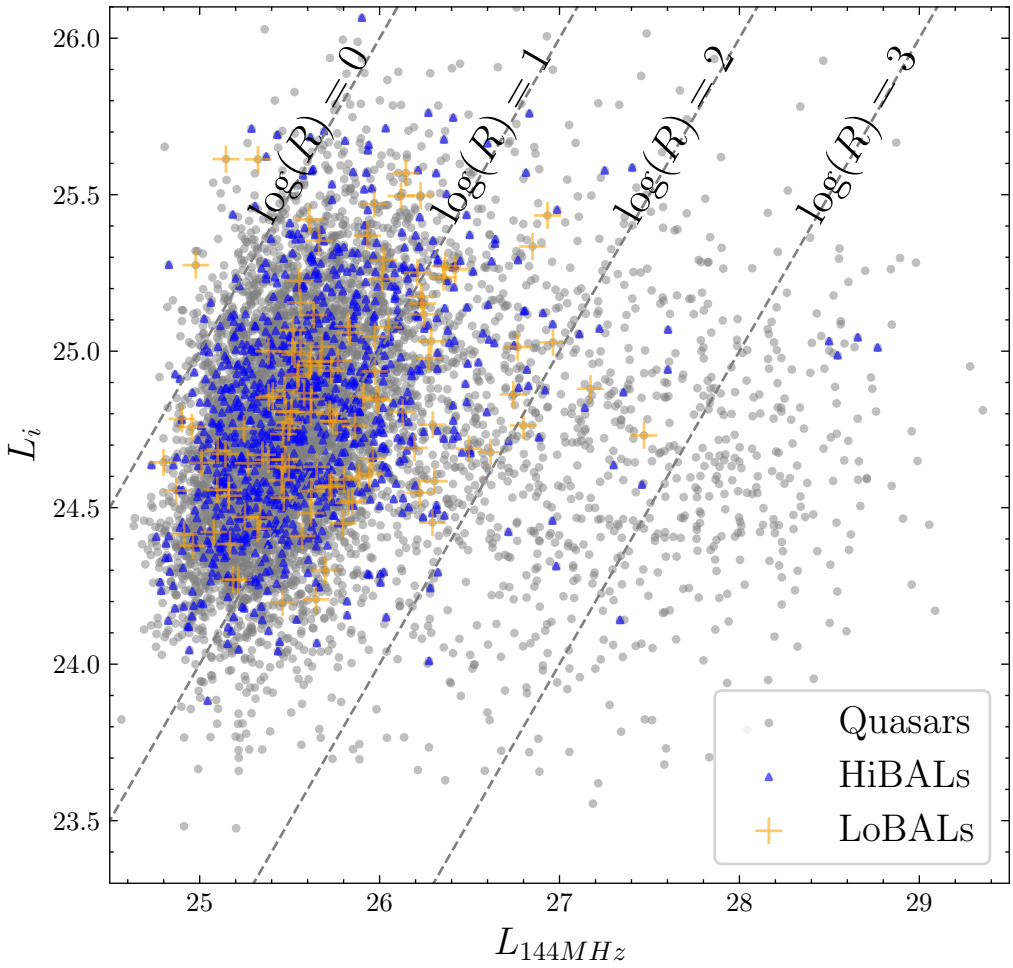

Figure 3.2: i band (806 nm) luminosity against LoTSS 144MHz luminosity for the full sample of radio-matched quasars with HiBALs in blue and LoBALs in orange. We overlay lines of constant radio-loudness to show to what loudness level our sample is complete.

a border around $\log(R) = 1.5$. The majority of the population lies above and to the left of $\log(R) = 1.5$ with outliers below and to the right in Figure 3.2. The population drops in number quickly in the radio-loud regime, especially for LoBALs. Previous radio studies investigating these distributions have often operated around 5 GHz frequencies and the radio-loud distinction occurs around $R = 10$. The border value we find at 144 MHz corresponds very closely to a scaling of the traditional value using the expected synchrotron spectral index of $\alpha = 0.7$, defined so that in the positive direction of the spectral index, as frequency increases the flux decreases. It is consistent with Morabito et al. (2019), who used the g band rather than the i band and thus found a slightly higher value of log(R) as the division between radio-loud and radio-quiet.

We provide the reader with the overall catalogue of LoTSS-detected SDSS DR12 quasars in the supplementary material for this work. A summary is provided in Table 3.1. The redshift range cut to the wavelengths that BALQSOs can be identified and also continuum SNR cuts have not been applied to the data.

3.2.3 Spectra

The spectroscopic data needed to identify BALQSOs is taken from the Sloan Digital Sky Survey (SDSS) DR12 quasar catalogue (Eisenstein et al., 2011; Alam et al., 2015). This contains 297301 QSO spectra along with auxiliary information including BALQSO classification, C IV Balnicity Index (BI) and Absorption Index (AI) (see Section 3.1) along with emission width information for selected other emission lines. 151595 of these quasars lie within the LoTSS DR2 coverage. BALQSOs in SDSS can only be defined with high-quality spectra, otherwise, the noise will overwhelm the absorption region, and within a redshift region where the CIV line can be observed completely; this restricts the catalogue to a redshift range of $1.7 < z < 4.3$ with a signal to noise ratio cut on the continuum at 1700Å of `SNR_1700` > 5.

This cut is important as SNR can have a large impact on both the BALQSO optical identification fraction in the sample and the BALQSO radio-detection fraction compared to non-BALQSOs. At low SNR BALQSOs are harder to identify in the SDSS data and so have a much lower fraction. Also, the ones that are identified

Column	Name	Format	Description
1	Source_Name	STRING	LoTSS DR2 Name
2	RA	DOUBLE	LoTSS DR2 J2000 Right Ascension (degrees)
3	E_RA	DOUBLE	LoTSS DR2 J2000 Right Ascension uncertainty (arcseconds)
4	DEC	DOUBLE	LoTSS DR2 J2000 Declination (degrees)
5	E_DEC	DOUBLE	LoTSS DR2 J2000 Declination uncertainty (arcseconds)
6	Peak_flux	DOUBLE	LoTSS DR2 144MHz peak flux (mJy/beam)
7	E_Peak_flux	DOUBLE	LoTSS DR2 144MHz peak flux uncertainty (mJy/beam)
8	Total_flux	DOUBLE	LoTSS DR2 144MHz integrated flux (mJy)
9	E_Total_flux	DOUBLE	LoTSS DR2 144MHz integrated flux uncertainty (mJy)
10	Maj	DOUBLE	LoTSS DR2 major axis (arcseconds)
11	E_Maj	DOUBLE	LoTSS DR2 major axis uncertainty (arcseconds)
12	DC_Maj	DOUBLE	LoTSS DR2 deconvolved major axis (arcseconds)
13	E_DC_Maj	DOUBLE	LoTSS DR2 deconvolved major axis uncertainty (arcseconds)
14	SDSS_NAME	STRING	SDSS DR12Q Name
15	RA_1	DOUBLE	SDSS J200 Right Ascension (degrees)
16	DEC_1	DOUBLE	SDSS J200 Declination (degrees)
17	THING_ID	INT32	Unique SDSS identifier
18	PLATE	INT32	Spectroscopic plate number
19	MJD	INT32	Spectroscopic MJD
20	FIBERID	INT32	Spectroscopic fiber ID
21	Z_VI	DOUBLE	Visually inspected redshift
22	SNR_1700	DOUBLE	Median signal-to-noise ratio per pixel in the window $1650 - 1750$Å
23	BAL_FLAG_VI	SHORT	BAL Flag from visual inspection
24	BI_CIV	DOUBLE	Balnicity index of C IV trough (km s^{-1})
25	ERR_BI_CIV	DOUBLE	Balnicity index uncertainty of C IV trough (km s^{-1})
26	REW_ALIII	DOUBLE	Rest frame equivalent width of the Al III trough (Å)
27	L3000	FLOAT	Estimated 3000Å luminosity ($10^{-7}W$)
28	MBHMgII	FLOAT	Black hole mass estimated from Mg II ($M_\odot$)
29	MBHCIV	FLOAT	Black hole mass estimated from C IV ($M_\odot$)
30	Lbol	FLOAT	Quasar bolometric luminosity ($10^{-7}W$)
31	e_Lbol	FLOAT	Quasar bolometric luminosity uncertainty ($10^{-7}W$)
32	nEdd	FLOAT	log(Eddington Fraction)
33	RAJ2000	DOUBLE	FIRST Right Ascension (degrees)
34	DEJ2000	DOUBLE	FIRST Declination (degrees)
35	Fpeak	DOUBLE	FIRST peak flux (mJy/beam)
36	Fint	DOUBLE	FIRST integrated flux (mJy)
37	Rms	FLOAT	FIRST rms noise around source (mJy)
38	Separation	DOUBLE	LoTSS-FIRST Source separation (arcseconds)
39	REST_B	DOUBLE	Estimated rest b band luminosity (W) - Values are 0 when Kozłowski (2017) data is missing
40	Radio_luminosity	DOUBLE	log(estimated 144MHz rest frame luminosity assuming $\alpha = -0.7$) (W)
41	Radio_loudness	DOUBLE	log(Radio/B_BAND radio loudness) - inf value when REST_B = 0

Table 3.1: Supplementary table column description - Horizontal lines denote sections from different source catalogues. From top to bottom, they are: LoTSS DR2 (Shimwell et al., 2022b), SDSS DR12 Quasars (Paris et al., 2017), (Kozłowski, 2017) quasar parameters, FIRST (Becker et al., 1995) and finally some derived values described in this section. The full table can be accessed online through the supplementary material. The table does not have a signal-to-noise or redshift cut applied.

tend to have a higher bolometric luminosity. These effects combine to exaggerate the radio-detection fraction of BALQSOs if no SNR cut is taken. On the other hand, higher SNR cuts ($SNR > 20$) select sources with higher bolometric luminosity; for the non-BAL quasars, this increases the chance of a source being radio-loud and also radio-detected, while BALQSOs are almost exclusively radio-quiet which then changes the value of non-BALQSOs as a comparison population. As a compromise, we choose SNR > 5 as a compromise between both of these selection biases and maximising the number of BALQSOs in our sample (see figures in § 3.A).

The overall BALQSO/non-BALQSO radio-detection fraction ratio across redshift is 1.93 but with a SNR cut of 5 this drops to 1.45. It remains relatively consistent out to a cut at 20 where the value is 1.24 but at this point we would only have 215 HiBALs and 29 LoBALs within LoTSS coverage, significantly limiting the study of these populations in greater detail. A repeated analysis of the radio detection fraction trends with colour and BI with an SNR cut of 10 showed no change in the extraction of correlations but would severely limit any composite spectra work.

To define BALQSOs using this catalogue we require visual confirmation via the `BAL_FLAG_VI` and a positive balnicity index (`BI_CIV` > 0). This gives us a BALQSO fraction of 10%. Rankine et al. (2020) use spectral reconstructions to de-noise quasar spectra and identify some different BALQSOs but also remove others and end up with a similar fraction of 11%. We then define LoBALs by using the rest emission width of the Al III species and require `REW_ALIII` > 0. This is based on the classical definition of rest emission width, which is used in SDSS DR12, where values greater than zero indicate absorption. This definition is conservative as we will miss sources that have significant absorption but an equivalent or higher amount of emission as the equivalent width measures the full profile. A visual inspection of the spectra for a substantial amount (25%) of HiBALs and LoBALs, and the full inspection of smaller HiBAL and LoBAL subsets later in this work, confirms this selection criteria is largely successful. We also use the extended catalogue created by Kozłowski (2017) which adds black-hole mass and bolometric luminosity estimates for all of the SDSS DR12 quasars. Finally, we also use the Faint Images of the Radio Sky at Twenty centimetres (FIRST) survey (Becker et al., 1995) which is the best comparative

	General Quasars	HiBALs	LoBALs
Within DR2 MOC	31752	3270	267
radio-detected	6813	1108	120

Table 3.2: Summary of the overall sample of SDSS quasars within the LoTSS DR2 coverage.

survey at a similar resolution (5 arcseconds) and higher frequency (1.4 GHz).

After restricting the SDSS data to lie within the Multi-Order Coverage map (MOC) of LoTSS DR2 we match SDSS and the optical counterpart coordinates within the LoTSS DR2 catalogue with a matching radius of 1 arcsecond. Since we are using the optical identifications available in the DR2 catalogue which are based on Pan-STARRS and WISE, this is likely to yield extremely little contamination when matched to SDSS. For a full discussion of the LoTSS optical identification process please refer to Williams et al. (2019). This yields 6813 radio-matched QSOs including 988 HiBALs and 120 LoBALs. These are larger numbers than were studied in Morabito et al. (2019) even with the SNR cut that we use in this work. This sample is large enough that the statistical properties of BALQSOs can be studied at a level previously unprecedented due to the scarcity of radio-detected BALQSOs, particularly the rarer LoBAL sub-class.

3.3 Results

3.3.1 Radio and Bolometric Luminosities

Using the bolometric luminosities provided by Kozłowski (2017) we show the distributions of radio luminosity at 144 MHz and bolometric luminosities for the sample in Figure 3.3. The BALQSOs within the radio-matched sample of quasars show very little difference in the distribution of their radio luminosities to the parent population. This is also true for LoBALs. Potentially, LoBALs show a slight increase in bolometric luminosities compared to HiBALs and the rest of the sample but this could be due to the inability to calculate the bolometric luminosity for low luminosity BALQSOs, which are likely to be highly reddened and have lower signal-to-noise spectra.

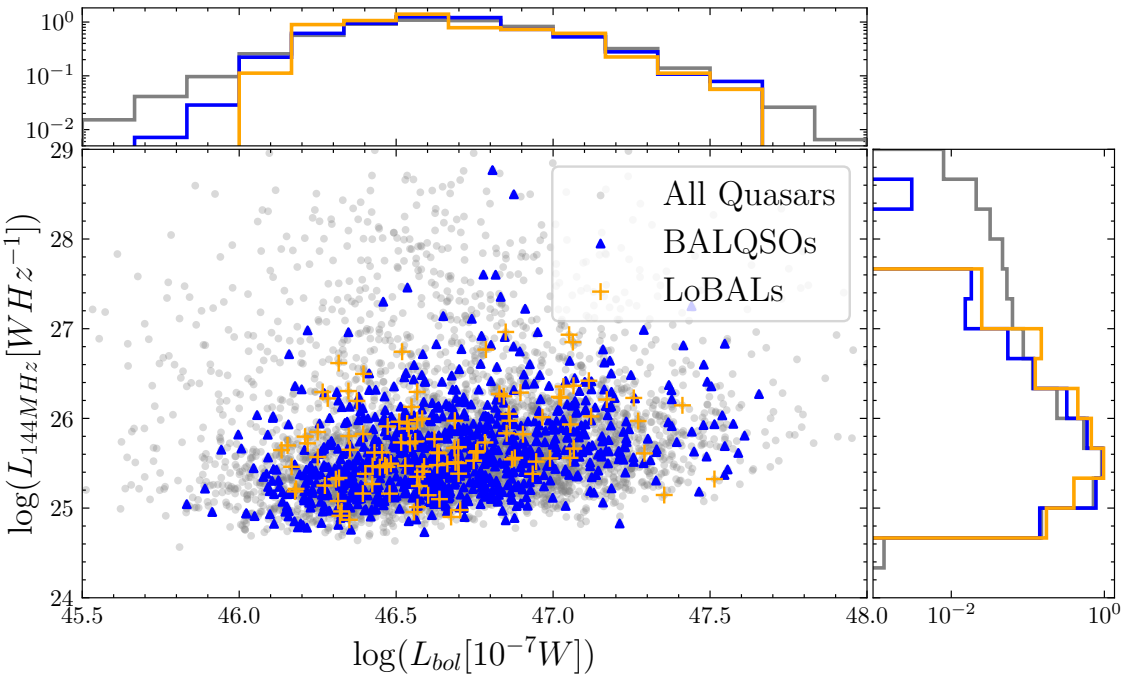

Figure 3.3: The radio and bolometric luminosity distributions for our HiBAL (blue) and LoBAL (orange) samples. The BALQSO and LoBAL samples do not reach as low bolometric luminosities as the general population likely due to the effects of reddening. However, this is a small difference and is mirrored in the absence of high radio luminosity BALQSOs and LoBALs. We therefore conclude that differences in radio properties cannot be primarily driven by increased luminosity.

BALQSOs show a difference to the general quasar population in radio-detection fraction, as shown in Figure 3.4. We present this in a similar fashion to Morabito et al. (2019), however, we now have the number of sources needed to constrain the uncertainty on detection fraction for HiBALs and LoBALs. We use bootstrap sampling of the whole SDSS DR12 quasar sample and recalculate LoTSS detection fractions to estimate the uncertainty at each point. BALQSOs show $\times 1.5$ the radio-detection fraction when compared to non-BALQSOs across the full redshift range of the sample. The difference only increases further when comparing LoBALs to non-BALQSOs where LoBALs show an even further enhancement in radio-detection fraction and detection rates approaching 50%. This is the strongest evidence yet that BALQSO winds (in particular LoBAL winds) and radio emission are connected and that this connection spans the era of maximum star formation in cosmic history ($2.5 < z < 3.5$). This high radio detection for BALQSOs highlights the importance of creating radio-selected samples of quasars when attempting to understand the intrinsic properties of BALQSOs. In the near future, this will be best achieved by WEAVE-LOFAR (Smith et al., 2016) which should yield a significant number of BALQSO spectra.

In combination with the radio loudness and radio luminosity data presented in Figure 3.2 and Figure 3.3, we see that although BALQSOs are more likely to be radio detected than non-BALQSOs that does not necessarily mean they are more luminous. For BALQSOs that are radio-detected, they are underrepresented in the high radio luminosity and radio-loud end of these distributions.

3.3.2 Detection Fraction Correlations

We investigate the LoTSS detection fraction further and test its correlation with the main measure of the strength of the outflow, BI. In Figure 3.5 we show that the radio-detection fraction does indeed correlate with the BI index and also that this relationship is not observed clearly at other radio frequencies such as FIRST. For the BALQSOs in the sample the Pearson correlation coefficient between BI and LoTSS radio-detection fraction is $r = 0.9609$ with a p-value, the probability that a random sample from the population would have an equal to or greater correlation coefficient,

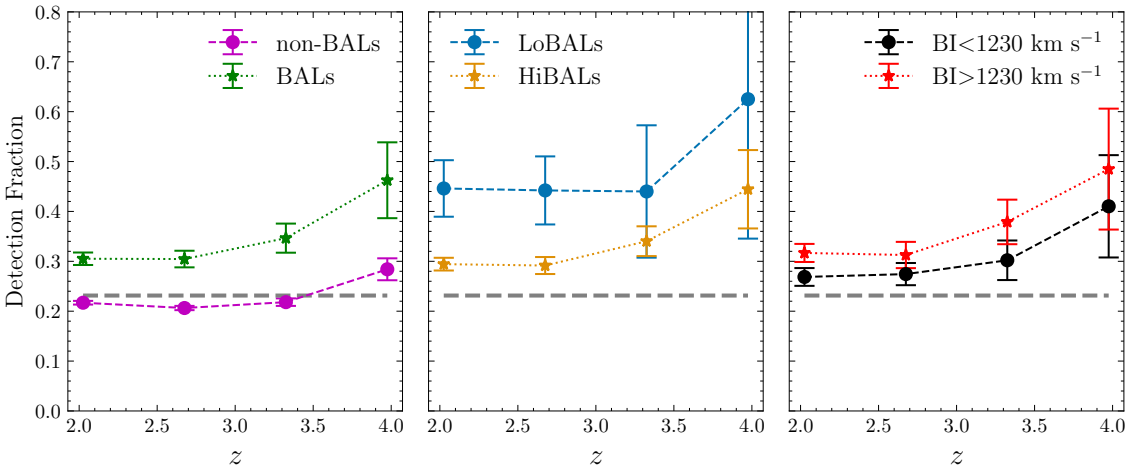

Figure 3.4: From left to right: the radio-detection fraction for BALQSOs and non-BALQSOs, LoBALs and HiBALs and finally weak and strong HiBALs based on a median BI cut. The uncertainties are estimated through bootstrap sampling of the SDSS sample and repeating the detection fraction calculations. The grey dashed line present in each panel is the mean detection fraction for non-BALQSOs across redshift. We find a dramatic difference in radio-detection fraction between BALQSOs and non-BALQSOs and furthermore between LoBALs and HiBALs. The orange line represents the mean detection fraction for the overall population. This is persistent across redshift and stays relatively constant across redshift. We also present the difference between high BI and low BI sources however it should be noted that the HiBALs and LoBALs also have very different BI distributions (Figure 3.1).

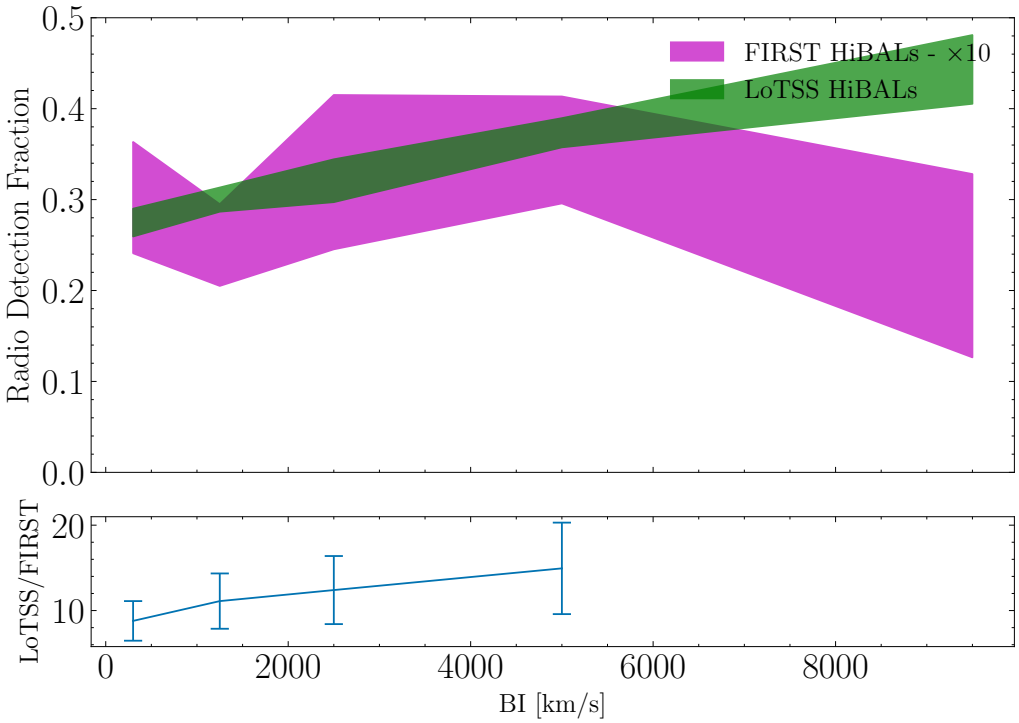

Figure 3.5: The correlation between BI, a measure of outflow strength, with radio-detection fraction for LoTSS (green) and FIRST (magenta) HiBALs where the first fraction is multiplied by 10 so that the two instruments can be more easily compared. The regions represent the one-sigma uncertainty region for the detection fraction calculated by taking bootstrapped samples of the full SDSS DR12 quasar catalogue and calculating the radio-detection fractions each time. The FIRST radio-detection fractions are multiplied by 10 so that they appear on a similar scale. The correlation is only present in LoTSS, the survey that is more sensitive to the radio-quiet population. We find more BALQSOs using LOFAR as BI increases in comparison to FIRST.

of $p = 5 \times 10^{-4}$. For the FIRST results, the Pearson coefficient is $r = -0.7$ and the p-value is $p = 0.10$ which is not as strong or significant. This provides a clear link between the appearance of BALQSOs and the low-frequency radio emission from their sources.

We test whether the increase in LoTSS-detection fraction with BI could be driven by factors other than BI. In Figure 3.6 we test whether radio-loudness or luminosity correlates with BI for our sample of BALQSOs. We do not find notable correlations for any of these radio measures leaving only the radio-detection fraction as the key measure that correlates with BI. The Spearman Rank correlation coefficients for BI with radio-loudness, LOFAR luminosity and FIRST luminosity are 0.03, -0.01 and

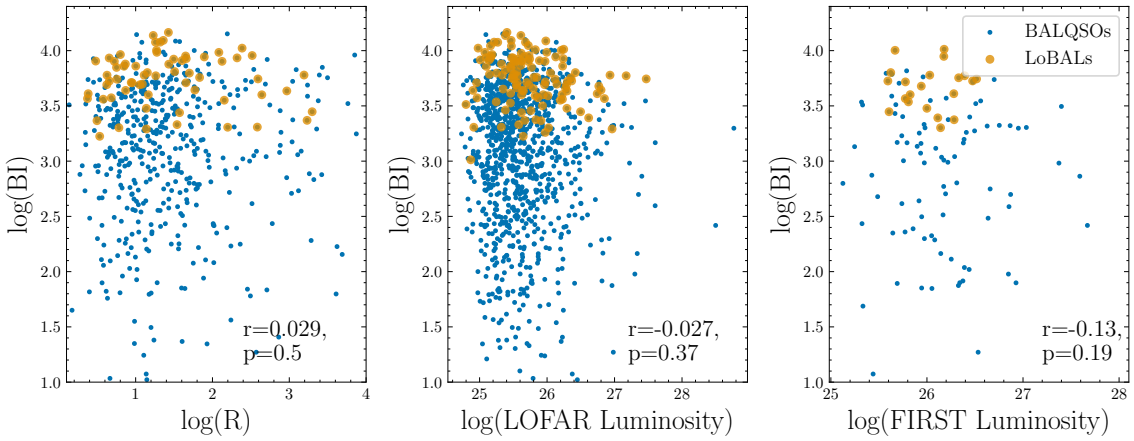

Figure 3.6: The relation between BI and radio-loudness, LOFAR luminosity and FIRST luminosity for all of the HiBALs (blue) and LoBALs (orange) in our radio matched sample. We display the Spearman Rank correlation coefficient, r, and p-value between the parameters for each figure. We do not find any significant correlations between each of these variables.

-0.13 respectively with p-values of 0.5, 0.37 and 0.19.

Recent work on red and blue quasars has shown similar radio-detection fraction differences between quasar populations, using LoTSS and FIRST, that are driven by optical/UV colour and support an evolutionary hypothesis for the appearance of red quasars (Klindt et al., 2019; Rosario et al., 2020; Fawcett et al., 2020). We investigate what impact the colour of our sample has on the detection fraction of BALQSOs. However, it is known that colour can have a strong dependence on redshift that should be factored in when trying to compare the colour change across a range of redshift. We use g and i band colours, consistent with work on red quasars, in this analysis. The overall trend in $g - i$ colour and redshift is shown in Figure 3.7. We limit to a redshift range $z < 3$ as beyond this point the Lyman break starts to affect the colour measurement.

It is clear that the redshift change should be accounted for so that we can properly determine the effect of colour on radio detection. In Figure 3.8 we show the effect on the radio-detection fraction of colour. We bin our sample first into ten equally spaced redshift bins and then into quartiles by colour in each redshift bin. This means that HiBALs and non-BALQSOs are grouped by the same bin edges. Then we average the detection fraction for each quartile across redshift. This allows for the overall trend in detection fraction with colour to be viewed while removing the

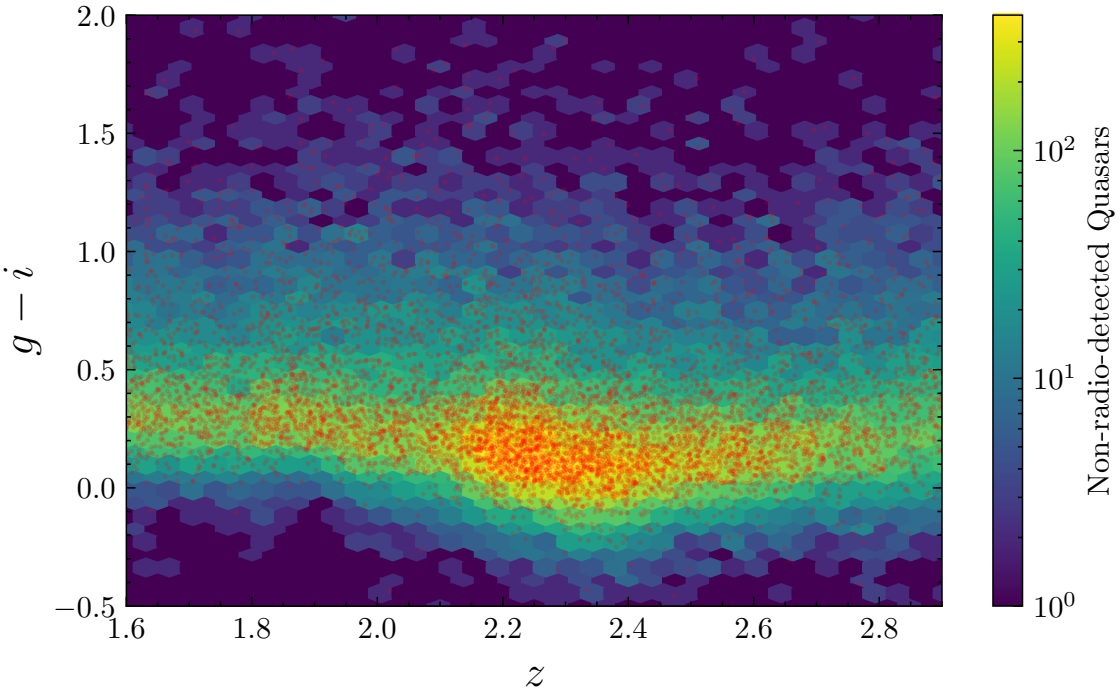

Figure 3.7: The colour-redshift distribution for all quasars in DR12 in the background with the radio-matched sources overlayed on top in red.

redshift effects clearly visible in Figure 3.7. We plot the median BI for HiBALs in each bin and the scale is shown on the y-axis. The change in median BI for each percentile bin shows that the radio-detection fraction of bluer (low $g - i$) HiBALs differs from that of non-BALQSOs.

3.3.3 Composite Spectra

We use composite spectra to compare the continuum and absorption properties of a variety of sources contained within our sample. Composite spectra allow for the characterisation of large populations and also provide a way of visually identifying potential areas of further study in the different properties of the detected and non-detected quasars in our sample.

To generate composite spectra we download spectra in batches from SDSS. We then shift these to rest wavelength and normalise by taking the median over a continuum emission range of $2575\text{Å} < \lambda < 2625\text{Å}$. This region is covered by all quasars in our sample from redshift $1.7 < z < 4.3$ and contains no strong emission or absorption features. This means that the flux scale is now in arbitrary units where

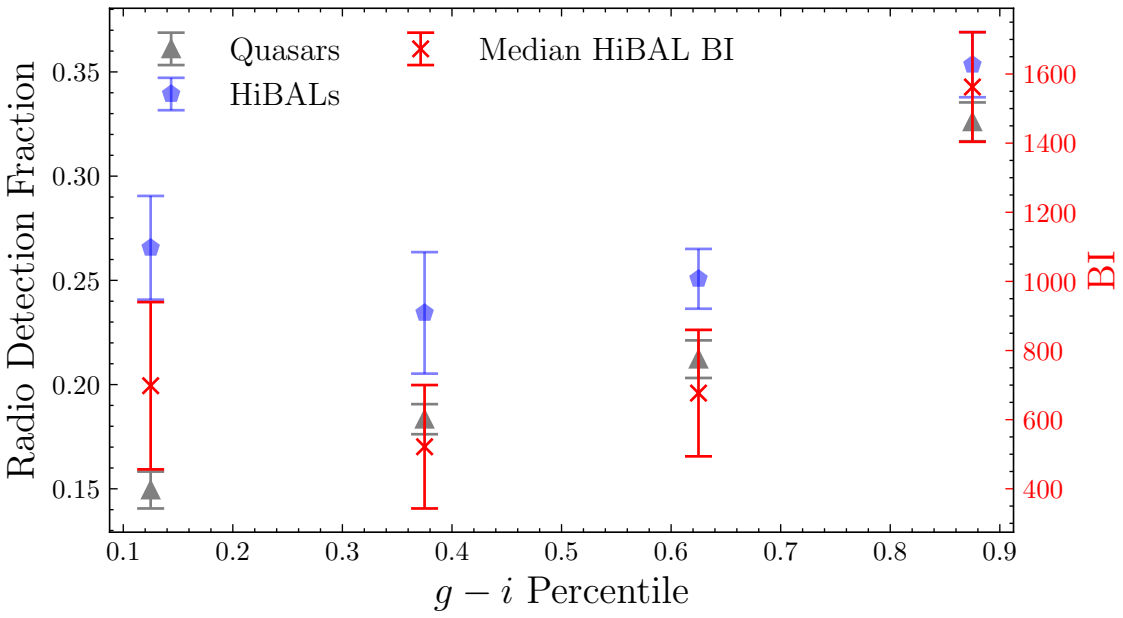

Figure 3.8: For each colour quartile for our quasar sample we split into general quasars and HiBALs across redshift. The colour quartiles are defined by the whole population. The median BI for HiBALs in each quartile is shown by the red dashed lines. The overall effect of this colour change from the lowest to highest quartile is close to 20% for non-BALQSOs, close to that of the change from lowest to highest BI in Figure 3.5.

all spectra have a value of 1 at their median point in this range. This removes effects due to the differing flux of each source and, since this point is not close to strong emission lines, it provides a good way of viewing the relative colour of different populations. Then we take a one-dimensional interpolation of the spectra using the `scipy interp1d` function. We can then map this interpolation to a common wavelength grid for all of the spectra. Finally, we take the median flux value at each point along the common wavelength grid to produce a final composite. We bootstrap sample the normalised spectra to obtain an uncertainty estimate on the median composite which we show as the shaded region in all composite spectra plots. One bootstrap sample consists of randomly taking 60% of the spectra for a composite with replacement and determining the median. The uncertainty is calculated as the standard deviation of the median after 500 bootstrap samples multiplied by the square root of 60%.

To quantify the different amounts of extinction present in our composite spectra we create a control composite of blue quasars. This was made by defining blue

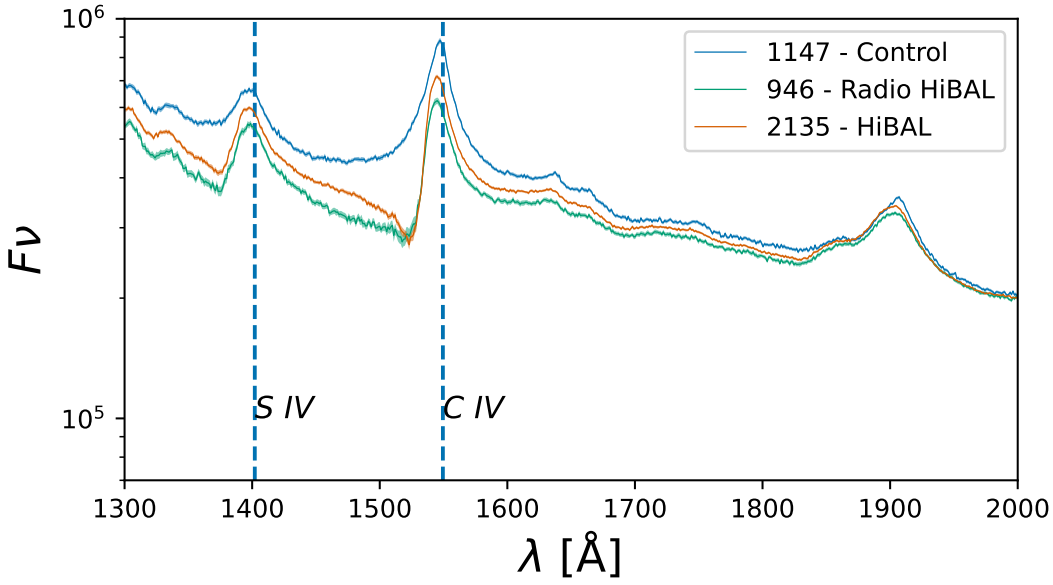

Figure 3.9: Overall composite for radio (green) and non-radio-detected (orange) HiBALs along with a blue quasar composite. The radio composite shows increased reddening compared to the non-radio and also an absorption profile that shows more absorption at lower wavelengths but lacks the narrow feature of the non-radio composite close to C IV.

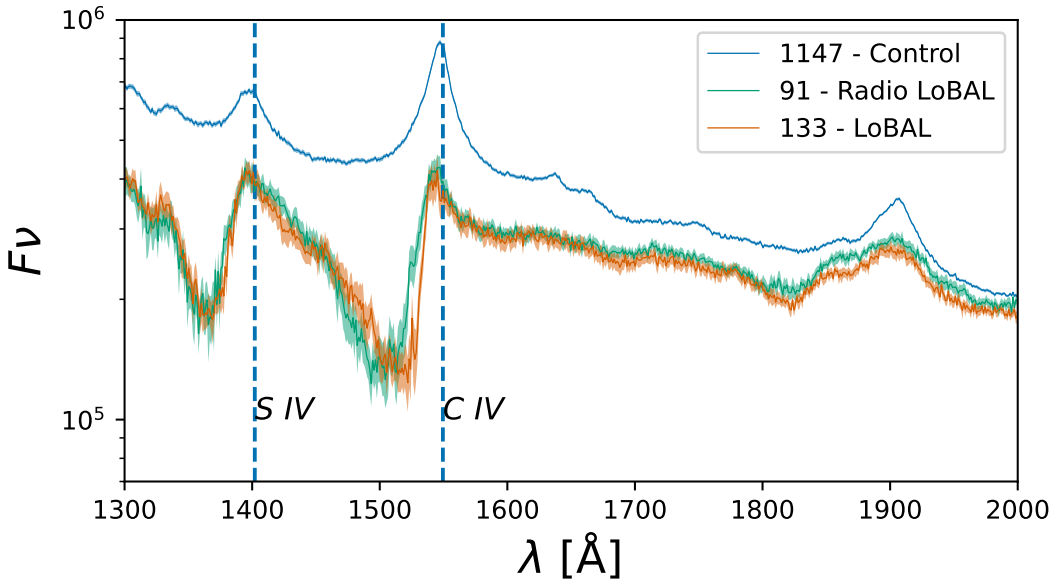

Figure 3.10: Overall composite for radio (green) and non-radio-detected (orange) LoBALs along with a blue quasar composite. The radio composite is less reddened compared to the non-radio, a behaviour that differs from the HiBAL populations. The radio composite also shows a small shift in the base of the absorption trough towards lower wavelengths.

quasars to be in the 25th-75th percentile range for $g - i$ colour in each redshift bin we take between $1.7 < z < 3.0$. This creates a large sample which when stacked gives a high-quality composite spectra that has a minimal amount of reddening, with a low fractional standard error at each wavelength point. It is important to note that this is not an entirely "de-reddened" spectra as typical quasars will still contain a modest amount of dust (Fawcett et al., 2022). We use it as a basis to compare the reddening of other composites.

The composite spectra we create can be used to compare continuum, emission and absorption properties when grouping the sources into meaningful samples. We construct composites based on several factors that we know connect with radio-detection fraction. This involves HiBAL and LoBAL sub-classes, BI and radio luminosity.

Composites created using all the radio-detected and non-detected HiBALs and LoBALs are shown in Figure 3.9 and Figure 3.10 along with the control composite. We see that as a whole, both populations show increases in reddening as expected. Radio-detected HiBALs show further reddening than the non-detected HiBALs while both LoBAL subsets are more affected by extinction but without a difference between each other. However, these overall differences are largely expected considering that we have shown how radio-detection correlates with both increased reddening and BI and these differences are reflected in the composite spectra.

We test the difference in composite spectra between radio and non-radio BALQSOs when matching in BI, to see if there are any changes to the absorption features and reddening with increasing wind strength. We take the HiBALs in our sample and split them into 4 BI bins in log-space. By doing this we are trying to remove the effects of wind "strength" and isolate the difference in spectra that may be connected to the radio emission. In Figure 3.11 we present the changing spectral features for radio-detected and non-detected HiBALs with BI. In general, the radio-detected BALQSOs are more reddened which is expected. The radio-detected BALQSOs have broader absorption features which are particularly apparent in the highest BI bin.

Next, we compare HiBALs and LoBALs while matching in BI to remove the

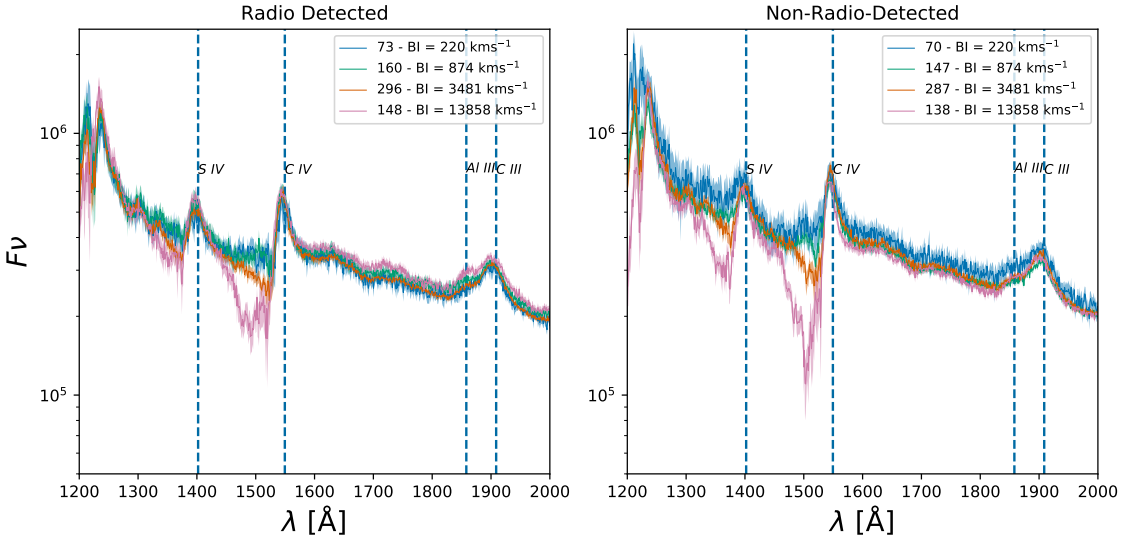

Figure 3.11: The reddening connection to BI, an attempt to measure wind "strength", differs for radio-detected sources compared to the general increases in reddening with BI for non-radio sources. We also demonstrate how radio BALQSOs have broader absorption features, suggesting that the radio emission could be connected with the velocity of the outflow.

previously indicated effects on HiBALs of increased reddening and radio detection at higher BI values. In Figure 3.12 we match the BI range of the HiBALs and LoBALs to 3500–7000 kms^{-1} and match the distributions within 5 smaller sub-bins of uniform width in that range. This gives radio and non-radio composites for HiBALs and LoBALs over the BI range. The two resulting HiBAL composites are very similar which is expected since they are at the high BI end of their distribution and in Figure 3.11 we show that differences in reddening between the radio and non-radio HiBALs spectra become indistinguishable at high BI. The HiBALs are less reddened than the LoBALs at the same BI. This could have implications for the dust fraction in LoBALs since if the dust causing the reddening is associated with the wind or the wind strength then this alone cannot explain the reddening differences as we have matched in BI and the reddening differences between HiBALs and LoBALs remain the same.

Overall the shape of the absorption features in Figure 3.12 are similar for HiBALs and LoBALs, although there is a wavelength shift in the absorption base of the radio LoBALs. This can be quantified using the relative velocity of the highest absorption (lowest flux) point of the absorption trough relative to the C IV emission line. For

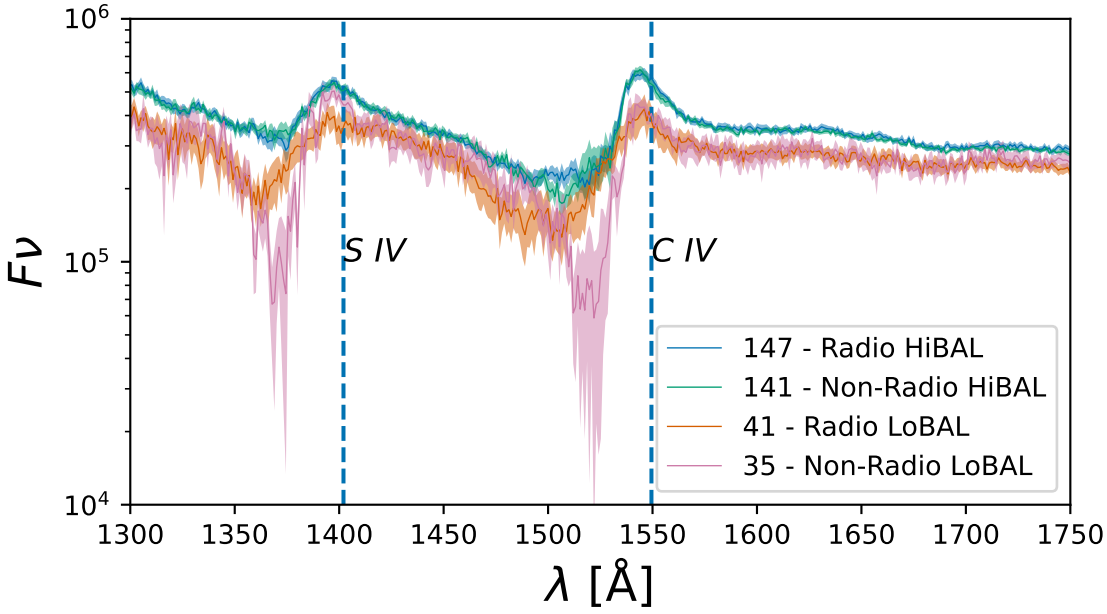

Figure 3.12: Composite spectra for HiBALs and LoBALs in the BI range of 3500 to 7000 kms^{-1}. Both LoBAL spectra show increased reddening compared to the HiBALs but they differ in their absorption properties. The radio LoBAL shows a wavelength shift in the absorption feature.

the non-radio HiBAL, the velocity shift is 5400 kms^{-1} while for radio HiBALs it is 5600 kms^{-1}. There is an order of magnitude change when looking at LoBALs however, implying a strong connection between the wind and radio emission in these sources. For non-radio-detected LoBALs the shift is 6000 kms^{-1} while for radio-detected LoBALs this value is 7100 kms^{-1}. We emphasise this change by showing only the LoBAL composites at matched BI, along with a control composite, in Figure 3.13.

LoBALs show significant reddening compared to control quasars, as has been seen in other studies of this population (Urrutia et al., 2009). Interestingly, there is no difference in the reddening between the radio and non-radio composites. This contrasts with the HiBALs where small differences were seen as BI changes, although this LoBAL sample is already at a higher BI due to the nature of the BI distribution of LoBALs and HiBALs (see Figure 3.1). In the HiBAL composites, we saw that the reddening differences are not so apparent in the high BI bin. Splitting LoBALs into BI bins greatly increases uncertainty due to their rarity making it difficult to test if the same trend is present in the LoBAL population.

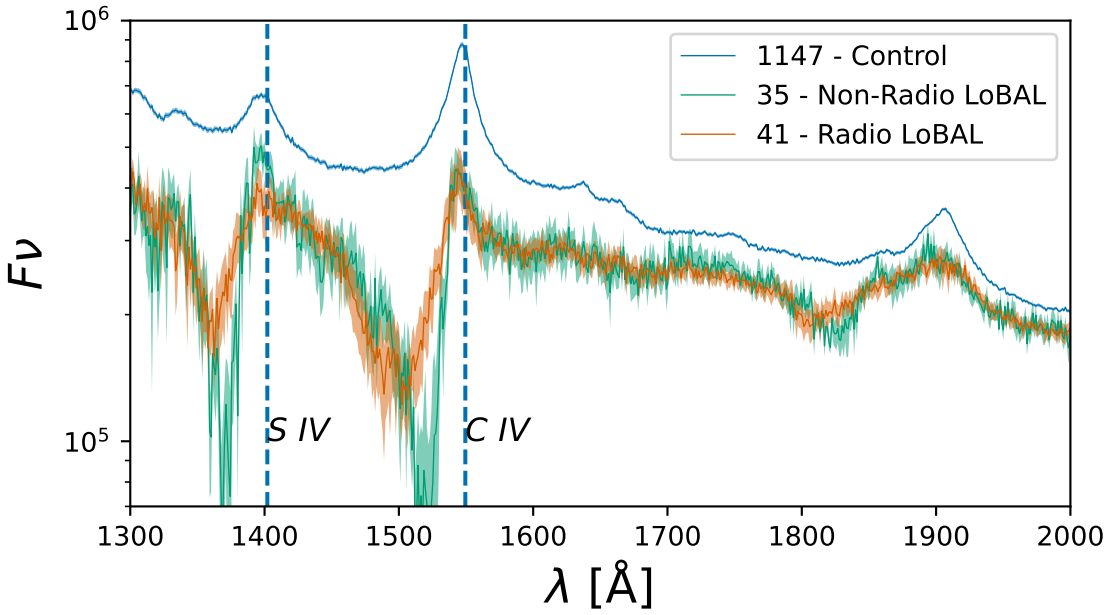

Figure 3.13: Both LoBAL populations show significant reddening compared to the overall control quasar composite. However, there appears to be no difference in the attenuation between the radio and non-radio-detected samples. Radio-detected LoBALs show an earlier saturated absorption trough. Saturated BAL troughs are usually explained either through the partial covering of the continuum source or through scattering from an opacity external to the wind.

3.3.4 C iv Emission Space

Recent work focusing on the C IV emission properties for SDSS quasars has found some important connections between key parameters in this space and radio detection. This space was initially identified in Richards et al. (2011) where C IV blueshift was found to be larger in radio-quiet quasars as compared to radio-loud and that this could be connected to a model in which radio-loud quasars are disk dominated systems while radio-quiet quasars are wind dominated. Kratzer et al. (2015) also finds that the radio loudness fraction of quasars decreases as the presence of strong radiation line-driven winds increases. Most recently Richards et al. (2021) finds that the radio detection fraction is a non-linear function of C IV emission properties. They argue that their sample of radio-quiet quasars may require multiple multiple radio emission mechanisms to fully explain their radio observations with the VLA and LOFAR.

The most direct comparison to the sample in this paper can be found in Rankine et al. (2021) where the LoTSS radio-detection of quasars at a similar redshift range from SDSS DR14 was found to connect to the C IV emission and specifically that it correlates with C IV blueshift. SDSS quasars with no C IV blueshift having a radio-detection fraction of 12% while those with a blueshift of 3000kms^{-1} having a radio-detection fraction of 40%.

An earlier study, investigating the properties of BALQSOs in this space, also outlined the method of using mean-field independent component analysis to create spectral reconstructions for each quasar (Rankine et al., 2020). They found that the fraction of BALQSOs increases with C IV blueshift and lower EW.

We wanted to test whether the radio-detection fraction behaviour we have observed so far can be explained by the C IV emission space trends and whether a connection between BI and blueshift is apparent and can explain the correlation we see between BI and radio-detection fraction. To that end, we use the method from Rankine et al. (2020) and Rankine et al. (2021) to create PCA spectral reconstructions of our composite spectra and place them in C IV EW and blueshift space (i.e. we fit the composites as if they are a single quasar spectrum using the same code developed in those papers).

We find that low BI BALQSOs occupy a similar blueshift to the control composite but at lower EW. Then as BI increases the blueshift also increases but this alone is not enough to explain the radio-detection fraction increase with BI for BALQSOs. Our highest BI bin we create a composite for has a blueshift of around 1500kms^{-1} for the non-radio-detected sample and 1900kms^{-1} for the radio-detected sample. The radio-detection fraction for BALQSOs at this point is close to 50% while for quasars in general with the same blueshift, Rankine et al. (2021) finds the radio-detection fraction to be 25%. BI and blueshift correlate with one another but blueshift alone cannot explain the correlation between BI and radio-detection fraction.

3.4 Discussion

Overall we find that BALQSOs show an increased LoTSS detection fraction compared to the general quasar population, consistent with previous studies, but further to this we show that these differences still persist when accounting for other known correlators with radio-detection fraction such as colour, bolometric luminosity and C IV emission properties. When comparing the sub-populations of HiBALs and LoBALs we find an increased detection fraction of LoBALs as compared to HiBALs. We show that the correlation of both BI and optical reddening is not enough to explain the detection fraction differences of HiBALs and LoBALs.

We return to the SDSS data to create composite spectra for important subsamples of quasars, HiBALs and LoBALs to investigate how the absorption profiles of these groups change depending on whether they are detected in LoTSS, on their wind strength measured by BI and on their colour. We find that radio-detected BALQSOs tend to show different C IV absorption, with broader absorption features compared to non-radio-detected BALQSOs, and that these differences are most clear at the highest BI values. We also show that at matched BI the absorption profiles of radio and non-radio LoBALs show a difference in the wavelength at which absorption reaches a maximum.

In this discussion, we aim to present different ways in which to link the intrinsic radio-detection enhancement of BALQSOs, and LoBALs, with the different spectral

features that we have identified with composite spectra.

3.4.1 BI - Reddening Connection

We turn to the results of Section 3.3.3, specifically the positive correlations between BI and reddening and also between radio-detection in BALQSO and reddening. These changes in reddening are quite small but we discuss how they may be interpreted.

The physical explanation for increasing reddening with BI could be simply that the wind is the direct cause of the reddening and that the higher BI values are mainly due to more absorbing gas in the wind and this connects to an increased amount of dust in the wind. For the non-radio case the material increase appears to be at lower velocities as the main cause of the increase in BI is the low-velocity absorption features close to the C IV emission line in the right-hand panel of Figure 3.11. For the radio sample, the absorption increases across a wider range of velocities in the high BI bin.

The trend in reddening and BI and the fact that BALQSO winds are consistent with being launched at scales from 10 to >100 pc from the AGN (Arav et al., 2018; Choi et al., 2022a; He et al., 2022) support the conclusion that the reddening seen in BALQSOs is caused by the BAL wind itself. However, how to connect the radio emission to this wind is not so clear. At low BI the composite spectra of radio-detected BALQSOs are more reddened. Assuming that dust grains are similar in radio and non-radio-detected BALs, the increase in reddening observed has to be caused by an increase in intervening material, either in the galaxy as a whole or in the particular line of sight through to the BAL wind. In the latter case, the radio must also then have an angular dependence causing its appearance, implying small-scale jets or radio emission from the wind itself while a galaxy-wide increase in dust causing the reddening could allow for star formation.

We do not investigate what reddening laws best fit our different BALQSO subclasses but we note that work from Fawcett et al. (2022) indicates that the more extreme reddening in quasars may be better characterised by steeper extinction laws, corresponding to smaller dust grains, but this is very tentative. Under the assump-

tion that the dust grains are similar in HiBALs and LoBALs, we can understand LoBALs as having higher strength winds, measured by BI, and having a denser ISM, as measured by the extinction, which could support increased radio emission through disk wind shocks.

3.4.2 How do absorption features in LoBALs differ from HiBALs?

The radio and non-radio-detected LoBAL composites show very different absorption features in Figure 3.13 and also different changes relative to each other when compared to HiBALs. Firstly, we consider the average shape of the C IV absorption features. The spectrum of the radio-detected LoBALs shows a flattening at the bottom of the trough in the absorption region starting at around 1475Å while the non-radio composite continues to have a deeper trough all the way up to the blue wing of the broad C IV emission line. Determining whether the depth of a BAL trough is the result of increased column density, 'non-black' saturation caused by partial covering of the emission source (Arav et al., 1999), scattering from another source that is not co-spatial to the wind (Lamy et al., 2000) or from the combination of several wind components at different velocities is an outstanding problem in the analysis of these winds. Whatever the cause of potential saturation, it more strongly affects the radio-detected BALQSOs.

Further evidence for this effect can be found when splitting the radio-detected sample into a high (bright) and low (faint) luminosity bin divided by the median BALQSOs radio luminosity (3×10^{25} WHz^{-1} for HiBALs and 3.7×10^{25} WHz^{-1} for LoBALs). Composite spectra for these samples, along with the non-radio-detected LoBAL composite, are shown in Figure 3.14. The faint population closely resembles the non-radio-detected population in terms of their absorption profiles and is interestingly less affected by reddening. However, in the higher radio luminosity bin, several changes occur. Firstly, the extinction increases so that the reddening is similar to the non-detected sample. The lower wavelength of the base of the absorption trough increases compared to the other samples, implying a higher velocity for the absorbing gas in this more radio-luminous sample or a greater launch radius from

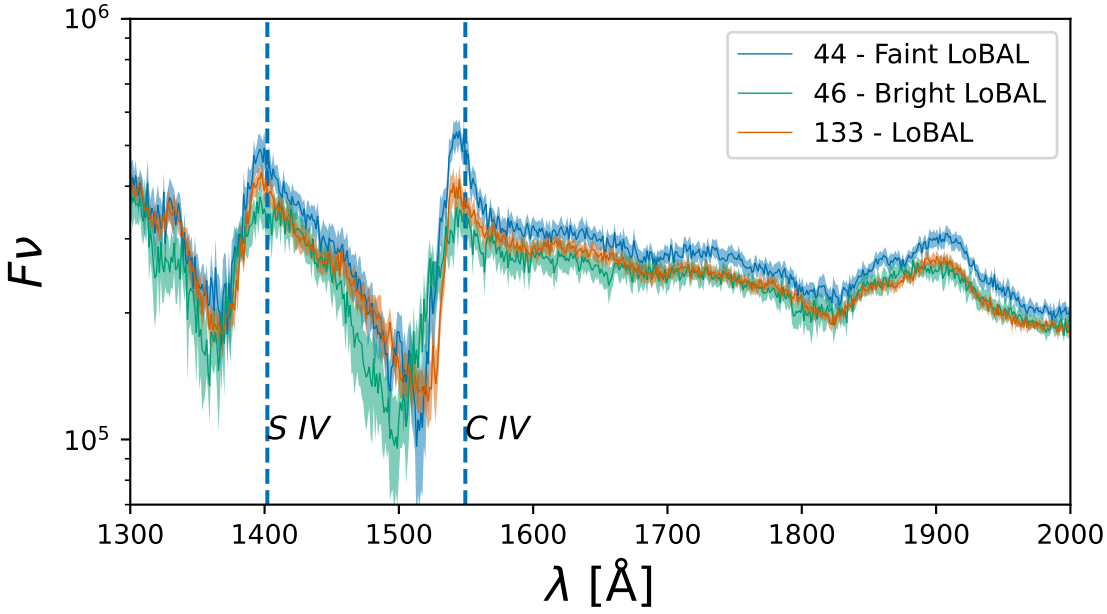

Figure 3.14: By splitting into a high and low radio luminosity sample, by the median LoBAL radio luminosity, we examine the dependency of absorption properties on the magnitude of the radio emission. We find connections between the velocity of the outflow and the radio emission. The blueshift of the radio composite implies higher velocity outflows along with an increased amount of intervening material responsible for the saturation and increased reddening in the radio composite.

the central black hole. Finally, the absorption profile also appears to be broader for radio-bright LoBALs. These results suggest that the velocity of the wind is a factor in radio emission, along with an increased amount of material responsible for the reddening, which could come from the wind or other in-situ dust.

Increased reddening for the radio-detected sources combined with the higher incidence of broader absorption in the C IV absorption region is potentially suggestive of an increased amount of material along the path of the high-velocity outflow. This could make radio emission from shocks, as the outflow interacts with this material, a potential mechanism for the radio-detection fraction increase in LoBALs compared to HiBALs. We explore this possibility, along with alternative explanations for radio emission, in the rest of this discussion.

3.4.3 Radio Interpretation

The origin of the radio emission in radio-quiet quasars is a topic of much debate and this extends to BALQSOs, an overwhelmingly radio-quiet population. Three main mechanisms have been proposed as the dominant contributor: star formation (Padovani et al., 2011), frustrated jets (White et al., 2015) and the disk wind (Blundell et al., 1999; Faucher-Giguère et al., 2012; Fukumura et al., 2013). Conversely, the consensus for the radio-loud population is that radio jets are the dominant factor and this has allowed for the orientation of radio-loud sources to be probed more easily as resolving the jet components can allow inclination to be determined under certain assumptions of symmetry. Connections have been made between the wind and jet for radio-loud sources; for example Mehdipour & Costantini (2019) find a negative correlation between radio-loudness and the column density of the ionised wind. They attribute this coupling to magnetic mechanisms powering both the winds and the radio-loud jet, providing a connection between the two and originating at the black hole scale. This connection is complicated by time scale being an important factor when considering radio-loud sources. The radio-loud emission attributed to large jets may take $\sim 10^7$ years to evolve (Hardcastle, 2018), while the magnetic field and wind column density evolve at smaller size scales and change on much faster timescales. Radio-loudness is not a measure of the current state of the black hole and will continue to increase if a jet can continue to be powered over a long period of time while the optical continuum emission, part of the loudness ratio, can change much more quickly as the accretion close the black hole is on a much smaller scale.

The connection between BI and radio-detection fraction presented in the previous section (see Figure 3.5) has a key role to play when attempting to constrain the source of the emission and the structure of BALQSOs. For example, if one takes the evolutionary theory for BALQSO occurrence, that BALQSOs are an early phase in the lifetime of a quasar in which much of the star formation quenching is triggered, and that jets are the radio source, then the connection with high BI and radio-detection fraction appears hard to explain as because the UV line-driven wind and the majority of radio originate on totally different size scales they also differ in time

by a large amount. The wind and jet connection from Mehdipour & Costantini (2019) cannot be due to synchronous effects, although the overall history of the AGN could be the connection. Studies of disappearing and appearing BALQSOs (De Cicco et al., 2017; Mishra et al., 2021) have placed the variational time scale for BALQSO winds, on the order of hundreds of years, to be much shorter than that of radio jets, on the order of Myrs. Therefore the BI to detection fraction correlation lacks the synchronicity one might expect in the evolutionary theory. This could be resolved by invoking a number of BALQSO phases, thereby extending the overall time in which a BALQSO wind could be observed and connecting these phases with the intermittent power changes that are known to occur in the production of radio jets around black holes (Nyland et al., 2021). However, since we do not understand the geometry of these variable systems we could be looking at some special subset that is not representative of the full BALQSO population.

Overall, we have established that both BI and colour correlate with radio-detection fraction but since these two parameters are likely connected it is hard to tell what is really driving the detection fraction increase. The absorption profiles of radio-detected BALQSOs show lower-wavelength absorption and also reduced narrow line absorption close to the C IV line when compared to the non-radio-detected BALQSOs, particularly at higher BI values. When we match in BI for both the HiBAL and LoBAL populations, we find differences in the radio-detected and non-radio-detected LoBAL populations but not for HiBALs.

We know from Figure 3.3 that HiBAL and LoBAL populations have similar distributions in radio and bolometric luminosity so the emission mechanisms are likely to be similar in both populations. The fact that at matched BI, HiBALs and LoBALs show different absorption feature changes depending on whether they are radio-detected or not, suggests that that an orientation model cannot explain the transition from HiBAL to LoBAL.

Ultimately, the radio-detection fraction differences between HiBALs, LoBALs and non-BALQSOs must be driven by one of two general mechanisms: either star formation or processes associated with the AGN. We now focus on each of these in more detail.

3.4.4 Radio Interpretation - Star Formation

We show clearly that the wind properties and radio emission are connected via our composite spectra, immediately making a star formation explanation for the radio detection fraction enhancement unlikely. Also, the correlation between BI and radio-detection fraction is hard to interpret in a star formation scenario as the increased wind strength would need to couple to the triggering of star formation bursts.

A case could be made for an indirect link via the fact that star formation and AGN accretion rely on the same fuel source. Maybe this could connect the BALQSO wind appearance to increased star formation. However, this would rely on a similar timescale for the fuelling of both the star formation and the BALQSO wind. Studies have shown that these timescales are not at all similar for star formation and other forms of AGN activity (Hickox et al., 2014), implying that this would also be the case for BALQSO winds.

Star formation as the primary radio emission mechanism for BALQSOs is not compatible with the angular interpretation for the presence of BAL emission troughs. Simply put, radio emission from galactic star formation should have no dependence on viewing angle. In general, after finding the strong radio-detection differences in BALQSOs, to maintain an orientation-based approach one must also find a radio emission mechanism that is also orientation-dependent as the cause, or one must involve relativistic beaming of the proposed mechanism at an angle that relates to the angle of the BALQSO wind.

Another way to interpret the increased detection fraction of BALQSOs, relative to the general population, is to actually consider the possibility of there being a deficit in flux density from typical quasars due to increased free-free absorption at these LOFAR frequencies. This would then be difficult to explain with either the orientation or evolutionary scenarios. BALQSOs do have flatter spectral indices in this sample which could be related to free-free emission. However, based on the calculations of Condon et al. (1992) we really do not expect a significant contribution from free-free emission at 144 MHz.

In the evolutionary explanation of BALQSO occurrence, LoBALs are typically placed at an early stage in the evolution of a quasar. Therefore it is expected

that LoBALs may have higher star formation rates as they are more reddened and potential quenching effects of the outflows and quasar more generally have had less time to take effect. The powerful winds in BALQSOs could then remove the dust associated with star formation and leave a blue quasar behind.

Previous studies have tried to find differences in the IR and line ratio properties of LoBALs and HiBALs that could suggest that they have different star formation rates to the general population. Recent examples such as Wethers et al. (2020) and Chen et al. (2021) both claim to find evidence that LoBALs show signs of being in a special phase of high star formation which is not seen in non-BALQSOs or HiBALs. However, these were certainly not conclusive findings and a larger study of HiBALs and LoBALs using more accurate star formation tracers with an instrument such as ALMA will be needed to test these results.

If star formation is the cause of enhanced radio-detection in HiBALs and then even further in LoBALs, then the differences between their composite spectra ought to remain consistent with this explanation. However, we find that radio LoBALs show different absorption features at matched BI to radio LoBALs. This would suggest that the wind properties cannot be related to the star formation that is causing the radio-detection fraction increase for BALQSOs compared to non-BALQSOs. The only resolution would be that both the BALQSO wind appearance and enhanced star formation have an evolutionary explanation that is separate for both but typically occurs on the same cosmological timescale giving rise to the radio-detection fraction increase for BALQSOs.

Generally, the energetic output of winds is thought to likely reduce star formation through the heating of molecular gas clouds which are much more likely to collapse and form stars when they are cooler. However, we do consider scenarios in which the presence of an outflow may in fact trigger star formation episodes, likely through the compression of the molecular star-forming gas and increasing subsequent star formation.

If star formation is the largest source of radio emission in BALQSOs then the trend in BI and radio-detection fraction would suggest that stronger winds can trigger more star formation, although it is important to note that no correlation was

found between BI and the radio luminosity itself. The timescale of both the wind lifetime and the time needed to trigger a significant amount of star formation are important when considering whether the direct connection is plausible. Star-forming clouds collapse on timescales on the order of Myrs to tens of Myrs. This is potentially much larger than the lifetimes of a BAL wind, especially when considering there is likely a delay between the hypothetical compression of the star-forming gas clouds and the time at which the star formation levels are high enough to drive a significant increase in the radio-detection fraction.

Even if there is an increased level of star formation, any radio emission from an AGN process could be added on top of the star formation level, potentially weakening observed trends with radio luminosity.

3.4.5 Radio Interpretation - AGN

AGN-related radio-quiet emission mechanisms include frustrated sub-galaxy scale jets, weak jets, wind emission and coronal emission (Panessa et al. 2019 and references therein). We can largely rule out coronal emission since the radio-detection fraction correlates with larger blueshifts which are not connected. In this subsection we take each mechanism in turn and, assuming that the mechanism is the largest contributor to radio emission in BALQSOs, consider that process' plausibility given the results of this work.

Frustrated Jets

Frustrated jets are used as an explanation for radio-quiet emission where the jet structure is similar or identical to that of radio-loud and FR1 type sources, but they have different efficiency in accelerating electrons (Falcke & Biermann, 1995). The clear signature for this process being the key contributor to radio emission in BALQSOs would be an excess of compact and flat spectrum sources. Using the LoTSS DR2 definition of whether a source is resolved from Shimwell et al. (2022b), we do in fact find that BALQSOs are slightly more likely to be unresolved at 6-arcsecond resolution than non-BALQSOs in LoTSS DR2. BALQSOs are 98% unresolved while the general population are 96% unresolved. They also have on

average flatter spectra when using LoTSS DR2 and FIRST, which was also found in DR1 (Morabito et al., 2019), with a median spectral index of 0.094 ± 0.25 compared to -0.65 ± 0.091 for non-BALQSOs. It is rare to find BALQSOs with spectral indexes < -0.5 in our sample. It should be noted that the requirement of FIRST detection to determine the spectral index biases the sample towards radio-loud sources. This could be seen as some small support for the jet hypothesis.

Jets are one possible emission mechanism that could allow for an angular interpretation of the BALQSO phenomena. The classic theory of radio jets suggests that they are launched perpendicular to the accretion disk (Begelman et al., 1984; Blandford et al., 1995). Therefore, one could interpret the increase in radio-detection with BI as a change in viewing angle, with LoBALs being at the closest angle to the jet (axis of rotation of the accretion disk), allowing for a clearer view of the compact jet or the effects of relativistic beaming as it becomes more likely that our viewing angle intersects with the jet. However, upon closer inspection, we suggest that in fact, with the standard model of winds being viewed closer to the accretion disk than the orthogonal jet axis (Matthews et al., 2016), this is the exact opposite of what we would expect. As our viewing angle gets closer to the accretion disk, and BI increases, we are in fact moving away from the jet axis and so would expect a decrease in radio-detection fraction. This seems to be strong evidence to rule out the combined theory of an orientation approach with radio jet emission for BALQSOs unless the orientation is that of a polar wind, as proposed by Ghosh & Punsly (2007). Doppler beaming is very unlikely to help here either for similar reasons and because we are observing at low frequencies where the radio emission is lobe-dominated.

A key issue facing a possible jet hypothesis is the fact that BALQSOs are a radio-quiet population. Therefore if jets are the explanation for the enhanced radio-detection fraction in BALQSOs, we also need an explanation for why there is a deficiency in high-power radio jets as compared to the general quasar population. Either the jets are different in nature to radio-loud quasars or somehow the the jet destroys the BALQSO wind as it expands.

Some research suggests that BALQSOs are more likely to be GigaHertz Peaked Spectrum (GPS) sources (Bruni et al., 2015, 2016). GPS sources are known to be

jet-dominated and likely have younger jets. They display a turnover in the radio SED due to synchrotron self-absorption. If it is the case that BALQSOs are GPS-like sources then we would expect BALQSOs to display flatter spectral indices compared to non-BALQSO quasars when measuring at the 144 MHz of LOFAR and the 1.4 GHz of FIRST which is indeed what we find. This means the spectral indices that we measure in the BALQSO sample may not need an orientation interpretation and could lie in a phase before a radio jet is relaunched or recollimated.

Disk Winds

Disk winds have two main theorised radio emission mechanisms. The first is in the form of disk wind shocks and the second is from bremsstrahlung free-free processes. However, the latter was found to be unable to explain the X-ray and radio luminosities for a sample of radio-quiet quasars in the Palomar Green sample (Steenbrugge et al., 2010). Also, the flat spectral shape of bremsstrahlung emission at radio wavelengths implies that its contribution to the LOFAR bands is minimal.

Evidence that outflows trigger shock synchrotron emission was found by Zakamska & Greene (2014) where they show that [O III] velocity had a positive correlation with radio luminosity for a sample of quasars. Calculations from Nims et al. (2015), using a model of a homogeneous and spherically symmetric ISM, suggest that the radio luminosity of winds with an energy of a few per cent of the bolometric luminosity of a powerful AGN would be at least as great as star formation.

The distance at which winds are typically launched in BALQSOs has large implications for their observational signatures and their energetic output into a galaxy. The fact that we cannot extract the velocity of the wind and distance from the AGN through the shift of the absorption trough allows for several interpretations of the BALQSO composites, in particular the differences between LoBAL groups in Figure 3.13 and Figure 3.14. In Figure 3.13 we emphasise the difference in the absorption features of radio and non-radio-detected LoBALs despite matching in BI. Although there is no clear reddening difference the absorption trough shows a blue shift at all three marked spectral lines, or maybe just a saturation at C IV, in the radio composite. This could potentially imply that radio emission is connected

to the velocity of the outflow in BALQSOs. Alternatively, the radio LoBAL winds are launched at greater distances from the central black hole. In Figure 3.14 we also see a strong difference in the reddening where the brighter LoBALs have increased attenuation. Together with the absorption trough shift, it could imply that radio emission is connected to higher velocity winds or simply to a more dense ISM where the shocks are triggered.

The saturation of features is also seen at the high BI end for HiBALs in Figure 3.11. Considering that LoBALs are at the high BI end of the overall BALQSO distribution it could be possible that the saturation features have the same underlying physical reason for HiBALs and LoBALs but we do not find the same shift in the absorption features. This feature is only seen when looking at the radio and non-radio LoBALs and noticing that it is more apparent at the high radio-luminosity end.

The fact that we observe changes in the absorption properties when looking at the radio-detected and non-detected samples strongly implies a connection between the BALQSO outflow and the radio emission.

3.5 Conclusions

In this study, we have created the largest sample of radio-detected BALQSOs by matching the latest LoTSS DR2 release to the SDSS DR12 quasar catalogue. By creating a large sample of BALQSO with a high SDSS signal-to-noise ratio to remove certain biases in the identification of BALQSOs, we have been able to approach this population on a larger statistical scale, even for the rarer LoBALs, than any previous radio study allowing us to achieve the following key results

1. The overall radio-detection of HiBALs and LoBALs across redshift is 30.2% and 44.9%. For general quasars, the fraction is lower at 20.2%.

2. The radio-detection fraction of BALQSOs has a weak correlation ($r = 0.9609$, $p = 5 \times 10^{-4}$) with balnicity index even when excluding LoBALs which account for many of the highest BI sources. This connects the absorption line properties of BALQSOs to their radio emission.

3. Radio-detection fraction for BALQSOs also correlates with $g - i$ colour but the behaviour of the bluest BALQSOs, entirely HiBALs, differs from the general quasar population. This subgroup will need further investigation. Also, BALQSOs still show an intrinsic increase in detection fraction compared to non-BALQSOs across colour space.

4. Radio-detection fraction also correlates with C IV blueshift in quasars. However, the BALQSO radio-detection fraction increases with BI at a rate beyond the expected change from C IV blueshift increase.

5. Composite spectra of HiBALs show that the radio-detected HiBALs are generally more reddened across BI but that this difference is reduced as BI increases. These reddening changes are small. Radio-detected HiBALs show more saturation in the absorption troughs at high BI.

6. HiBALs and LoBALs show different reddening and absorption features even when matched in BI. They also show differences in the relation between their radio and non-radio-detected spectra with the HiBAL composites being nearly indistinguishable.

7. The radio-detection fraction increase for LoBALs cannot be explained through relativistic beaming of jets that are also present in HiBALs, without a polar model for all BALQSOs.

8. Radio-detected LoBALs show a shift of around 20%, compared to non-radio-detected LoBALs, in the base of the absorption trough at C IV. This implies either a connection between the velocity of the BAL wind and the radio emission or in the radius of launch from the AGN. Each possibility leads to several different interpretations depending on which radio emission process is assumed to be primary.

Overall, the results from this paper point towards the radio emission of BALQSOs being connected directly to the wind, and hence to the radio emission of wind shocks in the ISM being the cause for the increased radio-detection fraction. The main evidence for this comes from the absorption property changes, shown in the

composite spectra, in sources that are radio-detected and from timescale issues for other explanations of radio emission with these shorter-term wind changes in mind. However, we cannot entirely rule out any of the radio emission mechanisms or favour a particular orientation or evolution model. We find that star formation is unlikely to be the contributing factor given the correlation between the balnicity index, absorption profiles and radio emission.

By utilising the sub-arcsecond resolution imaging capabilities of the LOFAR international stations (Morabito et al., 2022b) we intend to characterise the morphology of many of these compact BALQSOs by using international LOFAR stations to reach sub-arcsecond resolution. This means we will be able to see if the emission has structure (galaxy-scale jets), is distributed across the galaxy (star formation) or if it is still largely compact we can look at disk wind emission or frustrated small-scale jets. Combining this with e-MERLIN observations to extract spectral indices at similar resolution for multiple component sources, we aim to confirm which mechanisms are occurring in these sources.

3.A SNR Cuts

We present some additional information regarding the signal-to-noise cut made to the optical spectra. We studied the differences in bolometric luminosity and radio detection fraction for different SNR cuts. In Figure 3.15 we show that an SNR < 5 cut minimises the impact on our results while still maintaining a large number of sources.

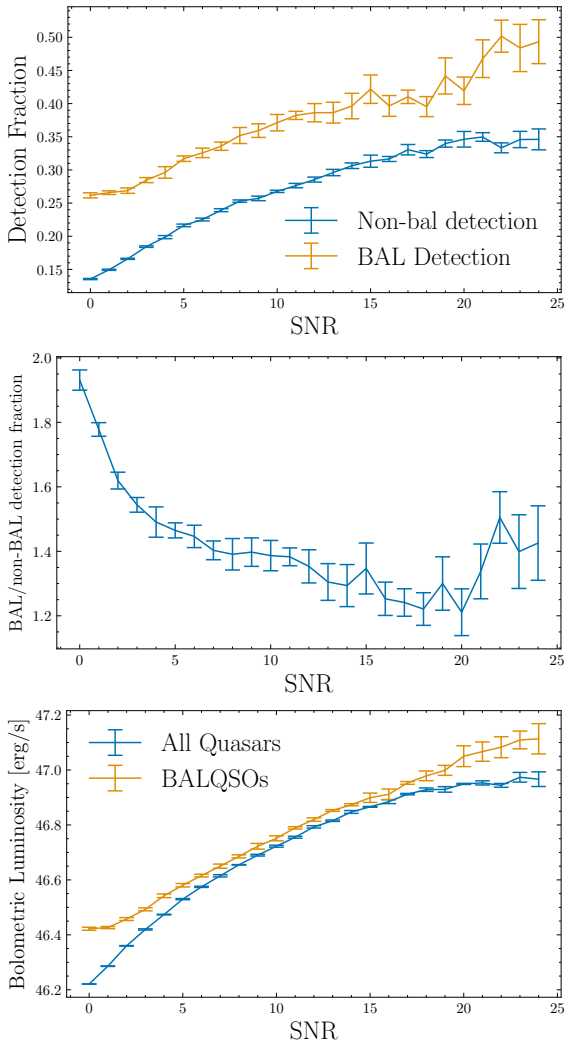

Figure 3.15: *Upper:* Radio detection fraction against SNR for BALQSOs and non-BALQSOs. *Centre:* We show that the BALQSOs present an enhancement in radio detection that is much stronger at SNR < 5. *Lower:* By studying the bolometric luminosity in each bin we show that the differences are likely driven by changes in bolometric luminosity which are enhanced at low SNR and motivate our decision to take a cut. Without this cut the radio results for BALQSOs would be even more enhanced

I'm bleeding mercury.
Caught in a time warp, and all I see is burgundy.
My fingertips glisten, gripping crystallised flowers,
Red and green sparkle
Marvel at the powers

The Cosmic Gypsies - Jehst

4

How does the radio enhancement of broad absorption line quasars relate to colour and accretion rate?

In this chapter, I present work that was also published in the Monthly Notices of the Royal Astronomical Society (Petley et al., 2024) which expands the connection between BALQSOs and red quasars. It answers several questions as to the relative contribution of these groups to radio-quiet quasar radio emission. I also test whether the accretion rate or luminosity of the AGN are underlying drivers that can explain both populations but find that colour and the presence of a BAL wind maintain their own contributions. I end by testing a wind shock model and deriving the required energy and relativistic electron conversion efficiencies needed to replicate the majority of radio-quiet sources.

4.1 Introduction

Black holes are now key to our understanding of the complex evolution of galaxies, despite being fundamentally simple to characterise (Kerr, 1963). Nearly all galaxies contain a super-massive black hole (SMBHs) and, during rapid growth, black hole systems can stimulate electromagnetic radiation in their surroundings. These black holes are considered to be "active" and referred to as Active Galactic Nuclei (AGN). Combined with the knowledge that SMBHs grow with their galaxies (Kormendy et al., 2013), AGN have become objects of great interest in many different areas of astronomy today.

Quasars (also known as QSOs) are the brightest of all AGN and are some of the most luminous objects at optical wavelengths in the observable universe (Schmidt et al., 1968). The massive amount of luminosity ($> 10^{44}$ erg/s) that quasars radiate could impact the future evolution of their host galaxies since, at least for a time when we observe them, they have a much greater energetic output than all the stars in their galaxy. However, it is often difficult to predict what will be observed across the full spectral energy distribution of a quasar even if some wavelength regions or physical properties (eg. accretion rate and black hole mass) are well understood or measured. Since different wavelength ranges offer information about different physical scales and processes, we cannot build a full picture of quasar behaviour without appreciating the longest, as well as the shortest, wavelengths.

Radio emission at low frequencies ($\lesssim 10$ GHz) in quasars is largely dominated by the synchrotron radiation process. Emission is released through the acceleration of electrons moving at relativistic speeds through a magnetic field (Condon et al., 1992). Radio emission is largely unaffected by sources of obscuration which significantly modulate what is observed at shorter wavelengths. For example, we avoid the effects of dust that impact optical and ultraviolet (UV) emission. Radio observations could therefore play a key role in understanding energetic interactions between a black hole and its galaxy. The most widely recognisable sources of synchrotron emission are famous *radio-jet* type galaxies with complex jet and filament type structures which extend well beyond the size of the host galaxy (Fanaroff & Riley, 1974). The mechanism which extracts energy into these jets from accretion around the black

hole is thought to be the Blandford-Znajek process (Blandford & Znajek, 1977). The formation of such jets likely has a significant connection with the spin of a black hole (Blandford, 1990; Wilson & Colbert, 1995), a property currently not measurable at significant redshift. These jets are increasingly incorporated into both single galaxy or cluster simulations (Huško et al., 2022) and cosmological simulations with AGN feedback (Davé et al., 2019; Thomas et al., 2021).

When studying the radio population, observers have typically made a distinction into two types of sources based on the apparent bi-modality in the radio-to-optical luminosity ratio distribution. *Radio-loud* sources have higher radio to optical luminosity ratios than *radio-quiet* sources (Kellermann et al., 1989). Although this can be a useful distinction, often splitting into these two groups can cause confusion amongst astronomers as it has sometimes been implied that radio-loud sources are jets and that radio-quiet sources are not. To be clear, many radio-quiet jetted AGN have been observed (Kukula et al., 1998; Leipski et al., 2006; Jarvis et al., 2019; Macfarlane et al., 2021; Girdhar et al., 2022) i.e. **radio-quiet $\neq$ no jet**. Consequently, while we are confident that the vast majority of radio-loud sources have jets, we lack the required information to make the contrary statement for radio-quiet sources.

The origin of radio emission in a given radio-quiet system is therefore a more complicated matter given there are essentially four emission mechanisms with the potential to be detected by modern radio surveys. These are: jets, star formation, disk winds and corona (Panessa et al., 2019; Kimball et al., 2011). Coronal emission is unlikely to be the dominant radio emission mechanism at the low frequencies which we study in this paper (Raginski & Laor, 2016; Behar et al., 2018; Baldi et al., 2022). Coronal emission is highly compact, optically thick and has a flat spectrum which is not observed for the populations we study. Therefore, we do not include a detailed discussion of this emission mechanism. Distinguishing between the remaining possible components with current large radio surveys is not a simple task since the vast majority of sources are unresolved by most large-scale survey instruments, which means we cannot determine the source of the radio emission directly without higher resolution information (Morabito et al., 2022a).

Radio emission from jets in radio-quiet and radio-loud sources is likely very similar but jets can be frustrated in size and lifetime, by high-density environments of gas and/or dust (White et al., 2015; Sadler, 2016; Calistro Rivera et al., 2023), or simply lower power (Hardcastle, 2018; Hardcastle et al., 2019). Star formation rate correlations with radio luminosity have now been calibrated at several frequencies, including low frequency (Calistro Rivera et al., 2017; Gürkan et al., 2018), based on the clear correlation between infrared thermal emission and non-thermal radio-emission (Helou et al., 1985; Bell, 2003). Although there is a scatter and a strong dependence on the stellar mass of a galaxy (Delvecchio et al., 2021), the fact that this correlation exists means that radio is regularly used as a measure for star formation in non-AGN sources. Radio emission from disk winds is probably the most poorly understood of the potential mechanisms. Quasars are known to possess various types or phases of outflows (e.g. Broad Absorption Line Quasars - (Weymann et al., 1991), [O III] outflows - (Weedman et al., 1970), Ultra-Fast Outflows (UFOs) - (Pounds et al., 2003a)) and that these outflow phases can also couple to each other (Feruglio et al., 2015; Girdhar et al., 2022). These high-velocity outflows have the ability to generate shock fronts which could emit synchrotron radiation although currently, only a few simple models of these shocks exist with limited prediction power (Ostriker et al., 2010; Faucher-Giguère et al., 2012; Nims et al., 2015).

The presence of radio emission has been found to connect to several other quasar properties. The investigation of the interaction between these properties is the focus of this work. A brief introduction to each of these follows.

4.1.1 Optical Reddening

The distribution of rest frame optical colours of quasars is resolved in the Sloan Digital Sky Survey (SDSS) photometry and shows a normal distribution with a longer tail of quasars with excess red colours (Richards et al., 2003). These red colours in this tail of the distribution are most likely caused by the effect of dust (Webster et al., 1995; Glikman et al., 2007; Krawczyk et al., 2015; Calistro Rivera et al., 2021; Fawcett et al., 2022). Quasars that show excess red colours are defined in various ways, usually by their particular percentile of the colour distribution, as

red quasars. The link between radio emission and red quasars was firmly established by Klindt et al. (2019) who found that red quasars were $\sim 3\times$ more likely to be radio detected than blue or *control* quasars using the Faint Images of the Radio Sky at Twenty centimetres (FIRST (Becker et al., 1995)).

This result has prompted further research to expand to other wavelengths and look at different morphologies and powers. Klindt et al. (2019) and Fawcett et al. (2020) found that the radio enhancement is likely due to emission on compact scales and from the radio-quiet or radio-intermediate population. Rosario et al. (2020) used the LOFAR Two Metre Sky Survey Data Release 1 (Shimwell et al., 2019) to show that the red quasar radio enhancement exists at low frequencies and at a similar level to Klindt et al. (2019). High-resolution e-MERLIN data on a small sub-sample of red and blue quasars revealed a statistically significant difference in the incidence of kpc scale emission between the two samples with the red sample having a greater fraction of extended sources at scales ≤ 2 kpc (Rosario et al., 2021).

The interpretation of these results is that red quasars are inconsistent with a simple orientation model for the dusty torus surrounding the black hole but are broadly consistent as a transition phase where red quasars transition to blue quasars. Some propose that this may fit into larger evolution models such as the one proposed in Hopkins et al. (2008). Furthermore, through modelling of the radio-UV spectral energy distribution and optical spectra of quasars, Calistro Rivera et al. (2021) found that the reddening may originate from dusty polar winds. The increased radio emission could then be due to shocks from AGN winds, or due to shocks from the interactions between compact AGN jets and dusty gas-dense regions (Fawcett et al., 2023; Calistro Rivera et al., 2023), or alternatively increased star formation during this earlier stage of evolution, although the latter has been excluded based on multiwavelength SED fitting by Calistro Rivera et al. (2023) and the high-resolution study of Rosario et al. (2021).

4.1.2 Broad Absorption Line Quasars

Around 10-20% of quasars selected by optical magnitude show broad absorption features bluewards of the C IV emission line, although the intrinsic fraction of quasars

with these features is expected to be higher (up to 40%, e.g(Dai et al., 2007; Allen et al., 2010; Dai et al., 2012)). These quasars are known as Broad Absorption Line Quasars (BALQSOs) and have often been characterised using the Balnicity Index (BI) measure of Weymann et al. (1991). BI is calculated as an integral of a region bluewards of the C IV emission line when absorption is more than 10% of the continuum level. Radio studies of BALQSOs have shown that they are more likely to be radio-quiet than non-BALQSOs (Stocke et al., 1992; Becker et al., 2000) and, similar to the red quasars, they are significantly more likely to be radio-detected (Urrutia et al., 2009; Morabito et al., 2019; Petley et al., 2022). Petley et al. (2022) found that radio-detected BALQSOs have different absorption profiles compared to non-radio-detected BALQSOs implying an intrinsic connection between the wind and the radio emission, with radio-emission coming from the wind itself (wind shocks) as the most likely explanation for this connection.

The true fraction of BALQSOs in the quasar population is hard to ascertain. In a purely geometric understanding (Weymann et al., 1991; Ghosh & Punsly, 2007), the observed BALQSO fraction is equal to the mean fractional solid angle that the BAL wind subtends of the quasar. However, BAL troughs are known to appear and disappear (Ak et al., 2012; Mishra et al., 2021) and if they are predominantly an evolutionary feature, as noted in Gregg et al. (2006), then their lifetime is likely on the order of $\sim$ 10 Myr based on a $\sim$ 10% fraction of quasars accreting for $\sim 10^8$Yrs (Hopkins et al., 2005). If indeed the lifetime of a BAL wind is shorter than the lifetime of the average quasar, the BAL wind must have a much larger covering angle than simply the observed fraction in order to maintain that fraction, or alternatively, many quasars go through several BAL phases. However, it is not clear whether this BAL lifetime is a feature of the wind turning on and off or a feature of a particular geometry such as a rotating clumpy wind. Whatever the scenario, their radio-detection enhancement is potentially an indicator that they can interact strongly with their environment even in a relatively short time. In addition, many quasars identified as non-BALQSOs may in fact be hosting BAL winds which are not currently in our line of sight, creating some level of contamination within the non-BALQSO population.

4.1.3 C iv Distance

The C IV emission line (λ 1549) is readily observable in the UV spectra of most quasars. The anti-correlation between the C IV equivalent width (EW) and UV continuum luminosity, known as the *Baldwin Effect* (Baldwin, 1977), was evidence that this line could probe some of the accretion properties of the SMBH. Subsequently, the informational content of this line has been explored further and specifically the blueshift of the line was found to be a feature of importance (Gaskell, 1982; Wilkes & J., 1984; Richards et al., 2002; Sulentic et al., 2003, 2007). Richards et al. (2011) investigated radio-quiet and radio-loud quasars in a 2D space of C IV EW and blueshift and found that the distributions observed could best be understood through a "disk" vs "wind" model with disk dominated systems having high C IV EW and low blueshifts and wind dominated systems having low C IV EW and high blueshifts.

Recent work on this 2D C IV space has found further evidence of its diagnostic power. Rankine et al. (2020) found that BALQSOs comprise a higher fraction of moderate EW, high blueshift sources but crucially that they can still be found in all regions of the space. This suggests that BALQSOs are simply QSOs with a probability of observation based on a particular line of sight or at a particular time such that a BAL wind is observed. This probability, and also the average absorption profile of the BALQSOs, changes across the C IV space. Richards et al. (2021) converted the position in 2D space into a single C IV distance value (low C IV distance: high EW and low blueshift; high C IV distance: low EW and high blueshift) and found that the Very Large Array (VLA) radio detection fraction of quasars varied non-linearly with this parameter, hinting at multiple radio emission mechanisms at play, a result also suggested in Rankine et al. (2021). Physical drivers of the changing C IV properties have been suggested. For example, a link between accretion rate and C IV blueshift was found in Wang et al. (2011) and Sulentic et al. (2017). Most recently Temple et al. (2023) connected this space to Spectral Energy Distribution (SED) models of accretion and showed that changes in the properties of quasars in this space could be connected to accretion rate and a likely change in the accretion geometry around an Eddington Ratio of $\lambda_{\rm Edd} \approx 0.2$, a transition

suggested in Giustini & Proga (2019). We therefore use C IV distance in this work as a proxy for the accretion rate in our quasars as it is measured for all of our sources and does not have any additional conversions or assumptions.

This work aims to explore each of these quasar properties - C IV distance, optical colour and BAL winds - in combination and attempt to understand their intrinsic connection to radio emission. Each of these properties show overall changes in detection fraction of a similar magnitude and previous work has not incorporated all of them simultaneously. With an improved picture of the connection between these properties, we can re-think the underlying physical scenarios that govern radio emission in quasars.

4.2 Data and Methods

To create our sample of quasars we begin with the SDSS DR14 quasar catalogue of Pâris et al. (2018). This catalogue summarises the properties of 526,356 quasars including redshifts and whether a BAL wind is present, although this is the first of the SDSS releases not to visually inspect all spectra for BAL signatures. To improve the quality of the spectral data and also extract several important parameters for this study we use spectral reconstructions of SDSS DR14 quasars created through mean-field independent component analysis and described by Rankine et al. (2020). The process improves the redshift measurements and redefines parameters such as the BI in comparison to the SDSS release. We therefore use these values to define our BALQSO sample.

Reconstructed spectra are used to obtain the C IV EWs and blueshifts and to parameterise the C IV EW-blueshift space (hereafter "C IV space") with a single value, the C IV distance. The method for this process is described in Rivera et al. (2020) and also improved in Rivera et al. (2022). Strictly, we use the parallel C IV distance (C IV $\|$) described within Rivera et al. (2022) but simply refer to it as the C IV distance. In summary, the distance is formed through a piece-wise polynomial fitting of all quasars in the C IV space which is then scaled using a *MinMaxScaler* algorithm to place all values between 0 and 1 with an equal weighting to both axes.

Code to calculate C IV distance is available from McCaffrey & Richards (2021).

We use a slightly different technique to characterise red and blue quasars in our sample compared to recent radio studies of red and blue quasars such as Klindt et al. (2019); Fawcett et al. (2020); Rosario et al. (2020). It is not only the most red sources that show radio enhancement and we aim to study the overall effect of changing colour. We attempt to capture the variation in colour of quasars independent of redshift and keep all of the quasars in our working sample. By obtaining the redshift-independent optical colour distribution, we can then assign some quasars as being excess red due to some extra component, most likely dust and the rest as normal variation captured by a Gaussian. This is more similar to the reddening studies of Richards et al. (2003) and Glikman et al. (2022).

To accurately determine the colours of our quasars using SDSS photometry, we restrict our sample to $1.7 < z < 2.5$. The lower limit of $z = 1.7$ is imposed by the observable range of the C IV emission and absorption region in all of the SDSS quasars. The upper limit of $z = 2.5$ is imposed by the contamination of the Lyman break in the SDSS g band photometry at higher redshifts.

We split the sample into 20 equally spaced redshift bins and calculate the galaxy extinction corrected $g - i$ band colour for each quasar in that bin. We then shift the entire distribution within that bin so that the median is at 0. We do this for every bin so that in the end we have a stacked distribution of all the quasars with a median of 0. We then fit two distributions to the data using the `scipy` Python package. First, a normal distribution with a $\mu = 0$ to capture the majority of the colour variation and then another distribution to capture the excess red quasars. We found that a log-normal distribution worked best to capture this tail (see Figure 4.1).

We define all quasars with their colour bluer than the median within their bin as blue quasars (shown in blue in all figures), quasars with their colour more red than the peak of the log-normal distribution as excess red quasars (shown in red in all figures) and those in between these two points as "red" quasars (shown in black in all figures).

We aim to observe how C IV distance relates to an independent measure of the AGN luminosity, the 6-micron luminosity ($L_{6\mu m}$). Therefore we require that our

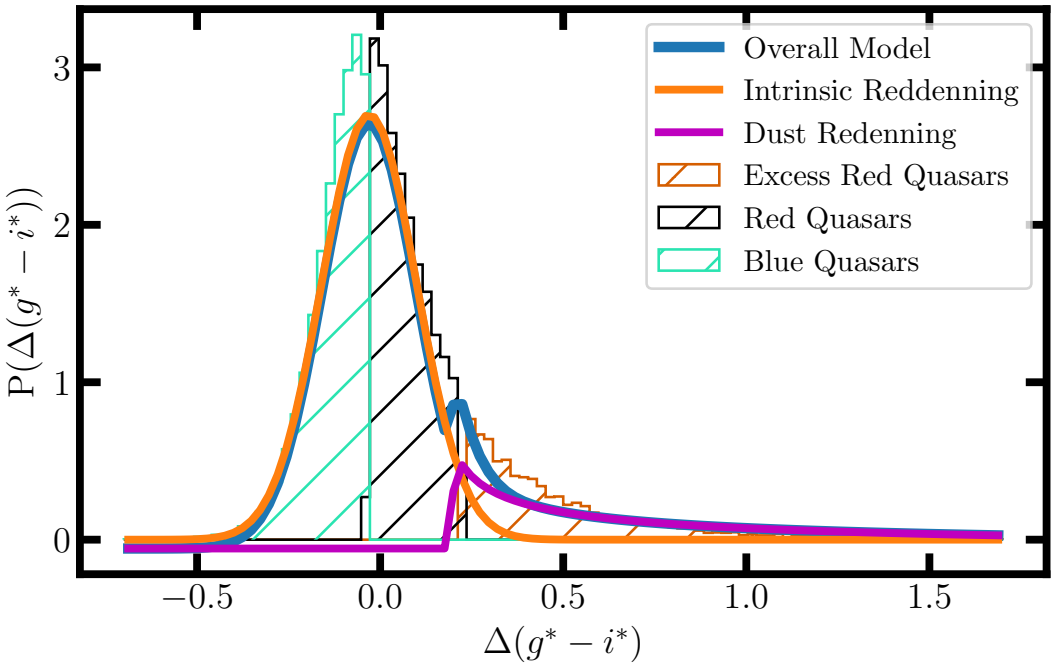

Figure 4.1: The probability density of redshift corrected quasar optical colour. We define different optical colours by splitting the quasars into redshift bins and then shifting the $g-i$ colour distribution in that bin to a median of zero. We then fit the stacked distribution with a normal (blue) and lognormal curve (pink). Excess red quasars are defined in the region beyond the peak of the lognormal, blue quasars are defined with a shifted colour below zero and red quasars are in between.

	Radio Detected	Non-radio detected	
BALQSOs	1463	3935	
Non-BALQSOs	6565	31175	
	Blue	Red	Excess Red
BALQSOs	903	2389	2106
Non-BALQSOs	16959	15325	5456

Table 4.1: We present the population numbers for BALQSOs and non-BALQSOs with respect to their radio detection and colour classification.

sample has detections in the first three bands of the Wide-field Infrared Survey Explorer (WISE). We perform a log-linear interpolation between the bands to estimate a rest-frame 6 micron luminosity which should capture the re-processed disk emission and be free from other extinction.

To understand the radio properties of the quasars, we use the LOFAR Two Metre Sky Survey (LoTSS) Data Release 2 described in Shimwell et al. (2022b). This is a radio survey of the Northern sky with over 4 million radio sources detected with a resolution of 6 arcseconds with a frequency range centred at 144MHz (wavelength of two metres). Specifically, we use the latest catalogue with optical counterparts identified using a combination of likelihood ratio matching (Kondapally et al., 2021), machine learning (Alegre et al., 2022) and citizen scientists (Hardcastle et al., 2023). LoTSS operates in a unique sensitivity and frequency range and is the best-suited survey for understanding large radio-quiet populations as it is around an order of magnitude deeper than FIRST (Becker et al., 1995), an example of an earlier widely used radio survey.

We restrict our quasar spectra sample to the LoTSS DR2 region and cross-match with a radius of 2 arcseconds to the LoTSS DR2 optical ID source catalogue. The overall population split for radio detection and colour is shown in Table 4.1.

4.3 Results

4.3.1 Populations in C iv Space

To understand the behaviour of different populations on their own with respect to C IV emission, we investigate the distribution of different populations of quasars in

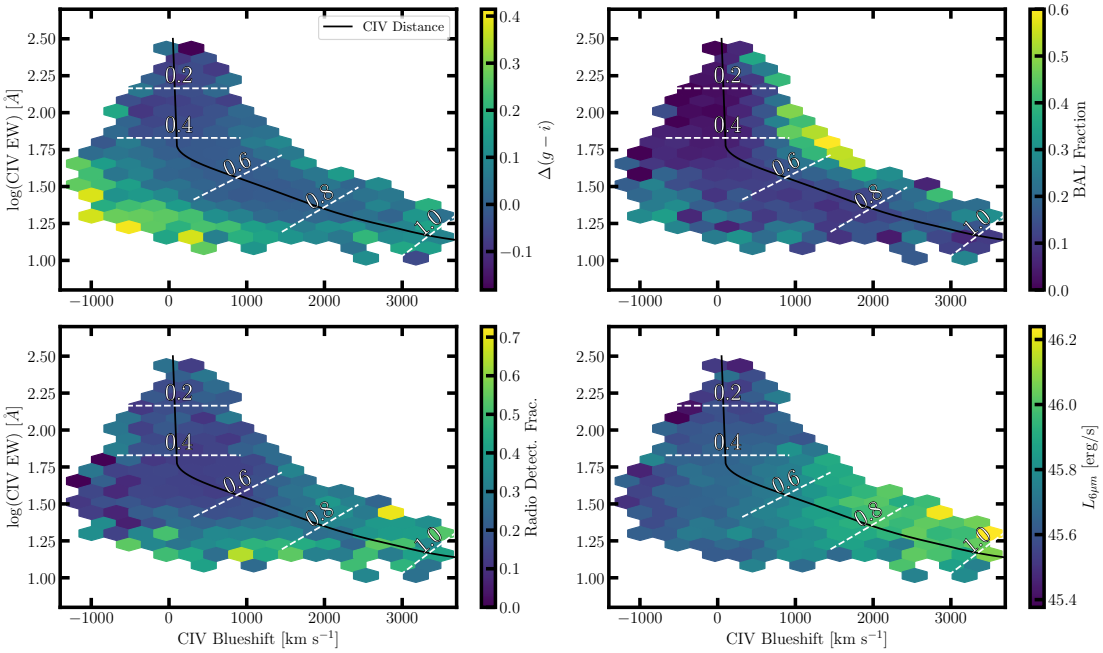

Figure 4.2: Density plots for different populations in the C IV EW and blueshift space. The white tracks indicate the value of the C IV distance at that point. A negative value for C IV blueshift indicates redshift. In each plot, we require a minimum of 10 sources in each bin. *Upper left:* The median value of $g-i$ colour in each bin. The distribution is relatively uniform apart from the most extreme red sources having low C IV blueshift and EW. *Upper right:* The fraction of BALQSOs in each bin. This distribution peaks at moderate C IV EW and higher blueshifts as previously shown in Rankine et al. (2020). *Lower left:* The LoTSS radio-detection fraction (RDF) in each bin. This fraction increases with C IV distance. *Lower right:* The median six-micron luminosity in each bin. This is a measure of the quasar luminosity which increases C IV distance.

the C IV EW and blueshift space.

We find that excess red quasars are mostly uniformly spread around the C IV space (upper left - Figure 4.2) apart from the most extreme red sources being at low C IV blueshift and C IV EW. This suggests that the C IV wind and the origin of the most red colours are not strongly coupled.

BALQSOs are preferentially found towards higher blueshifts and lower equivalent widths (upper right - Figure 4.2), although the densest BALQSO region in C IV space is at a moderate value for both. This result is not unexpected as the distribution of BALQSOs in C IV space was studied extensively in Rankine et al. (2020). As well as the BALQSO fraction they also look at the strength and velocity of the BALQSO winds and find that both increase at higher C IV distance. Even though the BAL

fraction change may not be large across the whole space, the average properties of the BAL winds do change quite significantly. There is also a tentative increase in BAL prevalence at low EW and blueshift, potentially connecting to the more red population.

The radio-detection fraction in C IV space was also studied in Rankine et al. (2021), but with the smaller LoTSS DR1. We find the same result here with a much larger sample (lower left - Figure 4.2). Radio-detection fraction increases with C IV distance.

We investigate an alternative measure of the accretion power of the black hole, the 6μm luminosity (lower right - Figure 4.2). This should probe the warm dust heated by the quasar and provide a measure of the overall AGN luminosity, $L_{\rm AGN}$ (Richards et al., 2006; Gallagher et al., 2007; Klindt et al., 2019; Calistro Rivera et al., 2021). We find that it correlates with the C IV distance quite well. If the black hole mass is constant along the space then it would track the accretion rate. In general, we favour the use of C IV distance as a measure of the accretion state as the line is driven closer to the black hole and is less contaminated by other infrared radiation.

4.3.2 Radio Properties and C iv Distance

We hypothesise that different processes dominate radio emission at different ends of the C IV distance space with low C IV distance objects having a greater jet component and high C IV distance having a greater wind component. We therefore split into C IV distance bins and measure the radio-detection fraction for different populations. The bins were selected to ensure a similar number in each bin in the moderate C IV distance range where most sources reside and to have reasonable statistics at the low and high C IV distance end. The populations within our chosen bins are listed in Table 4.2 along with the bin definitions.

In Figure 4.3 we show these radio-detection fractions. The error bars in these figures indicate the standard deviation within each bin. We find that all 3 of the parameters, C IV distance, colour and the presence of a BAL wind, have their own effects as expected but we also find different behaviour at each end of the C IV

Quasar Pop.	0<C IV Dist.<0.2			0.2<C IV Dist.<0.4		
	B	R	ER	B	R	ER
BALQSOs	26 / **6**	11 / **4**	7 / **6**	99 / **23**	210 / **72**	105 / **73**
Non-BALQSOs	242 / **45**	132 / **30**	39 / **20**	3028 / **397**	2166 / **470**	538 / **236**
	0.4<C IV Dist.<0.5			0.5<C IV Dist.<0.6		
	B	R	ER	B	R	ER
BALQSOs	149 / **16**	346 / **81**	227 / **79**	272 / **35**	835 / **201**	536 / **228**
Non-BALQSOs	3423 / **352**	3605 / **713**	880 / **317**	4612 / **475**	5183 / **1078**	1156 / **486**
	0.6<C IV Dist.<0.8			0.8<C IV Dist.<1		
	B	R	ER	B	R	ER
BALQSOs	190 / **64**	581 / **250**	417 / **268**	13 / **9**	45 / **55**	57 / **80**
Non-BALQSOs	3363 / **662**	4127 / **1342**	881 / **539**	235 / **115**	444 / **285**	157 / **129**

Table 4.2: We present the populations in each C IV distance bin for BALQSOs and non-BALQSOs. Radio non-detections are in normal font, radio detections are in bold and colour classifications are: B - blue, R - red, ER - excess red.

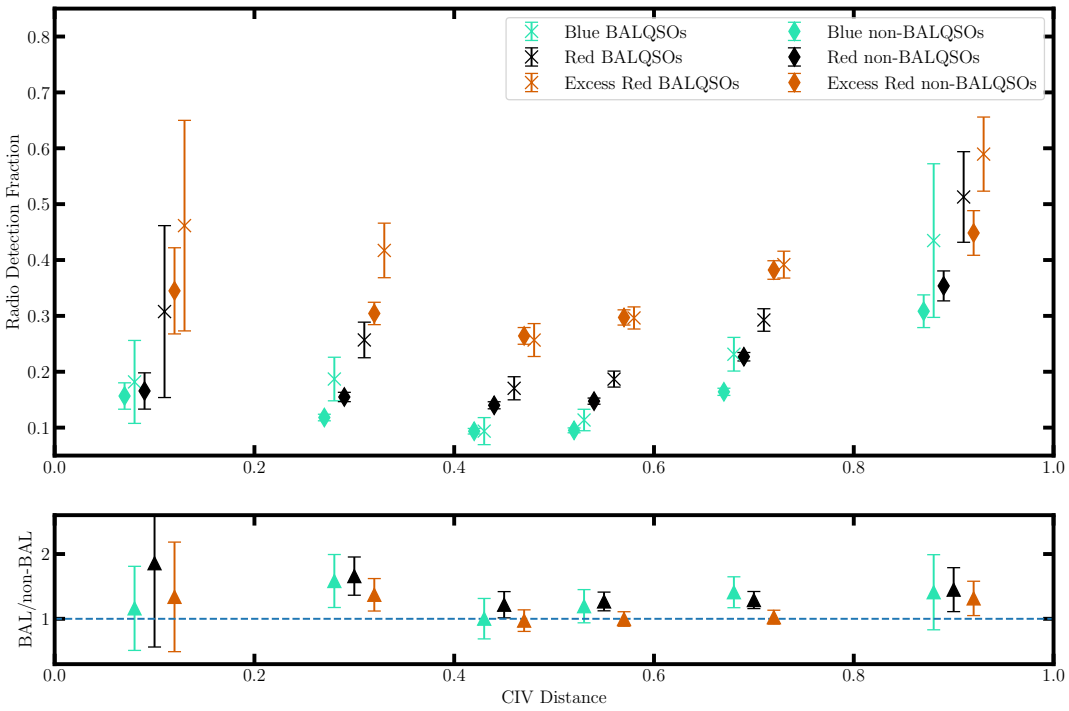

Figure 4.3: Radio-detection fraction for six C IV distance bins split into populations based on colour and whether a BAL wind is present. The spread around each C IV distance value is just to aid the eye. The colour represents the colour of the quasar: blue for blue, black for red and red for excess red quasars. Non-BALQSOs are represented by diamonds and BALQSOs are represented by crosses. In the lower panel, the ratio of radio-detection fraction for BALs and non-BALs is displayed as a clearer quantification of the BAL effect in each bin.

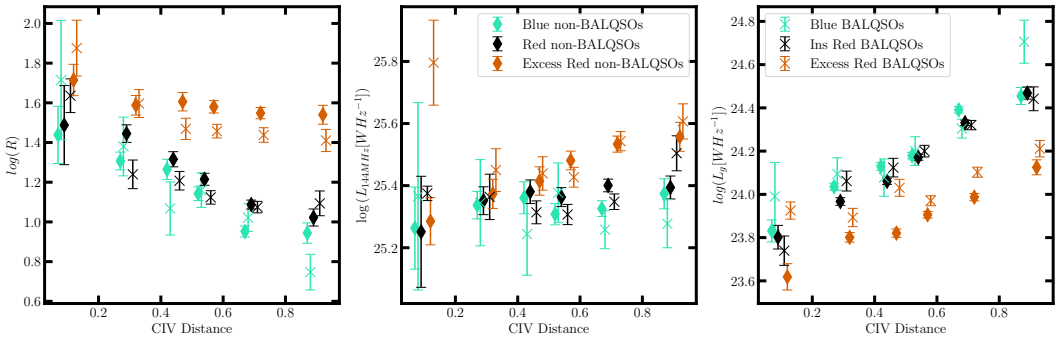

Figure 4.4: In all plots non-BALQSOs are represented with diamonds and BALQSOs are represented with crosses. *Left:* The radio loudness as a function of C IV distance shows a decrease for all populations. We suggest that the trend observed is largely due to the changing SED of the quasar as the accretion rate increases. The classical radio-loud threshold would be $\log(R) > 2.5$. *Centre:* The median radio luminosity as a function of C IV distance, assuming a spectral index of $\alpha = -0.7$, of different quasar populations in C IV distance bins. We find that radio luminosity remains constant at moderate C IV distance which accounts for the majority of most quasars. We only see a definitive increase in the highest bin at the highest accretion rates. *Right:* g-band optical luminosity as a function of C IV distance for radio-detected quasars. The optical luminosity is increasing, driving down the radio-loudness suggesting that radio-loudness is not a useful measure in determining radio-emission mechanisms without controlling for accretion rate.

emission space. Radio detection fraction increases from blue to excess red quasars. The change in radio-detection fraction from blue to red is of a similar magnitude, around 5%, to that of the change from red to excess red quasars. This is consistent with the recent work of Fawcett et al. (2023) which analysed the connection between dust extinction and radio emission using quasars identified with the Dark Energy Spectroscopic Instrument (DESI Collaboration et al., 2016) and LoTSS, finding a strong positive correlation between the two properties.

Overall the radio detection fractions decrease with C IV distance to 0.5 and then increase with increasing C IV distances, with the largest change, both in overall percentage and percentage per unit C IV distance (the gradient), coming between the two highest bins. This behaviour is similar for all populations, suggesting that different accretion properties are not the driving force behind the radio differences between BALQSOs and non-BALQSOs or behind reddening in quasars.

In Figure 4.4 we also look at the median radio luminosity, median g-band optical luminosity and the radio loudness parameter (the ratio of radio to optical luminosity)

as a function of C IV distance for sources that are radio detected in the same bins as Figure 4.3 and for the same populations. We find again that the largest changes for the whole population of quasars occur at the low and high C IV distance extremes although it should be noted that the uncertainty is much more considerable at low C IV distance.

Firstly, it should be noted that the overall range in median radio luminosity for the whole sample is less than one dex. The radio luminosity results generally indicate that, when detected, BALQSOs have similar radio luminosities compared to non-BALQSOs despite their higher radio detection fractions. For non-BALQSOs, the increase in radio luminosity from blue to red and from red to excess red quasars is similar and only ~ 0.05 dex.

The radio loudness parameter is typically used to identify excess radio emission in sources relative to their optical emission. In quasars, the optical luminosity is thought to be a good measure of the power of the quasar since it is assumed we are obtaining a largely unobscured view of the accretion disk. In Figure 4.4 we use the g-band luminosity to calculate the radio-optical radio-loudness. The classical divide from radio-quiet to radio-loud populations would occur at $\log(R) > 2.5$ at the LoTSS 144MHz frequency. Clearly, our sample is dominated by radio-quiet sources.

We observe a decrease in the radio loudness parameter as C IV distance increases. This was similarly observed when only looking at C IV blueshift in Rankine et al. (2021). However, we show that this change in radio loudness is largely driven by an increase in the g-band optical luminosity. The radio luminosity for all populations across C IV distance changes by less than 1 dex. Therefore it is the increase in optical luminosity with C IV distance that is driving this behaviour. This shows some of the limits of radio-loudness as an idealistic measure of "jettedness" as two sources with similar radio power, accretion rate and radio emission mechanism can have different radio-loudness measures based on different optical continuum spectral slopes (Balokovic et al., 2012).

4.4 Discussion

We consider the following different interpretations of these results with regard to the main potential radio emission mechanisms in radio-quiet quasars: star formation, jets and wind shocks. We provide a brief introduction to each mechanism here but for a detailed review see Kimball et al. (2011); Panessa et al. (2019).

Synchrotron emission from star-forming regions occurs due to the presence of free electrons and magnetic fields in supernova remnants. The radio flux from star-forming galaxies has been found to correlate extremely well with the far infrared emission, a presumed indicator of the star formation rate (Sopp et al., 1991; Appleton et al., 2004; Sargent et al., 2010; Calistro Rivera et al., 2017; Smith et al., 2021). This correlation has been shown to hold for low radio luminosity quasars to moderate redshifts (Bonzini et al., 2015; Gürkan et al., 2018). However, many studies find radio-quiet AGN with a compact core that lies on this correlation (Maini et al., 2016; Herrera Ruiz et al., 2016; McCaffrey et al., 2022), suggesting an AGN origin for at least some of the radio-quiet emission. A multi-resolution radio study of sources can allow for a better characterisation of star formation and AGN components (Morabito et al., 2022a).

Radio jets dominate the radio-loud population, but whether their contribution extends to many of the radio-quiet sources is a topic of much research. It is possible to model the radio emission and attempt to split contributions from star formation and AGN components (Mancuso et al., 2017). Specifically for LOFAR, Macfarlane et al. (2021) fit a two-component, star formation and jets, model to the radio-quiet LoTSS population. They find that jets could contribute the majority of radio emission in 10-20% of all quasars across redshift and optical luminosity. Yue et al. (submitted) extend this analysis through a Bayesian framework and apply their models to quasar reddening, showing that the radio enhancement of reddened quasars is due to the AGN component and not star formation. This is also shown by Fawcett et al. (2020) and Rosario et al. (2020) for radio-faint quasars. High-resolution studies of radio-quiet quasars have uncovered systems with compact core regions implying the presence of small-scale jets (Kukula et al., 1998; Leipski et al., 2006; Herrera Ruiz et al., 2016; Jarvis et al., 2019).

AGN outflows have been observed at many different scales and in different phases. When a wind interacts with the intragalactic medium, if it has sufficient velocity it will generate a shock. These shocks can generate relativistic electrons and corresponding synchrotron emission. If the wind is generated from the accretion disk, then we expect an anti-correlation between the jet and wind prevalence since jets are typically formed at lower accretion rates when the disk truncates at a greater distance from the black hole and can generate larger magnetic fields. This is indeed observed in Mehdipour & Costantini (2019) who found an inverse correlation between radio loudness and the column density of the ionising wind in radio-loud AGN.

With this wind-jet inverse correlation in mind, the hypothesis for radio emission mechanisms across C IV distance space is that jets dominate the radio emission at low C IV distance (low Eddington ratio) and that winds contribute more and more as the C IV distance increases (higher Eddington ratios).

4.4.1 Does radio emission in radio-quiet quasars connect to accretion?

From Figure 4.3 we observe all populations to increase in radio-detection fraction with increasing C IV distance above a C IV distance of 0.5 and decreasing with increasing C IV distance below that point. Therefore, it is clear that in some way radio detection fraction across the whole quasar radio-quiet population responds to the accretion properties of the quasar. Even though the changes may not be consistent for each group at all points in C IV distance, the fact that they all do couple to accretion is illuminating. For example, if one is to assume that star formation is the dominant factor in the radio-emission of radio-quiet quasars, then an increase in radio-detection fraction for quasars with potentially high accretion rates implies that the same gas is fuelling both star formation and accretion or that a significant positive feedback effect can occur on the timescale at which a quasar exists with a high C IV distance.

In general, the radio luminosity changes are minimal across moderate C IV distance from 0.3-0.6. This is the region in which the system is neither jet nor wind-

dominated. Richards et al. (2021) also found this was the region of lowest radio detection fraction for VLA quasars. Since we are tracing the behaviour of radio detection fraction with a proxy for accretion rate, could this be the area where AGN contributions are minimal and the radio emission is dominated by star formation? Under that assumption, we would conclude that BALQSOs and red/excess red quasars in this range have higher star formation rates (SFRs) than blue non-BALQSOs. The SFR-radio luminosity correlation for LOFAR is studied in Smith et al. (2021) and is roughly linear in the radio luminosity region our sample covers. The fact that when they are radio-detected, BALQSOs and red/excess red quasars do not have significantly different radio luminosities to the rest of the population at moderate C IV distances, Figure 4.4, suggests that SFR alone cannot explain the increase for both BALQSOs and red/excess red quasars.

Increased SFRs for red quasars and BALQSOs is a key prediction of the hypothesis that both these populations are linked to earlier stages in the evolution of galaxies than typical quasars if the timescale of the red phase is long enough to observe a decrease in SFR. However, several studies have tried to test this connection and have not found any link between red quasars and enhanced SFRs (Fawcett et al., 2020; Calistro Rivera et al., 2021; Andonie et al., 2022). It could also be that star formation contributions are similar to AGN in this region (moderate C IV distance), emphasising differences in the connection between black holes and radio emission between the various populations. We hope to explore this further in the future through extensive SED fitting of sources in the LoTSS Deep-Fields (Tasse et al., 2020; Best et al., 2023).

It has been noted in previous work that the radio-detection fraction could have a significant correlation with the luminosity of the AGN itself. To investigate the effect that this has, previous red quasar studies have used a redshift and six-micron luminosity-matched sample to study the radio properties independently of the AGN luminosity (Klindt et al., 2019; Fawcett et al., 2020). When performing any luminosity matching we have to be cautious as we are explicitly looking to test correlations with the C IV distance which we are claiming is a proxy for the accretion rate and will therefore correlate strongly with the six-micron luminosity. Indeed it is clear from

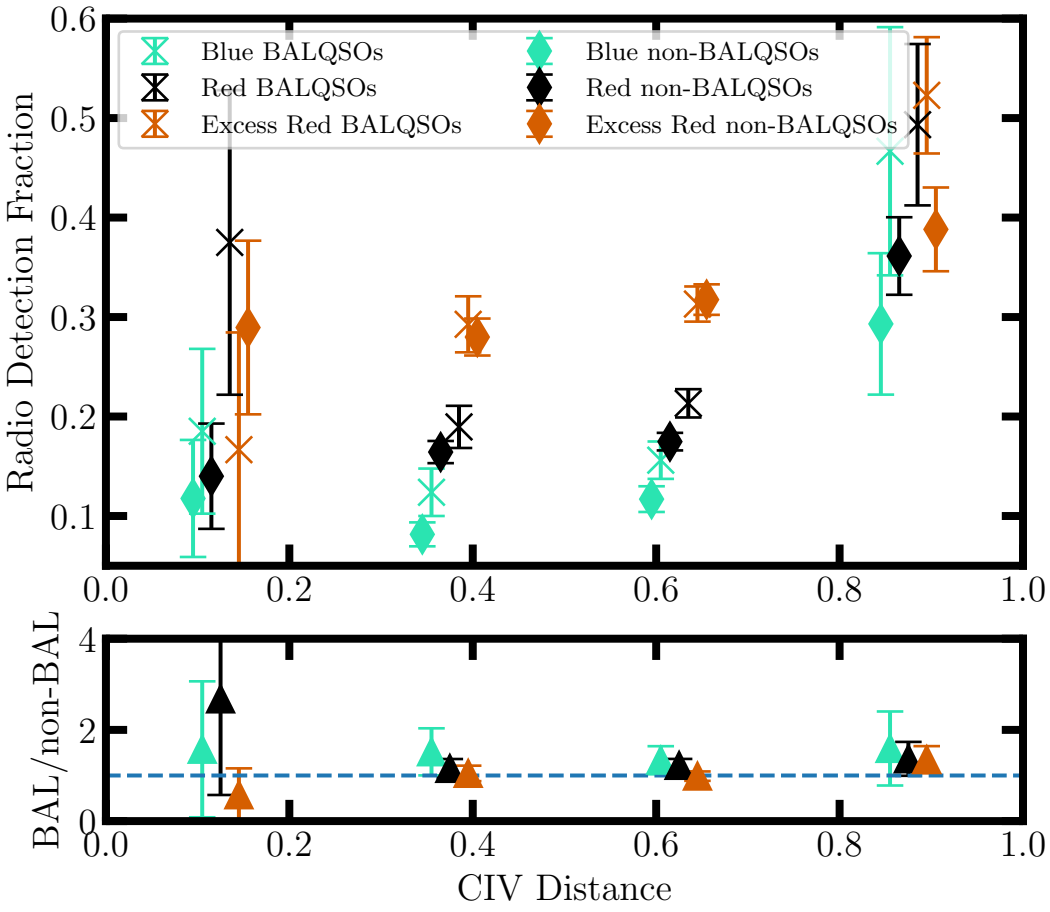

Figure 4.5: The radio detection fraction with C IV distance for samples matched in redshift and six-micron luminosity space. We use four bins of 0-0.25, 0.25-0.5, 0.5-0.75 and 0.75-1 in C IV distance. The radio enhancement of red quasars is still apparent and also the moderate enhancement of BALQSOs remains. The enhancement of low C IV distance samples appears to be somewhat diminished. Below is a panel displaying the ratio of radio detection fraction between BALs and non-BALs.

Figure 4.2 that this correlation does exist and trying to create a matched sample across six different populations (BALQSOs vs non-BALQSO × three colour bins) would remove a lot of sources and some of these trends we are interested in seeing.

We checked the luminosity and redshift distributions within each C IV distance bin of Figure 4.3 and did indeed find some differences between populations. We verify our key result by performing a 2d-rejection sampling method to match all populations to the redshift-six-micron distribution of the red quasars. We then repeat our previous analyses.

The results from the matched sample are presented in Figure 4.5 which is an

equivalent plot to Figure 4.3 but with fewer bins to maintain similar uncertainties. The same key features are present with this matching. The increase in radio-detection fraction from blue to excess red quasars and moderate enhancement of BALQSOs remains, demonstrating the robustness of our results to luminosity effects.

4.4.2 Are BALQSOs a distinct class of quasars?

Rankine et al. (2020) studied in detail the 2D C IV space properties of BALQSOs and non-BALQSOs and concluded that, since you can find a non-BALQSO with the same C IV position and SED hardness as any BALQSO, they must both originate from the same parent sample. Temple et al. (2021) found that the hot dust emission is also similar between BALQSOs and non-BALQSOs at the same C IV position. This supports a geometric interpretation for the BALQSO phenomena at a given position in C IV space. However, the recent radio studies of BALQSOs suggested that the more we explore the properties of BALQSOs at longer wavelengths the more they appear to differentiate themselves from non-BALQSOs. Morabito et al. (2019) highlighted the increasing radio-detection fraction with BI, well over 50% of quasars with the strongest winds being detected with LOFAR. In Petley et al. (2022) we showed further that this radio emission connects to the absorption profiles of the BALQSO and that this radio emission is extremely difficult to explain with an angular interpretation of BALQSOs with a standard equatorial wind. How then can we reconcile this apparent contrast between the UV and radio nature of BALQSOs?

In this work, we show that much of the BALQSO radio enhancement found in previous papers can be explained by their connection to optical colour. The enhancement is still present in the radio-detection fraction of BALQSOs compared to non-BALQSOs of the same colour classification and contributes around 5-10% in each bin. The effect is more easily seen as a ratio between BALQSO and non-BALQSO detection fraction in Figure 4.3. The median ratio across the bins is 1.29, 1.46 and 1.17 for blue, red and excess red quasars respectively. The ratios are a much smaller enhancement than that observed when not accounting for optical colour such as the detection fractions presented in Morabito et al. (2019) and Petley

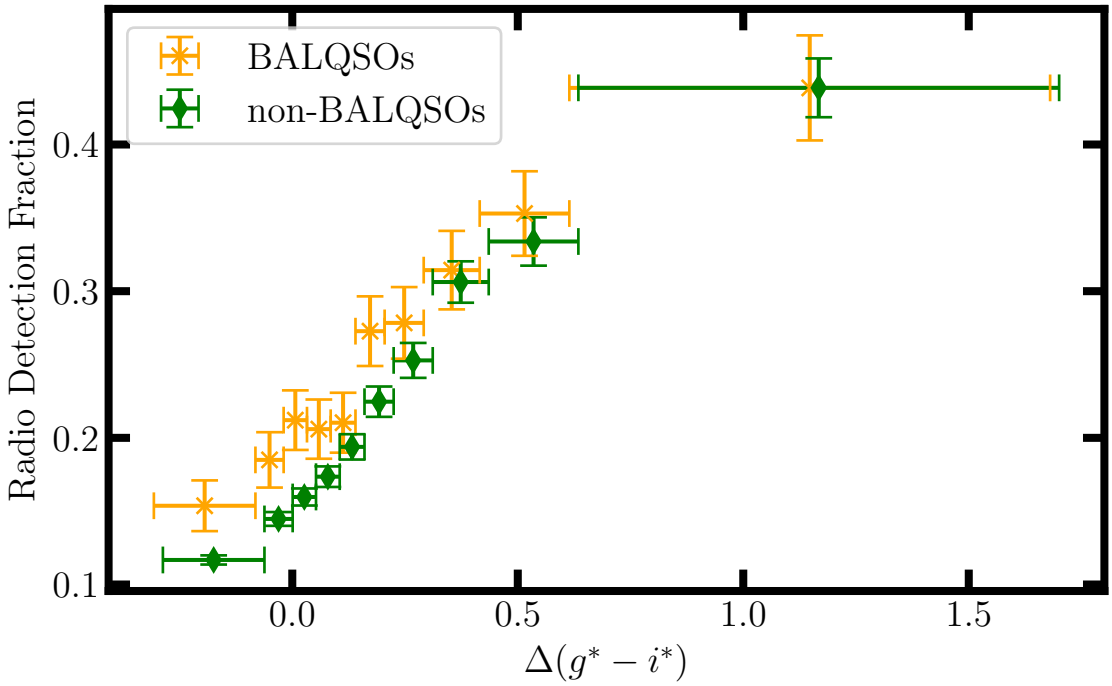

Figure 4.6: Radio-detection fraction against corrected colour for BALQSOs (orange) and non-BALQSOs (green). Each bin was defined by having an equal number of BALQSOs and the points are separated slightly horizontally to aid the eye. The BALQSO contribution to the radio-detection fraction is most prominent for bluer colours.

et al. (2022). The difference in these studies opens many further questions about the connection between these two samples as in the reddest colour bins the BALQSO fraction can be well over 25%. This feature has been observed in other samples such as in (Vejlgaard et al., 2024). They create a red quasar sample that would not be selected in SDSS and find that it does not have a higher radio-detection fraction than a comparative SDSS blue sample using FIRST. The red sample had a much higher BAL fraction than in SDSS and they suggest this may be the reason that they do not observe a radio difference. To test this we looked at the BALQSO and non-BALQSO radio-detection fraction relationship with colour alone.

In Figure 4.6 one can see that the BALQSO radio-detection contribution within SDSS occurs primarily within the normal distribution of quasar colours and not in the most excess red systems. This figure is somewhat similar to those found in Fawcett et al. (2023) and Calistro Rivera et al. (2023) but with a focus on the BALQSO effect as colour increases. We find a similar behaviour of increasing

detection-fraction with colour for both populations. We, therefore, conclude that the BALQSOs fraction is unlikely to be the origin of the difference in radio emission for red and blue populations of quasars as in (Vejlgaard et al., 2024). The differences could reside in the use of LoTSS which is deeper than FIRST and also the selection of the two samples. There are some non-optically spectroscopic surveys (WEAVE-LOFAR - radio-selected (Smith et al., 2016); 4G-PAQS - astrometrically-selected (Krogager et al., 2023)) upcoming which may provide samples with much higher BALQSO fractions than SDSS. These will allow us to study the BALQSO-radio connection in even greater detail.

If one considers the idea that increasing C IV distance relates to increasingly wind-dominated systems, one could interpret the radio-detection fraction of blue non-BALQSOs at a low or moderate C IV distance to be a measure of the fraction from the combined effect of small-scale jets and star formation. If we then make the assumption that the contribution to the radio from star formation and jets does not increase with C IV distance, then the increasing radio detection fraction with increasing C IV distance could be related to shocks. With regards to jets, the motivation that their contribution does not increase with C IV distance is supported by jets being largely stochastic sources and also radio loudness having an anti-correlation with accretion rate (Sikora et al., 2007). For star formation, our assumption that it has no correlation with C IV distance finds some support from Stanley et al. (2015) which found that the relationship between star formation rate and AGN luminosity was remarkably flat. They argue that the AGN luminosity varies much more rapidly than the star formation rate, washing out any underlying correlations. If a BALQSO wind is observed then it means conditions around the SMBH are suitable for the creation of the BALQSO wind. Are these conditions stable for a sufficient period of time for us to both observe the BAL wind and any resultant radio emission (see § 4.4.4)? Presumably, BALQSO winds transport gas and dust from a more central region out into the ISM adding another uncertain timescale to pair with any proposed connection between BALQSOs, reddening and radio emission.

In Choi et al. (2022a) a large sample of BALQSOs with lower ionisation and iron absorption troughs, FeLoBALs, was studied using the spectral analysis code

SimBAL (Leighly et al., 2018). This represents the most detailed analysis of the physics of BALQSO outflows although admittedly for a highly extreme sub-sample. They found that nearly 18% of the FeLoBALs contained multiple BAL components and that the objects with the highest kinetic energy fractions were found closer to the SMBH in the vicinity of the torus. Dust could have a key part to play in the expansion of a wind (Everett & Churchwell, 2010) and a recent study of the interaction between a torus-like dusty structure and quasar radiation found that dust is the key to generating high-velocity winds without over-ionising the gas (Soliman & Hopkins, 2023). This could be a key connection between BALQSOs and their increased fraction in reddened samples. Since BALQSOs likely require some amount of shielding, and LoBALs even more so, dust could be a key factor in launching the BALQSOs winds in the first place.

4.4.3 Importance of Colour

The fact that in Figure 4.3 and Figure 4.5 we see clear changes in the radio detection fraction even for the red population, suggests that colour, which is likely connected to dust, couples very strongly to radio emission. Klindt et al. (2019) showed the radio-detection fraction for SDSS quasars as a function of $g-i$ colour for different redshift cuts. They found the 1.4GHz FIRST detection fraction increases steeply around the 80th percentile. We use a different definition for our red quasar population in this study, which means our red quasars are not as red as in that study, but we do find that even the quasars with these intermediate colours have a clear increase in radio-detection fraction. FIRST is a less sensitive survey than LoTSS and operates at a higher frequency. This makes it harder to observe detection fraction differences between blue and moderately reddened systems since FIRST observes a greater radio-loud fraction thereby potentially missing lower luminosity emission.

To make use of the high number of sources at moderate C IV distance and the fact that we resolve the colour distribution with SDSS photometry, we look again at the radio-detection fraction of quasars but with a focus on the colour in Figure 4.7. This is similar to Figure 4.3 but this time we take the excess red population of quasars and split it into two colour bins of equal number and then for the rest

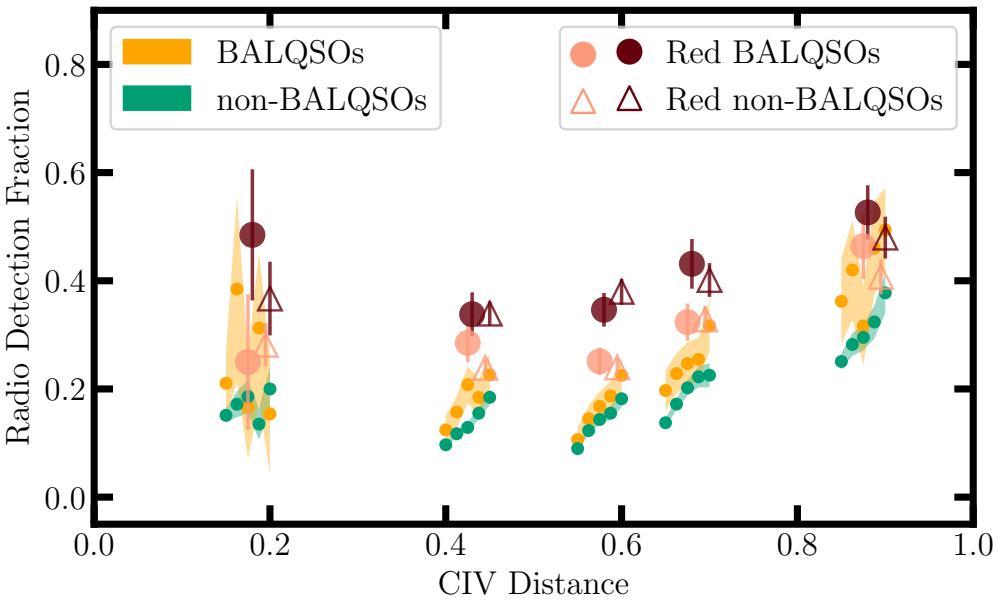

Figure 4.7: Radio-detection fraction for a smaller number of C IV distance bins with different colour splits for blue/red quasars and excess red quasars. We use 5 colour bins with an equal number of quasars in each bin for the blue and red groups. From left to right within each shaded region at each C IV bin the colour is increasing. The BALQSOs are in orange and the quasars are in green with the shaded region representing 1σ uncertainties. We use 2 equal number bins for the excess red quasars with circles indicating BALQSOs and triangles for quasars. The darker shade is the most reddened bin. Colour increases enhance the radio detection fraction even at the blue end and the difference between BALQSOs and red quasars is minimal in the most red colour bins.

of the population, the "blue" and "red" quasars within the normal distribution of Figure 4.1, we split into five colour bins of equal number. We use fewer C IV distance bins to keep the uncertainties lower and focus on the central region which contains the vast majority of quasars.

The reddened quasars show an enhanced radio-detection fraction at all C IV distances. This is also seen when comparing blue to red BALQSOs. Hence, dust content could be important for radio emission even when a system is not overwhelmingly disk-dominated and producing high C IV blueshifts. In fact, the change in the ratio between the red quasar detection fraction and the blue quasar detection fraction is relatively constant across C IV distance. One hypothesis for red quasars is that they exist as a brief intermediate phase between a dusty star-forming source and a blue

quasar (Sanders et al., 1988; Hopkins et al., 2008). It has recently been shown that the more extreme counterparts of red quasars, known as obscured quasars, have potentially 3 times the star formation rate at the same mass as unobscured quasars and also enhanced radio emission (Andonie et al., 2022). However, the work of Rosario et al. (2021) showed that the physical scale on which the majority of the radio enhancement of red quasars exists is on a scale <= 2 kpc implying an AGN origin for a significant fraction of the radio emission in red quasars. An alternative explanation could be that the radio emission comes from circumnuclear star formation rates are increased and that as the C IV distance increases we are heightening the effect of positive feedback from the winds that trigger nuclear starbursts (Silk, 2003). But, as discussed in § 4.4.1, this appears to be unlikely, at least for the non-BALQSO colour connection to radio emission.

4.4.4 Timescale Issues

One aspect of radio emission that we have not discussed to this point is the timescale over which radio-emitting sources need to be powered to reach luminosities that we can observe. Radio jets originating from the SMBH typically reach peak luminosities around 10-100Myrs after they are first powered (Hardcastle, 2018). If the power stops then the synchrotron luminosity is expected to decrease rapidly. In the models of Hardcastle (2018) the luminosity drops around 3 orders of magnitude in around 10Myrs after the jet stops being powered (see Figure 6 of that paper). The light travel time for a jet of size 100kpc is 326,000 years which is much lower than this decrease. Since these are radio-quiet AGN and are largely unresolved at 6 arcseconds, we know that they cannot have powerful jets that have been active for 100s of Myrs.

The lifetime of BAL winds themselves is also largely uncertain. The most recent estimates are that BAL troughs exist for around 100 years but that a BAL phase lifetime is much harder to estimate as BAL troughs could also appear during that time frame (De Cicco et al., 2018; Mishra et al., 2021). This variability is generally thought to arise due to changes in the gas shielding the BAL from the quasar and hence changing the ionising flux incident upon the wind. The scale on which the

overall BAL wind varies or whether winds are always present and just the ionisation state changes is uncertain.

The timescale over which a wind shock can generate significant luminosity is expected to be much shorter than the time scale of a radio jet. Supernova shocks create radio emission and this has been observed and modelled for decades. Typically supernova shock radio emission quickly reaches a peak ($\sim$0.1 years) before decaying more slowly (Chevalier et al., 1982; Weiler et al., 1986). Presumably this time is much longer due to the larger size of an AGN outflow but perhaps this is a way to constrain the connection between a BALQSO lifetime and its radio emission. If we can definitively show that the radio emission is triggered by the BALQSO wind itself then this would allow us to connect the lifetime of the BALQSO to the lifetime of the radio emission by looking at the ratio of radio-detected and non-detected BALQSOs. The radio-detection fraction for a population is modulated by the overlap in the lifetime of that population and the lifetime at which the radio emission is luminous enough to be detected. The likely short lifetime of a BALQSO compared to a quasar in general therefore also implies that the radio emission exists over a similarly short timescale so that the difference in radio detection fraction between BALQSOs and non-BALQSOs can be observed.

4.4.5 Testing a wind shock emission model

Nims et al. (2015) provide a model for wind shocks from AGN winds and has been widely cited in the field. The model makes some simple assumptions for an energy-conserving wind. They first show that for a wind travelling at 10% the speed of light through a typical ambient medium over a quasar lifetime, the wind can achieve > 1 kpc scales. They then analyse both the thermal and non-thermal emission processes that would be associated. Important to low-frequency radio observations is the synchrotron emission for which a formula is provided in Equation 32 of Nims et al. (2015):

$$\nu L_\nu = 10^{-5} \xi_{-2} L_{\rm AGN} \left(\frac{L_{kin}}{0.05 L_{\rm AGN}} \right)$$

Here the ξ_{-2} parameter represents the percentage of the shock kinetic energy which is converted into relativistic electrons (i.e. if we assume 5% of the energy goes into relativistic electrons, $\xi_{-2} = 5$).

We attempt to test whether this model can account for all of the observed emission given the large number of quasars we have that are both radio-detected and have an estimate for their overall luminosity. We are also claiming that the C IV distance traces the influence of winds, hence we can test whether the wind-dominated systems adhere to the Nims et al. (2015) model more than the whole quasar population.

To construct the predicted wind shock radio-luminosity at 144MHz from the Nims et al. (2015) model we need to obtain the overall AGN luminosity, $L_{\rm AGN}$, and then pick appropriate values for the fraction of AGN energy in the wind and the fraction of wind energy that goes into relativistic electrons, ξ_{-2}. To obtain AGN luminosities we convert our interpolated six-micron luminosities from WISE and use the bolometric corrections from Richards et al. (2006). We apply the same correction to all quasars, $L_{\rm AGN} = 8 \times L_{6\mu m}$, and then assume that $L_{kin} = 0.05 L_{\rm AGN}$.

We compute models for the expected wind shock radio luminosities at 144MHz for all of our quasars with a C IV distance above 0.25, which should increase the prevalence of winds compared to jets. We create three models for the wind shock luminosity as follows:

1. Fixed conversion rate to relativistic electrons of $\xi_{-2} = 5$

2. Varying the conversion rate ξ_{-2} to minimise the Kolmogorov-Smirnov (K-S) test statistic between the observed radio luminosities and the model

3. Giving the conversion rate a linear dependence on the AGN luminosity such that $\xi_{-2} = \frac{L_{\rm AGN}\alpha}{\max(L_{\rm AGN})}$ and fitting for α to minimise the K-S test statistic

The results of these different models along with the observed radio flux distribution are shown in Figure 4.8. We find that a similar assumption to the AGN to kinetic luminosity conversion of 5%, model (i), largely over-predicts the observed flux for our quasar sample. The value for this conversion factor that minimises the difference between the observed and model distributions is a more modest 1.36%,

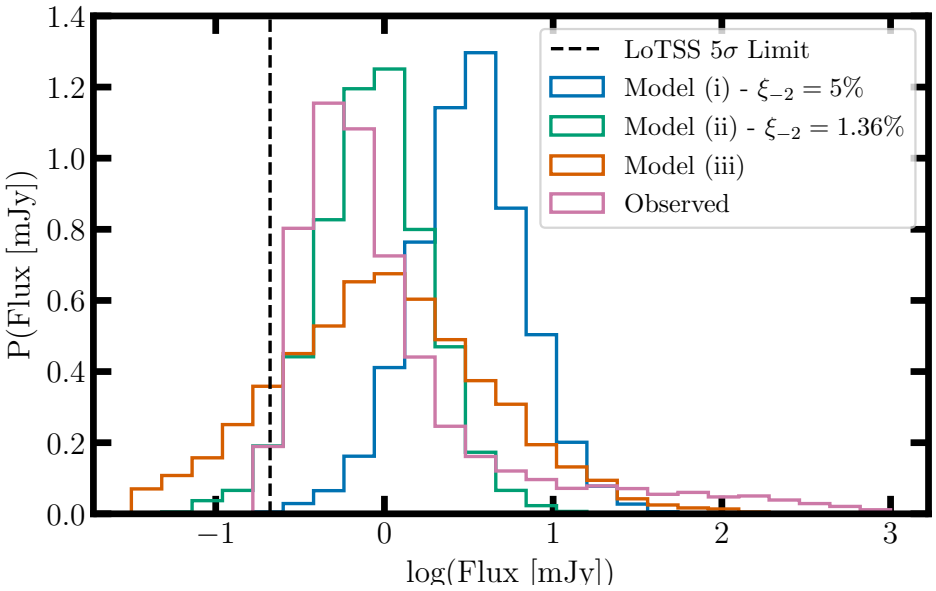

Figure 4.8: Three models of the wind shock radio flux as predicted by the prescription of Nims et al. (2015) using the AGN luminosity of radio-detected quasars. The observed radio flux is shown in pink, a constant 5% of shock energy in relativistic electrons in blue, model (i), a best fit constant conversion of 1.36% in green, model (ii), and a best fit functional form with a linear dependence on the AGN luminosity in red, model (iii).

model (ii). The fit here is quite good, especially between the LoTSS flux limit and 10mJy. The fact that the shape is similar is not so surprising since the six-micron luminosity is roughly normal distribution and we are mostly shifting this distribution with some dependence on the redshift to obtain the fluxes.

These models perform poorly for higher flux sources, which are a small fraction of the overall population, which suggests that wind shocks cannot explain all of the sources. These higher flux sources form a tail with the majority of sources fitting occupying a roughly Gaussian distribution centred just below 1 mJy. We interpret the high tail as a population of jetted sources which follow a different distribution to the sources which could be attributed to wind shocks. We introduced the third model, model (iii), as a way to potentially allow for these higher flux sources. This model includes a linear dependence of the efficiency on the AGN luminosity. Physically this would mean that higher luminosity AGN can convert more of their outflow energy to relativistic electrons. We do not have a specific assumption for how this would work but one example could be that a more powerful AGN creates a wider covering angle for outflows which allows for a larger shock front and more relativistic electrons. This model allows for the distribution to spread out in both directions. We do not recover the correct shape for the distribution and still cannot obtain the highest flux sources with just a linear connection between AGN luminosity and efficiency. Presumably, jets also contribute in some fraction of the sources so including some model for the jet flux could be an alternative way to fit the higher flux sources.

4.5 Conclusions

We have studied a sample of SDSS quasars within the LoTSS footprint. We have cut to a redshift range of $1.7 < z < 2.5$ to allow for BALQSO and quasar colour classification. We use spectral reconstructions as described in Rankine et al. (2020) to de-noise the spectra, improve the redshift estimates and characterise the C IV emission more accurately. We look at trends for different quasar populations as a function of their C IV distance, a tracer of the accretion rate. We focus on the radio

properties of these sources as the origin of radio emission for most quasars is an open question.

Our main findings are:

1. Radio-detection fraction has a strong correlation with C IV distance for all populations. Radio-detection fraction decreases with increasing C IV distance up to 0.5 and then begins to increase. In the lowest C IV distance bin the difference in radio properties for all groups narrows but this is also where we have the most uncertainty due to lack of sources. This narrowing could potentially be linked to the work of Temple et al. (2023) where trends with accretion rate and black hole mass become apparent above some threshold;

2. Radio luminosity does not change significantly with increasing C IV distance while the radio-loudness of the populations decreases with increasing C IV distance. This shows that g-band luminosity is increasing due to the changing shape of the SED of quasars across the C IV distance space. This is further evidence that radio-loudness is not a suitable parameter to split radio populations without controlling for at least the accretion rate.

3. The colour of quasars is linked to their radio-detection fraction independent of C IV distance and whether a BAL wind is present. The most reddened quasars have slightly higher radio luminosities than blue quasars when detected. The difference between moderately reddened and the most reddened quasars is less significant for BALQSOs;

4. BALQSOs have a marginally higher radio-detection fraction than non-BALQSOs but overall the difference in detection fraction between these two populations is largely explained by their colour. This is further evidence that the BAL wind itself is connected to dust;

5. The Nims et al. (2015) wind shock model works well in modelling the observed radio-flux for radio-detected quasars. This is mainly just an appropriate scaling of the distribution of AGN luminosities, but the best fit relativistic electron

coupling of 1.36% is quite modest, giving wind shocks the potential to account for the radio emission of many sources;

Are BALQSOs and red quasars distinct from the general population when it comes to their accretion and radio properties? For BALQSOs, their radio properties appear to be largely explained by their relation to optical colour. Although they have a preference for a particular region of the C IV space, it is still true that BALQSOs exist with a wide range of C IV EWs and blueshifts. It therefore appears that some combination of accretion rate, dust and orientation with respect to the observer is the origin of BALQSO winds. Red quasars have a similar connection between radio-detection fraction and accretion as blue quasars but then show different radio properties compared to the BALQSOs/non-BALQSOs. Their radio-detection enhancement is observable across C IV space while detection fraction differences between red non-BALQSOs and red BALQSOs are narrower, indicating that the emission mechanism linked to colour could dominate over the BALQSO contribution.

Two key steps are needed to advance the studies of these populations with respect to their radio emission; one is observational and the other is theoretical. First, we need a statistically significant population of these populations to be studied at sub-galaxy scale resolution in the radio across the C IV distance/accretion rate and optical colour space. This population will allow us to separate star formation and AGN components of the radio emission and then isolate the behaviour of the AGN component with an accretion state. Therefore, we should be able to distinguish between jets and wind shocks, a current limitation of our work. Secondly, we need more detailed theory and/or simulations of the behaviour and radiative transfer of wind shocks, which currently has the freedom to fit the entire population with the right energetic scaling, and the interaction of both wind shocks and jets with dust. Timescales are still a great uncertainty in this field and new simulations could be vital in constraining likely timescales for the presence of a BAL wind and the overlap with the radio emission it may be linked to or produce itself.

Vocals spill over like the rolling hills of Dover
Or the Gulf Oil Disaster if preferred you're after
Depends on your status or your stature
Whether you benefit from the prior or the latter-er
Get the fatter check split
And how much for a hundred-thousand tons of Corexit?

Guv'nor - MF Doom

5

High resolution study of the LoBAL-HiBAL radio connection

In this chapter, I present research on a sample of HiBALs and LoBALs matched in their AGN luminosity and wind strength. We observe with the high-resolution interferometer eMERLIN in search of morphological and spectral index differences. These targets also have good international LOFAR coverage which provides a long-term goal of sub-arcsecond resolution images of the sample with an order of magnitude difference in observing frequency. There will be future work to post-process all these targets to inspect low-frequency morphology and produce spectral index maps of any detected components.

5.1 Introduction

It is now understood that supermassive black holes (SMBHs) are intimately connected to the host galaxies in which they reside (Ferrarese et al., 2000; Kormendy et al., 2013; Bower et al., 2006; Croton et al., 2006), despite the gravitational force of the black hole being negligible for the vast majority of stars and gas within each galaxy. Black holes can instead convert potential energy from their enormous gravitational wells into radiation and kinetic energy. The most apparent to our telescopes is emission across a wide range of frequencies associated with accretion onto the black hole. We refer to sources that show such signatures as Active Galactic Nuclei (AGN).

AGN exhibit a range of phenomena generally referred to as *"outflows" or "winds"* in which gas can be observed in various phases moving outwards from the central region of the galaxy. These range from X-ray observed "Ultra-Fast Outflows" (Pounds et al., 2003a) through to molecular gas outflows observed with millimetre wave interferometers (e.g. Cicone et al., 2014). Sources that display these phenomena are often suggested to be examples of AGN feedback in action. However, as noted in the recent review of Harrison & Ramos Almeida (2024) the presence of these phenomena alone is several steps away from understanding whether they observably impact the course of a galaxy's evolution.

The first clear indicator of gas outflows in AGN came in the form of Broad Absorption Line Quasars (BALQSOs) first review in Weymann et al. (1981). These sources display blueshifted, broad absorption associated with species seen in optical/UV spectra, most distinctly bluewards of the C IV and Si IV emission lines. The clear interpretation of these features is that of gas moving towards our line of sight intercepting the ionising continuum of the quasar accretion disk. These outflows can have speeds of $\sim 0.1c$ but more recent studies have even found analogous sources with velocities $\geq 0.2c$ (Extreme High-Velocity Outlows - Rodríguez Hidalgo et al., 2020).

BALQSOs themselves have been split into a few sub-classes based on the presence of additional absorption features from species which are more easily ionised than C IV and Si IV. The more common sources with absorption from high ioni-

sation species, most commonly C IV and Si IV features, are termed High Ionisation Broad Absorption Line Quasars (HiBALs) while quasars with HiBAL features and additional low-ionisation absorption profiles, most typically at Mg II and Al III, are referred to as Low Ionisation Broad Absorption Line Quasars (LoBALs). A further extreme class can show absorption at several iron (Fe) emission lines as well as the previous features and are referred to as FeLoBALs. Whether these classes originate in physically distinct objects or a product of different viewing angles is a key focus of this work.

BALQSOs are a large subset of the overall quasar population, accounting for $\sim 10\%$ of quasars in wide-area optically selected surveys (Trump et al., 2006; Gibson et al., 2009). As noted in Filbert et al. (2023), BALQSOs can be a troublesome population as typical quasar fitting tools can struggle to obtain accurate redshifts for BALQSOs which can impact the often cosmological aims of these surveys. In addition, the definition of a BALQSO is somewhat unclear and varies between a qualitative (e.g. Shen et al., 2011) and quantitative (eg. BI + AI Weymann et al., 1981; Trump et al., 2006) approach in different work. This is a key issue, as an important area of research for BALQSOs is their covering fraction. That is the fraction of viewing angles in which a BALQSO wind can be observed.

The covering fraction of BALQSOs has a direct impact on their phenomenological interpretation and their candidacy as examples of AGN feedback in action. The covering fraction of a BAL wind and the fraction of quasars that are BALQSOs are only the same if all quasars possess a BAL wind. If this is not the case, and BALQSOs are short-lived or occupy a special phase in the quasar lifetime, then the covering fraction will be larger than the observed fraction. Therefore measuring the covering fraction of BALQSOs provides us with a way of testing whether their geometry is consistent with their section of the quasar population.

BALQSOs are likely launched in the vicinity of the torus (Choi et al., 2022a,b) or are a lower-velocity larger-radius phase of the Ultra Fast Outflows that are thought to be launched from the accretion disc (Chartas et al., 2002; Pounds et al., 2003a). Either way, we expect these winds to occupy some fraction of a solid angle, rather than being spherical in structure. Curiously, Bischetti et al. (2023) recently found

evidence for an increased fraction of BALQSOs at $z > 4$ without finding as much evolution in bolometric luminosity or Eddington ratio.

There have been suggestions that in an evolutionary scheme, LoBALs would occupy the earliest phase of a BALQSO. One avenue of exploration has been to test whether LoBALs have increased star formation rates (SFRs) as compared to HiBALs. Wethers et al. (2020) found that the SFRs of LoBALs were much higher than HiBALs and non-BALQSOs for a sample of IR-selected quasars which received near-IR spectroscopic follow-up. (Chen et al., 2021) studies the ratio between emission lines that ideally trace SFR and AGN contribution and also found that LoBALs showed signs of increased SFRs compared to HiBALs with non-BALQSOs in between the two. However, other studies argue against evolutionary unification since LoBAL wind features can be produced in radiative transfer models of winds which appear as HiBALs at other angles (Matthews et al., 2016) and that LoBALs have similar accretion rates and black hole masses compared to non-BALQOs (Schulze et al., 2017).

Radio observations of quasars are the perfect tool for testing unification theories, since at these wavelengths, emission travels from its source to our antennas without any further obscuration. Therefore if one defines precisely the way in which two populations should be unified (i.e. control for all factors other than this difference) then the radio properties between these two groups should be identical. If one finds a difference then the proposed unification picture cannot hold and is missing additional components that must be made consistent.

When differences in radio properties are found between quasar populations it can often be hard to extract the physical explanation for the differences. Modern, large-area radio sky surveys only resolve a small fraction of sources and additionally, as we push to fainter sources, we are definitively in the radio-quiet regime where the physical origin of the radio emission is uncertain. As the review of Panessa et al. (2019) highlights, in this faint radio population several emission mechanisms have the potential to create detectable radio flux density. For the quasars studied in this work, three viable mechanisms emerge. Firstly, radio flux density has long been known to correlate with star formation rate (SFR), or more precisely the far infrared

which is thought to be dominated by reprocessed stellar emission (Helou et al., 1985; Bell, 2003). These correlations have been calibrated at several frequencies, including low-frequency (Calistro Rivera et al., 2017), but are likely not directly applicable to luminous AGN sources.

AGN can power large-scale jets which can extend well beyond the scale of the host galaxy (e.g. Fanaroff & Riley (1974) type sources). However, jets have now been observed in faint and compact sources when moving to higher resolution (e.g. Kukula et al., 1998; Jarvis et al., 2019) and models suggest that jets should be present in sources down to the lowest luminosities (Hardcastle, 2018; Hardcastle et al., 2019). Modelling the entire radio population through a two-component model including star formation and jets has proven successful with LoTSS (Macfarlane et al., 2021; Yue et al., 2024) showing that a significant fraction of all radio sources, including classically radio-quiet sources, are dominated by radio jets. Finally, in a scenario analogous to stellar wind shocks (e.g. Thompson et al., 2006), it has been proposed that shocked regions produced by AGN outflows, such as BALQSOs or UFOs, could produce detectable radio emission in radio-quiet sources. Several simple models have been developed to estimate the properties of this radio emission (Faucher-Giguère et al., 2012; Nims et al., 2015). Most recently Yamada et al. (2024) studied a sample of UFO sources and found that, after developing the radio-emission model further, 11/15 of their sources could be explained by wind-shock emission.

Even very early in the literature on BALQSOs, their radio properties were being discussed as different compared to the general quasar population (Weymann et al., 1981). The key firmly established about the BALQSOs and radio-emission is that they are less likely to host large-scale radio-loud jets (Stocke et al., 1992; Becker et al., 1995). However, with the advent of the current generation of radio telescopes, recent studies have been able to focus on the radio-quiet population and BALQSOs have emerged with a radio-detection enhancement as compared to non-BALQSOs (Morabito et al., 2019; Petley et al., 2022).

In Petley et al. (2022) we studied a large sample of radio-detected BALQSOs created using the second data release of the LOFAR Two Metre Sky Survey (Shimwell et al., 2022b) and SDSS spectra (Pâris et al., 2018). Although BALQSOs were

already understood to have a radio-detection enhancement when compared to non-BALQSOs, we aimed to study whether one can observe different spectral features of the BALQSOs varying with radio-detection (and also radio luminosity). We found that radio-detected HiBALs and LoBALs had different absorption profiles compared to their non-radio-detected counterparts and that this held even when controlling for differences in balnicity index which was found to correlate with radio-detection fraction in Morabito et al. (2019). Interestingly, the difference between the absorption profiles was more apparent in the LoBAL population as compared to the HiBAL. Without galaxy-scale resolution, it was not possible to determine whether star formation, jets or wind shocks were responsible for these apparent differences.

There have been several VLBI studies of BALQSOs since the turn of the millennium. These have tended to focus on radio-loud BALQSOs which may bias results towards jet-like structures. Jiang & Wang (2003) and Doi et al. (2009) both find evidence of flat and/or inverted spectrum sources, implying the possibility of BAL winds close to the radio jet axis. Bruni et al. (2013) investigated 9 BALQSOs with the Very Long Baseline Array (VLBA) again finding a range of structures from several parsecs to 100 kpc. They suggest that this indicates different possible viewing angles for BALQSO winds with respect to the jet axis.

At this point, to push our understanding of radio-quiet BALQSOs, the majority of the BALQSO population, we need higher-resolution studies at multiple frequencies for a large number of BALQSOs. However, this work can be informed by differences between classes of BALQSOs which may help to elucidate the radio properties more clearly than taking an "average" population of BALQSOs. HiBALs and LoBALs show differences in their radio properties which provide a direct challenge to the geometric unification between each other model but we lack the detail in LoTSS alone to probe any further. If we can understand the HiBAL-LoBAL connection then we may be able to extend to BALQSO-non-BALQSO unification which has significant relevance to the study of AGN feedback in action.

In this study we aim to examine the HiBAL-LoBAL connection, utilising the potential of radio interferometry to reach a sub-arcsecond resolution for faint, high-redshift sources. By controlling for redshift, AGN luminosity and wind strength,

we highlight the radio properties of these two populations to see if they produce synchrotron emission in different ways and hence have potentially different feedback relationships with their host galaxies.

Throughout this paper, we assume a cosmology defined by the parameters determined by the **Planck 2015** observations which were published in Ade et al. (2016). This is a standard, flat ΛCDM cosmology with $H_0 = 67.8\,\mathrm{km\,s^{-1}\,Mpc^{-1}}$ and $\Omega_M = 0.308$. When discussing spectral index we use the convention of $S_\nu \propto \nu^{-\alpha}$ with α being the spectral index.

5.2 Data and Methods

Here we describe the target selection process before following up with the various radio and multi-wavelength data collected.

5.2.1 Target Selection

This work aims to compare the high-resolution radio properties of HiBALs and LoBALs with each other while controlling for the effect of the wind absorption profile on the radio-detection fraction noted in Petley et al. (2022). Here we describe the data and decisions taken and present the overall selection in Figure 5.1.

The original quasar sample is from the SDSS DR12 quasar sample (Paris et al., 2017) where to ensure good quality spectra we have taken a continuum signal-noise-cut of sources > 5. To avoid Lyman forest emission affecting measurements of colour we take a redshift range of $1.7 < z < 3$. We then cross-matched with the LoTSS DR2 data release (Shimwell et al., 2022b) using the optical counterpart positions presented in Hardcastle et al. (2023) with a search radius of $1''$. This is essentially the same data as used in Petley et al. (2022) but with the improvement of optical positions.

In Morabito et al. (2019) and Petley et al. (2022) a strong correlation was found between the Balnicity Index (BI) and radio-detection fraction. This index was originally defined in Weymann et al. (1991) and is essentially an equivalent width measurement with some modifications to obtain a clean selection of sources with clear

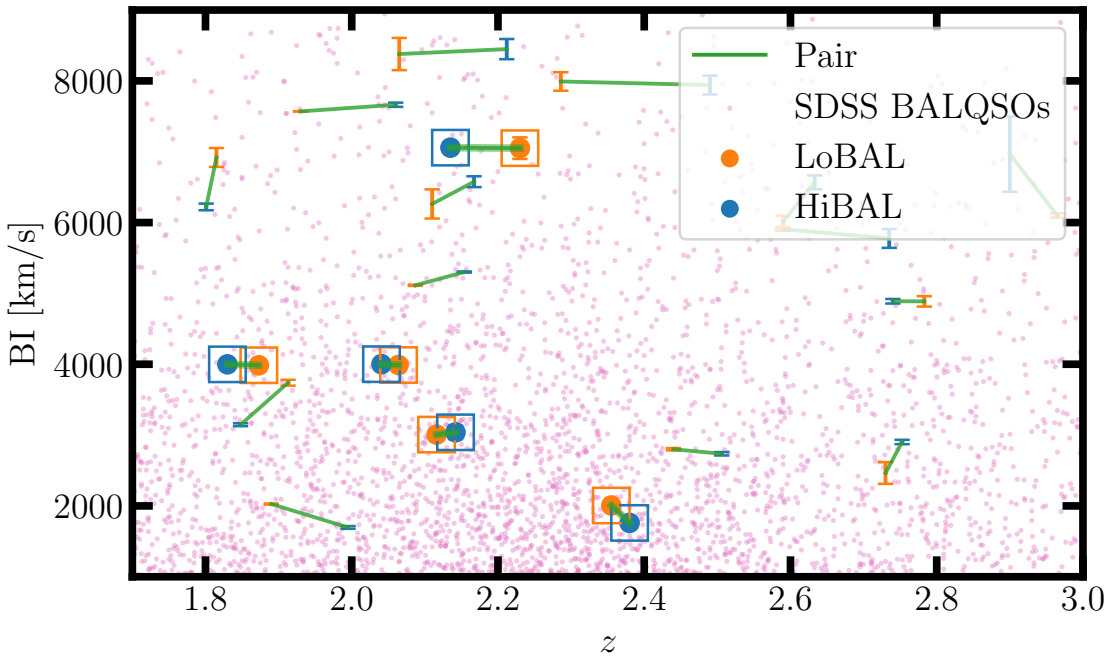

Figure 5.1: Our sample selection is shown in redshift and balnicity index. Six-micron luminosity was also used to identify the 20 closest pairs of HiBALs and LoBALs with similar accretion and wind properties. The five pairs in boxes were the sources selected for follow-up eMERLIN observations that we study in this work. The other pairs are those that have the potential for International LOFAR study as they have sufficient coverage from international stations. The background sources consist of all BALQSOs in the parent sample with WISE detections allowing for a $L_{6\mu m}$ measurement.

absorption profiles. After fitting the spectra continuum to extract a normalized spectrum $f(\nu)$, the BI is defined as:

$$\texttt{BI}[\mathrm{km\,s^{-1}}] = -\int_{25000}^{3000}\left[1-\frac{f(V)}{0.9}\right]C\,dV \tag{5.1}$$

where $f(V)$ is the normalized spectrum as a function of velocity displacement from the C IV line. The constant C is introduced to obtain a clean sample of broad absorption and works by being set to 1 when there is continuous absorption of at least 10% of the continuum for 2000 $\mathrm{km\,s^{-1}}$ and 0 otherwise. Sometimes we refer to the BI as a measure of "wind strength" which is not well defined. To be clear, in this study, we control for BI simply to remove the effect of the correlation between BI and radio-detection-fraction highlighted in Morabito et al. (2019).

We aim to control for the AGN luminosity within each of the sources so we

matched in six-micron luminosity (hereafter $L_{6\mu m}$). This luminosity aims to capture the output of the dusty torus surrounding an AGN which consists of reprocessed optical, UV and X-ray emission from the AGN. It itself is not affected by extinction allowing for a comparative measure of AGN luminosity between systems. To properly measure this luminosity we require that each source has a detection in the first three bands of the Wide-field Infrared Survey Explorer (WISE). To estimate the $L_{6\mu m}$ we perform a log-linear interpolation between the WISE bands in their rest-frame wavelength.

We then restricted the sample to only contain sources with LoTSS observations with at least 10 international stations. This is for planned work on these sources utilising the full International LOFAR Telescope to obtain low-frequency images at the same resolution as eMERLIN for all of the targets.

Broad absorption line quasars were selected from the Paris et al. (2017) catalogue via both a visual inspection flag for broad absorption line quasars and a measured C IV BI greater than zero. To identify LoBALs in Petley et al. (2022) we used the rest equivalent width of Al III and searched for positive values, indicating absorption. We found this selection to be quite successful as can be seen in the summary spectra of Figure 5.5. Target 10 is the only source with potentially a dubious LoBAL classification with this method. The absorption is at a low level around Al III and is very broad but this does appear to align with how broad the absorption is at C IV .

We found the 20 closest pairs within the 3-dimensional $z - \mathrm{BI} - \log(L_{6\mu m})$ space. We essentially normalise all sources to have a value of 0 to 1 in each of these dimensions and then find the pairs with the lowest euclidean distance. Our sample selection is presented in Figure 5.1 with the 10 sources selected for follow-up observation in bold. We do not indicate the differences in $L_{6\mu m}$, the largest separation in this study occurs for the lowest redshift pair in which the HiBAL as factor 2.19 higher $L_{6\mu m}$ compared to its LoBAL pair.

To summarise our selection, we started with the sample of radio-detected HiBALs and LoBALs from Petley et al. (2022) and then examined the 3D distribution of redshift, six-micron luminosity and balnicity index. We identified HiBAL-LoBAL pairs within a tolerance in this space, specifically 0.2 in redshift, 1000 km/s in BI

and 0.4 dex in six-micron luminosity.

5.2.2 eMERLIN - 1.4 GHz

Observations

The 10 targets were observed using the e-MERLIN L band receivers in February and March of 2022. The L band observations have a frequency range of 1.3-1.75GHz. Data is split into 8 spectral windows with a width of 64MHz and within each spectral window there are 512 channels. The observations were taken with full polarisation across one-second integration times. The standard data pre-processing procedure was run using the e-MERLIN CASA pipeline[1] (Moldon et al., 2021) which calibrates and further reduces the data to 128 channels per spectral window and a four-second integration time.

Overall, there were no major problems with the observations. Five of the six antennas were available depending on wind stows and availability due to engineering. Standard flagging was applied to all the observations which involved the removal of the first 40 channels of all spectral windows due to RFI and spectral window 3 being removed due to 4G+ filters.

Specific notes on each of the targets follow:

- 0933+2829 - The start of the observation was missing the Defford antenna due to a local power outage. Knockin was missing for three and a half hours. Spectral window 0 was impacted by RFI.
- 0049+2851 - Knocking had engineering issues and was flagged for large parts of the run. This led due to a loss in phase coherence at certain points for the phase calibrator.
- 1639+3338 - Mark II was wind-stowed for large parts of the run. This also led to a loss of phase coherence at some points for the phase calibrator.
- 1143+3629 - Defford was missing for a section of the run.

[1] https://github.com/e-merlin/CASA_eMERLIN_pipeline

- 0915+4628 - Defford was missing for a section of the run.
- 1159+6255 - There was a loss of phase coherence on the phase calibrator.
- 1015+6148 - Two separate runs taken within a week of each other were combined. Parts of each run were affected by outages.
- 1324+2452 - Three separate runs taken within a week of each other were combined. Parts of each run were affected by outages. Spectral window 0 was impacted by RFI.
- 2317+3227 - Two separate runs taken within a week of each other were combined. Parts of each run were affected by outages. Spectral window 0 was impacted by RFI.
- 1253+5024 - Two separate runs taken within a week of each other were combined. Parts of each run were affected by outages.

Additional Calibration

The targets were all quite faint, $< 10mJy$ in LoTSS, and we expected several of the sources to be around the detection limit of the instrument given the observation time. This, combined with the fact that it was already suggested we perform additional calibration on some specific sources, led to us engaging with the e-MERLIN support team to help advise on some additional calibration steps.

For all the sources we performed self-calibration on the phase calibrator. We performed at least 4 rounds of self-calibration including at least one round where we would solve for the amplitude as well as the phase. The imaging and cleaning were done using `wsclean` (Offringa et al., 2014) in most cases using the auto-mask and auto-threshold parameters to set masks and limits during each round of cleaning. In some cases where strong artefacts could be seen around the source we also used a custom mask created within CASA's `tclean` task to define the masking region for `wsclean` within the first few rounds of selfcal.

In some cases, where there were nearby sources to the phase calibrator or if initial beam effects appeared quite strong, we would also create a custom mask around the

location of the source during the cleaning process.

Source Extraction

To be consistent in our measurement of flux density values we use the radio source extraction code `pybdsf` (Mohan & Rafferty, 2015). This tool was developed originally for LOFAR but works well for any radio interferometry image. It produces rms images of the input and then selects source pixels and noise pixels based on flux density enhancement relative to a local rms threshold. The definition of this threshold can be selected by hand or can be calculated by using a false detection rate algorithm.

A contiguous region with pixels above the threshold is known as an island. Once all islands have been identified, the code attempts to fit them with Gaussian components. The user can return different catalogues with overall source parameters or parameters for all the Guassians used to fit the sources.

We used `pybdsf` with default settings on each of the eMERLIN images of our targets. Sources were extracted from 8/10 images with one target (eMERLIN target 1 - 0933+2829) resolved into two similar flux density components. For the other two sources, we measured the rms in a 5″x5″ box around the location of the source and report 5σ upper limits on the flux density as this was the threshold used in the `pybdsf` extraction for other sources.

5.2.3 Further Radio Data

In addition to the eMERLIN data obtained for this work, we supplement our radio analysis through cross-matching with other existing radio surveys at different frequencies.

Firstly, we use the LoTSS data that was originally used to select the targets. The survey was generated using only the Dutch stations of LOFAR and did not incorporate the full international array. LoTSS achieves a median sensitivity of $83\,\mu\mathrm{Jy\,beam^{-1}}$ at a resolution of 6″. We use images and flux density measurements

from the catalogue included in (Shimwell et al., 2022b)[2] which were also extracted using `pybdsf`.

We utilise the Faint Images of the Radio Sky at Twenty centimetres (FIRST; Becker et al., 1995) to obtain images and fluxes at the same frequency as eMERLIN. The typical rms of FIRST is 150 µJy beam^{-1}. This increased rms, combined with the typical synchrotron source emitting lower flux density at higher frequencies, means that it is unsurprising that we only detect 2/10 sources within FIRST.

We also utilise the Karl G. Jansky Very Large Array Sky Survey (VLASS; Lacy et al., 2020) to obtain higher frequency radio data. The VLASS survey goal is for 3 single-epoch observations, each with a target rms of 120 µJy beam^{-1}, to be combined into a final image targeting ∼70 µJy beam^{-1}. The survey operates at 3 GHz (S-band) with a resolution of around 2.5″. We cross-matched with a catalogue of sources produced for the first epoch of observations. The source extraction was also performed using `pybdsf`. We find detections for 3/10 sources, two of these were the ones also detected with FIRST but the additional detection (2317+3227) was interestingly a higher flux density source in VLASS than those detected in FIRST.

5.3 Results

5.3.1 eMERLIN Images

Cutouts of the eMERLIN images are presented in Figure 5.2. To be clear, the images do not have the same flux density scale and have been stretched and normalised to best highlight the morphology of the detections. Therefore, the features present in the two non-detected targets (2 and 5) are actually at a much lower level compared to the rest of the detections and simply a feature of noise that has been normalised in a similar way to the other targets.

The images are centred on the SDSS coordinates for the sources. Slight offsets can be seen from the centre for several sources. The astrometric performance of eMERLIN is typically higher (∼ 2 mas at L-band) than that of SDSS. The offsets

[2] `https://lofar-surveys.org/dr2_release.html` - (Shimwell et al., 2022a)

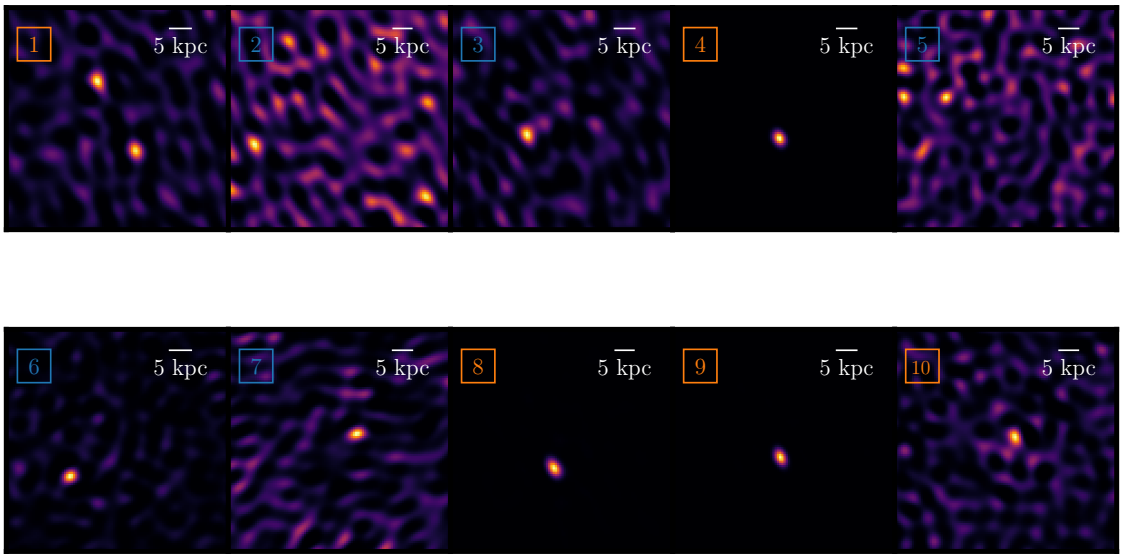

Figure 5.2: 5x5 arcsecond cutouts for each of the eMERLIN targets centred on the SDSS right ascension and declination coordinates. The images have been stretched by a power law after a 99% percentile cut. They are then normalised so that each image has the same colour range. The target number is indicated in the upper left with orange numbers indicating LoBALs and blue numbers indicating HiBALs. In the upper right, we display a 5 kpc scale bar highlighting the galaxy scale resolution we have obtained for these sources.

present are well below an arcsecond and so we are confident that these are true detections of each BALQSO.

The morphologies of the sources are 7 compact, 1 resolved double source and 2 undetected. For the compact sources, the sizes are all below 5 kpc indicating that we have reached our target of galaxy scale resolution.

5.3.2 Extracted Fluxes

The extracted eMERLIN integrated fluxes from `pybdsf` are reported in Table 5.1. We find a range of fluxes from 0.097 to 2.604 mJy. We present all of the radio data used throughout the rest of the work in Figure 5.3. LoTSS, eMERLIN, FIRST and VLASS data are all used but we only find FIRST and VLASS detections for a few of the LoBALs that were the brightest in LoTSS to begin with.

The flux density ratio between two images at the same frequency but at different resolutions places a direct constraint on the amount of compact and diffuse flux in a source. Ideally, we would have this measurement for all sources but for our sample,

Name	Target No. (Pair)	z	BI [km s^{-1}]	C IV Dist	eMERLIN Total Flux [mJy]	LoTSS Peak Flux [mJy]
0933+2829 - LoBAL	1 (6)	1.87	3986	0.66	0.295†	1.77
0049+2851 - HiBAL	2 (8)	2.38	1760	0.54	0.026 ↓	0.92
1639+3338 - HiBAL	3 (9)	2.04	4001	0.56	0.144	0.88
1143+3629 - LoBAL	4 (5)	2.12	3007	0.42	2.604	6.54
0915+4628 - HiBAL	5 (4)	2.14	3039	0.46	0.022 ↓	0.68
1159+6255 - HiBAL	6 (1)	1.83	3998	0.66	0.187	1.00
1015+6148 - HiBAL	7 (10)	2.14	7057	0.87	0.097	1.28
1324+2452 - LoBAL	8 (2)	2.34	2005	0.72	2.188	2.23
2317+3227 - LoBAL	9 (3)	2.06	3989	0.79	2.414	3.01
1253+5024 - LoBAL	10 (7)	2.23	7050	0.63	0.197	1.72

Table 5.1: Table of radio properties for each of the sources. The redshift is taken from the visually inspected redshift values from the DR12 quasar catalogue (Paris et al., 2017). The balnicity index (BI) values are taken from the same catalogue. The CIV distances were measured using PCA reconstructions provided by Amy Rankine.
† - Multiple component source - Upper component contains 0.157 ± 0.04mJy and the lower contains 0.138 ± 0.04mJy
↓ - 5 sigma upper limits for the two sources not detected in eMERLIN based on rms measurement of the source location.

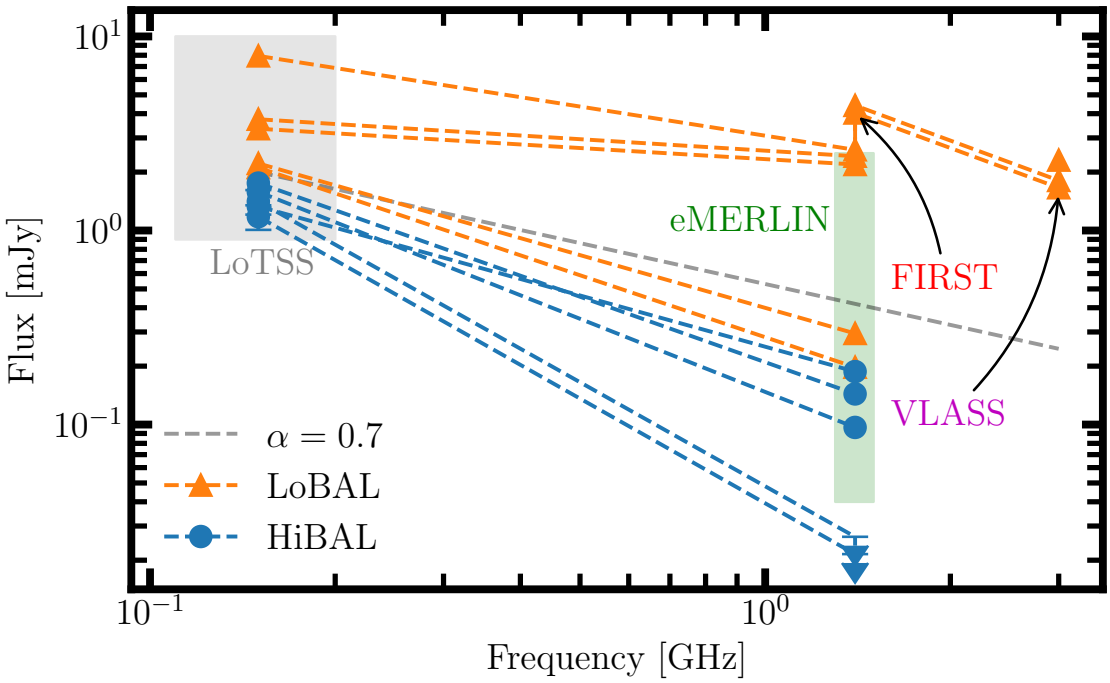

Figure 5.3: Flux density measurements at different radio frequencies for each of the 10 target sources with LoBALs as orange crosses and HiBALs as blue triangles. The error bars are relatively small and are not shown to make the figure more readable. We indicate the behaviour of a 2 mJy source at 150 MHz with a spectral index of 0.7 in black.

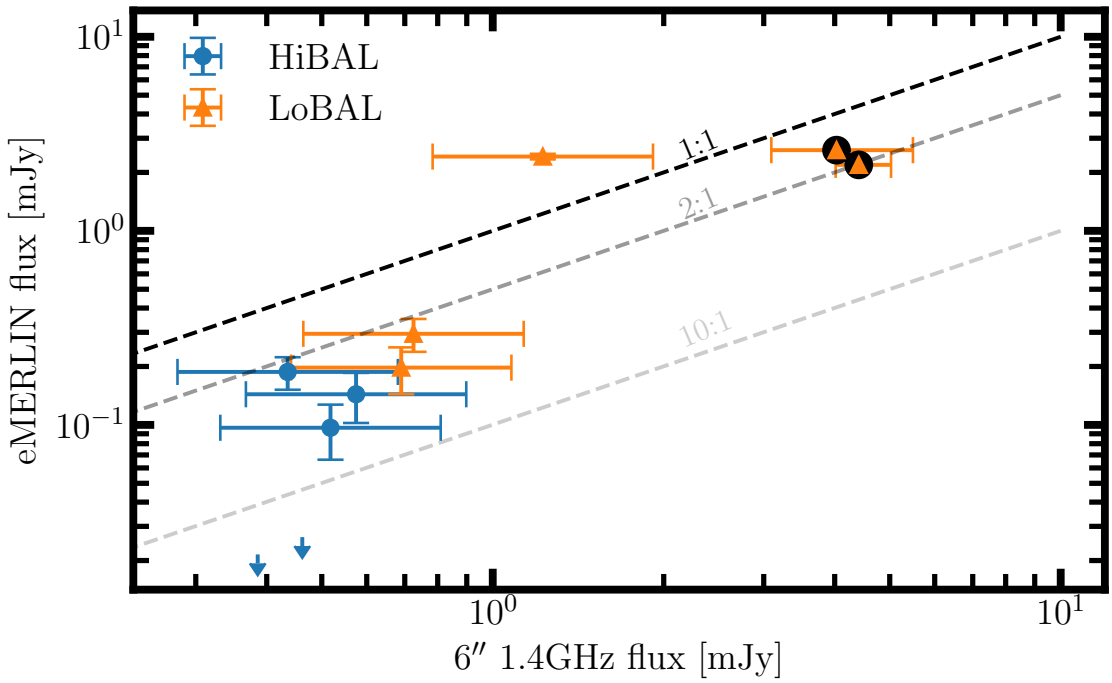

Figure 5.4: Measured (black circled) or inferred 1.4GHz fluxes against measured e-MERLIN fluxes for the 10 sources. Arrows indicate 5σ limits for the two undetected sources. Horizontal error bars are based on a change in spectral index from 0.3 to 0.7 for the inferred fluxes which are based on 144MHz LoTSS fluxes.

we only have it for the two sources with FIRST detections. Instead, we attempt to introduce an estimate of this flux density by utilising the LoTSS flux density measurements. This introduces a key uncertainty via the spectral index that we assume to estimate the 1.4 GHz flux density.

We extrapolate fluxes with a spectral index range of $0.3 < \alpha < 0.7$ in Figure 5.4 and find that the sources are consistent with retaining $\sim 50\%$ of their flux density at high resolution. With the LoTSS DR1 and DR2 radio studies of BALQSOs (Morabito et al., 2019; Petley et al., 2022) both found that BALQSOs had flatter spectral indices than non-BALQSOs, although these measurements were made without considering limits from sources undetected in FIRST which biases all indices to be flatter. There is significant noise in some of the eMERLIN images and fluxes could maybe increase if the calibration procedure was improved. However, both sources with FIRST detections lie below the 1:1 ratio line indicating that this flux density loss is maybe not a result of observational limitations. This indicates that for all but one of the sources, there is at least some flux density present on the 2-40kpc

scale.

5.4 Discussion

5.4.1 Radio Emission Mechanisms

We find clear evidence in one source for a jet-like structure in a LoBAL quasar. The flux density in each component is very similar indicating that we are looking at the jets at a low inclination. In an equatorial wind scheme for BALQSOs, this kind of structure should be common since a low inclination view of the jets implies a sight line more likely to cut through the accretion disc and/or dusty torus. Although we do not see this structure in the other sources there are several ways in which jets could still be the dominant mechanism in the other detected sources.

Firstly, the jets could typically be smaller-scale and within $\lesssim 5\,\mathrm{kpc}$ in order for the other detected sources to remain compact. Jet sizes and luminosities depend on the lifetime, power and the environment in which the jet imparts its energy. Jarvis et al. (2019) studied nearby radio-quiet quasars and found the majority of objects exhibited radio emission on scales of 1-25kpc. These objects could be resolved as they were all $z < 0.2$ where eMERLIN possesses a physical resolution below $1\,\mathrm{kpc}$. Therefore the lack of structure in these higher-redshift sources cannot discount the jet scenario.

5.4.2 Radio differences between HiBAL-LoBAL pairs

Our selection did not include matching in radio flux density between HiBAL-LoBAL pairs. We, therefore, expected to find that the LoBALs had slightly higher radio fluxes since they are more likely to be radio-detected in general and at the same BI as HiBALs. For all of our target pairs, the LoBALs have around twice the LoTSS peak flux density of their corresponding HiBAL. Therefore, to test the differences between LoBALs and HiBALs at our two resolutions, we study the ratio of flux density between pairs at each resolution.

In Figure 5.5 we examine how the LoBAL flux density enhancement, which is

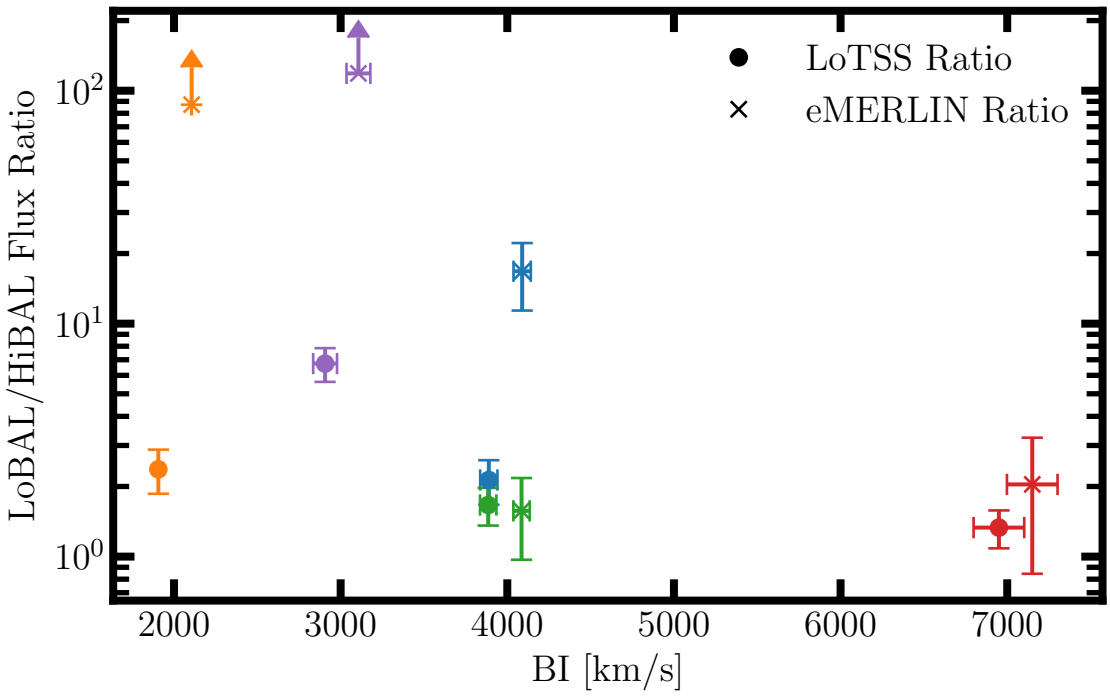

Figure 5.5: The ratio of flux density between each LoBAL-HiBAL pair for LoTSS and the high-resolution eMERLIN images. Each pair is shown in a different colour with a slight artificial offset in BI between LoTSS and eMERLIN introduced to more easily distinguish between close points.

present in a sample not selected on radio properties, varies when we move to the higher-resolution and higher-frequency measurements of eMERLIN. The LoBAL enhancement increases for 4/5 pairs. This would imply that LoBALs retain greater flux density on compact scales compared to HiBALs and/or they have different spectral indices. Since our eMERLIN observations are at a higher frequency than LoTSS, a flatter spectral index for LoBALs would allow for greater flux density at eMERLIN compared to HiBALs. However, since we are also measuring the flux density on a scale 20 times smaller than LoTSS, the LoBAL enhancement could be related to the compactness of the emission as compared to HiBALs. Either way, this is a new result for the BALQSO population and probably relates either to the emission mechanism (spectral index) and/or the environment in which the radio emission is produced (compactness).

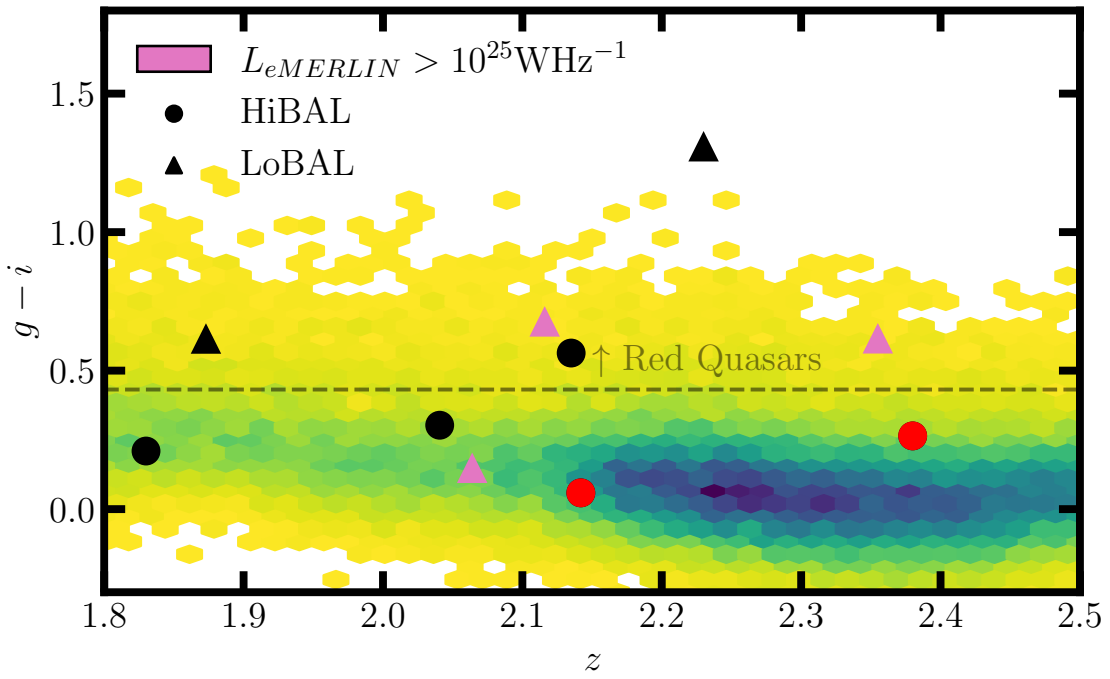

Figure 5.6: The redshift-colour space for our target sample as compared to the parent SDSS DR12 quasars. In the hexbin map, we require 5 sources in order for a bin to be filled. The two red markers indicate the two HiBALs that were not radio-detected. We indicate a "red quasar" border based on the 90th percentile $g-i$ value in this redshift range. The higher luminosity sources are highlighted.

5.4.3 Reddened Sources

The results of Petley et al. (2024) indicated that reddening could be the key contributor to radio-detection fraction differences between BALQSOs and non-BALQSOs but could not explain the differences entirely.

We look at the fraction of our sources that would be selected as "red quasars" in radio studies of this population (Klindt et al., 2019; Fawcett et al., 2020; Rosario et al., 2021). The selection proposed in Klindt et al. (2019) was to take the 10% most red sources in different redshift bins for SDSS quasars. Over the redshift range of our pairs, the distribution is quite steady so we simply take this percentile over the whole range at once as an approximation of this method. In Figure 5.6 we show that half of our sample and 4/5 LoBALs would meet this red quasar definition. This is essentially the same finding as that of (Urrutia et al., 2009) who find a large fraction of LoBALs in a red and radio-detected sample of quasars.

We calculate the rest frame 1.4 GHz radio luminosity of each source based on

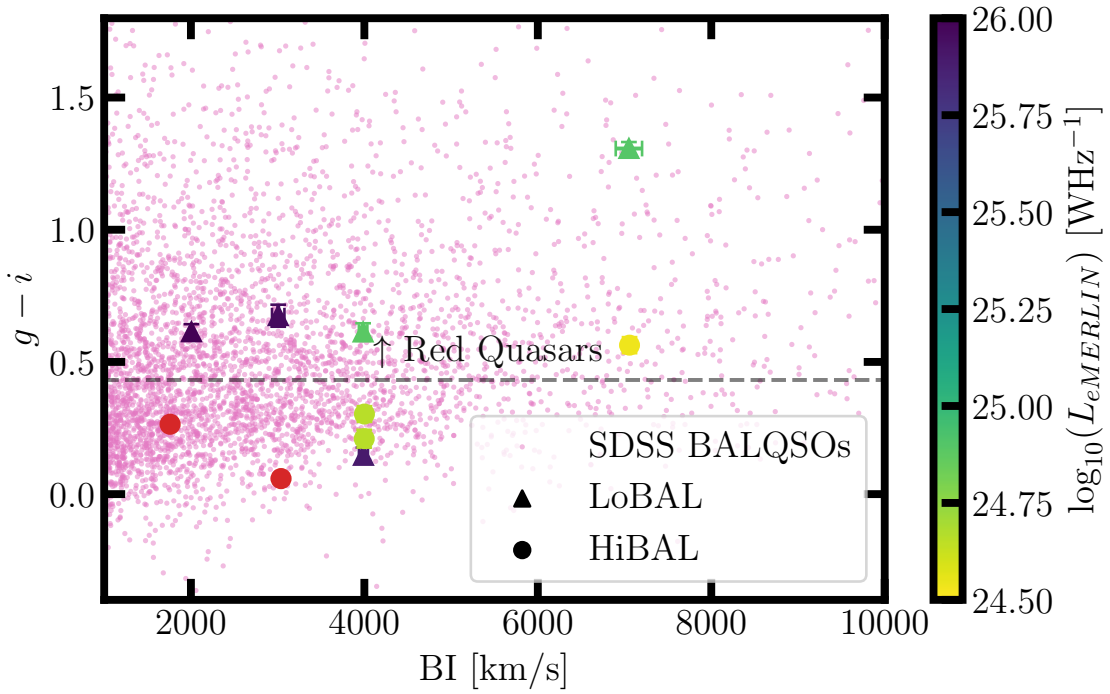

Figure 5.7: $g-i$ colour against BI for our target sample coloured by their radio luminosity. The two solid red points indicate the sources that were not detected by eMERLIN. Similarly, to Figure 5.6, we indicate a red-quasar border based on the 90th percentile $g-i$ value for all SDSS quasars in the redshift range of our targets. There is some evidence that at the same balnicity index, radio luminosity increases with reddening.

the eMERLIN fluxes and a k-correction assuming a spectral index of 0.7. We find a distribution between $3 \times 10^{24}\,\mathrm{W\,Hz^{-1}}$ and $1 \times 10^{26}\,\mathrm{W\,Hz^{-1}}$ with a cluster of sources at each end.

If reddening is due to dust then it may have an important role to play in the launching mechanism of the BALQSO winds (Leftley et al., 2019; Soliman & Hopkins, 2023). In Figure 5.7 we present the full SDSS BALQSO population and study the connection between optical colour and balnicity index. On top, we show the sample from this paper coloured by their eMERLIN radio luminosity.

Although a clear correlation is not present, one can see that the most powerful outflows are present in more reddened systems. As an example, 38% of BALQSOs with BI $< 2000\,\mathrm{km\,s^{-1}}$ are red quasars while 74% of BALQSOs are red quasars with a BI $> 5000\,\mathrm{km\,s^{-1}}$. How do the radio properties of LoBALs and HiBALs vary across this space? We see that at a given BI value, the more red sources have a

higher compact eMERLIN luminosity. However, these are also the LoBALs somewhat confusing what is driving the difference between the sources. We do not see a correlation between BI and eMERLIN luminosity. However, maybe this analysis could be enhanced by studying the specific properties of the low-ionisation absorption profiles in the future rather than characterising them via their C IV properties.

5.5 Conclusions

In summary, we have studied 5 pairs of HiBALs-LoBALs with similar AGN power and wind properties with the high-resolution interferometer eMERLIN. The pairs were selected to highlight the intrinsic differences between LoBALs and HiBALs and avoid the influence of AGN luminosity and wind strength highlighted in Petley et al. (2022, 2024).

1. We detect 8/10 of BALQSOs in our sample with a SNR > 5. One of these sources is resolved into two symmetrical and roughly equal flux density components, suggestive of a view of a jet at high inclination. This source also has the strongest LoBAL absorption features.

2. We find that the majority of sources have steep spectral indices (average of $\alpha = 0.76$) from LoTSS to eMERLIN but without matched resolution, we cannot distinguish between the presence of diffuse emission and an actual spectral index. The LoBALs have flatter indices ($\alpha = 0.57$) implying more compact emission. When detected in FIRST the sources have a spectral index of ($\alpha = 0.40$) implying that resolution may be the key factor.

3. We show that LoBALs maintain a greater fraction of their radio flux density at high resolution when compared to the flux density of their matched HiBAL source.

4. Half of the sources would be selected as red quasars using the definition outlined in Klindt et al. (2019). Colour was not part of the selection process so we confirm a similar result as to that in Urrutia et al. (2009).

5. We find some evidence that at a given balnicity index, more red sources have a greater radio luminosity for BALQSOs. The red sources are typically also LoBALs suggesting that the link between radio emission - reddening - low-ionisation absorption persists on compact scales.

The sources studied in this paper are all part of LoTSS observations with at least 10 simultaneous international station observations. This means that there is the potential to study these sources at 144 MHz and matched resolution to eMERLIN. This was the initial goal of the project and much of the LOFAR data has received initial processing. We have been delayed slightly due to transitioning the pipeline to a new framework and then refocusing on an automated pipeline to reprocess all of LoTSS at high resolution (LoTSS-HR; Morabito et al. in prep.). However, we already have a detection of one source with high-resolution LOFAR and hope to present the full sample at high resolution in the future along with other fainter pairs utilising the high-resolution LOFAR data alone.

This work represents a focused effort to elucidate the radio differences between populations of BALQSOs in the radio-quiet regime. This has implications for the interpretation of the general radio enhancement of BALQSOs and the relationship between reddening and outflows which should inform future discussion of their relevance to AGN feedback.

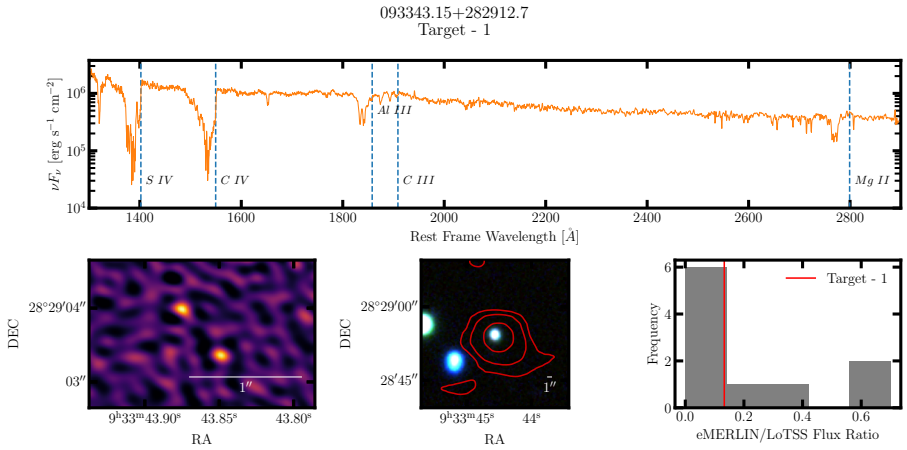

(a) Most prominent LoBAL profile. LOFAR contours show minor extension but it is still classified as compact

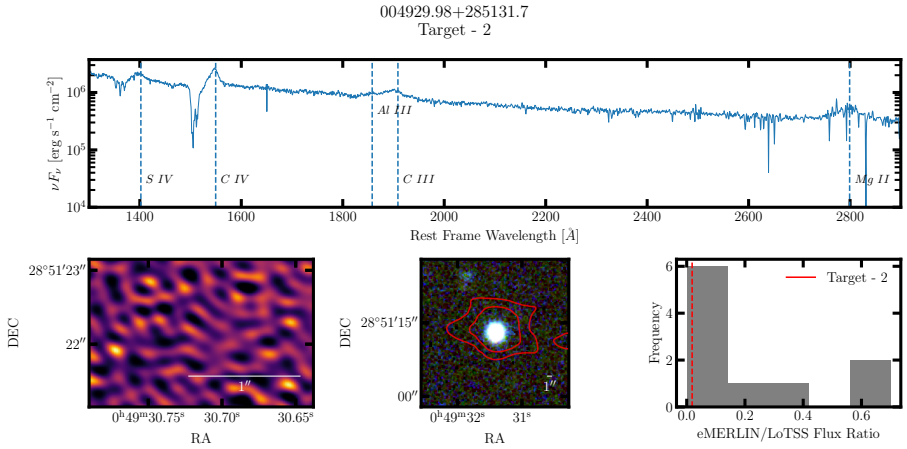

(b) Source undetected at eMERLIN frequency and sensitivity

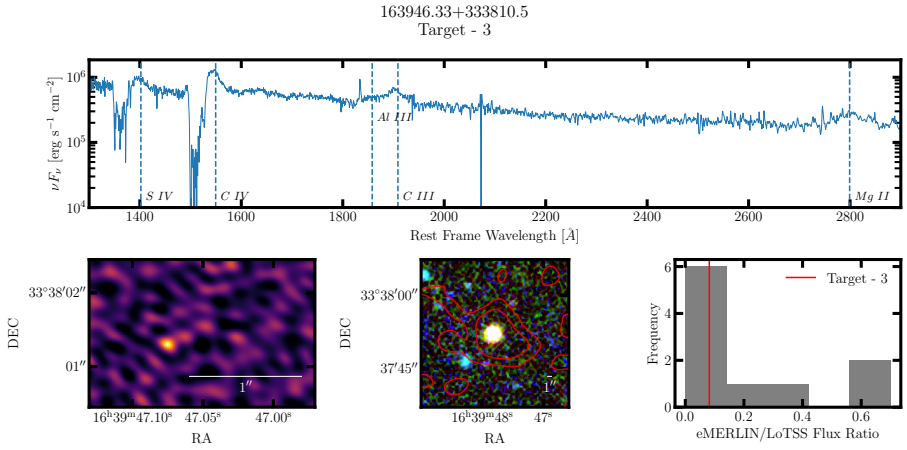

(c) eMERLIN image looks like it may show extended source but only single Gaussian picked out using pybdsf

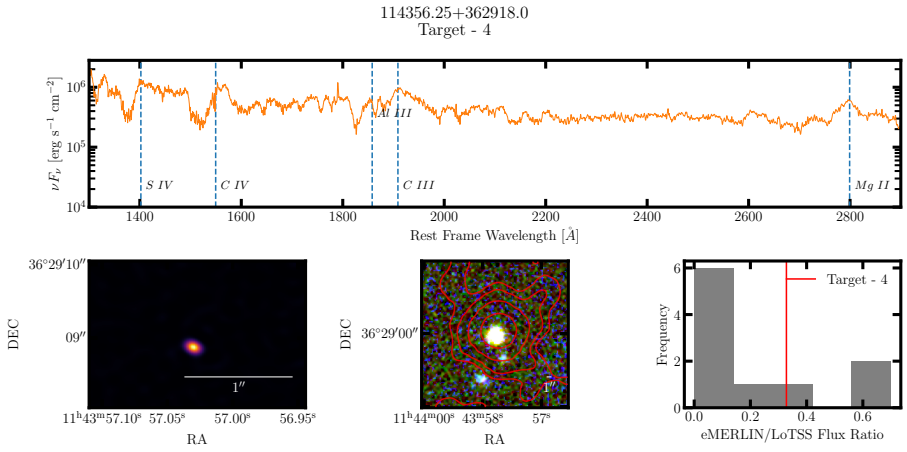

(d) More complex spectra showing additional absorption features

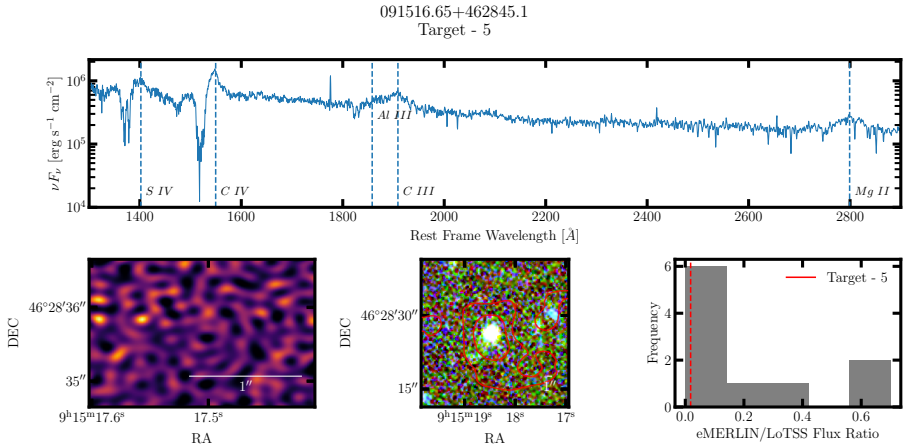

(e) Possible LoBAL but did not meet our definition

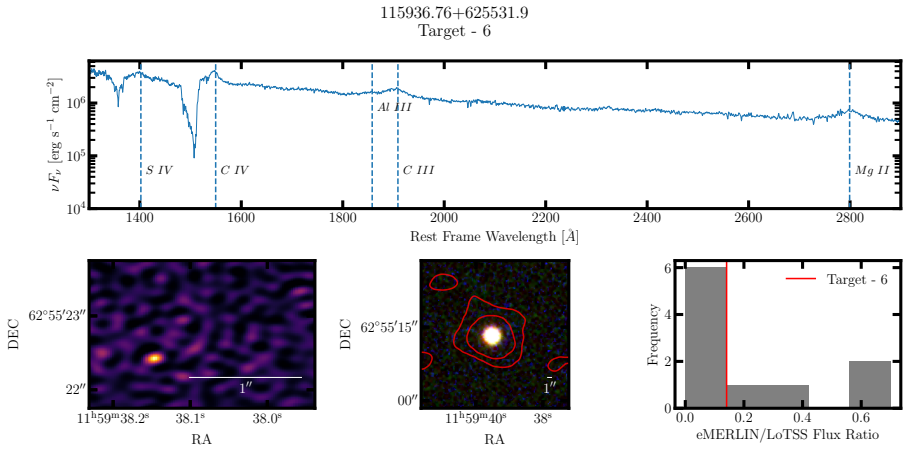

(f) Slight offset in astrometry between the LoTSS and eMERLIN source position

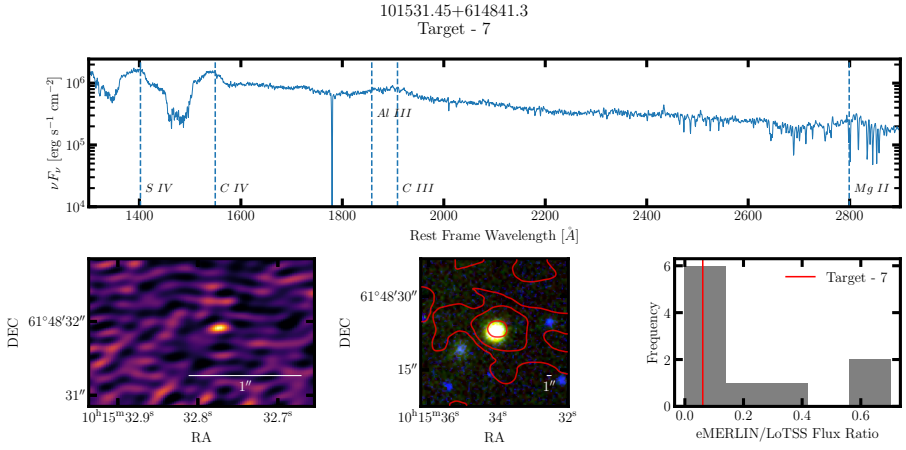

(g) LoTSS contours extend but source finder identifies as a single source

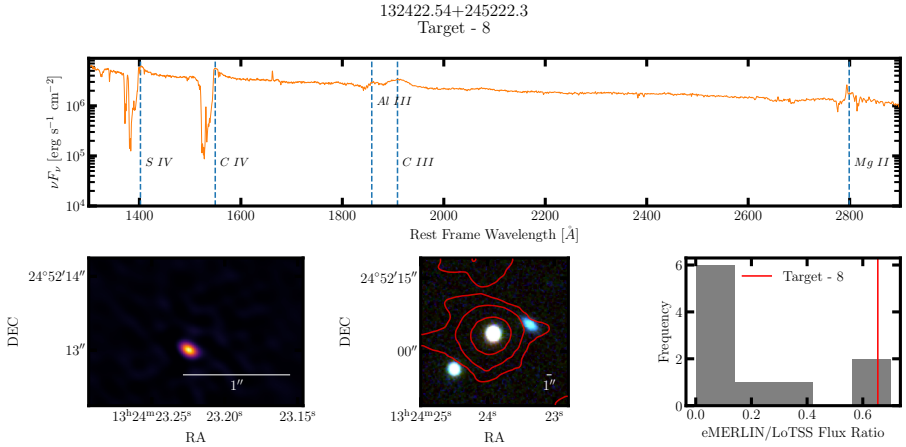

(h) Small offset in eMERLIN position appears to align with offset in LoTSS contours but both within uncertainties

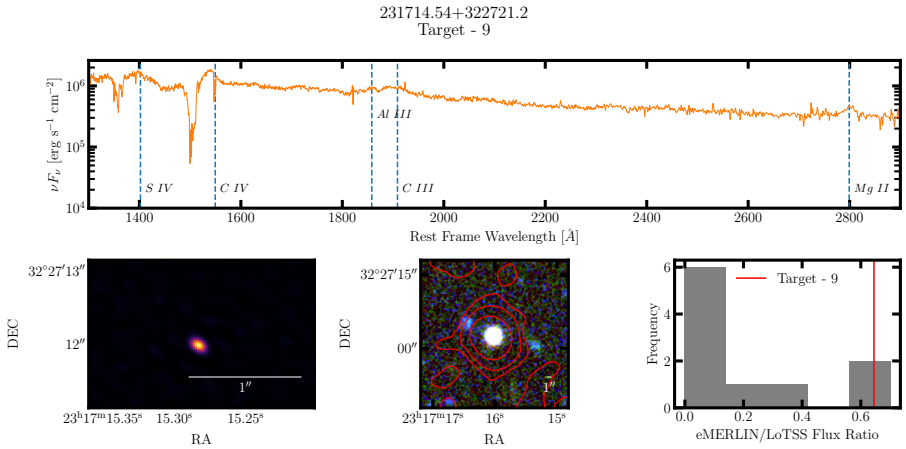

(i) No comments

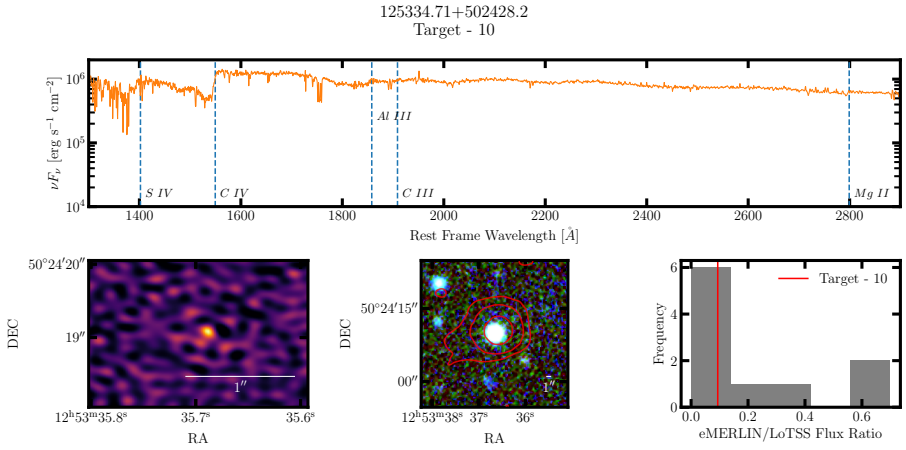

(j) LoTSS contours show slight extension

Figure 5.5: Summary plot for each of the 10 target sources. *Upper:* The spectrum in the upper panel has been shifted to the rest frame and smoothed using a Gaussian filter. The orange spectra are LoBALs and the blue are HiBALs. *Lower left:* 5″x5″ image from eMERLIN of each source. We use a one-arcsecond scalebar to compare to the central image. *Lower centre:* Background 30″x30″ image is a colour image from the Legacy survey. The red contours are from LoTSS. The contours are five log-spaced levels from the 3σ noise detection limit of LoTSS up to the integrated flux density of the brightest source in our sample. *Lower right:* The eMERLIN/LoTSS flux density ratio for all sources with the position of the current source highlighted.

That you should write down valuable ideas that occur to you as soon as possible goes without saying: we sometimes forget even what we have done, so how much more what we have thought.

Arthur Schopenhauer

6

Conclusions and Future Work

Although the central content of this thesis was written in three separate publications, each with its own individual results and conclusions, here I collate the overall effect of my work and reading during my studies.

I conclude the thesis by outlining and suggesting future work on the radio properties of BALQSOs and highlighting the potential of new radio facilities and surveys in elucidating the connection further.

6.1 Conclusions

In this thesis, I set out to answer questions raised by the recent discovery of BALQSO radio enhancement at low frequencies observed in Morabito et al. (2019). BALQSOs are possibly the clearest examples of black holes creating energetic outflows which have the potential to affect their host galaxy. A picture of BALQSOs as an equatorial

wind with a solid angle fraction equal to their incidence seems to have risen in the community but this radio result presents itself as the single greatest challenge to such a model.

I have made progress in understanding the exact nature of this radio enhancement by expanding to a much larger sample, moving to higher resolution and then drawing connections between BALQSOs and other populations, such as red quasars, which will allow us to make progress more broadly in the field.

Along the way, I have engaged with the scientific community researching BALQSOs, radio emission and black hole growth in general. Demonstrated through my contribution to the work of other authors and my own studies, the skills and understanding I have developed are valued by my colleagues.

This work should inform future studies of BALQSOs and radio properties of quasars particularly as we move into a new era of sensitivity and resolution with JWST, Euclid and the SKAO. In my opinion, the key findings of this thesis are:

1 - Radio detection of quasars is connected to wind properties

§ 3 and Appendix 4 both studied a very large population of radio-detected BALQSOs and found that both spectral shape and measured properties of the absorption profiles are connected to radio detection. This result is demonstrated via large statistical samples of quasar populations and should be considered in future discussions of BALQSOs.

2 - Colour appears to be the greatest driver of radio emission

The aforementioned radio enhancement can largely, but crucially not entirely, be attributed to the more red colours of BALQSOs Appendix 4. This places a greater emphasis in the future on understanding the connection between these two populations as conclusions made about each population may need to inform the other.

3 - LoBALs have distinct radio properties compared to comparable HiBALs

§ 3 and Appendix 5 show that LoBALs show a stronger connection to radio emission than HiBALs even when they contain extremely similar HiBAL winds. Given that studies show LoBALs have similar accretion properties to HiBALs, either the increased shielding that can allow for LoBAL signatures must have implications (e.g. increased wind velocity, density) for the radio emission or LoBALs occupy a distinct phase in the life-cycle of a quasar.

6.2 Future Work

Fortunately, my work in this field will not end with this thesis. I would like to briefly highlight potential developments that will allow for new tests and studies of BALQSOs.

6.2.1 Current Data

The sample of Appendix 5 was selected to ensure coverage from the full International LOFAR telescope for every source. This processing is ongoing but I do already have one detected source with LOFAR-VLBI which has the same compact morphology as its corresponding eMERLIN detection. Unfortunately, there has not been enough time during the thesis to achieve this goal for all 10 sources. This is partly due to a changing pipeline and also a change of focus towards longer-term goals for the whole community.

The LOFAR-VLBI working group is involved in an ongoing project to reprocess the entire LOFAR Two Metre Sky Survey at High Resolution (LoTSS-HR). We have been working on automated processing for every LoTSS pointing with the full international array. This is a major effort since previous work on processing individual fields often requires a lot of data inspection and insight from expert users throughout the process. Once this work has been concluded, I will be able to study nearly all BALQSOs with a flux above 10mJy in the northern sky at sub-arcsecond

resolution. This should be $\sim$ 100 sources given that 132 SDSS BALQSOs have a LoTSS flux above this limit.

Deep Fields

As well as the northern sky survey, LoTSS has focused repeat observations on a set of deep fields. These have included the Boötes field, Lockman Hole, Elais-N1 and the Euclid Deep Field North (Tasse et al., 2020; Sabater et al., 2020; Bondi et al., 2024). The rms sensitivity of each of these published images varies but ranges from 3-5 times more sensitive than LoTSS. For some of these fields, additional work has been done to provide robust optical cross-matching (Kondapally et al., 2021), photometric redshift estimates (Duncan et al., 2021) and source classification via SED fitting (Best et al., 2023).

This incredibly deep radio data has not yet been put to use for the study of BALQSOs or red quasars. The fields all overlap with the SDSS survey and contain a significant number of quasars and BALQSOs. Some initial investigations have begun but I would like to continue work to test whether BALQSO and red quasar detection fraction evolve with the sensitivity limit of the survey in the same way or if they diverge suggesting different emission mechanisms or jet powers.

Additionally, I will be able to utilise the extensive SED fitting which provides mass estimates and star formation rates to study comparative populations and separate radio contribution from AGN and star formation.

The final piece to this work will be the addition of high-resolution data for these fields. Sweijen et al. (2022) already produced a sub-arcsecond image of the Lockman hole. Work is also complete on the Elais-N1 field (de Jong et al. submitted) and an image of the Boötes field will be available soon (Escott et al. in prep). Although the number of BALQSOs yielded will be small, these images should provide additional size constraints and may produce some interesting sources that justify a follow-up study.

New spectroscopic instruments such as the Dark Energy Spectroscopic Instrument (DESI; DESI Collaboration et al., 2016) and the upcoming 4-metre Multi-Object Spectroscopic Telescope (4MOST; de Jong et al., 2016) represent a step

forward in quasar spectra observations as compared to SDSS. Both of these surveys will probe to fainter optical magnitudes across a wide area of the sky. The Early Data Release of DESI is now available (DESI Collaboration et al., 2023) and a value-added catalogue of automatically identified BALQSOs is available. Of the 28,000 or so BALQSOs identified, only ~ 4000 were identified in SDSS DR14. This could be a whole new avenue of investigation especially as our radio data also becomes more sensitive. One particularly relevant aspect of the 4MOST project is the 4MOST-Gaia Purely Astrometric Quasar Survey (4GPAQS Krogager et al., 2023). This survey will select quasars purely from astrometry and ignore colour-based selections which both past and present surveys typically use to identify quasars. As evidenced by this thesis, blue colour selections are biased against radio detection and the BALQSO signatures. This sample is therefore predicted to produce a large number of new BALQSO detections whose radio properties are completely unknown.

6.2.2 LOFAR 2.0

LOFAR recently closed down in order to implement new upgrades to all the stations across the array. The upgrade consists of several different projects which overall will create a much-improved array known as LOFAR 2.0.

The key upgrades are:

1. Simultaneous high and low band antenna observations should improve lower frequency observations by a factor of five
2. Building new stations in the Netherlands
3. Improving the correlator electronics to hand the resulting increased data throughput
4. Distributed clock system at all Dutch stations via a central clock

To go along with these major upgrades, the telescope will look to approve several large observing programmes which will best utilise a large number of hours on the new telescope. Although the final list of these projects has not yet been approved, I am a member of two of these projects, one of which I am part of the technical

team. It is very likely that these projects will be approved but may not receive the complete time allocations that they requested in their expressions of interest.

LOFAR Ultra Deep Observation

The LOFAR Ultra Deep Observation (LUDO) will obtain a single deep observation of the Euclid Deep Field North using the upgraded LOFAR2.0 telescope. This will utilise the high-band antennas with the full international array. The target rms noise is $2\,\mu\,\mathrm{Jy/beam}$ over a 3.7 deg^2 area of the sky which will be studied in great detail by the Euclid space telescope as well as other instruments at a variety of wavelengths.

The main benefit of this kind of study is the characterisation of star formation rates to high redshift without any effects of obscuration. At these low flux densities, the majority of sources will be star-forming galaxies and not AGN. LUDO will therefore allow us to accurately measure star formation history up to the epoch of reionisation.

For the study of AGN, this observation has several implications. It should allow for jetted radio AGN to be detected and resolved out to $z \sim 6$ and separation of star formation from AGN emission via brightness temperature allowing for a more accurate census of radio emission from quasars.

As a member of this proposal, I aim to utilise this data to push my studies of BALQSOs to higher redshift and use the complimentary Euclid data which also aims to detect a significant number of AGN out to $z \simeq 7$ (Euclid Collaboration et al., 2024). As an infra-red instrument, Euclid is likely to detect a large fraction of obscured AGN which should have interesting connections to the BALQSO and red quasar populations. At this redshift, the C IV line is observed just above 1 micron so we will require near-IR spectra to identify BALQSOs. This could be obtained through finding likely BALQSO candidates via reddening and radio emission and following up with ground-based instruments such as X-shooter or space telescopes such as JWST. The Spectro-Photometer for the History of the Universe, Epoch of Reionization and Ices Explorer (SPHEREx; Doré et al., 2014) instrument is planned to launch in April 2025 and will provide near-IR spectra of 450 million galaxies

including overlap with the Euclid Deep Field North although the spectral resolution is lower than ground-based instruments.

International LOFAR Two-metre Sky Survey

The other LOFAR 2.0 proposed large program that I am involved with is the International LOFAR Two-metre Sky Survey (ILoTSS). This proposal is a natural extension of the current LoTSS survey which is already producing ~ 50 publications a year. The idea is to perform a similar survey across 7600 deg^2 of the sky with a target rms sensitivity of $30\,\mu\,\mathrm{Jy/beam}$. The key difference is that the observing strategy will appreciate the narrower field of view of the international stations. Pointings must be designed with less separation between each centre in order to remove sensitivity gaps that will be present in LoTSS-HR. We will therefore be able to obtain more uniform sensitivity across the sky as compared to the LoTSS-HR post-processing work currently ongoing.

I have been asked to join the technical team for the proposal to work on the ILoTSS data products as someone who has been building experience with VLBI observations with LOFAR throughout my PhD. We expect that this survey will generate 21 petabytes of archived data over ~ 7 years.

6.2.3 SKAO

The next decade in radio astronomy will rapidly become centred on the commissioning, large programmes and science of the Square Kilometre Array Observatory (SKAO; Dewdney et al., 2009). The SKAO partnership is a massive operation backed by the governments of 16 countries with many institutions and companies involved in the design and development of the telescopes. This observatory will consist of two telescopes, operating at two different frequencies on two continents and should be a world-leading facility for several decades.

The two arrays are being built in a modular fashion and should become the most sensitive radio instruments on the planet sometime before their final configuration with sensitivities outlined in Figure 6.1.

LOFAR and eMERLIN are both “SKAO Pathfinders”, a title used to describe

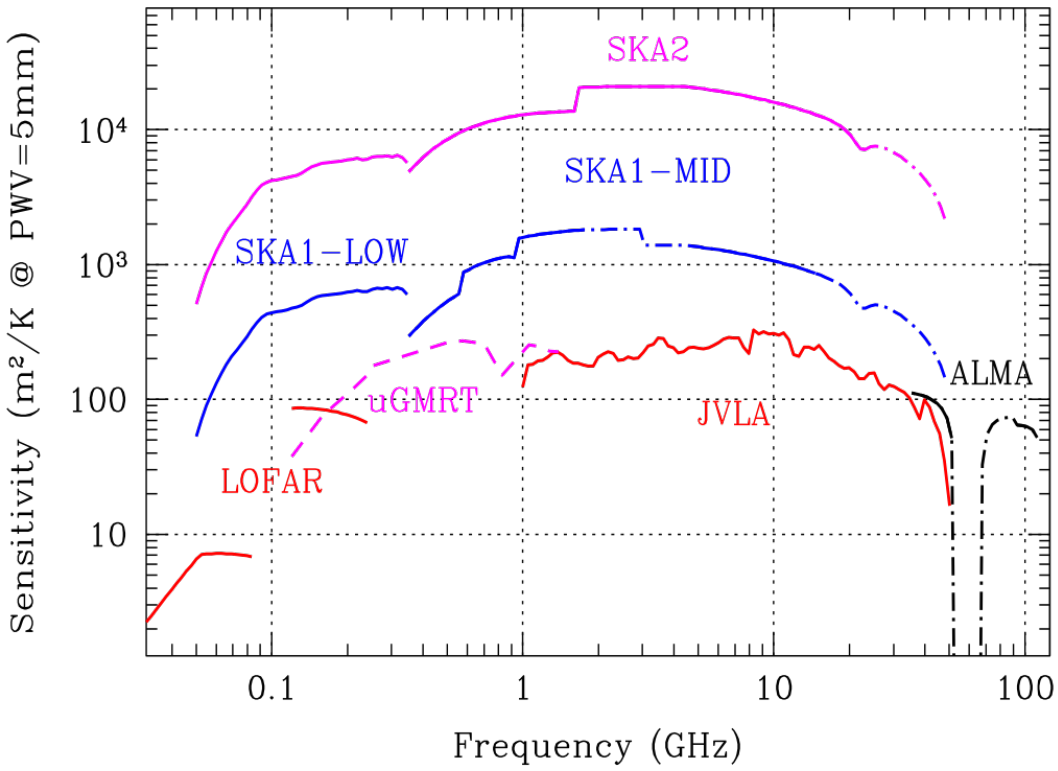

Figure 6.1: Sensitivity of the SKA1 and SKA2 design compared to other instruments. The exact timeline is not yet established but SKA1 should be completed in the late 2020s or early 2030s and SKA2 would be a planned extension to the late 2030s. Credits: Figure taken from Braun et al. (2019)

how techniques and software developed by the communities utilising these telescopes may be highly relevant or directly applicable to SKAO data. They also build up the expertise of engineers and scientists so that new solutions will be found to some of the complexities and problems which will arise with the SKAO.

The technical challenge that the SKAO represents will take a great deal of work from the radio astronomy community, both by those directly employed by the SKAO and those in institutions that aim to utilise SKAO data for science. Combined, the low and mid-frequency instruments will produce 16 petabytes of raw voltage data every second. Although much of this will be immediately thrown array as signals are calibrated, users will inevitably need to transition to a new model in which they interact with data. Processing will happen remotely, with users interacting with data products that have already been run through and reduced by reliable, quality-assured pipelines which have yet to be created.

I am passionate about contributing to this community and expect to play a part in science working groups and the SKAO in general in the next few years. When the first work is being done utilising the groundbreaking new data from the SKAO at the end of this decade, I hope to be a part of both the development and science that we will make possible. For BALQSOs, the sensitivity of the SKAO will only increase the number of detections but the separation of AGN and star formation will become more important than ever as we reach ever further into the radio-quiet population of quasars.

Bibliography

Ade P. A., et al., 2016, Astronomy and Astrophysics, 594, A13 3.1, 5.1

Adelman-McCarthy J. K., 2007, ApJS, 172, 634 3.1

Ai Y., et al., 2020, ApJL, 890, L29 1.1.2

Ak N. F., et al., 2012, ApJ, 757, 114 4.1.2

Alam S., et al., 2015, The Astrophysical Journal Supplement Series, 219, 12 3.2.3

Alegre L., et al., 2022, Monthly Notices of the Royal Astronomical Society, 516, 4716 4.2

Alexander D. M., Hickox R. C., 2012, New Astronomy Reviews, 56, 93 1.2.1

Allen J. T., Hewett P. C., Maddox N., Richards G. T., Belokurov V., 2010, MNRAS, 410, 860 1.3.1, 3.1, 4.1.2

Andonie C., et al., 2022, Monthly Notices of the Royal Astronomical Society, 517, 2577 4.4.1, 4.4.3

Andonie C., et al., 2023, Monthly Notices of the Royal Astronomical Society: Letters, 527, L144 1.4.2

Antonucci R., 1993, Annual Rev. Astron. Astrophys., Vol. 31, p. 473-521 (1993), 31, 473 1.1.4

Appleton P. N., et al., 2004, The Astrophysical Journal Supplement Series, 154, 147 4.4

Arav N., Becker R. H., Laurent-Muehleisen S. A., Gregg M. D., White R. L., de Kool M., 1999, ApJ, 524, 566 3.4.2

Arav N., et al., 2001, ApJ, 561, 118 1.3.1

Arav N., Liu G., Xu X., Stidham J., Benn C., Chamberlain C., 2018, The Astrophysical Journal, 857, 60 3.4.1

Balbus S. A., Hawley J. F., 1991, ApJ, 376, 214 1.1.2

Baldi R. D., et al., 2018, Monthly Notices of the Royal Astronomical Society, 476, 3478 1.4.1

Baldi R. D., Laor A., Behar E., Horesh A., Panessa F., McHardy I., Kimball A., 2022, Monthly Notices of the Royal Astronomical Society, 510, 1043 4.1

Baldwin J. A., 1977, Astrophysical Journal, Vol. 214, pp. 679-684 (1977)., 214, 679 4.1.3

Balokovic M., Smolcic V., Ivezic Z., Zamorani G., Schinnerer E., Kelly B. C., 2012, ApJ, 759, 30 4.3.2

Barthel P. D., Barthel D. P., 1989, ApJ, 336, 606 3.1

Bean B., et al., 2022, Publications of the Astronomical Society of the Pacific, 134, 114501 2.1.3

Becker R. H., White R. L., Helfand D. J., Becker R. H., White R. L., Helfand D. J., 1995, ApJ, 450, 559 1.4.2, 1.4.3, 3.1, 3.1, 3.2.3, 4.1.1, 4.2, 5.1, 5.2.3

Becker R. H., et al., 2000, ApJ, 538, 72 1.4.3, 1.4.3, 3.1, 4.1.2

Begelman M. C., Blandford R. D., Rees M. J., Begelman M. C., Blandford R. D., Rees M. J., 1984, RvMP, 56, 255 1.4.1, 3.4.5

Behar E., Baldi R. D., Laor A., Horesh A., Stevens J., Tzioumis T., 2015, Monthly Notices of the Royal Astronomical Society, 451, 517 1.4.1

Behar E., Vogel S., Baldi R. D., Smith K. L., Mushotzky R. F., 2018, Monthly Notices of the Royal Astronomical Society, 478, 399 4.1

Bell E. F., 2003, The Astrophysical Journal, 586, 794 4.1, 5.1

Best P. N., Heckman T. M., 2012, Monthly Notices of the Royal Astronomical Society, 421, 1569 1.4.1

Best P. N., et al., 2023, Monthly Notices of the Royal Astronomical Society, 523, 1729 4.4.1, 6.2.1

Bischetti M., et al., 2023, The Astrophysical Journal, 952, 44 1.3, 5.1

Blandford R. D., 1990, in Blandford R. D., Netzer H., Woltjer L., Courvoisier T. J. L., Mayor M., eds, Active Galactic Nuclei. pp 161–275 4.1

Blandford R. D., Znajek R. L., 1977, MNRAS, 179, 433 1.4.1, 4.1

Blandford R. D., Payne D. G., Falcke H., Biermann P. L., 1995, A&A, 293, 665 3.4.5

Blundell K. M., Rawlings S., Willott C. J., Blundell K. M., Rawlings S., Willott C. J., 1999, AJ, 117, 677 3.4.3

Bondi M., et al., 2024, Astronomy and Astrophysics, 683, A179 6.2.1

Bonzini M., et al., 2015, Monthly Notices of the Royal Astronomical Society, 453, 1079 4.4

Bower R. G., Benson A. J., Malbon R., Helly J. C., Frenk C. S., Baugh C. M., Cole S., Lacey C. G., 2006, Monthly Notices of the Royal Astronomical Society, Volume 370, Issue 2, pp. 645-655., 370, 645 3.1, 5.1

Braun R., Bonaldi A., Bourke T., Keane E., Wagg J., 2019, arxiv 6.1

Bridle A. H., Schwab F. R., 1999, ASPC, 180, 371 2.3.2

Brotherton M. S., van Breugel W., Smith R. J., Boyle B. J., Shanks T., Croom S. M., Miller L., Becker R. H., 1998, ApJL, 505, L7 1.4.3, 3.1

Bruni G., et al., 2013, A&A, 554, A94 3.1, 5.1

Bruni G., Mack K. H., Montenegro-Montes F. M., Brienza M., González-Serrano J. I., 2015, Astronomy and Astrophysics, 582, A9 3.4.5

Bruni G., Mack K. H., Montenegro-Montes F. M., Brienza M., González-Serrano J. I., 2016, Astronomische Nachrichten, 337, 180 3.4.5

Calistro Rivera G., et al., 2017, Monthly Notices of the Royal Astronomical Society, 469, 3468 1.4.1, 4.1, 4.4, 5.1

Calistro Rivera G., et al., 2021, Astronomy and Astrophysics, 649, A102 1.2.1, 4.1.1, 4.3.1, 4.4.1

Calistro Rivera G., et al., 2023, arXiv, p. arXiv:2312.10177 4.1, 4.1.1, 4.4.2

Cegłowski M., Kunert-Bajraszewska M., Roskowiński C., Cegłowski M., Kunert-Bajraszewska M., Roskowiński C., 2015, MNRAS, 450, 1123 3.1

Chartas G., Brandt W. N., Gallagher S. C., Garmire G. P., 2002, ApJ, 579, 169 1.3.1, 5.1

Chen Z., et al., 2021, arXiv, p. arXiv:2111.09594 1.3, 3.4.4, 5.1

Chevalier R. A., Chevalier A. R., 1982, ApJ, 259, 302 4.4.4

Choi H., Leighly K. M., Terndrup D. M., Dabbieri C., Gallagher S. C., Richards G. T., 2022a, arXiv e-prints, p. arXiv:2203.11964 1.3.1, 3.4.1, 4.4.2, 5.1

Choi H., Leighly K. M., Terndrup D. M., Dabbieri C., Gallagher S. C., Richards G. T., 2022b, The Astrophysical Journal, Volume 937, Issue 2, id.74, ¡NUMPAGES¿48¡/NUMPAGES¿ pp., 937, 74 1.3.1, 5.1

Cicone C., et al., 2014, Astronomy & Astrophysics, 562, A21 5.1

Clavel J., Schartel N., Tomas L., 2005, Astronomy and Astrophysics, 446, 439 3.1

Condon J. J., Condon J. J., 1992, ARA&A, 30, 575 1.4, 1.4.1, 3.4.4, 4.1

Condon J. J., et al., 1998, AJ, 115, 1693 3.1

Congiu E., et al., 2017, Frontiers in Astronomy and Space Sciences, 4, 298947 1.1.4

Corbel S., et al., 2000, A&A, 359, 251 1.1.2

Croton D. J., et al., 2006, MNRAS, 365, 11 3.1, 5.1

Crusoe M. R., et al., 2021, arXiv, p. arXiv:2105.07028 2.3.2

DESI Collaboration et al., 2016, arXiv, p. arXiv:1611.00036 4.3.2, 6.2.1

DESI Collaboration et al., 2023, arXiv, 46, arXiv:2306.06308 6.2.1

Dai X., Shankar F., Sivakoff G. R., 2007, ApJ, 672, 108 1.3.1, 3.1, 4.1.2

Dai X., Shankar F., Sivakoff G. R., 2012, Astrophysical Journal, 757, 180 4.1.2

Davé R., Anglés-Alcázar D., Narayanan D., Li Q., Rafieferantsoa M. H., Appleby S., 2019, Monthly Notices of the Royal Astronomical Society, 486, 2827 1.5, 4.1

De Cicco D., Brandt W. N., Grier C. J., Paolillo M., 2017, FrASS, 4, 64 3.4.3

De Cicco D., et al., 2018, A&A, 616, A114 4.4.4

De Gasperin F., et al., 2019, Astronomy and Astrophysics, 622, A5 2.2.1, 2.3, 2.3.2

Delvecchio I., et al., 2021, Astronomy and Astrophysics, 647, A123 4.1

Dewdney P. E., Hall P. J., Schilizzi R. T., Lazio T. J. L. W., 2009, IEEEP, 97, 1482 6.2.3

Dipompeo M. A., Brotherton M. S., Cales S. L., Runnoe J. C., 2012, Monthly Notices of the Royal Astronomical Society, 427, 1135 3.1

Doi A., et al., 2009, PASJ, 61, 1389 3.1, 5.1

Done C., Gierliński M., Kubota A., 2007, The Astronomy and Astrophysics Review, 15, 1 1.1.2

Donley J. L., Rieke G. H., Perez-Gonzalez P. G., Rigby J. R., Alonso-Herrero A., 2007, ApJ, 660, 167 1.2

Doré O., et al., 2014, arXiv, p. arXiv:1412.4872 6.2.2

Duncan K. J., et al., 2021, Astronomy and Astrophysics, 648, A4 6.2.1

Eisenstein D. J., et al., 2011, Astronomical Journal, 142, 72 3.2.3

Elvis M., et al., 1994, ApJS, 95, 1 1.1.3

Esin A. A., McClintock J. E., Narayan R., 1997, The Astrophysical Journal, 489, 865 1.1.2

Euclid Collaboration et al., 2024, J. W. Nightingale, 63 6.2.2

Everett J. E., Churchwell E., 2010, Astrophysical Journal, 713, 592 4.4.2

Falcke H., Biermann P. L., 1995, A&A, 293, 665 3.4.5

Fanaroff B. L., Riley J. M., 1974, Monthly Notices of the Royal Astronomical Society, Vol. 167, p. 31P-36P (1974), 167, 31P 1.4.1, 4.1, 5.1

Fath A. E., 1909, PA, 17, 504 1.1, 1.1

Faucher-Giguère C.-A., Quataert E., Faucher-Giguère C.-A., Quataert E., 2012, MNRAS, 425, 605 1.3.1, 1.4.1, 3.4.3, 4.1, 5.1

Fawcett V. A., 2022, PhD thesis, Durham University, Durham (document)

Fawcett V. A., et al., 2020, MNRAS, 494, 4802 1.4.2, 3.3.2, 4.1.1, 4.2, 4.4, 4.4.1, 5.4.3

Fawcett V. A., Alexander D. M., Rosario D. J., Klindt L., 2021, Galaxies, 9, 107 1.10

Fawcett V. A., Alexander D. M., Rosario D. J., Klindt L., Lusso E., Morabito L. K., Calistro Rivera G., 2022, Monthly Notices of the Royal Astronomical Society, 513, 1254 1.4.2, 3.3.3, 3.4.1, 4.1.1

Fawcett V. A., et al., 2023, Monthly Notices of the Royal Astronomical Society, 525, 5575 1.4.2, 4.1.1, 4.3.2, 4.4.2

Ferland G. J., et al., 2013, RMxAA, 49, 137 1.3.1

Ferrarese L., Merritt D., Ferrarese L., Merritt D., 2000, ApJL, 539, L9 3.1, 5.1

Feruglio C., et al., 2015, Astronomy and Astrophysics, 583, A99 4.1

Filbert S., et al., 2023, arXiv, p. arXiv:2309.03434 5.1

Foltz C. B., Weymann R. J., Morris S. L., Turnshek D. A., 1987, The Astrophysical Journal, 317 3.1

Fukumura K., Tombesi F., Kazanas D., Shrader C., Behar E., Contopoulos I., 2013, Astrophysical Journal, 780, 120 3.4.3

Gallagher S. C., Brandt W. N., Sambruna R. M., Mathur S., Yamasaki N., 1999, ApJ, 519, 549 1.3

Gallagher S. C., Richards G. T., Lacy M., Hines D. C., Elitzur M., Storrie-Lombardi L. J., 2007, ApJ, 661, 30 4.3.1

Garrington S. T., et al., 2004, Ground-based Telescopes. Edited by Oschmann, Jacobus M., Jr. Proceedings of the SPIE, Volume 5489, pp. 332-343 (2004)., 5489, 332 2.2.2

Gaskell C. M., 1982, Astrophysical Journal, Vol. 263, p. 79-86 (1982), 263, 79 4.1.3

Gebhardt K., et al., 2000, ApJL, 539, L13 3.1

Ghosh K. K., Punsly B., 2007, The Astrophysical Journal, 661, L139 3.1, 3.4.5, 4.1.2

Gibson R. R., et al., 2009, Astrophysical Journal, 692 3.1, 5.1

Gilli R., et al., 2022, Astronomy and Astrophysics, 666, A17 1.3

Girdhar A., et al., 2022, Monthly Notices of the Royal Astronomical Society, 512, 1608 4.1

Giustini M., Proga D., 2019, Astronomy and Astrophysics, 630, A94 4.1.3

Glikman E., Helfand D. J., White R. L., Becker R. H., Gregg M. D., Lacy M., 2007, The Astrophysical Journal, 667, 673 1.4.3, 4.1.1

Glikman E., et al., 2012, Astrophysical Journal, 757, 51 1.2.1

Glikman E., Simmons B., Mailly M., Schawinski K., Urry C. M., Lacy M., 2015, Astrophysical Journal, 806, 218 1.2.1

Glikman E., et al., 2022, The Astrophysical Journal, 934, 119 4.2

Green P. J., et al., 2001, ApJ, 558, 109 1.3, 3.1

Greenstein J. L., 1961, Astrophysical Journal, vol. 133, p.335-337, 133, 335 1.2

Greenstein J. L., Matthews T. A., 1963, Natur, 197, 1041 1.2

Greenstein J. L., Schmidt M., 1964, ApJ, 140, 1 1.2

Greenwell C., Gandhi P., Stern D., Lansbury G., Mainieri V., Boorman P., Toba Y., 2024, Monthly Notices of the Royal Astronomical Society, 527, 12065 1.2

Gregg M. D., Becker R. H., White R. L., Helfand D. J., McMahon R. G., Hook I. M., 1996, Astronomical Journal v.112, p.407, 112, 407 1.4.3

Gregg M. D., Becker R. H., de Vries W., Gregg M. D., Becker R. H., de Vries W., 2006, ApJ, 641, 210 4.1.2

Grupe D., Mathur S., Elvis M., 2003, AJ, 126, 1159 1.3

Gürkan G., et al., 2018, Monthly Notices of the Royal Astronomical Society, 475, 3010 1.4.1, 4.1, 4.4

Hall P. B., et al., 2002, The Astrophysical Journal Supplement Series, 141, 267 1.3.2, 3.2.2

Hamann F. W., Barlow T. A., Chaffee F. C., Foltz C. B., Weymann R. J., 2000, The Astrophysical Journal, Volume 550, Issue 1, pp. 142-152., 550, 142 1.3.1

Hamann F., Herbst H., Paris I., Capellupo D., Hamann F., Herbst H., Paris I., Capellupo D., 2019, MNRAS, 483, 1808 3.1

Hardcastle M. J., 2018, Monthly Notices of the Royal Astronomical Society, 475, 2768 1.4.1, 3.4.3, 4.1, 4.4.4, 5.1

Hardcastle M. J., et al., 2019, A&A, 622, A12 4.1, 5.1

Hardcastle M. J., Horton M., Williams W., Duncan K., Alegre L., Barkus B., Croston J., 2023, Astronomy & Astrophysics, 678, A151 4.2, 5.2.1

Harrison C. M., 2014, PhD thesis, Durham University, Durham 1.3

Harrison C. M., Ramos Almeida C., 2024, Galaxies, 12, 17 5.1

He Z., et al., 2022, Science Advances, 8 3.4.1

Heisler C. A., Lumsden S. L., Bailey J. A., 1997, Nature, Volume 385, Issue 6618, pp. 700-702 (1997)., 385, 700 1.1.4

Helou G., Soifer B. T., Rowan-Robinson M., Helou G., Soifer B. T., Rowan-Robinson M., 1985, ApJL, 298, L7 4.1, 5.1

Herrera Ruiz N., Middelberg E., Norris R. P., Maini A., 2016, Astronomy and Astrophysics, 589, L2 4.4

Hewett P. C., Foltz C. B., 2003, The Astronomical Journal, 125, 1784 1.3, 1.4.3

Hickox R. C., et al., 2007, The Astrophysical Journal, Volume 671, Issue 2, pp. 1365-1387., 671, 1365 1.2

Hickox R. C., et al., 2014, ApJ, 782, 9 3.4.4

Higginbottom N., Knigge C., Long K. S., Sim S. A., Matthews J. H., 2013, Monthly Notices of the Royal Astronomical Society, 436, 1390 1.3.1, 3.2.2

Högbom J. A., 1974, A&AS, 15, 417 2.1.2

Hopkins P. F., Hernquist L., Cox T. J., Di Matteo T., Robertson B., Springel V., 2005, ApJ, 632, 81 4.1.2

Hopkins P. F., Hernquist L., Cox T. J., Kereš D., 2008, The Astrophysical Journal Supplement Series, 175, 356 1.2.1, 4.1.1, 4.4.3

Hubble E. P., 1926, ApJ, 64, 321 1.1

Huško F., Lacey C. G., Schaye J., Schaller M., Nobels F. S., 2022, Monthly Notices of the Royal Astronomical Society, 516, 3750 4.1

Israel W., 1968, CMaPh, 8, 245 1.1.1

Jackson N., Rawlings S., 1997, Monthly Notices of the Royal Astronomical Society, 286, 241 1.4.1

Jackson N., et al., 2016, Astronomy and Astrophysics, 595, A86 2.3.1

Jackson N., et al., 2022, Astronomy and Astrophysics, 658, A2 2.3.1

Jannuzi B. T., et al., 1996, ApJL, 470, L11 1.3.2

Jansky K. G., 1933, Natur, 132, 66 1.2

Jarvis M. E., et al., 2019, Monthly Notices of the Royal Astronomical Society, 485, 2710 4.1, 4.4, 5.1, 5.4.1

Jarvis M. E., et al., 2021, Monthly Notices of the Royal Astronomical Society, 503, 1780 1.4.1

Jiang D. R., Wang T. G., 2003, Astronomy and Astrophysics, v.397, p.L13-L16 (2003), 397, L13 1.4.3, 3.1, 5.1

Kellermann K. I., Sramek R., Schmidt M., Shaffer D. B., Green R., 1989, The Astronomical Journal, 98, 1195 1.4.1, 3.1, 3.2.2, 4.1

Kerr R. P., 1963, PhRvL, 11, 237 4.1

Kimball A. E., Kellermann K. I., Condon J. J., Ivezic Z., Perley R. A., 2011, ApJL, 739, L29 4.1, 4.4

Klindt L., 2022, PhD thesis, Durham University, Durham (document)

Klindt L., et al., 2019, MNRAS, 488, 3109 1.4.2, 3.3.2, 4.1.1, 4.2, 4.3.1, 4.4.1, 4.4.3, 5.4.3, 4

Knigge C., Scaringi S., Goad M. R., Cottis C. E., 2008, Monthly Notices of the Royal Astronomical Society, 386, 1426 1.3.2, 3.2.2

Kondapally R., et al., 2021, Astronomy and Astrophysics, 648, A3 4.2, 6.2.1

Körding E. G., Jester S., Fender R., 2006a, Monthly Notices of the Royal Astronomical Society, 372, 1366 1.1.2

Körding E., Falcke H., Corbel S., 2006b, Astronomy and Astrophysics, 456, 439 1.1.2

Kormendy J., Ho L. C., Kormendy J., Ho L. C., 2013, ARA&A, 51, 511 1, 3.1, 4.1, 5.1

Kozłowski S., 2017, The Astrophysical Journal Supplement Series, 228, 9 **??**, 3.1, 3.2.3, 3.3.1

Kratzer R. M., Richards G. T., Kratzer R. M., Richards G. T., 2015, AJ, 149, 61 3.3.4

Krawczyk C. M., Richards G. T., Gallagher S. C., Leighly K. M., Hewett P. C., Ross N. P., Hall P. B., 2015, Astronomical Journal, 149, 203 4.1.1

Krogager J. K., et al., 2023, Msngr, 190, 38 4.4.2, 6.2.1

Kukula M. J., Dunlop J. S., Hughes D. H., Rawlings S., 1998, MNRAS, 297, 366 4.1, 4.4, 5.1

Kunert-Bajraszewska M., Marecki A., 2007, A&A, 469, 437 1.4.3

Lacy M., et al., 2020, Publications of the Astronomical Society of the Pacific, 132, 035001 5.2.3

Lamy H., Hutsemékers D., Lamy H., Hutsemékers D., 2000, A&A, 356, L9 3.4.2

Laor A., Behar E., 2008, Monthly Notices of the Royal Astronomical Society, 390, 847 1.4.1

Leftley J. H., Hönig S. F., Asmus D., Tristram K. R. W., Gandhi P., Kishimoto M., Venanzi M., Williamson D. J., 2019, The Astrophysical Journal, 886, 55 5.4.3

Leighly K. M., Terndrup D. M., Gallagher S. C., Richards G. T., Dietrich M., 2018, The Astrophysical Journal, 866, 7 1.3.1, 4.4.2

Leipski C., Falcke H., Bennert N., Huettemeister S., ; 2006, A&A, 455, 161 4.1, 4.4

Lipari S., et al., 2009, Monthly Notices of the Royal Astronomical Society, 392, 1295 3.1

Liu B. F., Taam R. E., 2009, The Astrophysical Journal, 707, 233 1.2

Liu Y., Jiang D. R., Wang T. G., Xie F. G., 2008, Monthly Notices of the Royal Astronomical Society, 391, 246 1.4.3

Lobanov A. P., 1998, A&A, 330, 79 1.4.1

Lynds C. R., 1967, ApJ, 147, 396 1.3

Ma Y., Goulding A., Greene J. E., Zakamska N. L., Wylezalek D., Jiang Y.-F., 2024, arXiv, p. arXiv:2401.04177 1.2.1

Macfarlane C., et al., 2021, Monthly Notices of the Royal Astronomical Society, 506, 5888 1.4.1, 4.1, 4.4, 5.1

Madau P., Dickinson M., 2014, Annual Review of Astronomy and Astrophysics, 52, 415 3.1

Maini A., Prandoni I., Norris R. P., Giovannini G., Spitler L. R., 2016, A&A, 589, L3 4.4

Mancuso C., et al., 2017, The Astrophysical Journal, 842, 95 4.4

Matt G., Guainazzi M., Maiolino R., 2003, MNRAS, 342, 422 1.1.2

Matthews T. A., Sandage A. R., 1963, ApJ, 138, 30 1.2

Matthews J. H., Knigge C., Long K. S., Sim S. A., Higginbottom N., Mangham S. W., 2016, MNRAS, 458, 293 1.5, 1.3.1, 3.2.2, 3.4.5, 5.1

Matthews J. H., Knigge C., Higginbottom N., Long K. S., Sim S. A., Mangham S. W., Parkinson E. J., Hewitt H. A., 2020, Monthly Notices of the Royal Astronomical Society, 492, 5540 3.2.2

McCaffrey T., Richards G. T., 2021, CIV Distance, doi:10.17918/CIVdistance 4.2

McCaffrey T. V., Kimball A. E., Momjian E., Richards G. T., 2022, AJ, 164, 122 4.4

McCready L. L., Pawsey J. L., Payne-Scott R., McCready L. L., Pawsey J. L., Payne-Scott R., 1947, RSPSA, 190, 357 2.1

Mehdipour M., Costantini E., 2019, Astronomy and Astrophysics, 625, 25 1.4.3, 3.4.3, 4.4

Mereghetti S., et al., 2021, Experimental Astronomy, 52, 309 1.1.2

Mingo B., et al., 2022, Monthly Notices of the Royal Astronomical Society, 511, 3250 1.4.1

Mishra S., Vivek M., Chand H., Joshi R., 2021, MNRAS, 504, 3187 3.4.3, 4.1.2, 4.4.4

Mohan N., Rafferty D., 2015, PyBDSF: Python Blob Detection and Source Finder, `https://ui.adsabs.harvard.edu/abs/2015ascl.soft02007M/abstract` 5.2.2

Moldon J., Moldon Javier 2021, ascl, p. ascl:2109.006 5.2.2

Montenegro-Montes F. M., Mack K. H., Vigotti M., Benn C. R., Carballo R., Gonzalez-Serrano J. I., Holt J., Jimenez-Lujan F., 2008, MNRAS, 388, 1853 1.4.3

Montenegro-Montes F. M., Mack K. H., Benn C. R., Carballo R., González-Serrano J. I., Holt J., Jiménez-Luján F., 2009, AN, 330, 157 1.4.3

Morabito L. K., Dai X., Leighly K. M., Sivakoff G. R., Shankar F., 2013, Astrophysical Journal, 786, 58 3.1

Morabito L. K., Dai X., Leighly K. M., Sivakoff G. R., Shankar F., 2014, The Astrophysical Journal, 786, 58 1.3

Morabito L. K., et al., 2019, Astronomy and Astrophysics, 622, A15 (document), 1.4.3, 1.11, 1.5, 3.1, 3.2.2, 3.2.2, 3.2.2, 3.2.3, 3.3.1, 3.4.5, 4.1.2, 4.4.2, 5.1, 5.2.1, 5.2.1, 5.3.2, 6.1

Morabito L. K., et al., 2022a, Monthly Notices of the Royal Astronomical Society, 515, 5758 4.1, 4.4

Morabito L. K., et al., 2022b, Astronomy and Astrophysics, 658, A1 2.2.1, 2.3.2, 3.5

Mulchaey J. S., Wilson A. S., Tsvetanov Z., 1996, ApJ, 467, 197 1.1.4

Murray N., Chiang J., Grossman S. A., Voit G. M., 1995, ApJ, 451, 498 1.3.1

Narayan R., Yi I., 1995, The Astrophysical Journal, 452, 710 1.1.2

Nims J., Quataert E., Faucher-Giguére C. A., 2015, Monthly Notices of the Royal Astronomical Society, 447, 3612 1.4.1, 1.9, 3.4.5, 4.1, 4.4.5, 4.8, 5, 5.1

Nyland K., et al., 2021, Proceedings of the International Astronomical Union, pp 27–32 3.4.3

Offringa A. R., et al., 2014, Monthly Notices of the Royal Astronomical Society, 444, 606 5.2.2

Oke J. B., 1963, Natur, 197, 1040 1.2

Ostriker J. P., et al., 2010, ApJ, 722, 642 4.1

Pacholczyk G. A., 1970, Radio astrophysics. Nonthermal processes in galactic and extragalactic sources. Freeman: Series of Books in Astronomy and Astrophysics, San Francisco, `https://ui.adsabs.harvard.edu/abs/1970ranp.book.....P/abstract` 1.6

Padovani P., Miller N., Kellermann K. I., Mainieri V., Rosati P., Tozzi P., 2011, Astrophysical Journal, 740, 20 3.4.3

Panessa F., Barcons X., Bassani L., Cappi M., Carrera F. J., Ho L. C., Pellegrini S., 2007, Astronomy and Astrophysics, 467, 519 1.4.1

Panessa F., et al., 2019, NatAs, 3, 387 1.4.1, 1.7, 3.4.5, 4.1, 4.4, 5.1

Paris I., et al., 2017, VizieR Online Data Catalog, p. VII/279 3.1, 5.2.1, 5.2.1, 5.1

Pâris I., et al., 2018, Astronomy and Astrophysics, 613, A51 1.4.3, 4.2, 5.1

Pei Y. C., Pei C. Y., 1992, ApJ, 395, 130 3.2.2

Petley J. W., et al., 2022, Monthly Notices of the Royal Astronomical Society, 515, 5159 3, 4.1.2, 4.4.2, 5.1, 5.2.1, 5.2.1, 5.3.2, 5.5

Petley J. W., et al., 2024, Monthly Notices of the Royal Astronomical Society, Volume 529, Issue 3, pp.1995-2007, 529, 1995 4, 5.4.3, 5.5

Pounds K. A., Reeves J. N., King A. R., Page K. L., O'Brien P. T., Turner M. J. L., 2003a, MNRAS, 345, 705 4.1, 5.1

Pounds K. A., King A. R., Page K. L., O'Brien P. T., 2003b, MNRAS, 346, 1025 1.3.1

Proga D., Stone J. M., Kallman T. R., 2000, The Astrophysical Journal, 543, 686 1.3.1

Raginski I., Laor A., 2016, Monthly Notices of the Royal Astronomical Society, 459, 2082 4.1

Ramos Almeida C., et al., 2011, ApJ, 731, 92 1.1.4

Rankine A. L., Hewett P. C., Banerji M., Richards G. T., 2020, Monthly Notices of the Royal Astronomical Society, 492, 4553 3.2.3, 3.3.4, 4.1.3, 4.2, 4.2, 4.3.1, 4.4.2, 4.5

Rankine A. L., Matthews J. H., Hewett P. C., Banerji M., Morabito L. K., Richards G. T., 2021, Monthly Notices of the Royal Astronomical Society, 502, 4154 1.5, 3.3.4, 4.1.3, 4.3.1, 4.3.2

Reber G., 1944, Astrophysical Journal, vol. 100, p.279, 100, 279 1.2

Reichard T. A., et al., 2003, AJ, 125, 1711 1.3, 1.3.1, 3.1, 3.2.2, 3.2.2

Ricci C., Trakhtenbrot B., 2023, Nature Astronomy, 7, 1282 1.1.2

Richards G. T., Vanden Berk D. E., Reichard T. A., Hall P. B., Schneider D. P., SubbaRao M., Thakar A. R., York D. G., 2002, The Astronomical Journal, 124, 1 4.1.3

Richards G. T., et al., 2003, AJ, 126, 1131 1.2.1, 1.3, 4.1.1, 4.2

Richards G. T., et al., 2006, The Astrophysical Journal Supplement Series, 166, 470 3.2.2, 4.3.1, 4.4.5

Richards G. T., et al., 2011, Astronomical Journal, 141, 167 3.3.4, 4.1.3

Richards G. T., McCaffrey T. V., Kimball A., Rankine A. L., Matthews J. H., Hewett P. C., Rivera A. B., 2021, The Astronomical Journal, 162, 270 1.4.3, 3.3.4, 4.1.3, 4.4.1

Rivera A. B., Richards G. T., Hewett P. C., Rankine A. L., 2020, The Astrophysical Journal, 899, 96 4.2

Rivera A. B., Richards G. T., Gallagher S. C., McCaffrey T. V., Rankine A. L., Hewett P. C., Shemmer O., 2022, ApJ, 931, 154 4.2

Rodríguez Hidalgo P., Khatri A. M., Hall P. B., Haas S., Quintero C., Khatu V., Kowash G., Murray N., 2020, The Astrophysical Journal, 896, 151 1.3.2, 5.1

Rogerson J. A., Hall P. B., Hidalgo P. R., Pirkola P., Brandt W. N., Ak N. F., 2015, MNRAS, 457, 405 1.3.2

Rosario D. J., et al., 2020, MNRAS, 494, 3061 1.4.2, 3.3.2, 4.1.1, 4.2, 4.4

Rosario D. J., et al., 2021, MNRAS, 505, 5283 1.4.2, 4.1.1, 4.4.3, 5.4.3

Rose M., Tadhunter C., Holt J., Zaurín J. R., 2013, MNRAS, 432, 2150 1.2.1

Ruan J. J., Anderson S. F., Eracleous M., Green P. J., Haggard D., MacLeod C. L., Runnoe J. C., Sobolewska M. A., 2019, The Astrophysical Journal, 883, 76 1.1.2

Ryle M., 1962, Natur, 194, 517 2.1.1

Sabater J., et al., 2020, Astronomy & Astrophysics, Volume 648, id.A2, ¡NUMPAGES¿20¡/NUMPAGES¿ pp., 648, A2 6.2.1

Sabra B. M., Hamann F., 2001, ApJ, 563, 555 1.3

Sadler E. M., 2016, Astronomische Nachrichten, 337, 105 4.1

Sanders D. B., Soifer B. T., Elias J. H., Neugebauer G., Matthews K., 1988, ApJL, 328, L35 4.4.3

Sargent M. T., et al., 2010, Astrophysical Journal Letters, 714, L190 1.4.1, 4.4

Schmidt M., 1963, Nature, Volume 197, Issue 4872, pp. 1040 (1963)., 197, 1040 1.2

Schmidt M., 1970, Astrophysical Journal, vol. 162, p.371, 162, 371 1.2

Schmidt M., Schmidt Maarten 1968, ApJ, 151, 393 4.1

Schulze A., et al., 2017, The Astrophysical Journal, 848, 104 1.3.1, 3.1, 5.1

Seyfert C. K., 1943, ApJ, 97, 28 1.1

Shakura N. I., Sunyaev R. A., 1973, A&A, 24, 337 1.1.2, 1.2, 1.3.1, 1.4.1

Shen Y., et al., 2011, The Astrophysical Journal Supplement Series, 194, 45 5.1

Shen X., Hopkins P. F., Faucher-Giguère C. A., Alexander D. M., Richards G. T., Ross N. P., Hickox R. C., 2020, Monthly Notices of the Royal Astronomical Society, 495, 3252 1.2

Shimwell T. W., et al., 2019, Astronomy and Astrophysics, 622, A1 1.4.2, 1.4.3, 3.1, 4.1.1

Shimwell T. W., et al., 2022a, VizieR Online Data Catalog, pp J/A+A/659/A1 2

Shimwell T. W., et al., 2022b, A&A, 659, A1 3.1, 3.2.1, 3.1, 3.4.5, 4.2, 5.1, 5.2.1, 5.2.3

Sikora M., Stawarz Ł., Lasota J.-P., 2007, ApJ, 658, 815 4.4.2

Silk J., 2003, Monthly Notices of the Royal Astronomical Society, 343, 249 4.4.3

Skrutskie M. F., et al., 2006, The Astronomical Journal, Volume 131, Issue 2, pp. 1163-1183., 131, 1163 1.4.3, 3.1

Smith D. J. B., et al., 2016, in Reylé C., Richard J., Cambrésy L., Deleuil M., Pécontal E., Tresse L., Vauglin I., eds, SF2A-2016: Proceedings of the Annual meeting of the French Society of Astronomy and Astrophysics. pp 271–280 3.3.1, 4.4.2

Smith D. J., et al., 2021, Astronomy and Astrophysics, 648, A6 1.4.1, 4.4, 4.4.1

Sniegowska M., Czerny B., Bon E., Bon N., 2020, Astronomy and Astrophysics, 641, A167 1.1.2

Sobolewska M. A., Done C., 2007, Monthly Notices of the Royal Astronomical Society, 374, 150 1.1.3

Soliman N. H., Hopkins P. F., 2023, Monthly Notices of the Royal Astronomical Society, 525, 2668 1.3.1, 1.4.2, 4.4.2, 5.4.3

Sopp H. M., Alexander P., Sopp H. M., Alexander P., 1991, MNRAS, 251, 14P 1.4.1, 4.4

Sprayberry D., Foltz C. B., Sprayberry D., Foltz C. B., 1992, ApJ, 390, 39 1.3, 3.1

Stalin C. S., Srianand R., Petitjean P., 2010, MNRAS, 413, 1013 1.3

Stanley F., Harrison C. M., Alexander D. M., Swinbank A. M., Aird J. A., Del Moro A., Hickox R. C., Mullaney J. R., 2015, Monthly Notices of the Royal Astronomical Society, 453, 591 4.4.2

Steenbrugge K. C., Jolley E. J. D., Kuncic Z., Blundell K. M., 2010, MNRAS, 413, 1735 3.4.5

Stocke J. T., Morris S. L., Weymann R. J., Foltz C. B., Stocke J. T., Morris S. L., Weymann R. J., Foltz C. B., 1992, ApJ, 396, 487 1.4.3, 3.1, 4.1.2, 5.1

Sulentic J. W., Zamfir S., Marziani P., Bachev R., Calvani M., Dultzin-Hacyan D., 2003, ApJL, 597, L17 4.1.3

Sulentic J. W., Bachev R., Marziani P., Negrete C. A., Dultzin D., 2007, The Astrophysical Journal, 666, 757 4.1.3

Sulentic J. W., et al., 2017, Astronomy and Astrophysics, 608, A122 4.1.3

Sweijen F., et al., 2022, NatAs, 6, 350 2.1.3, 2.2, 6.2.1

Tasse C., et al., 2020, A&A, 648, A1 4.4.1, 6.2.1

Temple M. J., Banerji M., Hewett P. C., Rankine A. L., Richards G. T., 2021, Monthly Notices of the Royal Astronomical Society, 501, 3061 4.4.2

Temple M. J., et al., 2023, arXiv, 000, arXiv:2301.02675 4.1.3, 1

Thomas N., Davé R., Jarvis M. J., Anglés-Alcázar D., 2021, Monthly Notices of the Royal Astronomical Society, 503, 3492 1.4.1, 4.1

Thompson T. A., Quataert E., Waxman E., Murray N., Martin C. L., 2006, ApJ, 645, 186 1.4.1, 5.1

Thompson T. A., Fabian A. C., Quataert E., Murray N., 2015, Monthly Notices of the Royal Astronomical Society, 449, 147 1.3.1

Trump J. R., et al., 2006, The Astrophysical Journal Supplement Series, 165, 1 1.3.1, 1.3.2, 1.4.3, 3.1, 3.2.2, 5.1

Urrutia T., et al., 2009, ApJ, 698, 1095 1.2.1, 1.3, 1.4.3, 3.1, 3.3.3, 4.1.2, 5.4.3, 4

Vejlgaard S., et al., 2024, arXiv, p. arXiv:2401.02783 4.4.2, 4.4.2

Wang R., Wu X.-B., Kong M.-Z., 2006, ApJ, 645, 890 1.4.1

Wang H., Wang T., Zhou H., Liu B., Wang J., Yuan W., Dong X., 2011, ApJ, 738, 85 4.1.3

Webster R. L., et al., 1995, Natur, 375, 469 4.1.1

Weedman D. W., Weedman W. D., 1970, ApJ, 159, 405 4.1

Weiler K. W., Sramek R. A., Panagia N., van der Hulst J. M., Salvati M., 1986, ApJ, 301, 790 4.4.4

Wethers C. F., Kotilainen J., Schramm M., Schulze A., 2020, Monthly Notices of the Royal Astronomical Society, 498, 1469 1.3, 3.4.4, 5.1

Weymann R. J., Carswell R. F., Smith M. G., 1981, ARA&A, 19, 41 1.3, 1.4.3, 5.1

Weymann R. J., Morris S. L., Foltz C. B., Hewett P. C., 1991, The Astrophysical Journal, 373, 23 1.3.1, 1.3.2, 3.1, 3.2.2, 4.1, 4.1.2, 5.2.1

White R. L., et al., 1999, ApJS, 126, 133 1.4.3

White S. V., Jarvis M. J., Häußler B., Maddox N., 2015, Monthly Notices of the Royal Astronomical Society, 448, 2665 3.4.3, 4.1

Whittam I. H., Prescott M., McAlpine K., Jarvis M. J., Heywood I., 2018, Monthly Notices of the Royal Astronomical Society, 480, 358 1.4.1

Whittam I. H., et al., 2022, Monthly Notices of the Royal Astronomical Society, 516, 245 1.4.1

Wilkes J. B., 1984, MNRAS, 207, 73 4.1.3

Wilkes B. J., Schmidt G. D., Cutri R. M., Ghosh H., Hines D. C., Nelson B., Smith P., 2001, ApJL, 564, L65 1.2.1

Williams W. L., et al., 2019, A&A, 622, A2 3.2.3

Wilson A. S., Colbert E. J. M., 1995, The Astrophysical Journal, 438, 62 4.1

Woltjer L., 1959, ApJ, 130, 38 1.1.4

Yamada T., Sakai N., Inoue Y., Michiyama T., 2024, arXiv, p. arXiv:2404.04632 5.1

York D. G., et al., 2000, The Astronomical Journal, 120, 1579 3.1

Yue B.-H., et al., 2024, Monthly Notices of the Royal Astronomical Society 1.4.1, 5.1

Zakamska N. L., Greene J. E., 2014, Monthly Notices of the Royal Astronomical Society, 442, 784 3.4.5

de Jong R. S., et al., 2016, Ground-based and Airborne Instrumentation for Astronomy VI, 9908, 99081O 6.2.1

de Kool M., Arav N., Becker R. H., Gregg M. D., White R. L., Laurent-Muehleisen S. A., Price T., Korista K. T., 2000, ApJ, 548, 609 1.3.1

de Kool M., Korista K. T., Arav N., 2002, ApJ, 580, 54 1.3.1

van Haarlem M. P., et al., 2013, A&A, 556, A2 1.4.3, 2.2.1, 3.1

Glossary

ADAF	Advection-Dominated Accretion Flow
AGN	Active Galactic Nuclei
BALQSO	Broad Absorption Line QSO
eMERLIN	enhanced Multi Element Remotely Linked Interferometer Network
FIRST	Faint Images of the Radio Sky at Twenty centimetres
GMRT	Giant Metrewave Radio Telescope
HiBAL	High-Ionisation Broad Absorption Line Quasar
LoBAL	Low-Ionisation Broad Absorption Line Quasar
LOFAR	LOw Frequency ARray - Radio telescope based in the Netherlands
LoTSS	LOFAR Two-metre Sky Survey
QSO	Quasi-Stellar Object - Identified using optical spectra
Quasar	Powerful AGN - Identified at any wavelength
SDSS	Sloan Digital Sky Survey
SKA	Square Kilometre Array
SMBH	Supermassive Black Hole
TEC	Total Electron Content
TGSS	Tata Institute of Fundamental Research GMRT Sky Survey
2MASS	Two Micron All Sky Survey
VLA	Very Large Array
VLASS	VLA Sky Survey

VLBI Very Long Baselines Interferometry

α Spectral Index

λ Either wavelength or black hole accretion rate